STATE OF CALIFORNIA • DEPARTMENT OF TRANSPORTATION

TECHNICAL REPORT DOCUMENTATION PAGE

TR0003 (REV 10/98)

ADA Notice

For individuals with sensory disabilities, this document is available in alternate formats. For information call (916) 654-6410 or TDD (916) 654-3880 or write Records and Forms Management, 1120 N Street, MS-89, Sacramento, CA 95814.

1. REPORT NUMBER CA15-2287 - Part 2 of 2	2. GOVERNMENT ASSOCIATION NUMBER	3. RECIPIENT'S CATALOG NUMBER

4. TITLE AND SUBTITLE

Analytical and Experimental Development of Bridges with Foundations Allowed to Uplift
Part II: Analytical Studies

5. REPORT DATE

October 2015

6. PERFORMING ORGANIZATION CODE

UCB

7. AUTHOR

A. G. Gavras, G. Antonellis, M. Panagiotou, and B. L. Kutter

8. PERFORMING ORGANIZATION REPORT NO.

UCB/CA15-2287

9. PERFORMING ORGANIZATION NAME AND ADDRESS

Department of Civil and Environmental Engineering
University of California, Berkeley
747 Davis Hall
Berkeley, CA 94720-1792

10. WORK UNIT NUMBER

11. CONTRACT OR GRANT NUMBER

65A0487

12. SPONSORING AGENCY AND ADDRESS

California Department of Transportation
Engineering Service Center
1801 30th Street, MS 9-2/5i
Sacramento, California 95816

California Department of Transportation
Division of Research and Innovation, MS-83
1227 O Street
Sacramento CA 95814

13. TYPE OF REPORT AND PERIOD COVERED

Final Report
2/1/2013 – 7/31/2015

14. SPONSORING AGENCY CODE

913

15. SUPPLEMENTARY NOTES

Prepared in cooperation with the State of California Department of Transportation.

16. ABSTRACT

Experimental research has shown that rocking shallow foundations have the potential to develop large earthquake-induced lateral displacements with acceptable permanent deformations. Therefore, this alternative seismic design philosophy has the potential to become an economical earthquake protection solution for bridges.

This study developed displacement-based analysis (DBA) guidelines for the seismic design of ordinary bridges with rocking shallow foundations. The guidelines cover the case of single rocking bents but especially address the system level design of bridges with columns on rocking foundations. For the single rocking bent model, the proposed method is based on the study by Deng et al. [2014], but with equivalent viscous damping ratios calibrated from nonlinear response history analysis (NRHA) of bridge columns on rocking foundations. The method also addresses the design of single bents that combine rocking of shallow foundations and plastic hinging at the top of the columns. For the system level design, guidelines on how to consider the interaction between the rocking bents and the abutments are developed.

17. KEY WORDS

Seismic, Rocking, Uplift, Column, Footing, Foundation

18. DISTRIBUTION STATEMENT

No restrictions.
This document is available to the public through the National Technical Information Service, Springfield, VA 22161

19. SECURITY CLASSIFICATION *(of this report)* Unclassified	20. NUMBER OF PAGES 177	21. COST OF REPORT CHARGED

Reproduction of completed page authorized.

DISCLAIMER STATEMENT

REPORT NO.
UCB/SEMM-2015/XX

STRUCTURAL ENGINEERING
MECHANICS AND MATERIALS

ANALYTICAL AND EXPERIMENTAL DEVELOPMENT OF BRIDGES WITH FOUNDATIONS ALLOWED TO UPLIFT.

PART II: ANALYTICAL STUDIES

BY

A. G. GAVRAS
G. ANTONELLIS
M. PANAGIOTOU
B. L. KUTTER

1868

DEPARTMENT OF CIVIL & ENVIRONMENTAL ENGINEERING
COLLEGE OF ENGINEERING
UNIVERSITY OF CALIFORNIA AT BERKELEY

September 2015

Analytical and Experimental Development of Bridges with Foundations Allowed to Uplift During Earthquakes.
Part II: Analytical Studies

A. G. Gavras[*], G. Antonellis[†], M. Panagiotou[†] and B. L. Kutter[*]

Structural Engineering Mechanics and Materials Report UCB/SEMM – 2015/XX

Acknowledgements

This work was supported by the California Department of Transportation under Agreement 65A0487. This support is gratefully acknowledged. Any contents, statements, or conclusions expressed in this report are those of authors, and are not necessarily endorsed by the sponsors.

---

[*] University of California at Davis
[†] University of California at Berkeley

Abstract

Experimental research has shown that rocking shallow foundations have the potential to develop large earthquake-induced lateral displacements with acceptable permanent deformations. Therefore, this alternative seismic design philosophy has the potential to become an economical earthquake protection solution for bridges.

This study developed displacement-based analysis (DBA) guidelines for the seismic design of ordinary bridges with rocking shallow foundations. The guidelines cover the case of single rocking bents but especially address the system level design of bridges with columns on rocking foundations. For the single rocking bent model, the proposed method is based on the study by Deng et al. [2014], but with equivalent viscous damping ratios calibrated from nonlinear response history analysis (NRHA) of bridge columns on rocking foundations. The method also addresses the design of single bents that combine rocking of shallow foundations and plastic hinging at the top of the columns. For the system level design, guidelines on how to consider the interaction between the rocking bents and the abutments are developed.

The seismic design concept of using rocking shallow foundations combined with column-top plastic hinging is validated at the system by redesigning two existing Caltrans bridges at a site of very high seismic hazard which is different than the sites of the built bridges. Using three-dimensional nonlinear response history analysis, it is shown that the redesigned bridges sustain the design earthquake with less than 6% drift ratio, less than 1.5% column plastic rotation, and less than 0.5% residual drift ratio. For both bridges this level of response corresponds to limited structural damage ensuring prompt post-earthquake functionality of the bridges.

The proposed system level design guidelines are validated using the case studies of the two bridges described above by comparing NRHA and DBA results. Finally, both the results of NRHA and DBA are compared with the results of commonly used response spectrum analysis.

Table of Contents

1 Introduction

1.1 BACKGROUND AND MOTIVATION

Traditional seismic design of new bridges is based on inelastic behavior of the columns (plastic hinging), while damage below ground is to be avoided [Caltrans 2010; European Committee for Standardization (CEN) 2005]. Such designs are susceptible to considerable damage and permanent lateral displacements that may require costly and time-consuming repairs (and perhaps even demolition) after a seismic event. For example, residual drifts of bridge columns resulted in demolition and replacement of over 100 bridges after the 1995 Kobe earthquake [Jeong et al. 2008].

Recent research and earthquake case histories in the 1995 Kobe earthquake have shown that controlled foundation uplift and/or controlled soil inelastic action, can reduce residual structural rotation, displacement demand, and the collapse potential [Gazetas et al. 2007; Gajan and Kutter 2008; Paolucci et al. 2008; Pecker et al. 2013]. Allowance of foundation rocking may also result in economic savings through reduced footing size and/or avoidance of the need for piles or tie-down anchors.

Foundation rocking can be used to dissipate hysteretic energy without column damage while providing a re-centering tendency [Pecker 2006; Anastasopoulos et al. 2010]. Anastasopoulos et al. [2010] presented a numerical study of a bridge column for which they weakened the foundation so that the soil capacity is mobilized prior to damaging the base of the column. Deng et al. [2012a] tested in centrifuge a simplified 2-span bridge model with columns on rocking foundations whereas Antonellis and Panagiotou [2014] conducted numerical simulations to address the system level seismic response of complete multi-span reinforced concrete bridges with foundations allowed to uplift. Both studies combined the rocking foundation at the base of the column with a pin connection between the column and the overlying deck to allow the bridge column to remain nominally elastic.

The merits and controlling parameters of rocking foundations have been extensively studied experimentally using small-scale 1g [Drosos et al. 2012; Anastasopoulos et al. 2012], large-scale 1g [Negro et al. 2000], and centrifuge [Gajan and Kutter 2008; Gajan and Kutter 2009; Deng and Kutter 2012; Hakhamaneshi et al. 201X] pseudo-static cyclic tests, as well as small-scale 1-g [Anastasopoulos et al. 2013], large-scale 1g [Shirato et al. 2008; Antonellis et al. 2015] and centrifuge [Ugalde et al. 2007; Hakhamaneshi et al. 2012; Deng et al. 2012a; Loli et al. 2014] shake-table tests for competent soil conditions. In addition, performance of rocking foundations on poor soil conditions have been investigated using concrete pads below the footing [Deng and Kutter 2012], footings rocking on unattached piles [Allmond and Kutter 2014; Antonellis and Panagiotou 2014], or shallow soil improvement by means of compaction for sandy soils [Kokalli et al. 2015; Tsatsis and Anastasopoulos 2015] or deep soil mixing for clayey soils [Khosravi et al. 2015].

Gajan and Kutter [2008] demonstrated that rocking shallow foundations exhibit a reliably predicted, non-deteriorated moment-rotation behavior, and that re-centering, energy dissipation, and settlement behavior of rocking footings are well correlated to the critical contact area ratio, $\rho_{ac} = A_c/A_f$, where A_f is the area of the footing and A_c is the minimum soil-footing contact area that supports the vertical load during rocking. Gajan and Kutter [2009] showed that foundations with normalized moment-to-shear ratio [$M/(V\times L)$] larger than 1, as in most practical cases of bridge columns, will have very small sliding and the deformation response of the foundation will mainly be in terms of rotation and settlement. Deng and Kutter [2012] and Deng et al. [2012a] showed that foundations with $\rho_{ac} < 0.13$ can develop rotations up to 5% with small residual rotations and settlements less than 1% of the footing dimension. More recently, Antonellis et al. [2015] demonstrated that rocking foundations can be detailed to sustain peak rotation of 6% with no structural damage and residual rotation of 0.3%.

As convincing evidence indicates that rocking foundations can be an efficient component of a seismic force resisting system, new and practical performance-based procedures for design of rocking foundations for bridges are needed.

Within this perspective, displacement-based analysis (DBA) procedures [Kowalsky et al. 1994; Chopra and Goel 2001; Blandon and Priestley 2005; Jara and Casas 2006; Dwairi and

Kowalsky 2006; Dwairi et al. 2007; Priestley et al. 2007], are an attractive framework as rocking foundations may coexist in a bridge system with other seismic resisting mechanisms (e.g., column plastic hinges at the top of the columns, passive soil resistance at the abutments, seismic isolation and damping devices) that have been already studied. In the DBA approach, the displacement demand of a structure is predicted using the design linear displacement spectrum and an equivalent linear viscoelastic single-degree-of-freedom (SDOF) model that represents the structural system. Previous studies have developed displacement-based analysis guidelines for single-column [Paolucci et al. 2013; Deng et al. 2014], or multi-span [Ni et al. 2013] reinforced concrete bridges.

This study develops guidelines for the seismic design of ordinary bridges with columns on rocking shallow foundations. Two existing Caltrans bridges are hypothetically redesigned using rocking shallow foundations, combined with plastic hinging at the top of the columns. The bridges are hypothetically located in a site at San Bernardino, California of very high seismic hazard (1.6 ft/s slope of the design displacement spectrum up to a period of 5 seconds). The design objectives for the redesigned bridges are minimal structural damage and prompt post-earthquake functionality. The seismic design guidelines developed here are based on displacement-based analysis and cover both the component level design of rocking bents as well as the system level design of bridges for excitation in either the transverse or the longitudinal direction of the bridge. The developed designs are validated by three-dimensional nonlinear response history analysis of the two bridge case studies. The NRHA analyses results are also used to validate the DBA method at the bridge system level.

1.2 REPORT OUTLINE

This report contains a total of 9 chapters. Chapter 2 provides a review of displacement-based seismic analysis based on SDOF idealization. Chapter 3 presents a calibrated, based on physical tests, beam-on-nonlinear-Winkler-foundation (BNWF) modeling scheme for rocking shallow foundations. Chapter 4 presents the development of the displacement-based analysis (DBA) method for single elastic flexible column on rocking shallow foundation. The method is based on the Deng et al. [2014] approach, but with equivalent viscous damping determined from nonlinear response history analyses (NRHA) of the calibrated BNWF models. Chapter 5 describes the

DBA guidelines for the case of a single flexible column with rocking foundation at the base and plastic hinging at the top. Chapter 6 presents the DBA method at the bridge level. In Chapter 7, two built bridges of Caltrans are redesigned with rocking shallow foundations based on the DBA method. In addition, three-dimensional NRHA are conducted to evaluate the proposed design method. Chapter 8 compares the NRHA results of the two redesigned bridges with those obtained from a response spectrum analysis. Finally, Chapter 9 presents the conclusions of this study.

2 Review of Displacement-Based Seismic Analysis

2.1 FORMULATION OF THE METHOD

The displacement-based seismic analysis method is illustrated with reference to Figure 2.1, which considers a SDOF representation of a fixed-base reinforced-concrete bridge column; nevertheless, the basic fundamentals apply to many types of earthquake resisting mechanisms and types of structures. The method characterizes the structure by the secant stiffness, K_e, at peak displacement, Δ_m [Fig. 2.1(b)], and a level of equivalent viscous damping, ξ_{eq}, that is representative of the combined elastic damping and hysteretic energy due to inelastic response [Fig. 2.1(c)]. Using these equivalent linear structure properties, the peak displacement demand is determined, using design linear displacement spectra reduced for the expected level of energy absorption [Fig. 2.1(d)].

The basic steps of the displacement-based method for the considered example can be summarized as follows:

1. Obtain the design linear displacement spectrum for 5% damping at the considered site.
2. Conduct a preliminary design of the reinforced concrete column and determine the force – displacement backbone.
3. Assume a peak lateral displacement (Δ_m).
4. For the assumed peak displacement demand, compute the secant stiffness at peak displacement (K_e) and the corresponding period (T_e) based on the effective mass of the structure (m_e) that participates in the fundamental vibration mode:

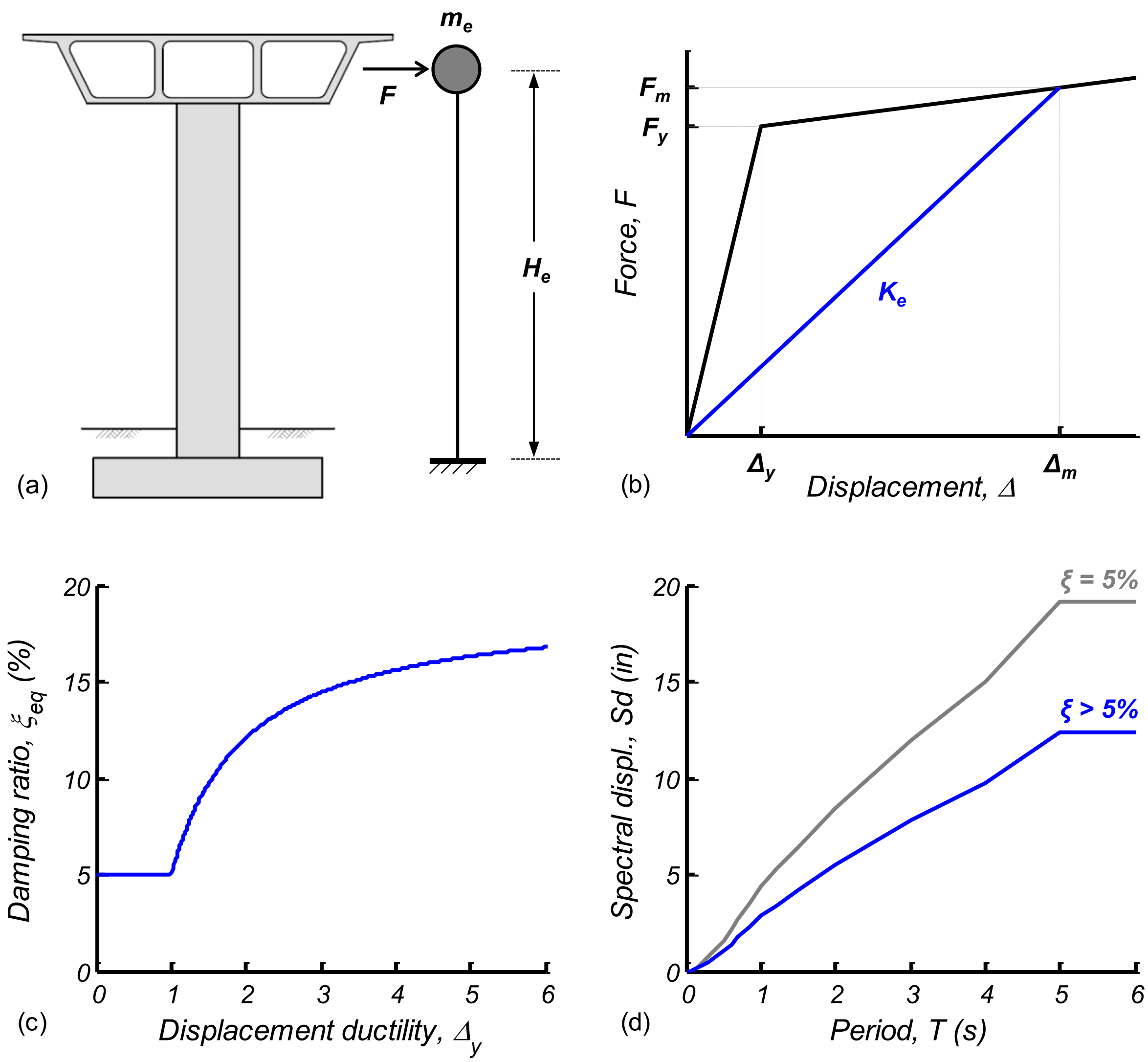

Figure 2.1 Fundamentals of displacement-based analysis method; (a) fixed-base bridge pier and SDOF idealization; (b) force – displacement backbone and secant stiffness to peak displacement; (c) equivalent viscous damping – ductility curves; and (d) linear design displacement spectra.

$$K_e = \frac{F(\Delta_m)}{\Delta_m} \tag{2.1}$$

$$T_e = 2\pi\sqrt{\frac{m_e}{K_e}} \tag{2.2}$$

5. Based on the peak displacement (Δ_m) and the yield displacement of the structure (Δ_y), estimate the displacement ductility demand ($\mu_\Delta = \Delta_m/\Delta_y$) and the corresponding equivalent viscous damping (ξ_{eq}).

6. Determine the reduction factor to the 5% damped linear displacement spectrum (R_D) due to the increased viscous damping:

$$R_D = \left(\frac{0.07}{0.02 + \xi_{eq}} \right)^{\alpha} \tag{2.3}$$

where $\alpha = 0.5$ for a site with expected "normal" broadband motions [European Committee for Standardization (CEN) 1998], or $\alpha = 0.25$ for a site where forward directivity velocity pulse motions might be expected [Priestley 2003].

7. Update the peak displacement demand prediction:

$$\Delta_m = R_D \cdot Sd\left(T_e, 0.05\right) \tag{2.4}$$

8. Repeat steps 3 to 7 until the displacement demand computed at step 7 is close enough to the one used in step 3, e.g. within 2%.

9. Evaluate if the predicted displacement demand is satisfactory, or if the structure needs to be redesigned.

The described design procedure requires knowledge of the force – displacement and the equivalent viscous damping – ductility relationships for the calculation of the effective elastic stiffness and viscous damping, respectively. While determination of the force – displacement relationship is straightforward for a given earthquake resisting mechanism, discussion on the calculation of the equivalent viscous damping is required.

2.2 EQUIVALENT VISCOUS DAMPING

The equivalent viscous damping used in the displacement-based analysis is representative of the combined elastic damping and hysteretic energy dissipated during inelastic response:

$$\xi_{eq} \approx \xi_{el} + \xi_{hys} \tag{2.5}$$

The components of Eqn. (2.5) are discussed next.

2.2.1 Hysteretic Damping

The equivalent viscous damping due to hysteretic energy dissipation may be computed from the energy absorbed by the hysteretic steady-state cyclic response at a given displacement. This approach was proposed by Jacobsen [1930] for determining the peak displacement demand of a hysteretic system under steady-state harmonic forced vibration. Initial work on the displacement-based analysis of inelastic structures under earthquake excitation [Rosenblueth and Herrera 1964; Kowalsky 1994] has also used the Jacobsen [1930] approach due to its simplicity and the ease with which the relations between the hysteretic shape and the equivalent damping are obtained.

Chopra and Goel [2001] showed that this approach may seriously overestimate the effective viscous damping in earthquake applications, as in these cases, the assumptions of Jacobsen [1930] are not met. More specifically, earthquakes tend to have varied frequency content rather than a single harmonic. In addition, in many cases the peak displacement occurs before the transient response damps out. As an extreme example a nonlinear elastic and a nonlinear inelastic system, with identical monotonic force – displacement backbones may develop the same peak displacement demand under a single strong velocity pulse despite of the second system dissipating energy upon unloading. Lastly, the response of a yielding system to an earthquake is typically asymmetric, and contains cycles of smaller and larger amplitude. Determining the equivalent viscous damping based on the maximum single-sided displacement will overestimate the average energy dissipation through all cycles that take place prior to reaching the maximum demand [Gulkan and Sozen 1974].

As a result, Grant et al. [2005], Dwairi et al. [2007] and Priestley et al. [2007] showed that correction factors should be applied to the area-based damping for use in displacement-based analysis, and they developed a set of correction factors required to make the peak drift in an earthquake event, as predicted by DBA, match the peak drift predicted by nonlinear response history analyses. The matching of drift demand was done in an average sense for a set of earthquake ground motions, and they found that the correction factors were different for different shapes of hysteresis loops. Figure 2.2 plots the area-based correction factors as summarized by Priestley et al. [2007] for a variety of hysteretic rules.

2.2.2 Elastic Damping

The first component of equivalent viscous damping of Eqn. (2.5) is an elastic component that is commonly used in nonlinear response history analysis (NRHA) to model damping not captured by the hysteretic rule (due to its initial linear response), foundation radiation damping and damping from interaction between structural and nonstructural components. As DBA is calibrated to match peak drift predicted by NRHA, the selection of elastic damping in DBA is

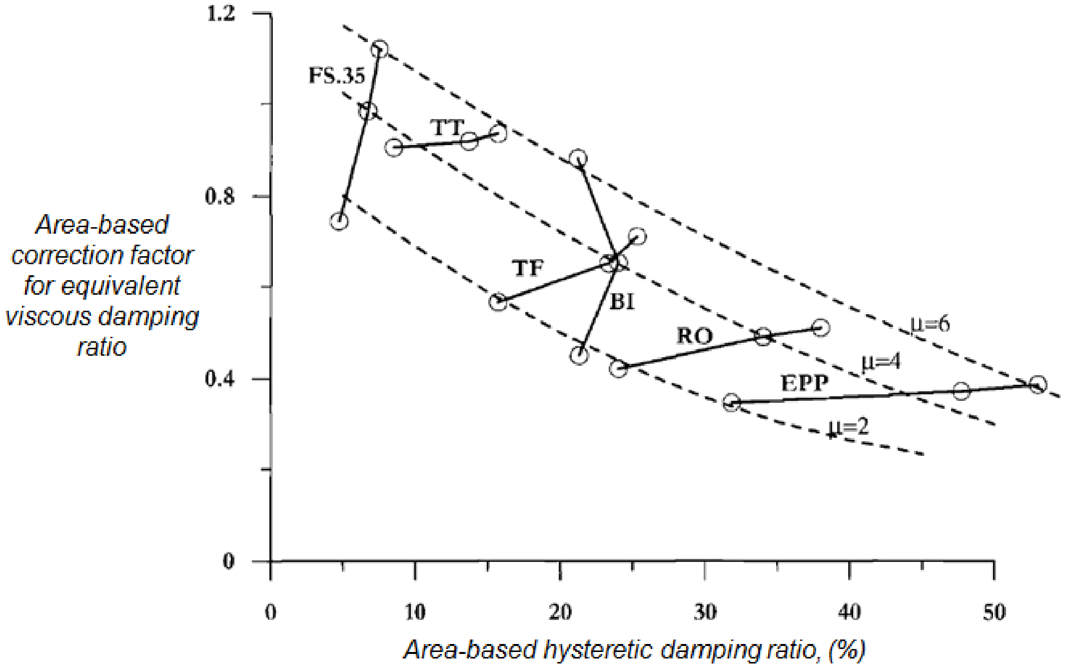

Figure 2.2 Correction factors to be applied to area-based equivalent viscous damping ratio for a variety of hysteretic rules: FS = flag shaped (unbonded post-tensioned structures); TT = Takeda thin (reinforced concrete column or wall); TF = Takeda fat (reinforced concrete frames); BI = bilinear inelastic with 20% post-yield stiffness (isolation systems); RO = Ramberg Osgood (steel structures); EPP = elastic-perfectly-plastic (friction sliders) [Priestley et al. 2007].

dependent on whether the elastic damping in the NRHA is initial or tangent stiffness proportional.

Wang et al. [1998] analyzed experiments of seismic soil-pile interaction and showed that initial stiffness damping produces large and spurious damping forces not observed experimentally, whereas Priestley and Grant [2005] argued that hysteretic models are calibrated to match the full energy dissipation after the onset of yielding. Hence, a tangent stiffness proportional damping may be more appropriate as the damping coefficient subsequent to onset of yielding is reduced.

In any of the two cases however, the elastic damping in DBA is associated to the secant stiffness to peak displacement whereas the elastic damping in NRHA is associated to the constant initial stiffness (initial stiffness proportional damping), or to the varying tangent stiffness (tangent stiffness proportional damping). Hence, the elastic damping used in NRHA cannot be directly added to the equivalent hysteretic damping to obtain the equivalent viscous damping for DBA. In addition, determining the elastic damping component of DBA based on the total energy absorbed by the viscous dashpot in NRHA may not be appropriate for reasons similar to those described in the case of hysteretic damping and appropriate adjustment factors are needed [Grant et al. 2005].

2.2.2 Equivalent Viscous Damping for Selected Hysteretic Rules

This subsection lists the equivalent viscous damping (ξ_{eq}) – displacement ductility (μ_Δ) relationships as obtained from Priestley et al. [2007] for selected hysteretic rules as rocking foundations may coexist in a bridge system with other seismic resisting mechanisms (e.g., column plastic hinges at the top of the columns, passive soil resistance at the abutments, seismic isolation and damping devices). These hysteretic rules are: Takeda thin (TT), applicable to reinforced concrete columns; Elastic-perfectly-plastic (EPP), applicable to friction sliders and to abutments passive resistance if multiplied by a factor of 0.5, as the two abutments combined, dissipate energy during the first and third quadrant of a complete cycle; and Bilinear inelastic with 20% post-yield stiffness (BI), applicable to some isolation systems. It is noted that Eqn, (2.6) are applicable to cases with tangent stiffness proportional elastic damping of 5%. For different elastic damping or for initial stiffness proportional damping, Eqn. (2.7) should be used together with Tables 2.1 and 2.2.

$$\xi_{eq\_TT} = 0.05 + 0.444\left(\frac{\mu_\Delta - 1}{\mu_\Delta \cdot \pi}\right) \tag{2.6a}$$

$$\xi_{eq\_EPP} = 0.05 + 0.670\left(\frac{\mu_\Delta - 1}{\mu_\Delta \cdot \pi}\right) \tag{2.6b}$$

$$\xi_{eq\_BI} = 0.05 + 0.519\left(\frac{\mu_\Delta - 1}{\mu_\Delta \cdot \pi}\right) \tag{2.6c}$$

$$\xi_{eq} = {\mu_\Delta}^{\lambda} \cdot \xi_{el} + \alpha\left(1 - \frac{1}{{\mu_\Delta}^{b}}\right)\left(1 + \frac{1}{(T_e + c)^d}\right) \tag{2.7}$$

Table 2.1 Equivalent viscous damping coefficients for hysteretic damping component using Eqn. (2.7) [Grant et al. 2005].

Model	a	b	c	d
TT	0.215	0.642	0.824	6.444
EPP	0.224	0.336	-0.002	0.250
BI	0.262	0.655	0.813	4.890

Table 2.2 Equivalent viscous damping coefficient (λ) for elastic damping component using Eqn. (2.7) [Grant et al. 2005].

Model	Initial Stiffness	Tangent Stiffness
TT	0.340	0.378
EPP	0.127	-0.341
BI	0.193	-0.808

2.3 CONSIDERATION OF P-Δ EFFECTS FOR REINFORCED CONCRETE SYSTEMS

The presented in Section 2.1 displacement-based analysis method does not directly account for P-Δ effects. These are typically quantified by the instability ratio ($\theta_{P\text{-}\Delta}$):

$$\theta_{P-\Delta} = \frac{P \cdot \Delta_m}{M(\Delta_m)} \tag{2.8}$$

which is the fraction of the base moment at the predicted displacement demand (Δ_m) that is due to the P-Δ moment. Priestley et al. [2007] recommend that P-Δ effects for reinforced concrete systems can be safely ignored if $\theta_{P\text{-}\Delta} \leq 0.10$. For $\theta_{P\text{-}\Delta} > 0.10$, but smaller than the suggested limit case of 0.33, they recommend that the predicted displacement demand from DBA should be increased as follows:

$$\Delta_{m\_P-\Delta} = (1 + 0.5 \cdot \theta_{P-\Delta}) \cdot \Delta_m \tag{2.9}$$

2.4 INCORPORATING ROCKING SHALLOW FOUNDATIONS IN DISPLACEMENT-BASED SEISMIC ANALYSIS

The proposed, in this study, displacement-based guidelines for the seismic analysis of bridges with rocking shallow foundations adopt concepts presented in the Deng et al. [2014] study. These concepts, reviewed in this section, are: (i) a multilinear moment – rotation hysteretic model for rocking foundations that allows determination of the secant rotational stiffness at peak footing rotation as well as the area-based hysteretic damping ratio under a complete symmetric hysteresis loop; and (ii) a combination rule for integrating radiation damping, hysteretic damping due to rocking-induced soil inelasticity, and column elastic damping for the case of flexible elastic cantilever columns on rocking foundations.

2.4.1 Multilinear Hysteretic Model

Figure 2.3(a,b) shows the schematic of a flexible elastic cantilever bridge column on a rocking shallow foundation as well as the corresponding multilinear hysteretic model proposed by Deng et al. [2014]. The proposed multilinear hysteretic model was developed by analyzing a large set of pseudo-static cyclic centrifuge and large-scale 1g tests of rocking shallow foundations. The hysteretic model is constructed using a trilinear virgin loading and reloading backbone and a linear unloading. Based on their analysis, Deng et al. [2014] showed that during virgin loading and reloading from zero moment, a rocking footing will reach 50% of the rocking moment capacity at a rotation of approximately 1/600 rad ($0.5\cdot h_f$ = 1/600 rad), while the full rocking moment capacity is reached at a rotation of 0.012 rad (b_f = 0.012 rad). Assuming that the total vertical load at the base of the footing (W_{f_b}) and the footing length in the direction of excitation (L_f) are known, the strength and energy dissipation (i.e. slope of linear unloading) characteristics of the rocking footing can be determined based on the critical contact area ratio (ρ_{ac}) defined as:

$$\rho_{ac} \equiv \frac{A_c}{A_f} \tag{2.10}$$

where A_f is the plan area of the footing and A_c is the critical contact area, defined as the area required to support W_{f_b} when the soil's ultimate bearing capacity (q_c) is fully mobilized under rocking. Deng and Kutter [2012] showed that A_c, and hence ρ_{ac}, can be determined using conventional bearing capacity theory for the reduced due to uplifting soil-footing contact area. Note that for a rectangular critical contact area as in Figure 2.3(a)

$$\rho_{ac} \equiv \frac{A_c}{A_f} = \frac{L_c}{L_f} \tag{2.11}$$

where L_c is termed critical contact length.

Having calculated ρ_{ac}, the rocking moment capacity (M_{fc}) of the footing is derived from static analysis [Gajan and Kutter 2008] as

$$M_{fc} = \frac{W_{f\_b}\cdot L_f}{2}\cdot\left(1-\rho_{ac}\right) \tag{2.12}$$

while the residual rotation (i.e. rotation at zero moment), z_f, after unloading from a peak footing rotation of θ_f is determined as

$$z_f = \left(1-R_d\right)\cdot\theta_f \tag{2.13}$$

where the displacement re-centering ratio (R_d) is correlated to ρ_{ac} as follows:

$$R_d = \frac{1}{2.6 \cdot \rho_{ac} + 1} \tag{2.14}$$

Note that as ρ_{ac} decreases, meaning that less soil-footing contact area is required to support the total vertical load and thus less rocking-induced soil inelasticity is induced, R_d increases also, resulting in improved re-centering (smaller residual rotation) and less energy dissipation.

Figure 2.4 compares the multilinear hysteretic model with experimental results from a pseudo-static cyclic centrifuge test [Deng et al. 2014], and a dynamic large-scale 1g test [Antonellis et al. 2015] at both small and large rotations. It is noted that while the centrifuge test was included in the development of the hysteretic model, the large-scale 1g test was conducted afterwards. It is concluded that the discussed hysteretic model provides a very good approximation of the actual cyclic moment – rotation envelope as well as of the hysteretic energy dissipated through rocking.

2.4.2 Combination of Elastic and Hysteretic Damping

Deng et al. [2014] determine the equivalent viscous damping ratio (ξ_{eq}) due to the combined effects of radiation damping (ξ_{rad}), hysteretic damping due to rocking (ξ_{f_hys}) and column elastic damping (ξ_c) [Figure 2.5(a)] based on an SDOF model supported by in-series pairs of spring and dashpots, where each damping source is associated to the corresponding flexibility source [Figure 2.5(b, c)]. This approach is described in Wang et al. [1998] and Priestley and Grant [2005], and is used to avoid spurious damping forces that would be produced by placing radiation and/or column elastic dashpots in parallel to the spring representing the hysteretic response of the rocking foundation.

Figure 2.6 shows the decomposition of the multilinear rocking foundation hysteretic model into an elastic rocking element modeling the initial elastic rocking response (before footing uplifting and soil yielding) and radiation damping, and into a plastic rocking element modeling the rocking-induced hysteretic damping.

The rotational stiffness of the elastic rocking element (K_{f_50}) is

$$K_{f\_50} = 300 \cdot M_{fc} \tag{2.15}$$

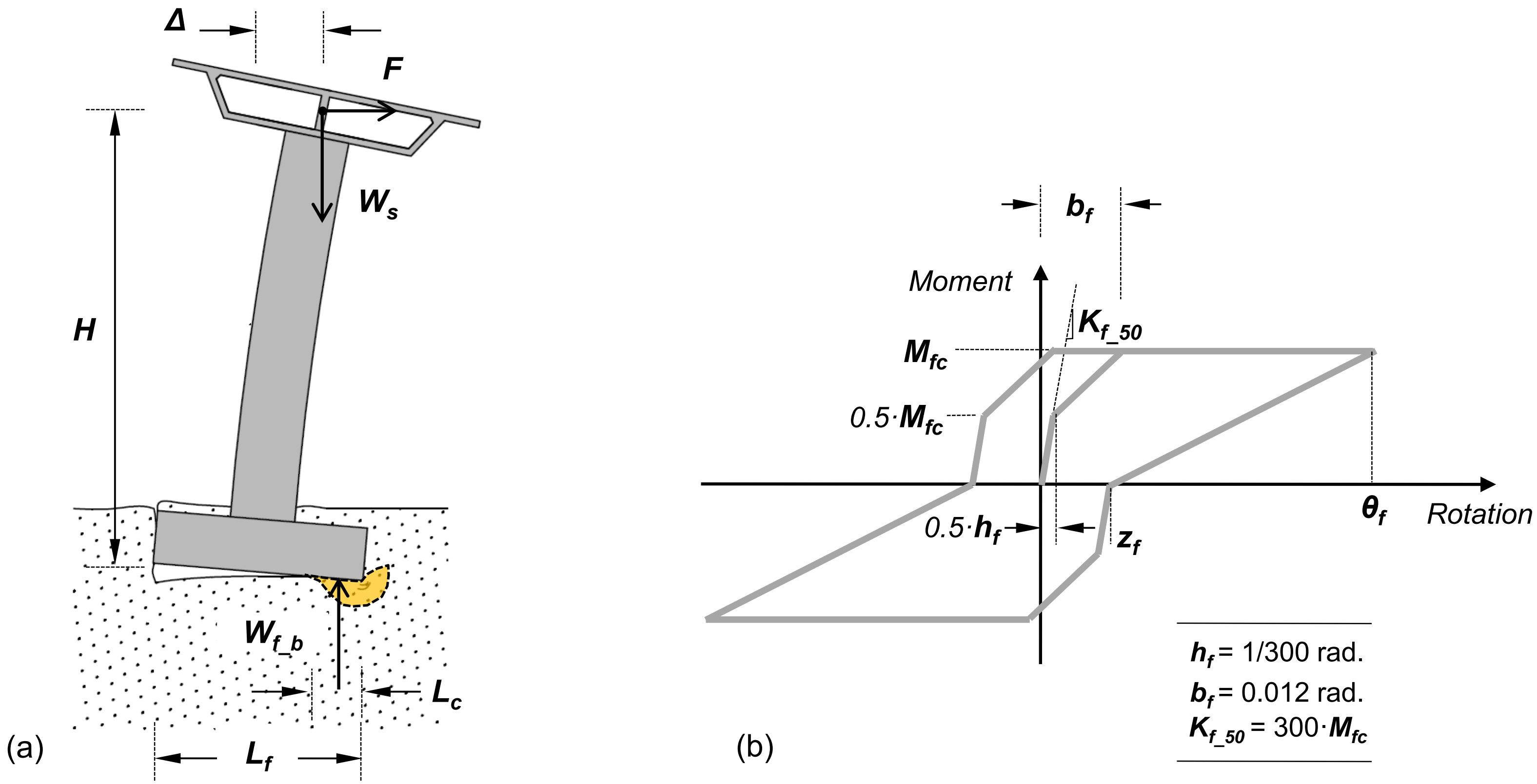

Figure 2.3 (a) Schematic of a flexible elastic cantilever bridge column on a rocking shallow foundation; and (b) Deng et al. [2014] multilinear hysteretic model for rocking shallow foundations.

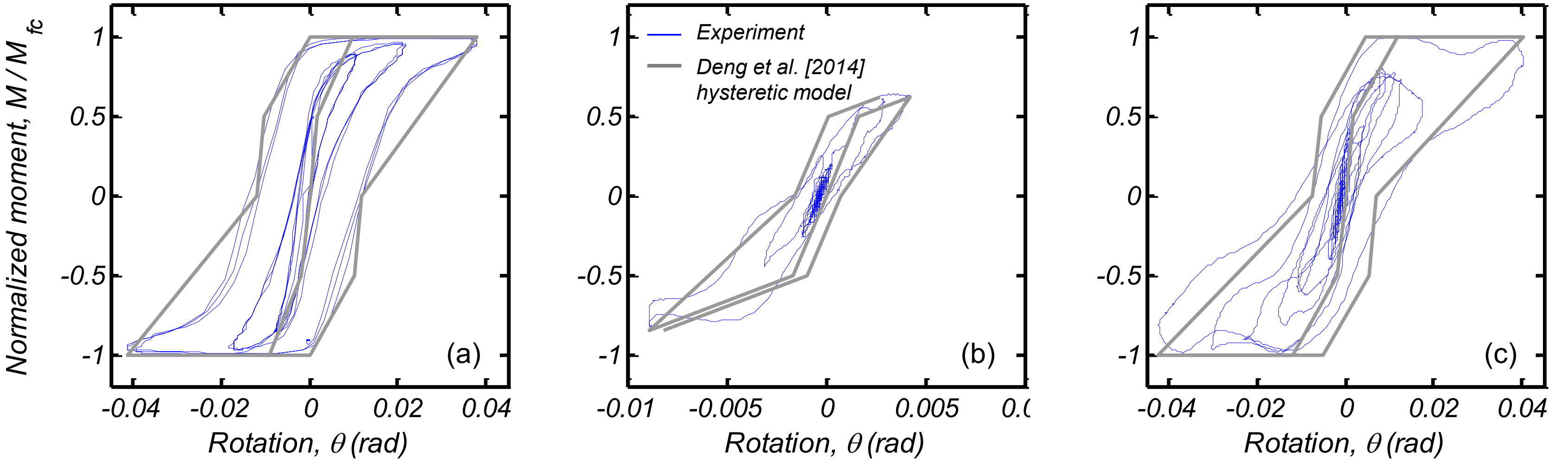

Figure 2.4 Comparison of the Deng et al. [2014] multilinear hysteretic model for rocking shallow foundations with (a) a pseudo-static cyclic centrifuge test [Deng et al. 2014], and (b, c) a dynamic large-scale 1g test [Antonellis et al. 2015] at small and large rotations.

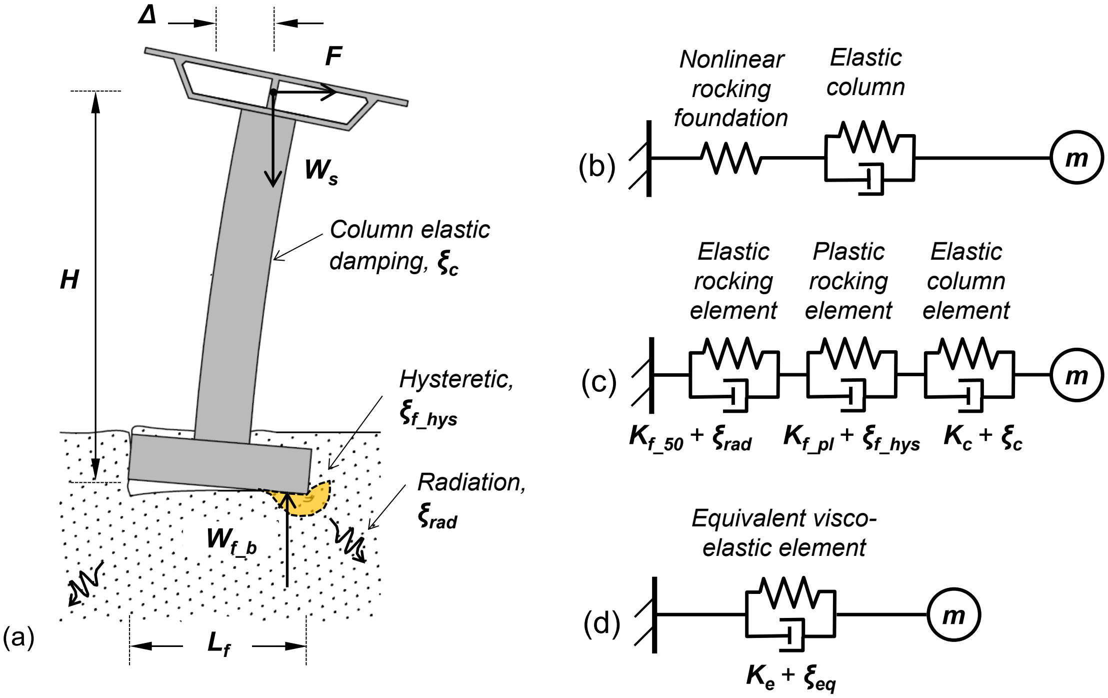

Figure 2.5 (a) Schematic of a flexible elastic cantilever bridge column on rocking shallow foundation; (b) spring-dashpot representation of the system; (c) decomposition of multi-linear hysteretic model of the rocking foundation into an elastic and a plastic spring-dashpot element; (d) integration of the in-series spring-dashpot elements into a single equivalent visco-elastic element.

Assuming that the footing rotation (θ_f) is larger than b_f (i.e. 0.012 rad), the plastic rocking element is substituted with an equivalent linear viscoelastic element that has the same secant stiffness to peak rotation (K_{f_pl})

$$K_{f\_pl} = \frac{M_{fc}}{\theta_f - h_f} \tag{2.16}$$

and hysteretic damping ratio (ξ_{f_hys}) based on the area of the hysteresis loop

$$\xi_{f\_hys} = \frac{1}{2\pi}\left(4 - \frac{3}{2.6 \cdot \rho_{ac} + 1} - \frac{b_f}{\theta_f}\right) \tag{2.17}$$

With the stiffness and damping properties of each spring-dashpot pair known, the secant period (T_e) and equivalent viscous damping (ξ_{eq}) of the flexible elastic cantilever column on rocking foundation are determined by in-series integration as

$$T_e = \sqrt{T_c^{\,2} + T_{f\_50}^{\,2} + T_{f\_pl}^{\,2}} \tag{2.18}$$

$$\xi_{eq} = \left(\frac{T_c}{T_e}\right)^2 \xi_c + \left(\frac{T_{f\_50}}{T_e}\right)^2 \xi_{rad} + \left(\frac{T_{f\_pl}}{T_e}\right)^2 \xi_{f\_hys} \tag{2.19}$$

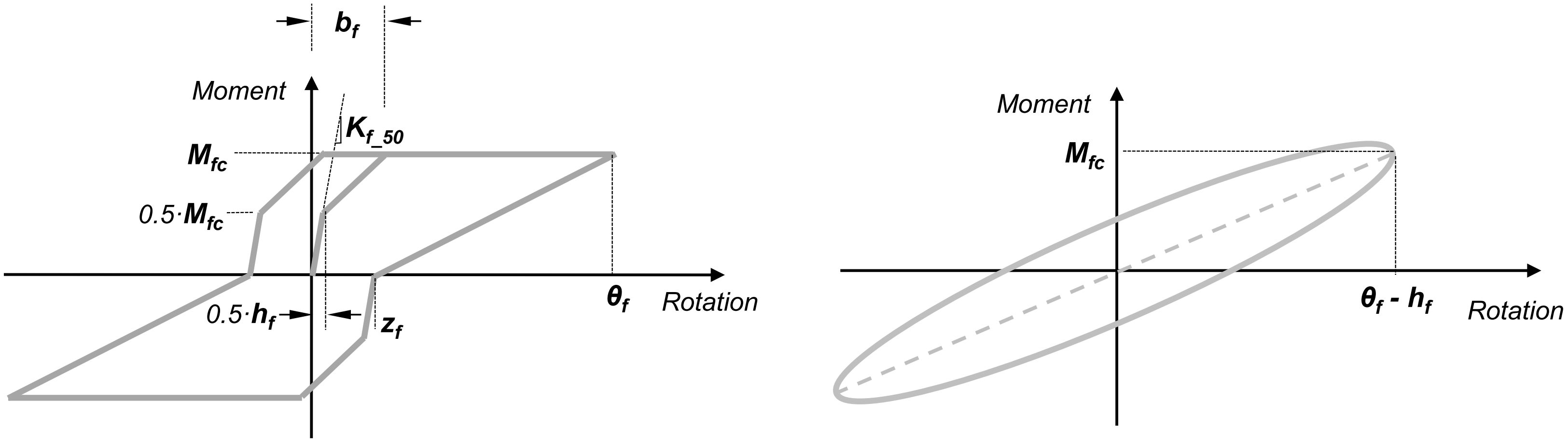

(a) *Multilinear hysteretic model*

(d) *Equivalent linear visco-elastic substitute element for the nonlinear inelastic response of the rocking foundation:* $K_{f\_pl} + \xi_{f\_hys}$

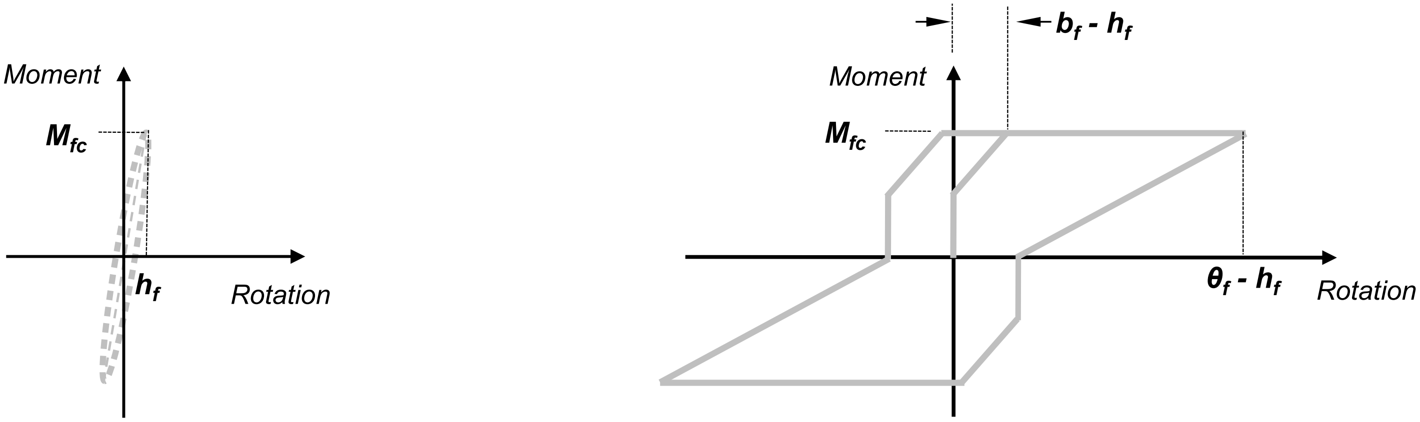

(b) *Linear visco-elastic element for the elastic response of the rocking foundation:* $K_{f\_50} + \xi_{rad}$

(c) *Plastic element for the nonlinear inelastic response of the rocking foundation*

Figure 2.6 Decomposition of (a) the multilinear hysteretic response to (b) a linear visco-elastic rocking element for radiation damping and (c) a plastic rocking element for hysteretic damping; and (d) substitute equivalent linear visco-elastic element of the plastic rocking element.

3 Beam-on-Nonlinear-Winkler-Foundation Model

3.1 INTRODUCTION

In this Chapter, four physical experimental tests on sand are used to calibrate a beam-on-nonlinear-Winkler-foundation (BNWF) modeling scheme for rocking shallow foundations on sand. The BNWF model is used subsequently in the proposed displacement-based analysis method (Chapter 4), as well as for the three dimensional Nonlinear Response History Analysis (NRHA) of two bridge systems with columns on rocking foundations (Chapter 7).

3.2 EXPERIMENTAL DATA USED IN THIS STUDY

Four rocking shallow foundation tests are considered here to calibrate the BNWF model. The considered tests were selected to meet the following conditions: (i) they are rocking-dominated footings; (ii) they cover a reasonably wide range of rocking-induced soil inelasticity; (iii) their response is not affected by sand falling from the backfill under the gapping side of the footing as such a mechanism cannot be modeled by BNWF.

Table 3.1 summarizes the main properties of the tests. Three of the tests are slow-cyclic displacement-controlled centrifuge tests of a rigid shear wall supported on a surface footing [Hakhamaneshi et al. 2014; Liu et al. 2015]. The fourth test is a dynamic 1g test of a 1:3 scale reinforced-concrete bridge pier supported on a shallow embedded footing tested at the UCSD shake table [Antonellis et al. 2015]. The models were founded on a dense to very dense sand (D_R = 80% or 90%), and had a normalized moment-to-shear ratio $M_{fc}/(V \times L_f)$ larger than 1, indicating a rocking-dominated response and small sliding [Gajan and Kutter 2009]. The critical contact area ratio of the rocking foundations (ρ_{ac}) varied between 8.8% and 25%; hence, it spanned a range from very limited to moderate soil inelasticity. The centrifuge tests used rectangular footings with length to width ratio between 0.64 and 1.75, while the 1g test used a square footing.

It is noted that from the Antonellis et al. [2015] experimental dataset only the response of the aligned specimen during Day 1 has been modeled, in which, significant sand falling has not been observed due to the apparent cohesion in the backfill soil (except for the last ground motion in the loading protocol). Day 2 results have been affected more by this mechanism, due to the reduced apparent cohesion of the backfill soil; hence, they have not been considered here. Also, Day 3 results have not been modeled. Albeit cast concrete blocks around the footings have eliminated the sand falling mechanism, the experimentally observed partial interlocking of the footing and the concrete blocks would require a more elaborate model that is beyond this study's scope.

Table 3.1 Rocking shallow foundation tests used for BNWF calibration (dimensional quantities are reported in model scale).

Test No.	1	2	3	4
Reference	Hakhamaneshi (2014)	Hakhamaneshi (2014)	Liu et al. (2015)	Antonellis et al. (2015)[2]
Test type	Centrifuge (1:35[1])	Centrifuge (1:35[1])	Centrifuge (1:30[1])	1g (1:3[1])
Loading type	Slow cyclic	Slow cyclic	Slow cyclic	Dynamic
Idealized superstructure type	Rigid shear wall	Rigid shear wall	Rigid shear wall	SDOF with flexible column
Soil relative density, D_R (%)	80	80	90	90
Total load, W_{f_b} (kip)	0.886	0.639	0.408	65.6
Footing length, L_f (in)[2]	4.33	5.91	7	60
Footing length, B_f (in)[3]	6.69	3.54	4	60
Embedment depth, D_f (in)	0	0	0	26
Critical contact length, L_c (in)	1.08	1.44	1.03	5.31
Critical contact area ratio, $\rho_{ac} = L_c/L_f$	0.24	0.244	0.147	0.088
Moment capacity, M_{fc} (kip-in)	1.44	1.43	1.22	2027
Moment-to-shear ratio, $M_{fc}/(V \times L_f)$	2.0	1.4	1.7	2.0

[1] Length scale factor; [2] Only the response of the aligned specimen in Day 1 is considered; [3] Footing side dimension in the loading direction; [4] Footing side dimension normal to the loading direction.

3.3 BNWF MODEL DESCRIPTION AND CALIBRATION

3.3.1 Description of Model

Figure 3.1(a) shows the side view of a bridge pier supported on a rocking shallow foundation, as well as the corresponding BNWF model [e.g. Harden and Hutchinson 2009; Gajan et al. 2010; Antonellis and Panagiotou 2013] within the Open System for Earthquake Engineering Simulation (*OpenSees*) [Mazzoni et al. 2014] platform. In this approach the soil – foundation interaction is modeled with an array of uncoupled nonlinear springs, namely *QzSimple1*, *TzSimple1* and *PySimple1*, that have been originally developed by Boulanger et al. [1999] to model the end bearing, passive and skin friction resistance against a pile. More specifically, the foundation is supported on a bed of vertical nonlinear gapping springs (*QzSimple1*) that model the contact behavior of the footing with the underneath soil, and determine the vertical and rotational (in the absence of embedment) load – deformation response of the foundation. *TzSimple1* springs model the sliding behavior at the base of the footing, while *PySimple1* springs model the passive soil resistance against the vertical sides of the footing. The three spring types are internally similar in nature, and consist of an elastic spring in series with a plastic spring and a drag-closure spring [Figure 3.1(b)]. The three internal elements capture the "far-field" elastic response, the "near-field" inelastic response, and the soil-footing gap opening and closure, respectively. In addition, a viscous dashpot is used in parallel with the elastic element to model radiation damping [Wang et al. 1998]. Figure 3.2 shows the typical cyclic force – displacement relationship of the springs for the case of a sandy soil.

It is noted that the *QzSimple1* material implementation in *OpenSees* [Boulanger 2000] assumes as a hard-wired parameter in the computer code, a minimum tensile stiffness that overrides the tension capacity of the spring. Although the stiffness is small (i.e. 10^{-3} of the secant compressive stiffness at 50% of the compression capacity), it can produce significant tensile forces for footings with small ρ_{ac} during large rotations that affect the rocking footing moment capacity [Liu et al. 2015]. To minimize the unrealistic tensile forces, the *QzSimple1* material was modified herein by further reducing the tensile stiffness by a factor of 10^6. Note that this change is not reflected in the online version of *OpenSees*.

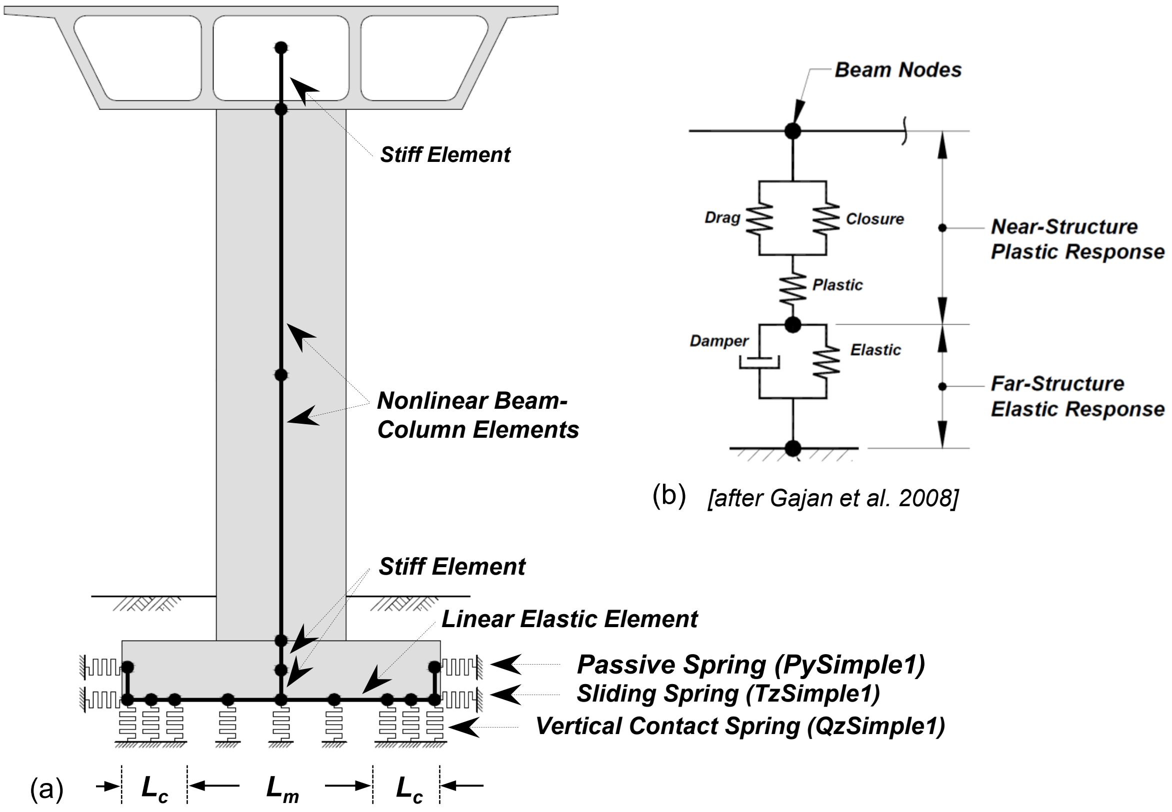

Figure 3.1 (a) Two-dimensional generic beam-on-nonlinear-Winkler-foundation modeling for a column supported on a rocking shallow foundation; (b) components of the QzSimple1 zero-length spring used to model the vertical soil-footing contact behavior.

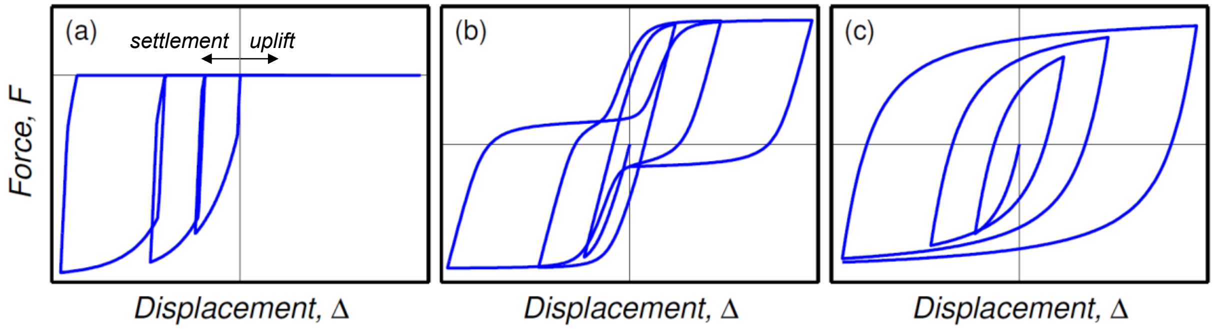

Figure 3.2 Typical cyclic nonlinear force-displacement relationships for sandy soil: (a) vertical force – displacement response (QzSimple1); (b) lateral passive response (PySimple1); and (c) lateral sliding response (TzSimple1).

3.3.2 Calibration of the BNWF model

Stiffness and capacity distribution of vertical springs

The BNWF model response is governed by the stiffness and strength properties of the vertical springs. Harden and Hutchinson [2009] have proposed a parabolic capacity distribution, which is based on experiments of footings on sand under pure vertical loading that well exceeds working level, and the use of higher stiffness springs near the footing edges in order to match the Gazetas [1991] global vertical and rotational elastic stiffness (Figure 3.3). Here we determine a different stiffness and strength distribution that results in more accurate responses of rocking shallow footings with moderate to limited soil inelasticity (i.e. ρ_{ac} smaller than approximately 0.2).

In the proposed scheme, the footing is divided to two identical end regions with length equal to the critical contact length of the rocking foundation (L_c), and to a middle region (L_m); see Figure 3.1(a) and Table 3.2. In each region, the bearing capacity and the elastic stiffness per tributary area are constant. First, the critical contact length (L_c) and the corresponding bearing capacity (q_c) are determined by conventional bearing capacity equations for the reduced soil – footing contact geometry [Deng and Kutter 2012]. Based on the critical contact area ratio, $\rho_{ac} = A_c/A$ ($= L_c/L_f$ for a rectangular critical contact area), the capacity ratio ($q_{ratio} = q_c/q_m$) and stiffness ratio ($k_{ratio} = k_c/k_m$) determine the bearing capacity magnitude distribution and the elastic stiffness relative distribution of the vertical springs, respectively. Lastly, the elastic stiffness magnitude of the springs is determined iteratively by monotonic pushover analysis, so that the foundation moment at a rotation of 1/600 radians equals to 50% of the foundation moment capacity [$M_{fc} = 0.5 \cdot W_{f\_b} \cdot (1-\rho_{ac})$].

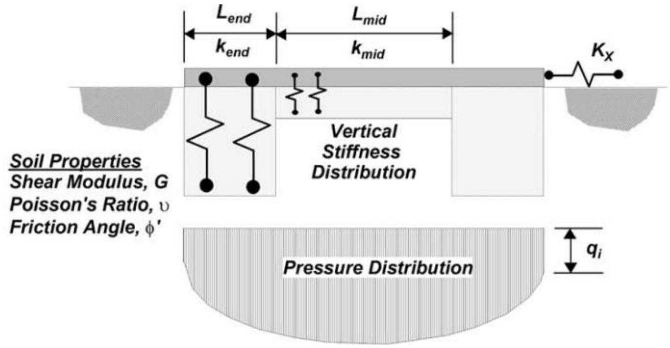

Figure 3.3 Graphical representation of Harden and Hutchinson [2009] modeling scheme for the stiffness and capacity distribution of the vertical Winkler springs.

Table 3.2 Modeling scheme considered in this study for the elastic stiffness and capacity distribution of the vertical Winkler springs.

ρ_{ac}	$q_{ratio} = q_c / q_m$	$k_{ratio} = k_c / k_m$	q_c (ksf)	k_c (ksf/ft)
≥ 0.25	1	1	W_{f_b} / A_c	Iteratively until $0.5 \times M_{fc}$ is reached at 1/600 rad.
$= 0.147$	2	1		
≤ 0.088	2	5		

A $q_{ratio} \geq 1$, oppositely to what is suggested by Harden and Hutchinson [2009] modeling approach, underestimates the capacity of the foundation against a purely vertical load. However, a $q_{ratio} \geq 1$ provides a way to promote soil inelasticity in the middle region and thus, to counteract the bias of BNWF models to underestimate cyclic moment – rotation energy dissipation due to their limitations. These limitations are:

(i) Soil yielding underneath the foundation occurs due to concentration of normal and shear stresses at the reduced, due to uplifting, soil – footing contact area. This coupling is not included in the BNWF model, where soil yielding is only due to normal stresses.

(ii) Bearing failure of a foundation rocking on the critical contact area pushes some loose soil back under the gapping footing side, which will yield upon the unloading and reloading of the foundation in the opposite direction. In the BNWF model, the vertical springs at the base of the footing are uncoupled; hence, the response of a spring under the gapping side of the footing is not affected by the response of the nearby plastically deforming spring.

Lastly, it was observed that BNWF models with $\rho_{ac} < 0.15$ experienced a slow mobilization of the theoretical foundation moment capacity if a uniform stiffness distribution was used. For that purpose, a $k_{ratio} > 1$ is used in these cases so that the foundation moment capacity is mobilized at an appropriate footing rotation by promoting uplifting at the middle region through transfer of vertical forces to the stiffer and stronger (since also, $q_{ratio} > 1$) springs of the end region.

Horizontal springs

The initial stiffness of the horizontal sliding and passive springs is determined based on the corresponding global elastic stiffness from Gazetas [1991]. The capacity of the sliding spring is calculated as the vertical load acting at the base of the footing multiplied by the frictional coefficient, which is taken as the tangent of the constant volume friction angle. The capacity of the passive spring is determined by conventional passive earth pressure theory.

3.4 VALIDATION OF BNWF MODEL

The considered physical tests have been modeled in OpenSees based on the described BNWF approach. Dashpots have been included in the BNWF model of test 4, and were determined from Gazetas [1991] elastic solutions for the initial fundamental period of the specimen. It is noted that the dashpot coefficient of the individual vertical springs were determined assuming a uniform distribution of the global vertical dashpot coefficient.

3.4.1 Slow Cyclic Centrifuge Tests

Figures 3.4 and 3.5 compare the experimental response of tests 1 and 2, with that obtained from the numerical simulations. Both tests have a critical contact area ratio equal to 0.25. The comparison is made in terms of (i) cyclic moment – rotation hysteresis loops, (ii) moment – rotation energy dissipation ratio versus rotation amplitude, (iii) settlement – rotation response; and (iv) settlement - cumulative rotation behavior. In the latter comparison, cumulative rotation is defined as the sum of the peaks of the rotation time history that exceed a threshold elastic rotation of 1 mrad [Deng et al. 2012a]. Based on part (a) of the figures, the numerical models are observed to approximate well the experimental cyclic moment – rotation response of the rocking foundations, at least for the packets of loading with large rotation amplitudes that are visible. Part (d) of the figures, plots the ratio of the hysteretic energy dissipation of the BNWF model to that of the physical tests, for loading packets of different rotation amplitudes, as well as for every cycle within each packet. For example, test 1 contained 7 loading packets of increasing single-sided rotation amplitude with 3 cycles at each of them. For rotations larger than 0.01 rad, the hysteretic energy dissipation of the BNWF model is shown to be approximately 65 to 85% of that in the experiments, with the ratio being fairly constant with increased cycling at the same amplitude. Foundation settlement response of the BNWF models compares reasonably with the experimental data up to the 6th loading packet of test 1 (rotation amplitude of 0.042 rad and cumulative rotation of 0.4 rad) and the 5th loading packet of test 2 (rotation amplitude of 0.04 rad and cumulative rotation of 0.4 rad). Upon continued cyclic rocking, BNWF models accumulate significant settlement not observed in the experiments, with the permanent settlement at the end of the tests being overestimated by approximately 100%.

Figure 3.6 shows the comparison of the BNWF model against test 3 ($\rho_{ac} \approx 0.15$) in terms of cyclic moment versus rotation, and hysteretic energy dissipation versus rotation. Observations are similar as for the previous two tests.

3.4.2 Dynamic 1g Test

Figures 3.7 to 3.12 compare the BNWF model response against the experimental data of test 4 for the each of the 6 ground motions used in the loading protocol. Comparison is made in terms of response histories of selected parameters (e.g., mass horizontal acceleration, column drift ratio, foundation moment, rotation and settlement), as well as in terms of cyclic moment – rotation and cyclic settlement – rotation response. In general, the computed response agrees well with the experimental response except for the last ground motion, where sand falling from the backfill under the gapping side of the footing at large rotations, results in increased energy dissipation, significant footing residual rotation, and incremental permanent footing uplifting.

Figure 3.13 provides a comparison summary for the peak footing rotation demand, hysteretic moment – rotation energy dissipation, residual footing rotation and settlement. BNWF model captures peak footing rotation demand within 20%, while consistently under-predicts hysteretic energy dissipation and residual footing settlement by a factor of 1.3.

3.5 SUMMARY

This chapter has shown that the behavior of shallow foundations in centrifuge and 1g shake table experiments can be adequately modeled using BNWF models for rocking-dominated foundations. As a good approximation, the foundations will be rocking dominated if the normalized moment-to-shear ratio [$M_{fc}/(V \times L_f)$] is greater than 1. An improved BNWF model for rocking foundations is described. Having demonstrated in this chapter the adequacy of BNWF models for NRHA, the BNWF will be further used as a tool for testing the validity of the simplified displacement-based analysis method for bridges on rocking foundations.

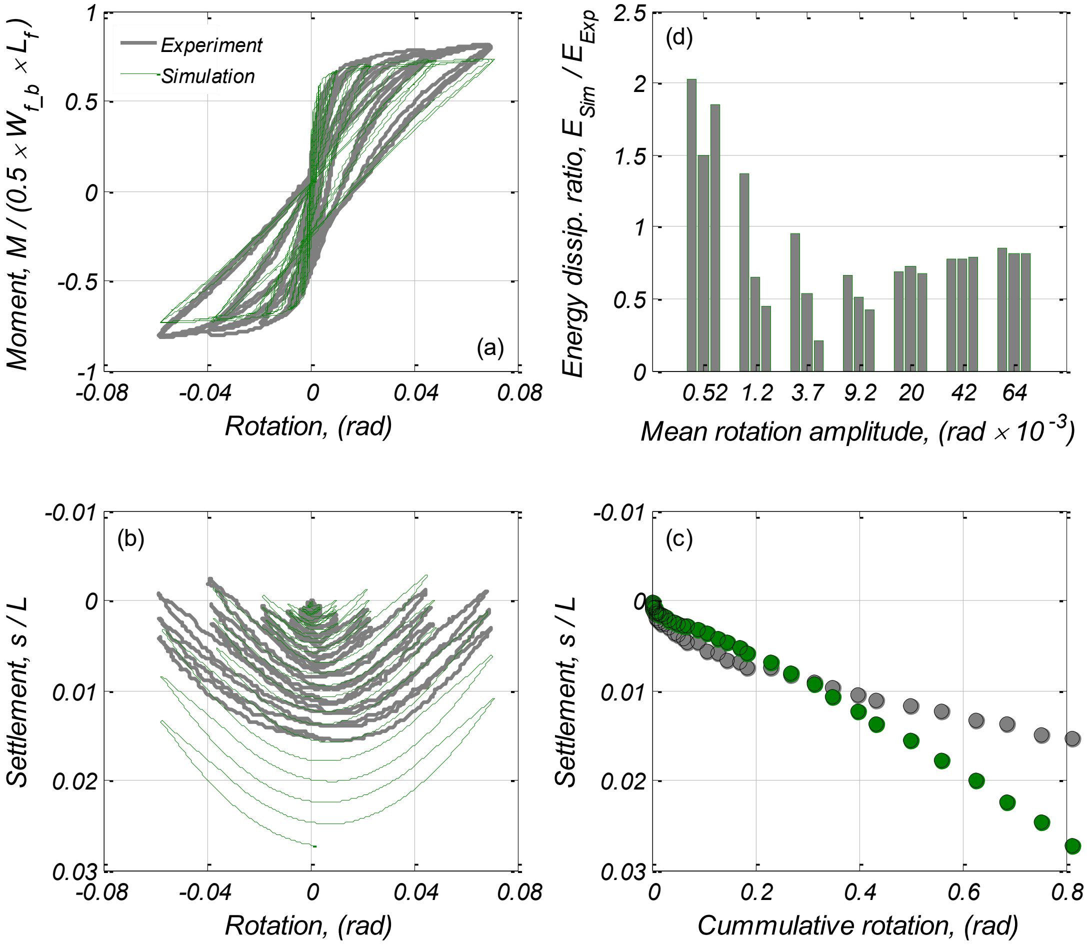

Figure 3.4 Comparison of BNWF model against Test No. 1 [Hakhamaneshi et al. 2014]: (a) moment – rotation; (b) settlement – rotation; (c) settlement – cumulative rotation; and (d) energy dissipation due to moment – rotation hysteresis.

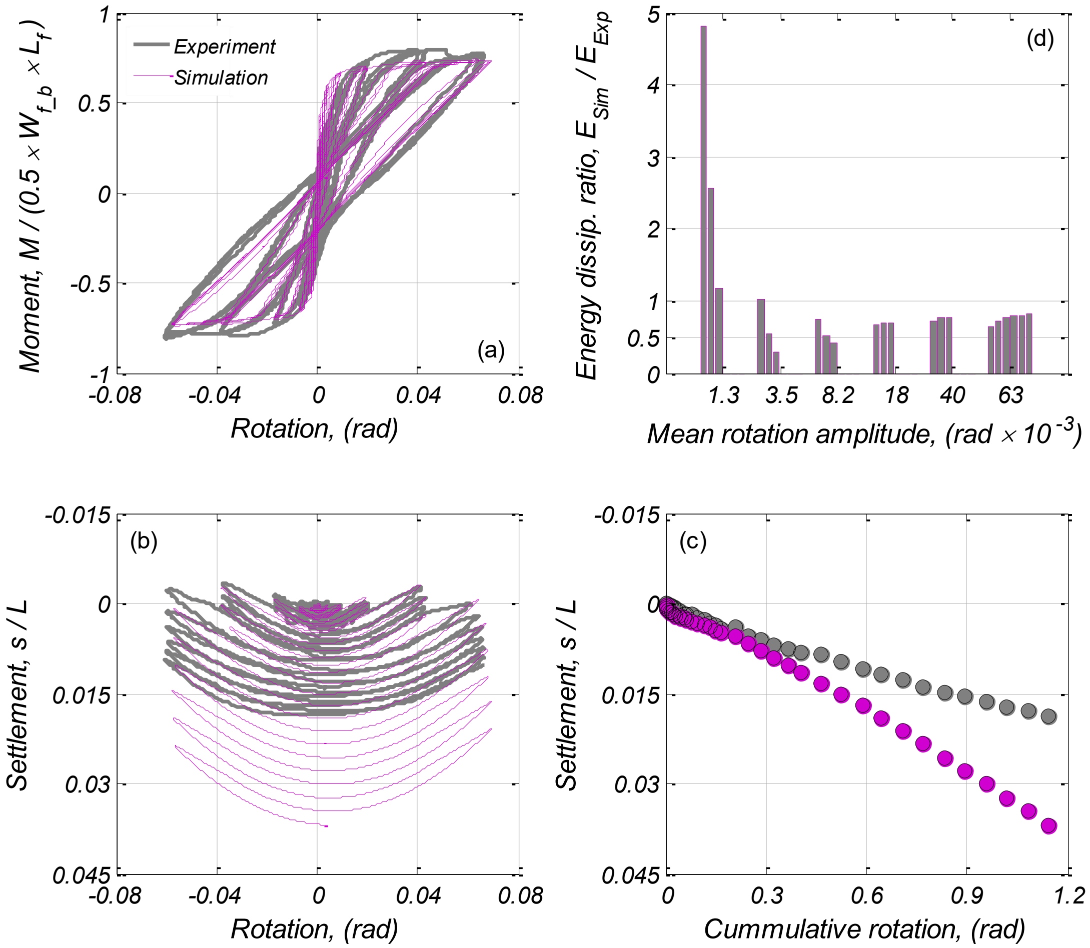

Figure 3.5 Comparison of BNWF model against Test No. 2 [Hakhamaneshi et al. 2014]: (a) moment – rotation; (b) settlement – rotation; (c) settlement – cumulative rotation; and (d) energy dissipation due to moment – rotation hysteresis.

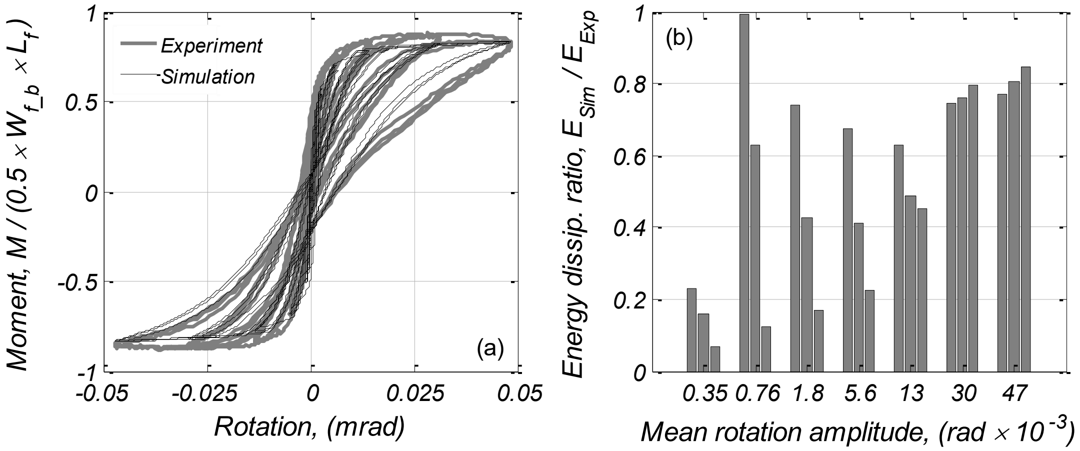

Figure 3.6 Comparison of BNWF numerical model against Test No. 3 [Liu et al. 2015]: (a) moment – rotation; and (b) energy dissipation due to moment – rotation hysteresis.

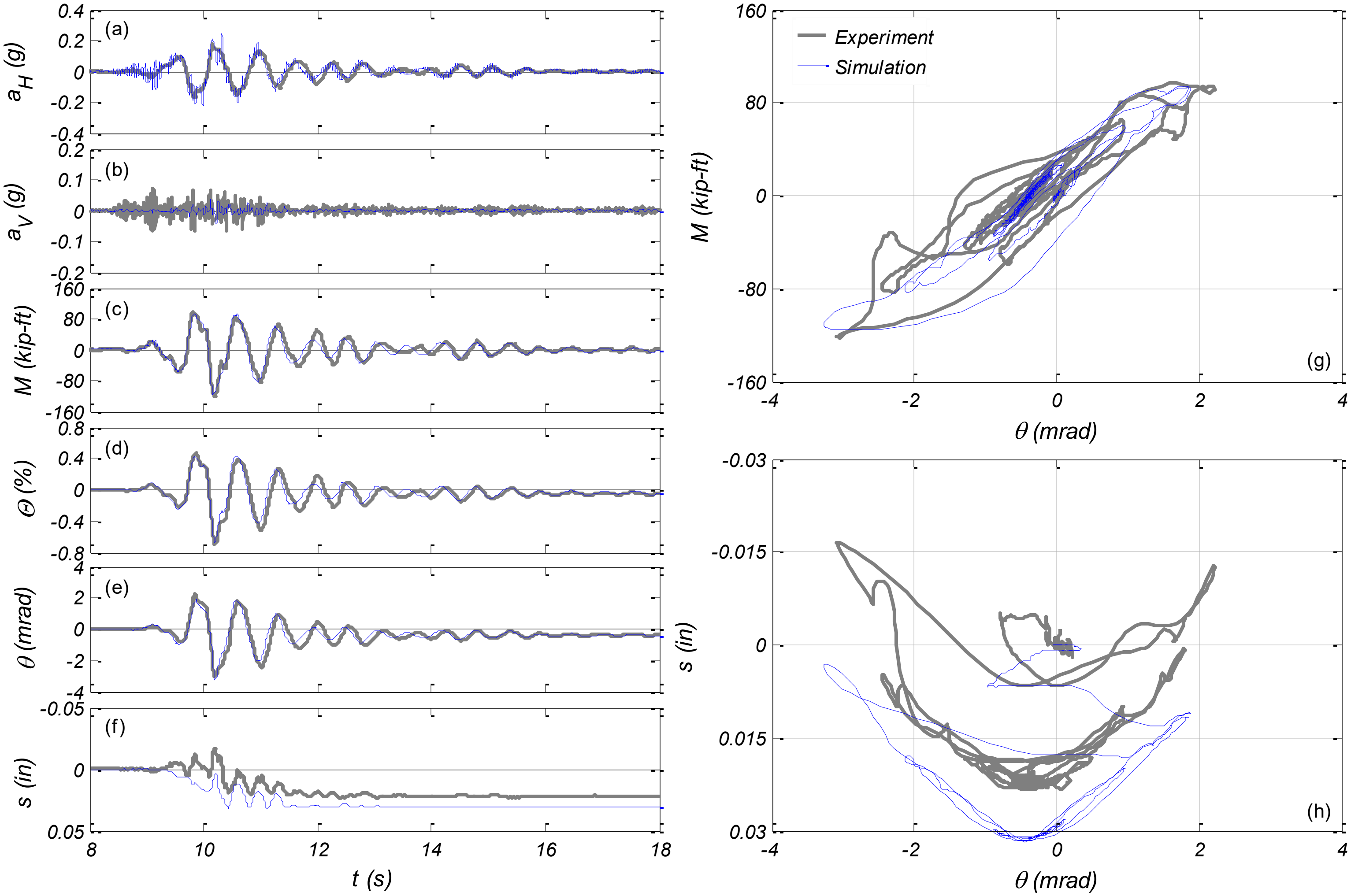

Figure 3.7 Comparison of BNWF model against Test No. 4 [Antonellis et al. 2014] for the Gilroy #1 (100%) motion: (a) mass lateral acceleration; (b) mass vertical acceleration; (c) foundation moment; (d) column drift ratio; (e) foundation rotation; and (f) foundation settlement response histories; (g) foundation moment –rotation; and (h) foundation settlement – rotation responses.

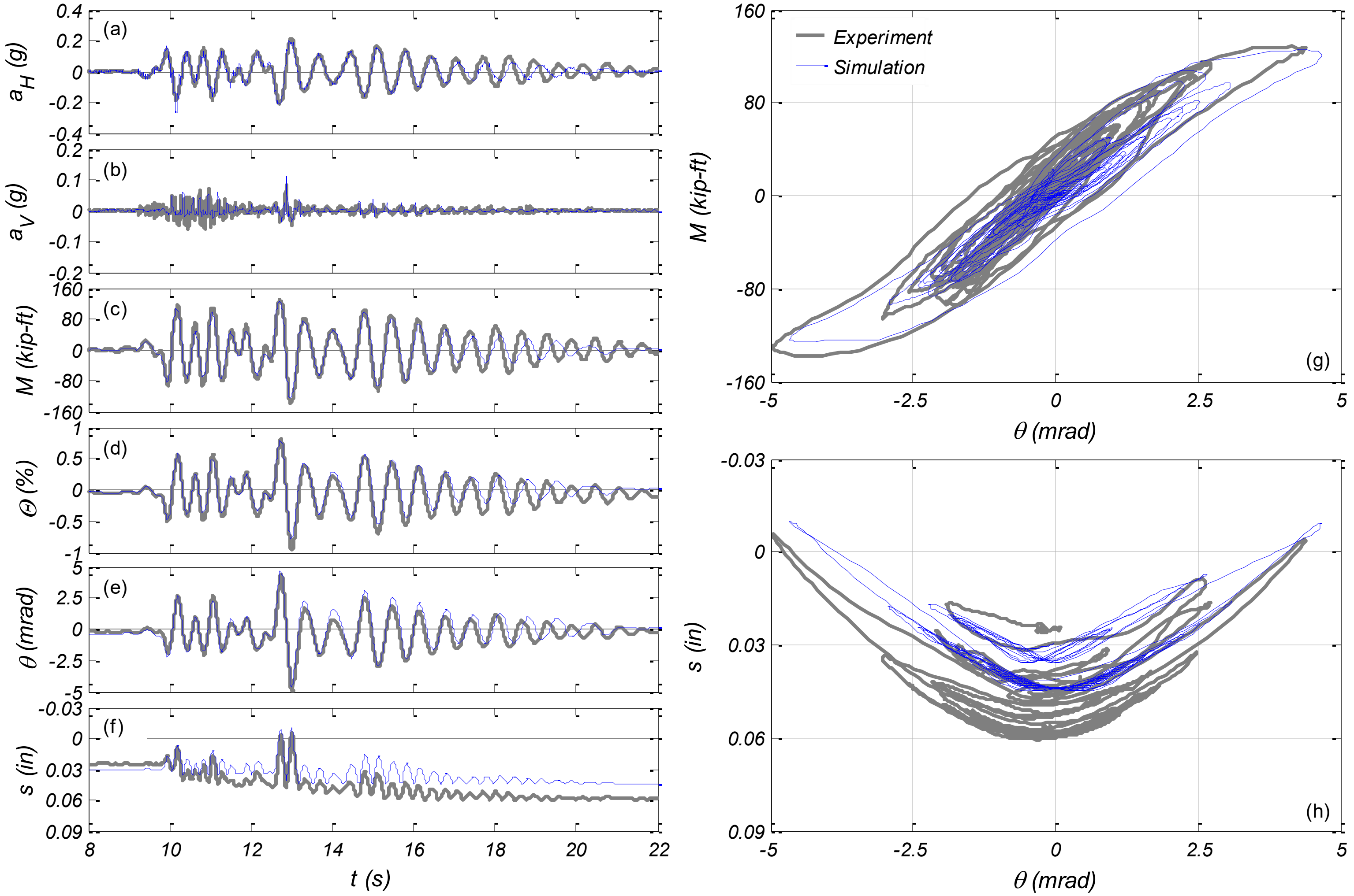

Figure 3.8 Comparison of BNWF model against Test No. 4 [Antonellis et al. 2014] for the Corralitos (80%) motion: (a) mass lateral acceleration; (b) mass vertical acceleration; (c) foundation moment; (d) column drift ratio; (e) foundation rotation; and (f) foundation settlement response histories; (g) foundation moment –rotation; and (h) foundation settlement – rotation responses.

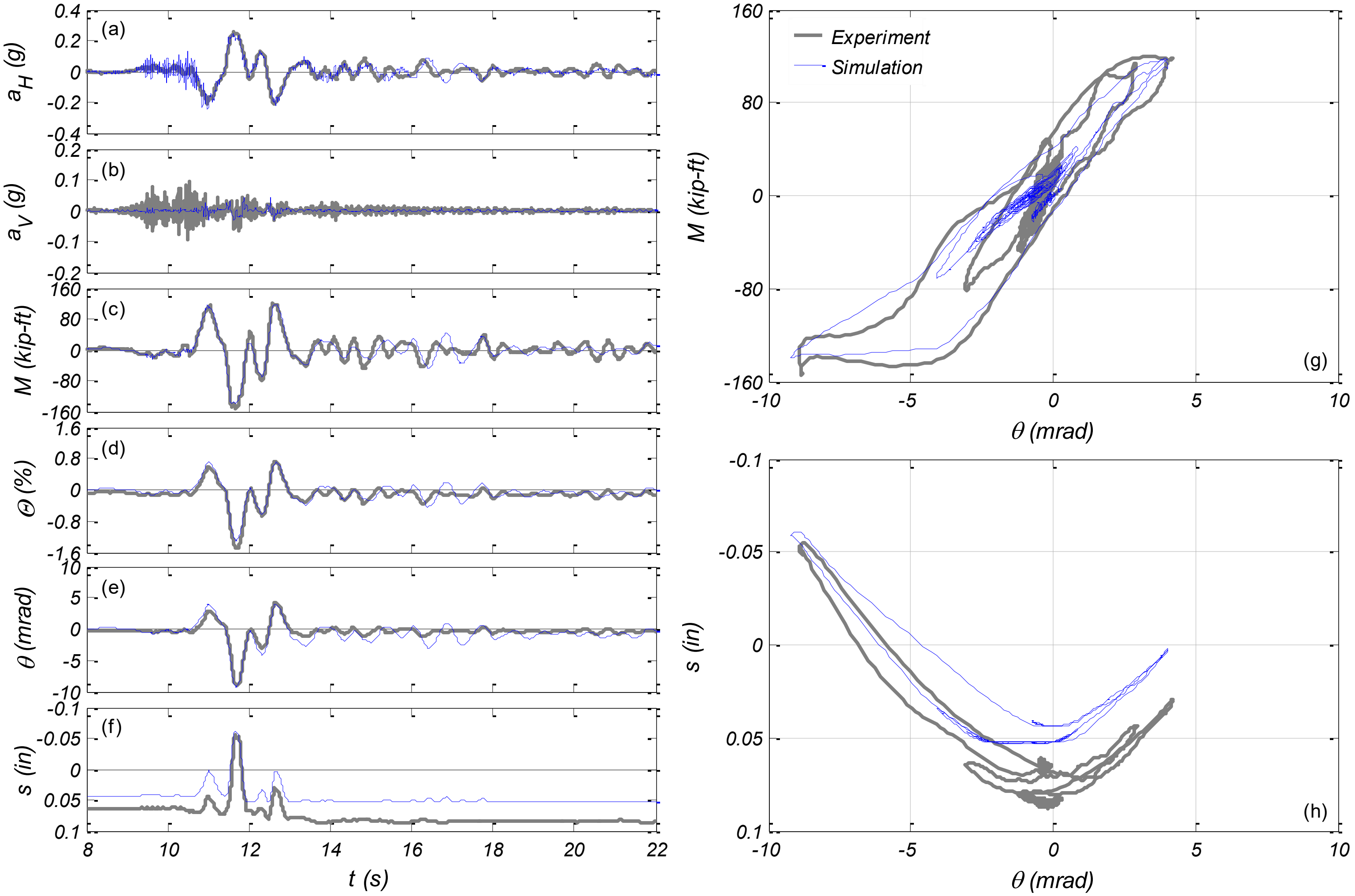

Figure 3.9 Comparison of BNWF model against Test No. 4 [Antonellis et al. 2014] for the El Centro #6 (110%) motion: (a) mass lateral acceleration; (b) mass vertical acceleration; (c) foundation moment; (d) column drift ratio; (e) foundation rotation; and (f) foundation settlement response histories; (g) foundation moment –rotation; and (h) foundation settlement – rotation responses.

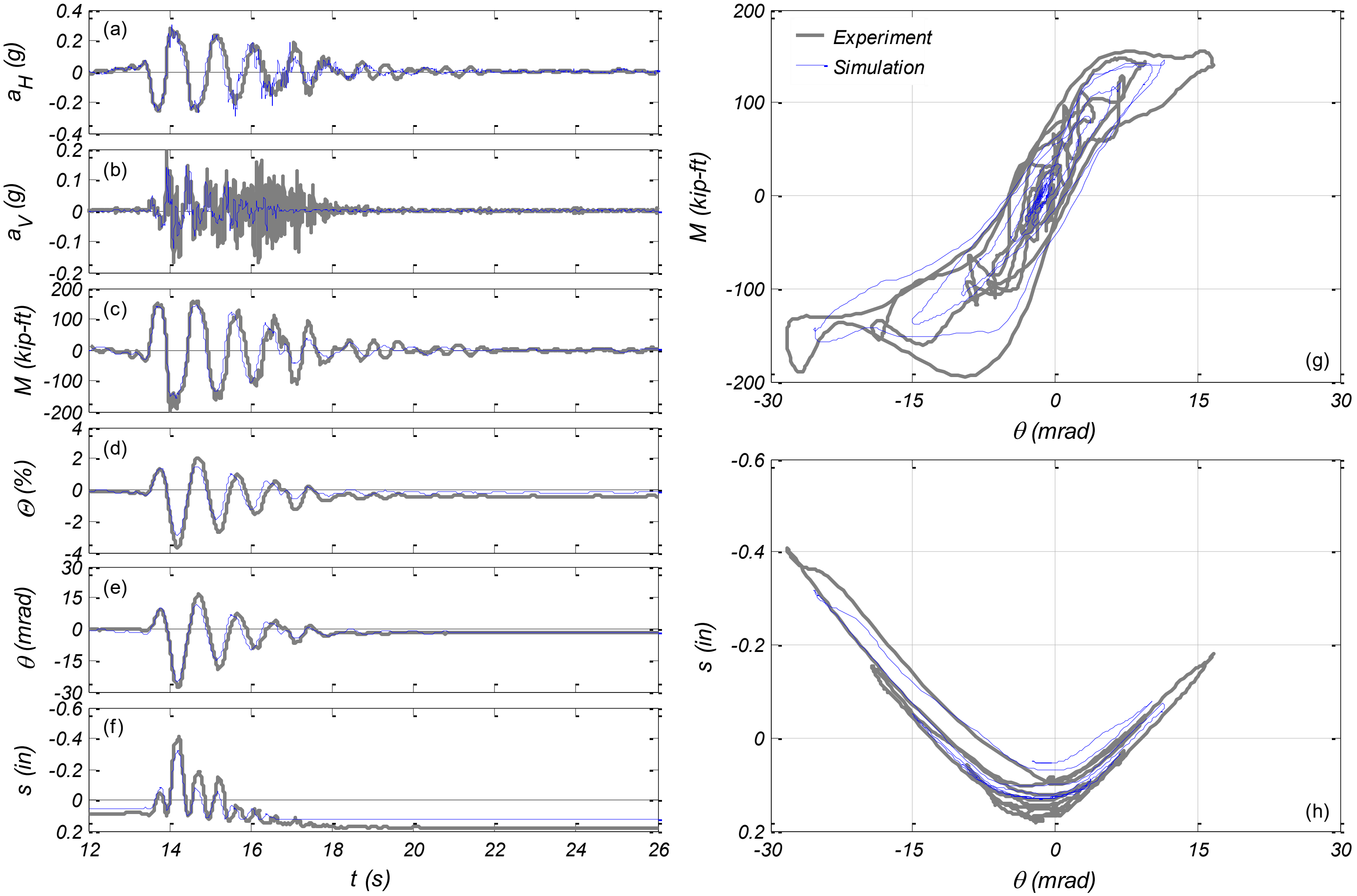

Figure 3.10 Comparison of BNWF model against Test No. 4 [Antonellis et al. 2014] for the Pacoima Dam (80%) motion: (a) mass lateral acceleration; (b) mass vertical acceleration; (c) foundation moment; (d) column drift ratio; (e) foundation rotation; and (f) foundation settlement response histories; (g) foundation moment –rotation; and (h) foundation settlement – rotation responses.

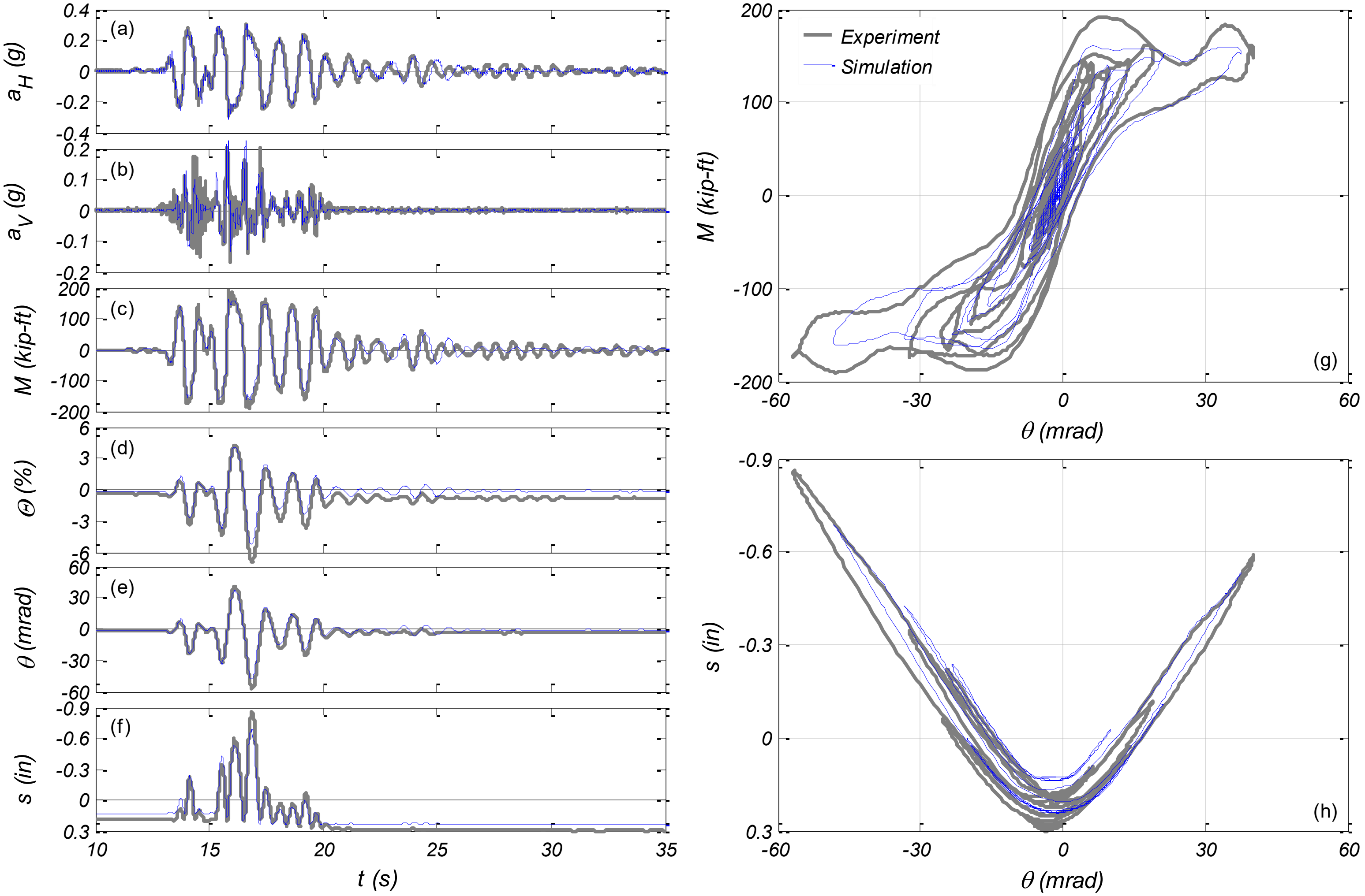

Figure 3.11 Comparison of BNWF model against Test No. 4 [Antonellis et al. 2014] for the Takatori (50%) motion: (a) mass lateral acceleration; (b) mass vertical acceleration; (c) foundation moment; (d) column drift ratio; (e) foundation rotation; and (f) foundation settlement response histories; (g) foundation moment –rotation; and (h) foundation settlement – rotation responses.

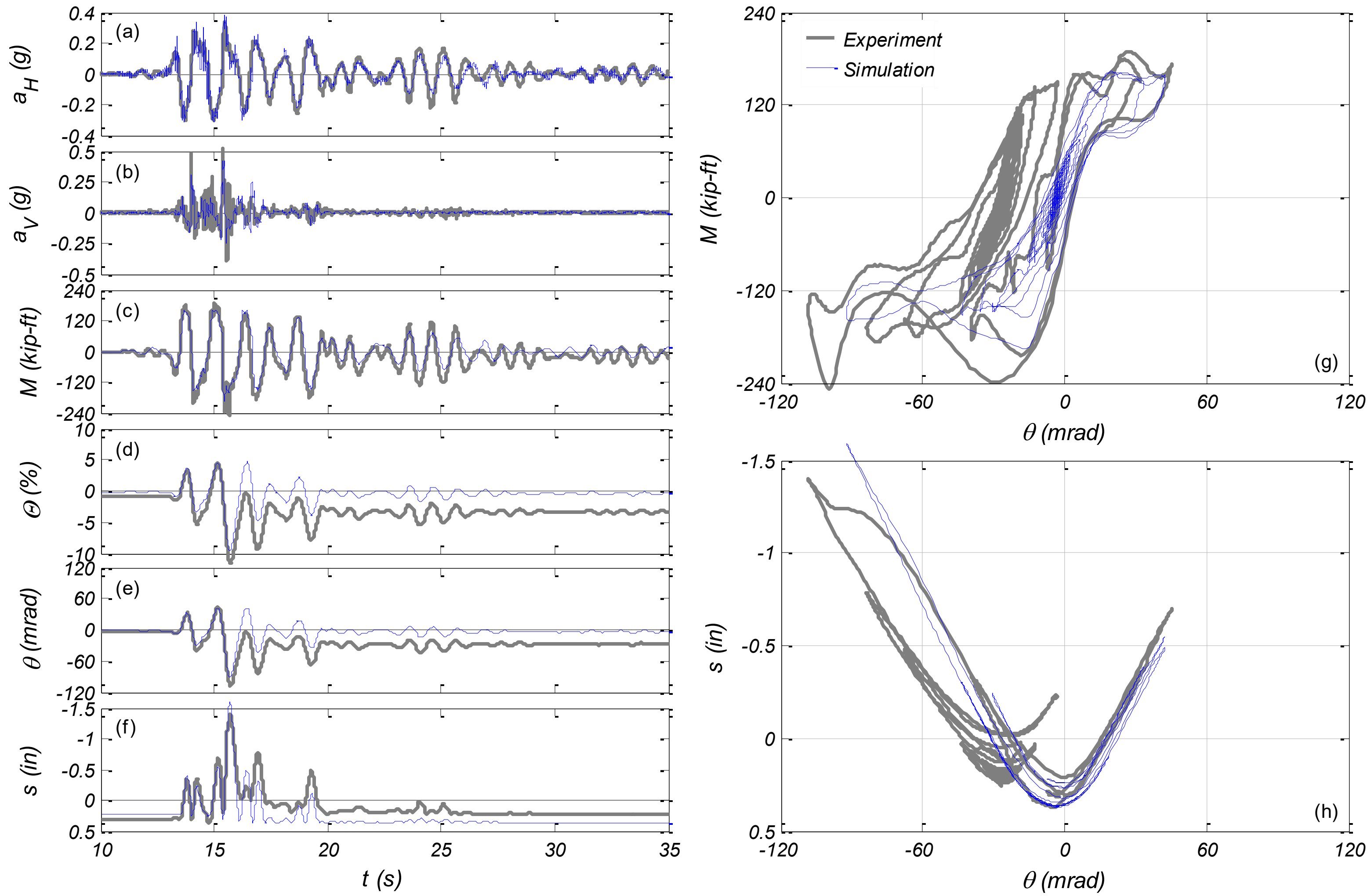

Figure 3.12 Comparison of BNWF model against Test No. 4 [Antonellis et al. 2014] for the Takatori (100%) motion: (a) mass lateral acceleration; (b) mass vertical acceleration; (c) foundation moment; (d) column drift ratio; (e) foundation rotation; and (f) foundation settlement response histories; (g) foundation moment –rotation; and (h) foundation settlement – rotation responses.

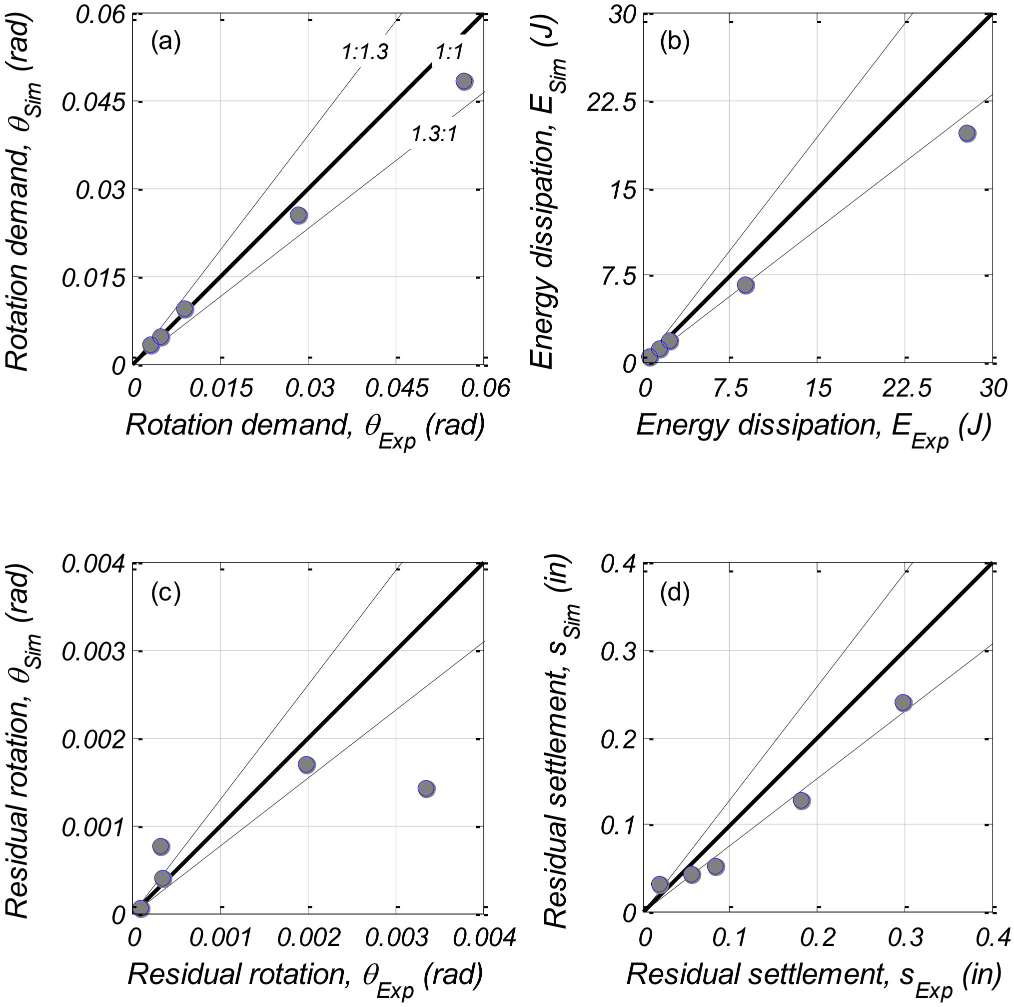

Figure 3.13 Comparison summary between BNWF model and Test No. 4 [Antonellis et al. 2014], excluding the Takatori (100%) motion: (a) peak footing rotation demand; (b) energy dissipation due to moment – rotation hysteresis; (c) residual footing rotation; and (d) residual footing settlement.

4 Displacement-Based Analysis for Single Elastic Cantilever Column Supported on Rocking Foundation

4.1 INTRODUCTION

This chapter develops and validates a displacement-based analysis method of a single elastic cantilever column supported on rocking foundation as shown in Figure 2.5(a). The method extends the Deng et al. [2014] formulation, summarized in Section 2.4, by determining the following: (i) the appropriate equivalent viscous damping due to rocking-induced soil inelasticity; and (ii) the P-Δ effects. For that purpose, nonlinear response history analyses (NRHA) are conducted for the calibrated BNWF models presented in Chapter 3. It is noted that the Deng et al. [2014] combination rule for integrating the rocking foundation hysteretic damping with the elastic radiation and column damping is maintained; appropriate adjustment factors, similar to those proposed Grant et al. [2005] for other hysteretic rules, are not studied here; the proposed elastic damping values are small and are not expected to significantly impact the design.

Firstly, the ground motion sets used, and the studied bridge pier characteristics are presented in Sections 4.2 and 4.3, respectively. Secondly, the BNWF models (Section 4.4) and their static monotonic and cyclic response (Section 4.5) is briefly discussed. Thirdly, the NRHA results are used to determine the correction factor that needs to be applied against the Deng et al. [2014] area-based hysteretic damping expressions so that the drift demand predicted by the displacement-based analysis method matches that of the NRHA (Section 4.6). Alternative to that approach, a purely BNWF-derived equivalent viscous damping expression is presented in

Section 4.7. Lastly, the importance of P-Δ effects is discussed in Section 4.8, and the proposed displacement-based analysis method is summarized in Section 4.9.

4.2 GROUND MOTIONS

4.2.1 Set of Broadband Ground Motions Representing M_w 7 Event

The first set of ground motions used (Table 4.1), consisted of 40 broadband records selected so that the mean response spectrum of the fault-normal components matched the median spectrum computed from Boore and Atkinson [2008] in the period range of 0-5 seconds, for a magnitude 7 (M_w 7) strike-slip earthquake at a site with distance of 10 km from the fault rupture plane and with V_{s30} equal to 820 ft/s [Baker et al. 2011]. Figure 4.1 shows the linear acceleration and displacement response spectra for each of the 40 fault-normal (FN) and fault-parallel (FP) components of the ground motions, as well as the mean spectra, for a damping ratio of 2%. For the numerical analyses conducted, the fault-normal and fault-parallel components of each ground motion record were applied separately to the bridge pier models with amplitude scale factors of 1/3, 1/2, 2/3, 1, 1.5, 2 and 3.

4.2.2 Set of Near-Fault Pulse-Like Ground Motions

Table 4.2 lists the 40 historical near-fault pulse-like ground motion records, studied by Lu and Panagiotou [2014], which were used in this study. The motions are rotated to the fault-normal (FN) and fault-parallel (FP) directions. The 40 ground motion records come from 17 earthquakes with magnitude (M_w) varying from 6.3 to 7.9; the recorded peak ground velocity (PGV) of the FN horizontal component of the 40 records ranges between 19.3 and 72.8 in/s, with a mean value of 41.7 cm/s. The specific earthquakes and their associated records are numbered in ascending order of earthquake magnitude. For each motion, the first two predominant pulses are identified by wavelet analysis (the CPEV_EN method as described in Lu and Panagiotou 2014) and the pulse period, acceleration and velocity amplitude, energy and area are also listed in Table 4.2. Additionally, the following parameters of the records are listed in Table S1 in the electronic supplement to the paper of Lu and Panagiotou [2014]: strike angle, distance from fault rupture plane (R_{rup}), peak ground acceleration (PGA), peak ground velocity (PGV), peak ground displacement (PGD), and shear wave velocity of the top 30 m of soil (V_{s30}).

These 40 records were selected by the following criteria: (a) earthquake magnitude $M_W \geq 6.3$; (b) distance from the fault rupture plane less than 10 km; and (c) PGV ≥ 23.6 in/s in any of the two recorded horizontal components. The 1979 Imperial Valley (CA), 1994 Northridge (CA), and 1999 Chi-Chi (Taiwan) earthquake records were limited to 5, 8, and 9 records, respectively, those with the largest PGV. The 2011 Christchurch (New Zealand) earthquake resulted in four more ground motion records (in addition to the PRPC record studied here) with $R_{rup} \leq 10$ km and PGV ≥ 23.6 in/s that were not included. It should be noted that these 40 records are about 40% of the total number of historical records to date with $M_W \geq 6.3$ and $R_{rup} \leq 10$ km.

Figure 4.2 shows the 2% damped acceleration and displacement response spectra for each of the 40 fault-normal (FN) and fault-parallel (FP) components of the ground motions along with the mean spectra. Similar to the broadband set of ground motions, the numerical analyses were conducted with the fault-normal and fault-parallel components of each ground motion record applied separately to the bridge pier models, while the amplitude scale factors used were 1/3, 1/2, 2/3, 1, 1.5, 2 and 3.

Table 4.1 Broadband set of ground motions.

No.	Earthquake Location	Year	M_w	R_{rup} (km)	Station Name
1	Mammoth Lakes	1980	6.0	15.5	Long Valley Dam (Upr L Abut)
2	Chi-Chi, Taiwan	1999	7.6	16.1	CHY036
3	Cape Mendocino, CA	1992	7.0	14.3	Rio Dell Overpass – FF
4	Imperial Valley, CA	1979	6.5	22	Delta
5	Kocaeli, Turkey	1999	7.5	4.8	Yarimca
6	Imperial Valley, CA	1979	6.5	24.6	Calipatria Fire Station
7	Chi-Chi, Taiwan	1999	7.6	14.8	CHY034
8	Chi-Chi, Taiwan	1999	7.6	38.4	NST
9	Kocaeli, Turkey	1999	7.5	15.4	Duzce
10	Trinidad	1980	7.2	-	Rio Dell Overpass, E Ground
11	Spitak, Armenia	1988	6.8	-	Gukasian
12	Loma Prieta, CA	1989	6.9	14.3	Gilroy Array #4
13	Chi-Chi, Taiwan	1999	7.6	8.5	TCU060
14	Victoria, Mexico	1980	6.3	19	Chihuahua
15	Loma Prieta, CA	1989	6.9	39.9	Fremont - Emerson Court
16	Chalfant Valley	1986	6.2	7.6	Zack Brothers Ranch
17	Chi-Chi, Taiwan	1999	7.6	26.8	TCU118
18	Denali, Alaska	2002	7.9	2.7	TAPS Pump Station #10
19	Imperial Valley, CA	1979	6.5	7.1	El Centro Array #4
20	Big Bear	1992	6.5	-	San Bernardino - E & Hospitality
21	Landers, CA	1992	7.3	23.6	Yermo Fire Station
22	Northridge, CA	1994	6.7	5.4	Sylmar - Converter Sta
23	San Fernando, CA	1971	6.6	22.8	LA - Hollywood Stor FF
24	N. Palms Springs, CA	1986	6.0	12.1	Morongo Valley
25	Loma Prieta, CA	1989	6.9	27.9	Hollister - South & Pine
26	Chi-Chi, Taiwan	1999	7.6	6.4	TCU055
27	Chi-Chi, Taiwan	1999	7.6	19.1	CHY025
28	Imperial Valley, CA	1979	6.5	10.4	Brawley Airport
29	Chi-Chi, Taiwan	1999	7.6	37.5	CHY088
30	Duzce, Turkey	1999	7.1	6.6	Duzce
31	Chi-Chi, Taiwan	1999	7.6	17.2	TCU061
32	Loma Prieta, CA	1989	6.9	8.5	Saratoga - Aloha Ave
33	Imperial Valley, CA	1940	7.0	6.1	El Centro Array #9
34	Chi-Chi, Taiwan	1999	7.6	31.8	TCU123
35	Northridge, CA	1994	6.7	5.4	Jensen Filter Plant
36	Chi-Chi, Taiwan	1999	7.6	35.1	CHY104
37	Loma Prieta, CA	1989	6.9	32.8	Salinas - John & Work
38	Loma Prieta, CA	1989	6.9	20.8	Coyote Lake Dam (Downst)
39	Chi-Chi, Taiwan	1999	7.6	40.4	CHY008
40	Chi-Chi, Taiwan	1999	7.6	45.7	TCU141

Table 4.2 Near-fault pulse-like set of unscaled ground motions.

No.	Earthquake Location	Year	M_w	Station Name	R_{rup} (km)	1st pulse (FN)					2nd pulse (FN)				
						T_p (s)	a_{max} (g)	v_{max} (in/s)	E (ft^2/s)	A (ft)	T_p (s)	a_{max} (g)	v_{max} (in/s)	E (ft^2/s)	A (ft)
1	Christchurch, NZ	2011	6.3	PRPC	2.5	2.3	0.26	35.6	8.0	4.2	4.6	0.04	11.2	2.2	3.8
2	Coalinga, CA	1983	6.4	Pleasant Valley P.P. - Yard	8.4	0.7	0.49	22.8	1.0	0.8	1.1	0.18	13.9	0.8	1.1
3	Superstition Hills, CA	1987	6.5	Parachute Test Site	1.0	2.2	0.30	38.1	9.6	4.5	5.0	0.03	10.4	1.8	3.4
4	Imperial Valley-06, CA	1979	6.5	EC Meloland Overpass FF	0.1	2.7	0.19	34.4	8.3	4.8	2.0	0.08	10.9	0.9	1.6
5	Imperial Valley-06, CA	1979	6.5	El Centro Array #7	0.6	3.4	0.13	28.9	9.0	6.1	0.7	0.29	13.0	0.6	0.9
6	Imperial Valley-06, CA	1979	6.5	El Centro Array #6	1.4	3.5	0.16	33.2	14.9	8.0	7.7	0.01	2.8	0.3	2.2
7	Imperial Valley-06, CA	1979	6.5	El Centro Array #5	4.0	3.8	0.14	31.9	10.7	6.3	2.9	0.05	8.1	0.6	1.5
8	Imperial Valley-06, CA	1979	6.5	El Centro Array #4	7.1	4.3	0.10	27.2	8.8	6.1	1.3	0.13	9.7	0.4	0.9
9	San Fernando, CA	1971	6.6	Pacoima Dam	1.8	1.4	0.41	38.7	5.4	2.8	5.4	0.03	10.8	1.8	3.5
10	Erzincan, Turkey	1992	6.7	Erzincan	4.4	2.4	0.20	31.1	6.1	3.9	0.9	0.24	14.4	0.9	1.1
11	Northridge, CA	1994	6.7	Sylmar - Converter Sta East	5.2	2.8	0.10	18.6	5.1	5.3	1.0	0.31	18.7	1.0	1.0
12	Northridge, CA	1994	6.7	Sylmar Olive View Med FF	5.3	2.4	0.15	25.0	7.1	5.8	1.2	0.21	17.4	1.7	2.0
13	Northridge, CA	1994	6.7	Sylmar - Converter Sta	5.4	2.6	0.16	27.6	9.9	7.2	1.2	0.29	24.0	3.2	2.8
14	Northridge, CA	1994	6.7	Jensen Filter Plant	5.4	2.7	0.15	29.2	9.5	6.6	1.1	0.21	16.9	1.1	1.3
15	Northridge, CA	1994	6.7	Newhall W. Pico Canyon Rd	5.5	2.4	0.24	30.5	7.4	4.1	1.0	0.17	11.7	0.6	1.1
16	Northridge, CA	1994	6.7	Newhall Fire Station	5.9	0.9	0.65	37.5	3.3	1.7	2.0	0.17	19.3	2.2	2.0
17	Northridge, CA	1994	6.7	Rinaldi Receiving Station	6.5	1.2	0.70	50.9	8.6	3.2	1.8	0.17	19.0	1.8	1.8
18	Northridge, CA	1994	6.7	Pacoima Dam	7.0	0.9	0.66	26.3	3.1	1.6	0.7	0.36	17.1	0.9	1.0
19	Kobe, Japan	1995	6.9	Takarazuka	0.3	1.5	0.24	23.4	2.2	1.8	1.6	0.09	9.2	0.6	1.5
20	Kobe, Japan	1995	6.9	KJMA	1.0	0.8	0.69	37.4	4.7	2.6	2.2	0.14	16.7	2.0	2.1
21	Kobe, Japan	1995	6.9	Takatori	1.5	1.9	0.36	45.1	17.2	7.5	1.1	0.44	32.4	5.6	3.5
22	Loma Prieta, CA	1989	6.9	LGPC	3.9	2.9	0.10	20.9	6.0	5.9	1.2	0.32	25.6	2.0	1.6
23	Cape Mendocino, CA	1992	7.0	Cape Mendocino	7.0	5.0	0.05	13.8	2.6	3.6	0.9	0.29	17.6	0.8	0.8
24	Cape Mendocino, CA	1992	7.0	Petrolia	8.2	0.9	0.49	26.5	1.7	1.2	3.3	0.05	9.9	0.9	1.7
25	Duzce, Turkey	1999	7.1	Duzce	6.6	5.5	0.04	16.5	7.1	8.9	2.9	0.05	10.1	1.4	2.9
26	Landers, CA	1992	7.3	Lucerne	2.2	4.8	0.11	29.9	12.8	7.7	10.5	0.01	7.4	2.4	6.6
27	Tabas, Iran	1978	7.4	Tabas	2.1	4.7	0.12	39.6	25.9	13.5	3.8	0.05	12.3	2.9	4.7
28	Kocaeli, Turkey	1999	7.5	Sakarya	3.1	9.0	0.03	16.3	6.4	7.6	2.5	0.08	11.9	1.1	1.6
29	Kocaeli, Turkey	1999	7.5	Yarimca	4.8	7.7	0.03	12.6	4.1	5.5	3.0	0.06	12.1	2.0	3.5

Table 4.2 (Continued)

No.	Earthquake Location	Year	M_w	Station Name	R_{rup} (km)	1^{st} pulse (FN)					2^{nd} pulse (FN)				
						T_p (s)	a_{max} (g)	v_{max} (in/s)	E (ft^2/s)	A (ft)	T_p (s)	a_{max} (g)	v_{max} (in/s)	E (ft^2/s)	A (ft)
30	Chi-Chi, Taiwan	1999	7.6	TCU068	0.3	11.3	0.09	62.5	116.7	36.5	3.2	0.22	39.8	15.2	6.8
31	Chi-Chi, Taiwan	1999	7.6	TCU065	0.6	4.4	0.12	35.4	26.9	15.3	3.1	0.09	18.2	4.4	4.9
32	Chi-Chi, Taiwan	1999	7.6	TCU067	0.6	11.1	0.02	16.7	8.2	9.6	1.9	0.23	24.7	3.4	2.5
33	Chi-Chi, Taiwan	1999	7.6	TCU052	0.7	7.4	0.11	52.5	53.9	20.1	2.2	0.21	28.5	8.5	5.7
34	Chi-Chi, Taiwan	1999	7.6	TCU075	0.9	4.9	0.10	30.8	12.9	7.9	3.5	0.04	9.4	1.5	3.2
35	Chi-Chi, Taiwan	1999	7.6	TCU102	1.5	7.5	0.04	21.9	11.5	10.3	2.8	0.10	18.0	3.9	4.0
36	Chi-Chi, Taiwan	1999	7.6	CHY080	2.7	0.9	0.59	36.1	5.7	3.2	1.9	0.12	16.5	1.8	2.3
37	Chi-Chi, Taiwan	1999	7.6	CHY028	3.1	2.2	0.10	15.5	1.9	2.5	0.8	0.30	17.4	1.0	1.2
38	Chi-Chi, Taiwan	1999	7.6	TCU072	7.0	11.3	0.01	7.3	1.7	4.3	0.8	0.35	18.7	1.4	1.5
39	Denali, Alaska	2002	7.9	Alyeska Pump Station 10	2.7	7.4	0.04	18.5	7.6	7.3	2.4	0.14	20.9	5.5	5.1
40	Wenchuan, China	2008	7.9	Mianzuqingping	3.0	7.7	0.07	31.0	20.6	12.5	2.5	0.09	15.7	2.9	3.8

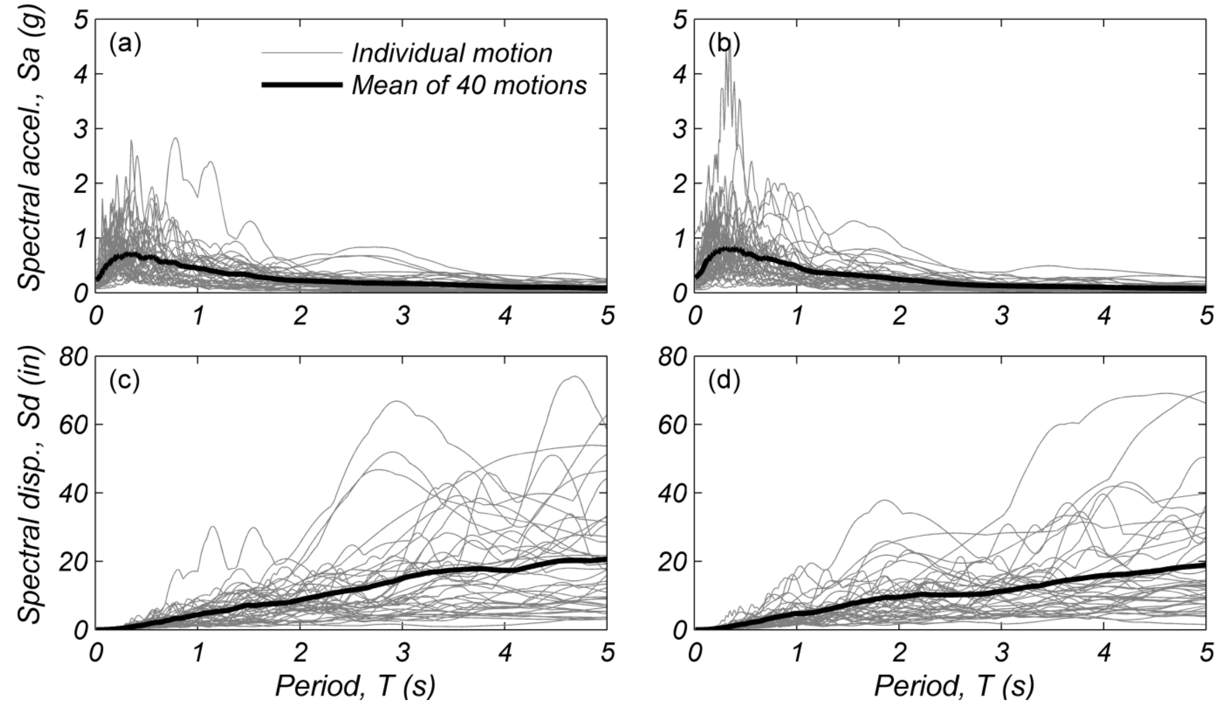

Figure 4.1 Linear acceleration and displacement spectra for 2% damping ratio for the unscaled (a, c) fault-normal and (b, d) fault-parallel components of the unscaled broadband ground motions.

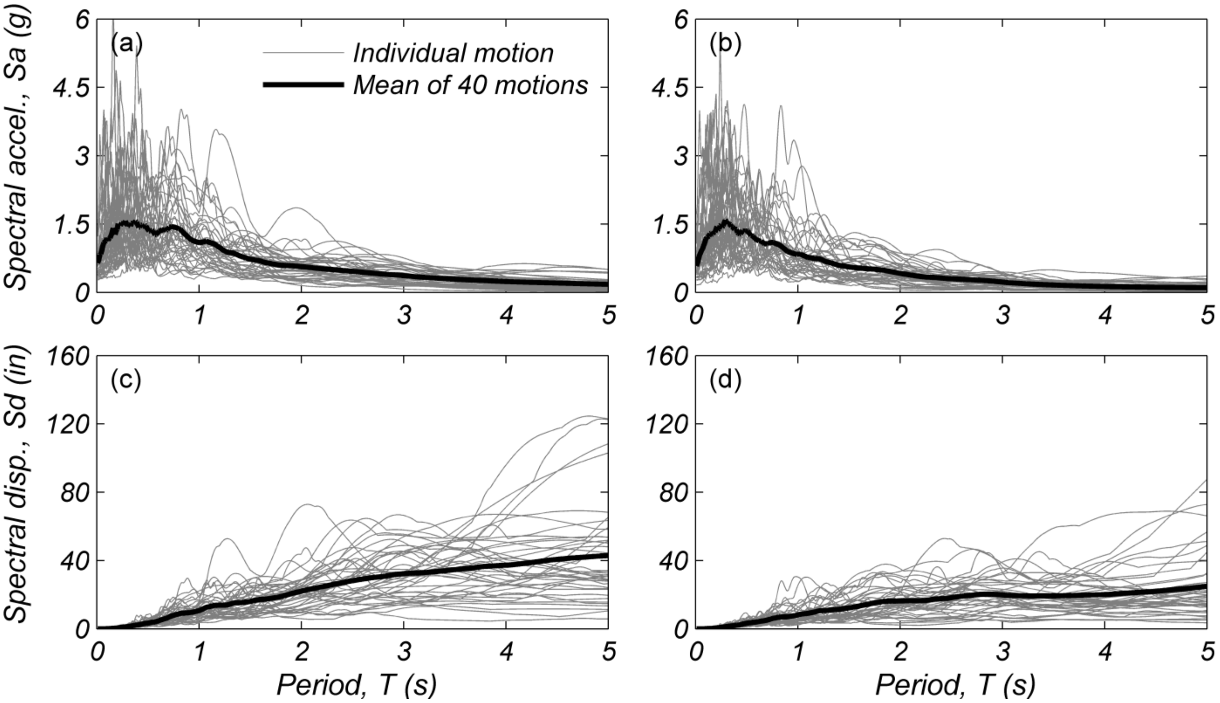

Figure 4.2 Linear acceleration and displacement spectra for 2% damping ratio for the unscaled (a, c) fault-normal and (b, d) fault-parallel components of the unscaled near-fault pulse-like ground motions.

4.3 BRIDGE PIER CHARACTERISTICS

In total, 688 idealized bridge piers supported on rocking shallow foundations were studied here to determine the appropriate equivalent viscous damping values due to the soil inelasticity beneath the footings. The bridge piers consisted of a square footing and a circular column supporting the effective deck weight. The key parameters varied between the models were: (i) the height of the column (H_c); (ii) the critical contact area ratio of the rocking foundation (ρ_{ac}); (iii) the rocking base shear coefficient (C_r); defined as the foundation base shear that mobilizes the moment capacity of the foundation divided by the seismic weight of the bridge pier; (iv) the deck weight (W_d); and (v) the inclusion or not of the P-Δ effects in the nonlinear response history analysis.

The different column heights were studied so that the initial elastic period of the rocking bridge piers would differ, when the other key parameters were the same. Specifically, five column heights (H_c) were investigated: 20, 40, 60, 80 and 100 ft. The critical contact area ratios of the footings (ρ_{ac}) studied here were equal to 0.33, 0.25, 0.14 and 0.09 to reflect different levels of soil inelasticity. Deng et al. [2012a] based on experimental studies showed that when $\rho_{ac} \leq 0.14$, the resulting residual settlements due to rocking are limited. However, as discussed in Section 3.4, BNWF numerical models underestimate on average the hysteretic damping observed in physical tests. With respect to the rocking base shear coefficient (C_r), a wide range of values was chosen (i.e. equal to 0.075, 0.1, 0.125, 0.15, 0.2, 0.25, 0.3, 0.35, 0.4 and 0.5) whereas the deck weights (W_d) were 1500, 3000 and 4500 kip. Finally, each model was analyzed with and without P-Δ effects.

The following simplifications were made to the studied bridge piers: (i) zero embedment depth; (ii) the footing and column elements were assumed stiff and massless; (iii) the mass moment of inertia of the deck was neglected; and (iv) the height of the footing and the vertical distance between the deck centroid and the top of the column were equal to zero.

Based on the above simplifications, assuming a column height (H_c), a critical contact area ratio (ρ_{ac}), a rocking base shear coefficient (C_r) and a deck weight (W_d), the required foundation moment capacity (M_{fc}) is calculated as $M_{fc} = C_r \cdot W_d \cdot H_c$. The required footing length (L_f), is then calculated as $L_f = (2 \cdot M_{fc})/[W_d \cdot (1-\rho_{ac})]$, while the bearing capacity of the soil at the critical contact area (q_c) is computed as $q_c = W_d / (A \cdot \rho_{ac})$. Finally, the foundation rocking stiffness at 50% of the moment capacity (K_{f_50}) is determined as $K_{f\_50} = 300 \cdot M_f$ [Deng et al. 2014]. Figure 4.3 plots the correlation between the main parameters of the studied models for an effective deck weight of 1500 kip.

Lastly, an additional set of bridge piers was analyzed with the inelastic mode of response to be that of column plastic hinging instead of foundation rocking. In that case an elastic-perfectly-plastic (EPP) rotational spring was placed at the base of the column. These piers were studied to confirm that the approach and set of ground motion used, for determining the appropriate equivalent viscous damping of rocking shallow foundations, can closely reproduce the published damping expression for the EPP hysteretic rule by Dwairi et al. [2007], Grant et al. [2005] and Priestley et al. [2007]. For the set of bridge piers with plastic hinging, the initial fundamental period of the pier was set equal to that of the respective rocking bridge pier (T_{f_50}) with $\rho_{ac} = 0.25$.

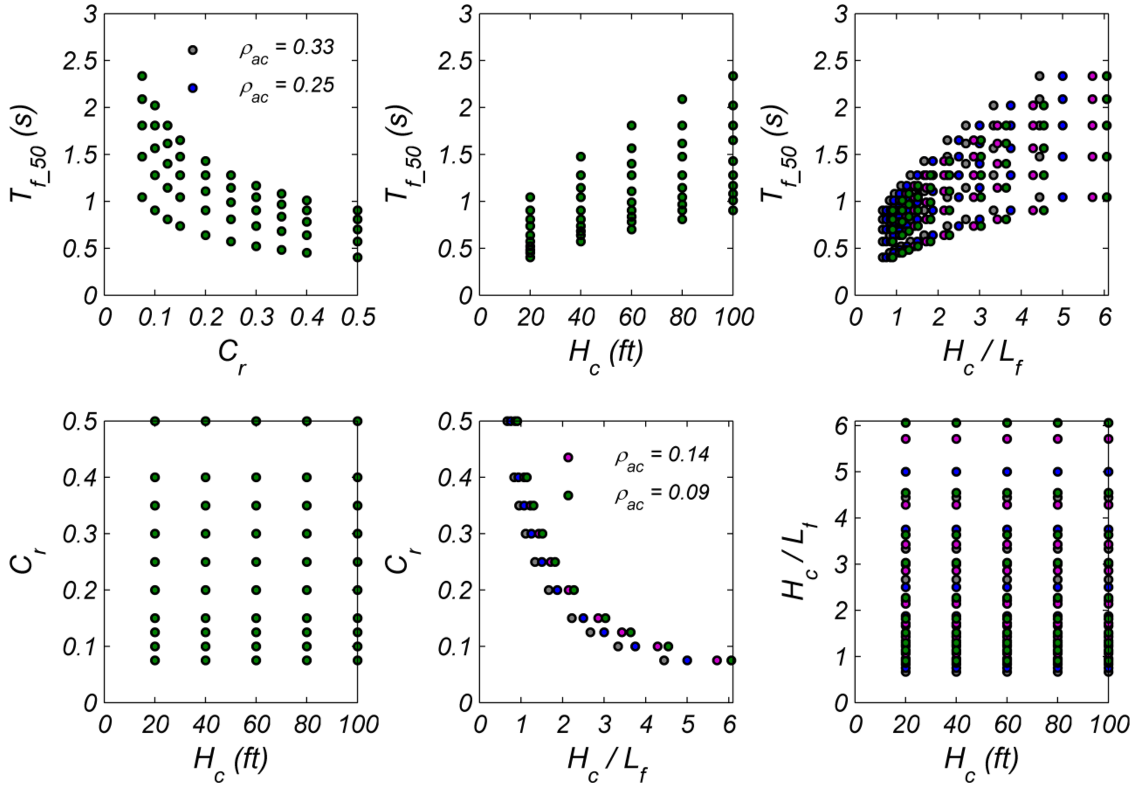

Figure 4.3 Correlation between the main parameters of the bridge pier models with deck weight of 1500 kip: rocking base shear coefficient (C_r); initial period (T_{f_50}); column height (H_c); and column height to footing length ratio (H_c / L_f).

4.4 NUMERICAL MODELS

Two-dimensional (2D) nonlinear response history analyses were conducted using the Open System for Earthquake Engineering Simulation (*OpenSees*) platform [Mazzoni et al. 2014]. The numerical model is similar to that shown in Figure 3.1(a), but with stiff linear elements used to model the column and the footing.

The soil underneath each surface footing was modeled using 43 vertical zero-length springs (*QzSimple1*) distributed in a non-uniform pattern. The number of springs within the critical contact length region ($L_c = A_c/L_f$) were equal to 14, 11, 5 and 5 for the critical contact area ratios (ρ_{ac}) equal to 0.33, 0.25, 0.14 and 0.09, respectively. The strength and stiffness of the vertical springs were obtained from the calibration procedure described in Section 3.3.2.

In addition, a zero-length horizontal spring using the *TzSimple1* force-displacement relation is attached to the base of the column. The stiffness of this spring is determined according to Gazetas [1991], while the ultimate force capacity is set equal to two times the deck weight to minimize sliding deformations, the effect of which is not studied here.

At the top of the column, a single translational mass was assigned to represent the deck effective weight, while the corresponding mass moment of inertia was set equal to zero. The gravity load was assigned as point load in the above location. Radiation dashpots for the soil-footing springs were not included. A small stiffness proportional damping was used to produce 0.1% damping ratio at the initial fundamental period. The tangent stiffness matrix of the previous time step was used to determine the damping matrix. A single horizontal direction of excitation was used for the numerical analyses.

The numerical model of the hinging column bridge piers is similar to that of the rocking foundation piers, but it used an elastic-perfectly-plastic rotational spring at the base of the stiff column. In addition, stiffness proportional damping was used to produce 2% damping ratio at the initial fundamental period, with the damping matrix updated based on the tangent stiffness matrix of the previous time step. The different viscous damping ratio is used to replicate the study by Dwairi et al. [2007].

4.5 STATIC MONOTONIC AND CYCLIC FOUNDATION RESPONSE

Figures 4.4 and 4.5 compare the normalized moment – rotation relationships of the BNWF numerical models and the Deng et al. [2014] trilinear backbone for the studied critical contact area ratios. The loading protocol for the static cyclic tests consisted of eight packets of increasing rotation amplitude, corresponding to normalized footing rotations (θ_f/b_f) of 0.1, 0.25, 0.5, 1, 2, 4, 6 and 8, with 3 cycles per packet. Figure 4.6 plots the area-based hysteretic damping ratios obtained from the cyclic static analysis of the BNWF models.

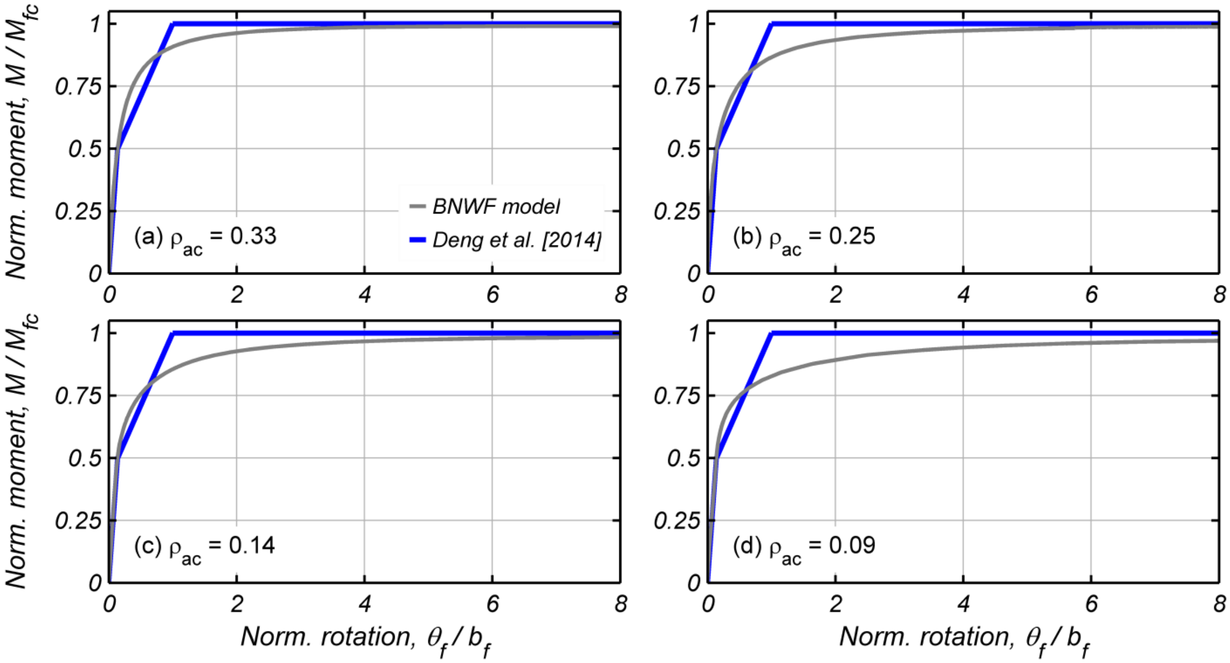

Figure 4.4 Monotonic moment – rotation foundation response compared with the Deng et al. [2014] trilinear backbone for the studied ρ_{ac} values.

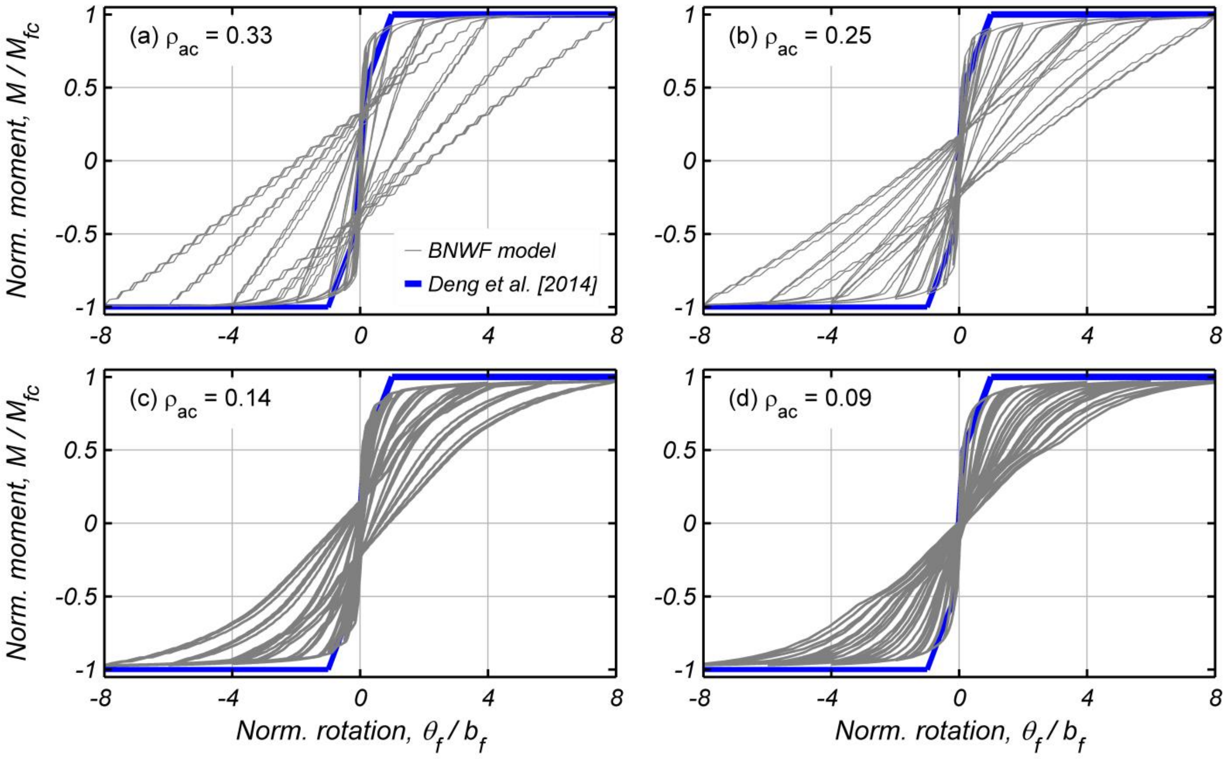

Figure 4.5 Static cyclic moment – rotation foundation response compared with the Deng et al. [2014] trilinear backbone for the studied ρ_{ac} values.

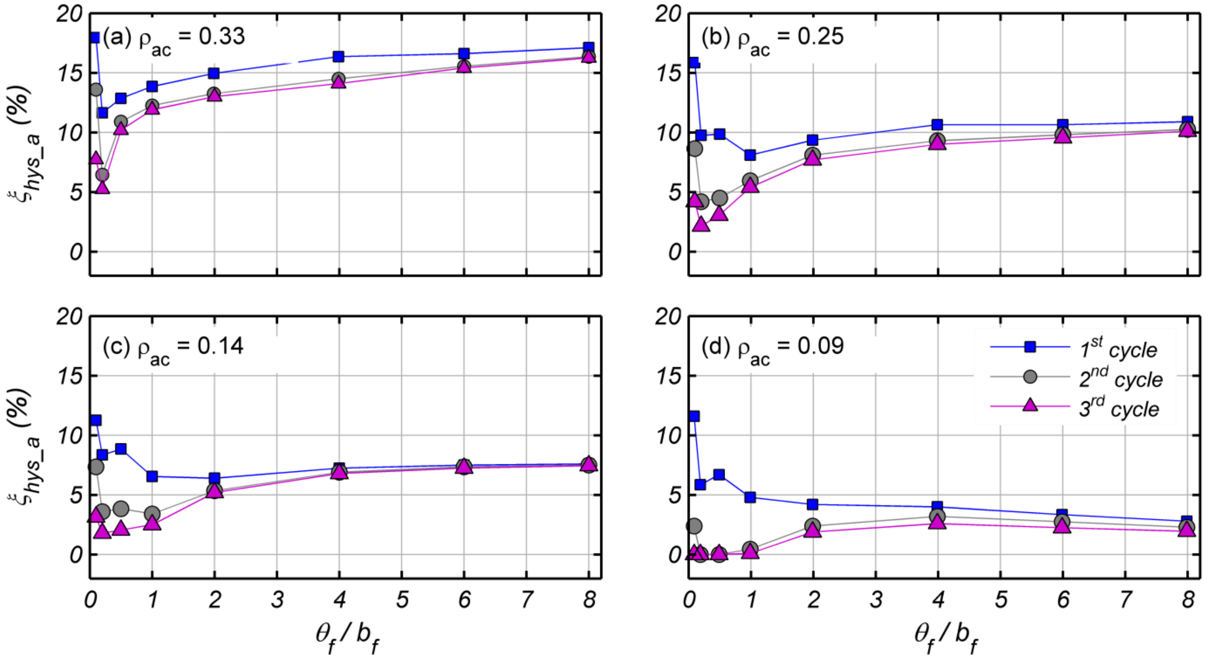

Figure 4.6 BNWF-derived (determined from Figure 4.5) area-based hysteretic damping ratios (ξ_{hys_a}) versus normalized footing rotation (θ_f / b_f) for the studied ρ_{ac} values.

4.6 CORRECTION FACTOR FOR THE DENG ET AL. [2014] AREA-BASED HYSTERETIC DAMPING RATIOS

The equivalent viscous damping for a hysteretic system may be computed from the area of a hysteresis loop as suggested by the Jacobsen [1930] approach for steady-state harmonic forced vibrations. Priestley et al. [2007], Dwairi et al. [2007], and Grant et al. [2005] showed that this approach seriously overestimates the effective viscous damping in earthquake applications, and that correction factors should be applied to the area-based damping for use in displacement-based analysis (see Section 2.2.1). They developed a set of correction factors required to make the mean peak drift for a set of ground motions, as predicted by DBA, equal to the mean (for the same set of motions) peak drift predicted by nonlinear response history analyses. The matching of drift demand is done in an average sense for a robust set of earthquake ground motions. They found that the correction factors were different for different shapes of hysteresis loops. In this section, we determine the appropriate correction factors for rocking foundation hysteretic systems. The reduction factors determined here will be applied to the Deng et al. [2014] area-based hysteretic damping ratio expressions.

4.6.1 Evaluation of the Ground Motion Sets Used

The results of the bridge piers with plastic hinging are presented to validate that the used ground motion sets can replicate the published equivalent viscous damping expressions of Dwairi et al. [2007] and Grant et al. [2005] for an elastic-perfectly-plastic hysteretic rule. Dwairi et al. [2007] used 100 unscaled far-field motions, while Grant et al. [2005] used a smaller number of spectrum-compatible artificial motions with longer strong motion duration. Priestley et al. [2007] combined the two studies by taking the average of them.

Procedure

The procedure closely follows that of Dwairi et al. [2007]. Specific steps followed are:

(i) Obtain the peak displacement demand from the nonlinear response history analysis (Δ_{NRHA}) and the corresponding ductility ($\mu = \Delta_{NRHA}/\Delta_y$) for each bridge pier model and ground motion. Discard the cases where peak displacement demand exceeds the static tip over displacement, Δ_{cr}, defined as $\Delta_{cr} = M_c/(H_c \cdot W_d)$.

(ii) Based on the peak displacement demand (Δ_{NRHA}) and the monotonic force-displacement backbone without P-Δ effects, compute the corresponding effective secant period (T_e).

(iii) Using T_e and Δ_{NRHA} calculate the equivalent system damping (ξ_{sys_eq}) needed so that the linear spectral displacement at T_e equals Δ_{NRHA}.

(iv) Recall that 2% elastic viscous damping (described in Section 4.4) was included in the NRHA. Hence, the equivalent hysteretic damping is obtained from $\xi_{hys\_eq} = \xi_{sys\_eq}$ - 2%. If the computed equivalent hysteretic damping system damping is negative, it was set to zero.

(v) Plot the equivalent hysteretic damping (ξ_{hys_eq}) versus ductility (μ_Δ) and determine a curve to fit the data based on the least squared error method.

Results

Figure 4.7 plots the ξ_{hys_eq} versus μ_Δ data, obtained from the nonlinear response history analyses for the fault-normal components of the broadband (BB_FN) set, based on the above procedure. The shown NRHA data are limited to those cases where displacement ductility is less than, or equal to 8, and $T_e > 1$ s. In addition, it shows the Dwairi et al. [2007] expression for $T_e \geq 1$ s, as well as the Grant et al. [2005] expressions for $T_e = 1$ s and $T_e = 6.6$ s that are the minimum and maximum effective periods in the plotted data set. Lastly, a moving median and a linear least square regression line, that is a scaled-down expression of the area-based hysteretic damping, are plotted based on the obtained data. It is observed that the moving median and regression lines, obtained from the BB_FN set, lie within the upper bound expression of Dwairi et al. [2007] and the lower bound expression of Grant et al. [2005].

Based on Figure 4.7, the area-based hysteretic damping ratio correction factor ($C_{\xi a\_\mu}$) for the EPP hysteretic rule and the BB_FN set can be obtained by dividing the empirical regression line of the NRHA data with the theoretical area-based hysteretic damping (ξ_{hys_a}). Figure 4.8 plots $C_{\xi a\_\mu}$ versus ξ_{hys_a} for displacement ductility of 2, 4 and 6, as obtained from the four ground motion sets considered here, and the Priestley et al. [2007] study. The broadband motions yield results that are in very good agreement with the Priestley et al. [2007] expression. A smaller $C_{\xi a\_\mu}$ is found to be needed for the near-fault motions; however, such motions have not been considered by Dwairi et al. [2007] and Grant et al. [2005].

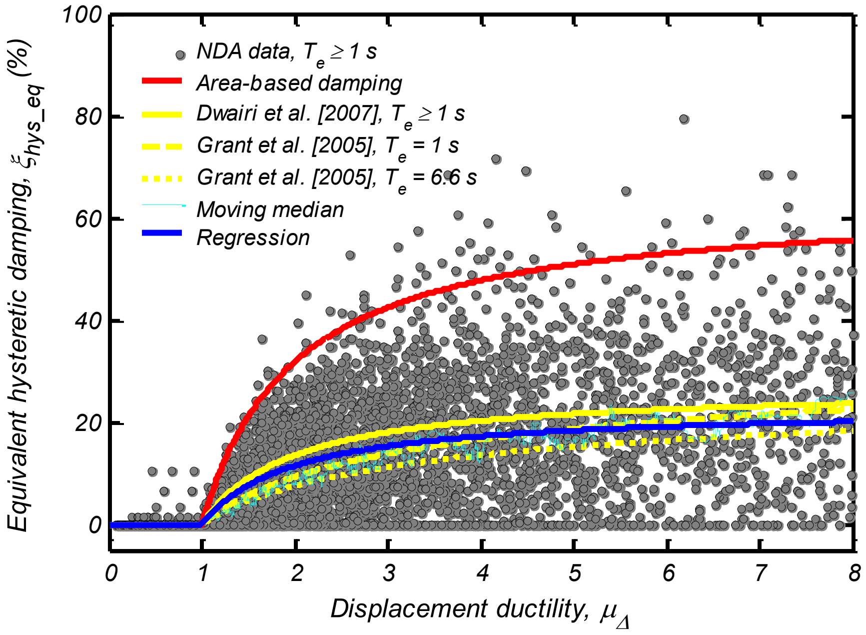

Figure 4.7 Nonlinear response history analyses – derived equivalent hysteretic damping versus ductility for the elastic-perfectly-plastic hysteresis rule for the fault-normal components of the broadband ground motions and comparison with published expressions.

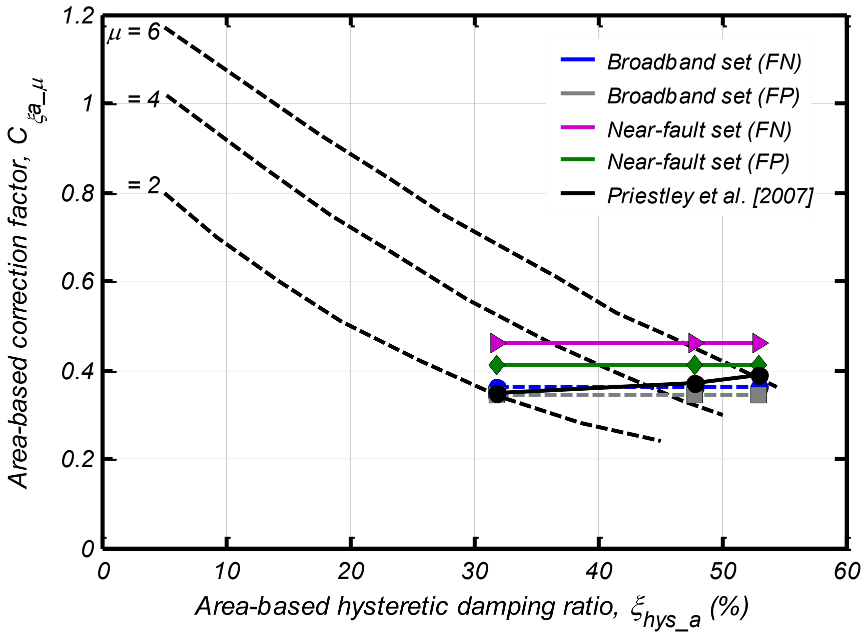

Figure 4.8 Correction factors to be applied to area-based hysteretic damping ratios ($C_{\xi a\_\mu}$) versus area-based hysteretic damping ratio (ξ_{hys_a}) for the elastic-perfectly-plastic hysteresis rule, for displacement ductility (μ) equal to 2, 4 and 6; comparison between present study and Priestley et al. [2007]. Note: Dashed black lines are approximate fit lines from Priestley et al. [2007] for various structural hysteretic rules and ductility of 2, 4 and 6 (see Figure 2.2).

4.6.2 Area-based Hysteretic Damping Ratio Correction Factor for Rocking Foundation

After demonstrating that our procedure was producing consistent results with other studies for elastic-perfectly-plastic systems, a similar procedure was followed to develop correction factors for the Deng et al. [2014] area-based expressions for hysteretic damping.

Procedure

The procedure is similar to the one used for the elastic-perfectly-plastic hysteresis rule. Specific steps are:

(i) Obtain the peak displacement (Δ_{NRHA}) and footing rotation demand (θ_{f_NRHA}) from the nonlinear response history analyses, and compute the corresponding normalized footing rotation (θ_{f_NRHA}/b_f) for each bridge pier model and ground motion using the BNWF model described in Section 4.4. Neglect the cases where peak displacement demand exceeds the static tip over displacement, Δ_{cr}, defined as $\Delta_{cr} = M_{fc}/(H_c \cdot W_d)$.

(ii) Based on the peak footing rotation demand (θ_{f_NRHA}) and the monotonic moment-rotation backbone of the BNWF models, compute the effective period (T_e) without elongation of period due to P-Δ effects.

(iii) Utilizing the T_e and Δ_{NDA}, calculate the equivalent hysteretic damping (ξ_{hys_eq}) so that the linear spectral displacement at T_e equals Δ_{NRHA}. If the equivalent hysteretic damping is less than zero, set $\xi_{hys\_eq} = 0$.

(iv) Plot the equivalent hysteretic damping (ξ_{hys_eq}) versus actual footing rotation demand (θ_{f_NRHA}/b_f) and smooth the data by a two-pass median filter, where first-pass and second-pass window width included 1/50 and 1/10 of the total number of data points respectively.

(v) For normalized footing rotations equal to 1, 2, 4, 6 and 8, compute the area-based correction factor ($C_{\xi a\_\mu}$) as the ratio between the first-cycle BNWF area-based hysteretic damping ratio and the median fit line. Normalized footing rotations less than 1 are not used for the regression, as the corresponding BNWF area-based hysteretic damping ratios are larger than those observed in physical tests, and hence, are considered to be unreliable (see Section 3.4 and Figure 4.6). In addition, the first-cycle BNWF area-based hysteretic damping curve is chosen, over those for the second and third cycle, as more relevant to the Deng et al. [2014] expressions that do not consider energy dissipation degradation upon continued cycling at the same amplitude.

Results

Figure 4.9 and Figure 4.10 plot the equivalent hysteretic damping ratio (ξ_{hys_eq}) versus normalized footing rotation (θ_f/b_f) as obtained from the NRHAs for ρ_{ac} values of 0.25 and 0.14, respectively. They also plot the area-based hysteretic damping ratio as obtained from the BNWF numerical model for the first cycle and the moving median fit-line to the NRHA data. It is observed that the moving median fit-line for the fault-normal components of the broadband set follows fairly closely the shape of the area-based damping, while for the other ground motion sets, the moving median line shows a constant or slightly decreasing equivalent hysteretic damping ratio with increasing footing rotation. The significant scatter of the data is also noticeable.

Figure 4.11 plots the correction factors for the area-based hysteretic damping ratios ($C_{\xi a\_\mu}$) as a function of the area-based hysteretic damping ratio (ξ_{hys_a}) for rocking shallow foundations for normalized footing rotations (θ_f/b_f) ranging from 1 to 8 for the different ρ_{ac} and ground motion sets. It is noticed that for the fault-normal components of the broadband set, $C_{\xi a\_\mu}$ is fairly independent of ρ_{ac} and footing rotation, ranging from 0.84 to 1.08, as opposed to the other ground motion sets studied. For these ground motion sets, $C_{\xi a\_\mu}$ decreases as footing rotation increases for a given ρ_{ac} value from about 1.36 for $\theta_f/b_f = 1$ to approximately 0.5 for $\theta_f/b_f = 8$. Nevertheless, given the simplifying nature of the displacement-based analysis method, it is proposed that $C_{\xi a\_\mu}$ can be taken, for all cases, as

$$C_{\xi a\_\mu} \approx 0.9 \tag{4.1}$$

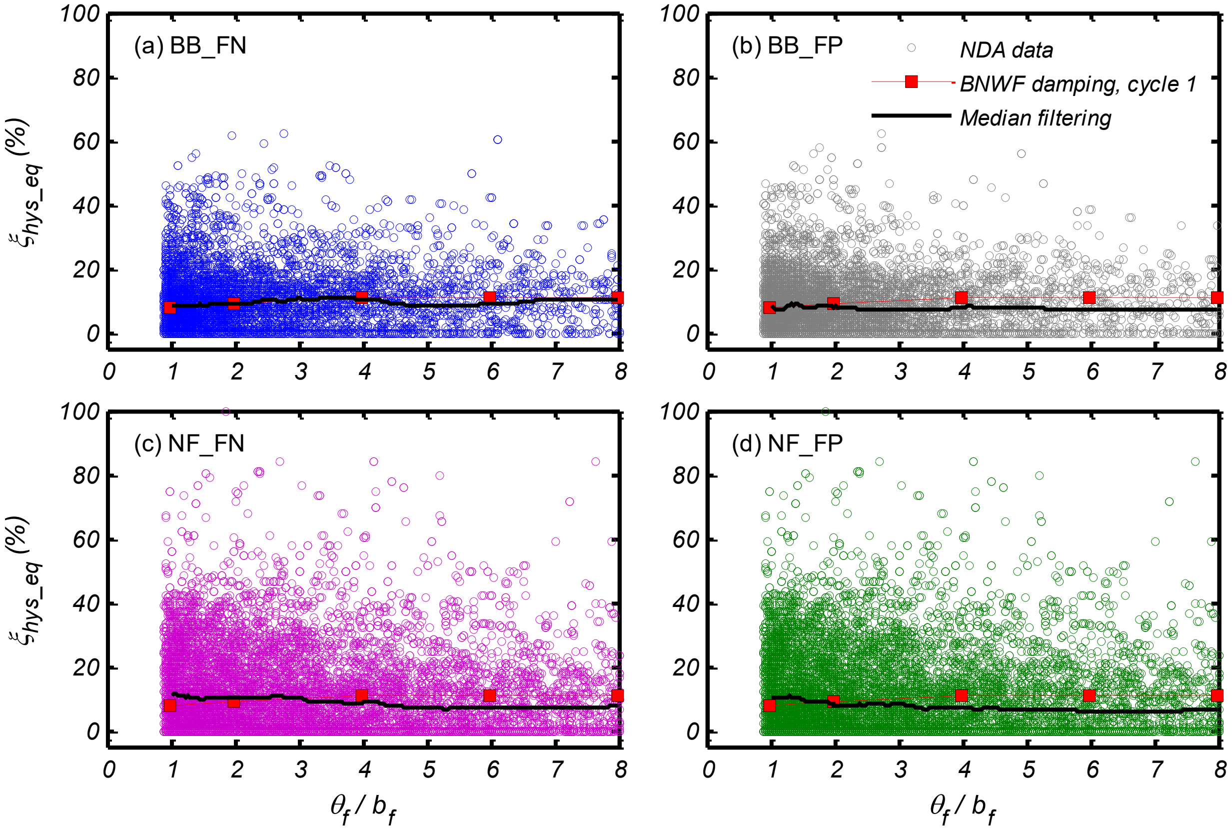

Figure 4.9 Nonlinear response history analyses – derived equivalent hysteretic damping (ξ_{hys_eq}) versus normalized footing rotation (θ_f/b_f) for the rocking bridge piers with ρ_{ac} = 0.25: (a) broadband set – fault-normal components; (b) broadband set – fault-parallel components; (c) near-fault set – fault-normal components; and (d) near-fault set – fault-parallel components.

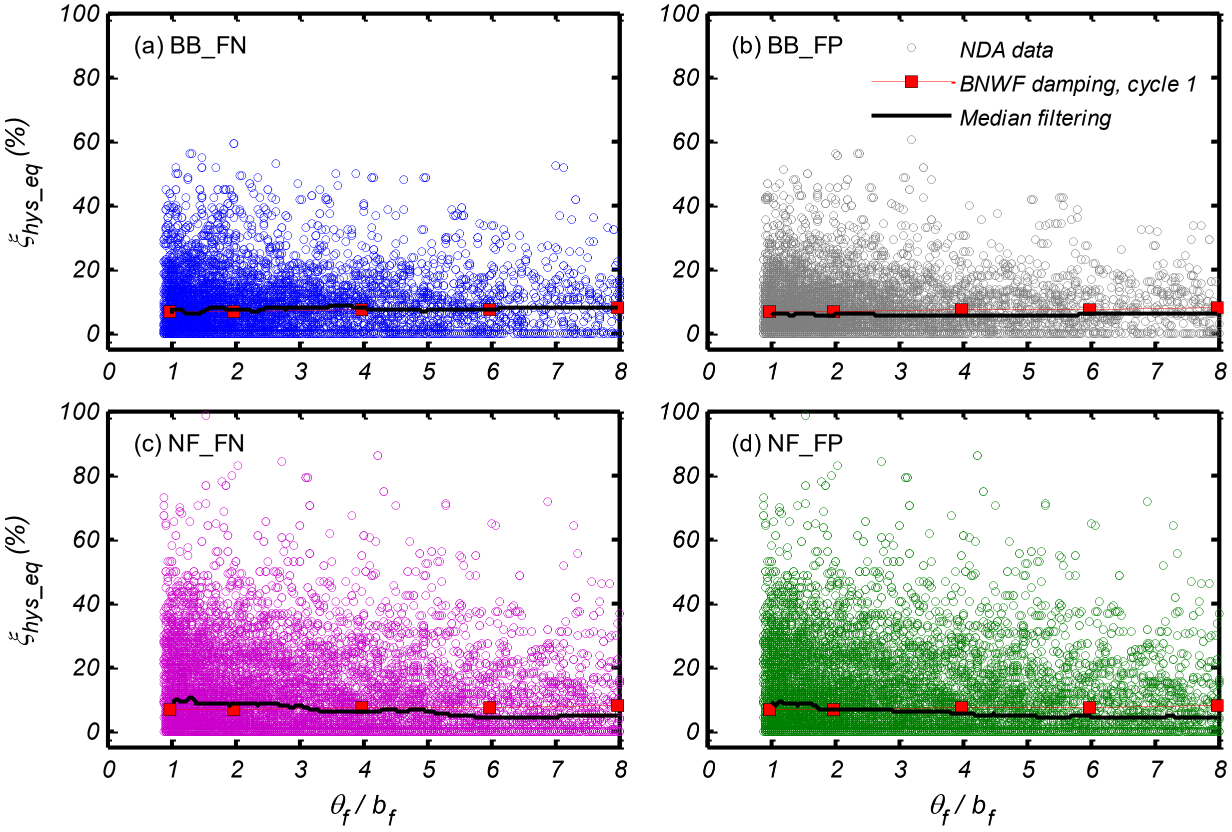

Figure 4.10 Nonlinear response history analyses – derived equivalent hysteretic damping (ξ_{hys_eq}) versus normalized footing rotation (θ_f/b_f) for the rocking bridge piers with ρ_{ac} = 0.14: (a) broadband set – fault-normal components; (b) broadband set – fault-parallel components; (c) near-fault set – fault-normal components; and (d) near-fault set – fault-parallel components.

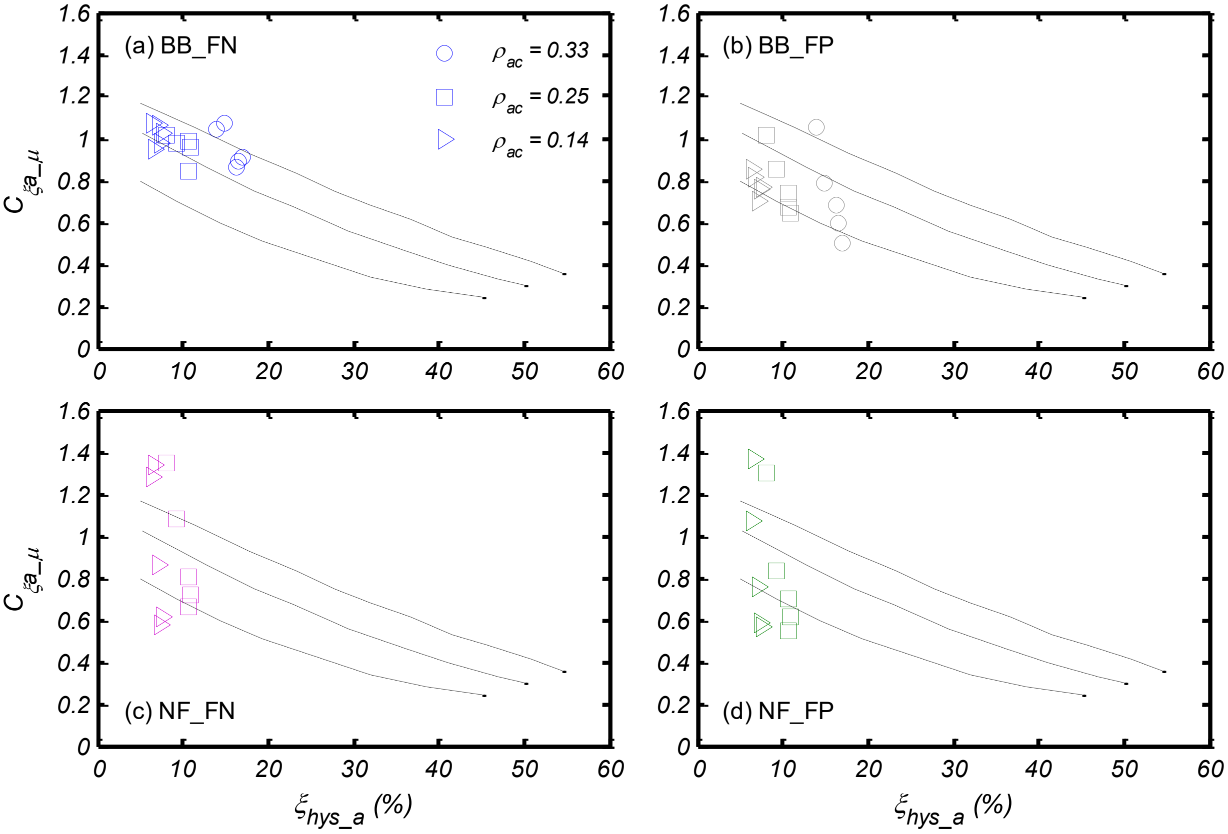

Figure 4.11 Plot of correction factors for the area-based hysteretic damping ratios ($C_{\xi a\_\mu}$) versus area-based hysteretic damping ratio (ξ_{hys_a}) for rocking shallow foundations at normalized footing rotations (θ_f/b_f) equal to 1, 2, 4, 6 and 8 for different ρ_{ac} cases: (a) broadband set – fault-normal components; (b) broadband set – fault-parallel components; (c) near-fault set – fault-normal components; and (d) near-fault set – fault-parallel components.

Evaluation procedure

A forward evaluation algorithm is used here to compare the peak drift ratio demands as computed by the nonlinear response history analyses (NRHA) and predicted by the displacement-based analysis (DBA) method for the rocking bridge piers without P-Δ effects with $\rho_{ac} = 0.25$. The purpose of this evaluation is: (i) to identify how the significant scatter observed in the equivalent hysteric damping ratios of Figure 4.9 translates into scatter of predicting the peak drift ratio demand that is the outcome of the displacement-based analysis; and (ii) to assess how the area-based hysteric damping ratio correction factor of Eqn. (4.1) improves the prediction of peak displacement response. The steps of the evaluation procedure are:

(i) For each bridge pier model and ground motion, assume an input trial lateral displacement at the top of the column (Δ_i). For first iteration Δ_i is taken so that is corresponds to a drift ratio of 1.2%.

(ii) Based on Δ_i compute the corresponding footing rotation ($\theta_{f,i}$) assuming the column to be rigid (assumption that is very close to the numerical model), the normalized footing rotation ($\theta_{f,i}/b_f$), the footing moment ($M_{f,i}$) from the BNWF model's monotonic moment – rotation backbone, and the lateral force as $F_i = M_{f,i}/H_c$.

(iii) Based on the normalized footing rotation, compute the equivalent hysteretic damping ratio (ξ_{hys_eq}) from the BNWF model's area-based hysteretic damping curve for cycle 1 and correct this value based on Eqn. (4.1) if applicable.

(iv) Based on the lateral displacement (Δ_i) and force (F_i), compute the effective lateral stiffness and period ($T_{e,i}$).

(v) From the linear displacement spectrum of the considered ground motion for $T_{e,i}$ and ξ_{hys_eq}, compute a new lateral displacement at the top of the column (Δ_f).

(vi) Return to step (i) and repeat procedure using Δ_f as Δ_i, until the initial and final value converge within 1% error. Compute the predicted drift ratio demand corresponding to Δ_f when convergence has been achieved.

(vii) Compare the drift ratio predicted by DBA to the drift ratio predicted by the NRHA.

Results

Figure 4.12 compares the peak drift ratio demand computed from the NRHA and that predicted by the DBA method using the BNWF area-based hysteretic damping ratio for cycle 1, for the rocking bridge piers with $\rho_{ac} = 0.25$ and the four different ground motion sets. The DBA method slightly underestimates the median drift ratio demand as computed by the NRHAs by a factor of approximately 1.15 with small differences between the ground motion sets. Overall, it is shown that the direct use of the area-based hysteretic damping ratio in the displacement-based analysis framework is un-conservative.

A similar comparison is shown in Figure 4.13, but in this case, the equivalent hysteretic damping ratio obtained from the area-based one, is corrected based on Eqn. (4.1). It is noticed that the median drift ratio demand predicted by DBA is close to that of the NRHA for all cases. The slightly less favorable comparison for the near-fault motions can possibly be attributed to the fact that the correction factor $C_{\xi a\_\mu}$ plotted in Figure 4.11 is not as stable as it is shown to be for the broadband motions. It is also noted that from the arithmetic mean point of view, the proposed correction factor in Eqn. (4.1) is conservative.

Figures 4.12 and 4.13 also plot the moving 16th and 84th percentile lines to identify the scatter in the prediction capability of the DBA method. Figure 4.13 shows that irrespective of the ground motion set, the DBA yields results than in 68% of the cases are within a factor of 2 higher and a factor of 1.3 lower than the drift ratio demand computed from the NRHA.

The introduction of the area-based correction factor, while it improved the median prediction of the displacement-based analysis method, it also slightly increased the scatter. This is due the peaks and troughs of the linear displacement spectrum that become more dominant as the equivalent viscous damping decreases. Dwairi et al. [2007] have also shown this side effect of the use of area-based correction factors for different hysteretic rules.

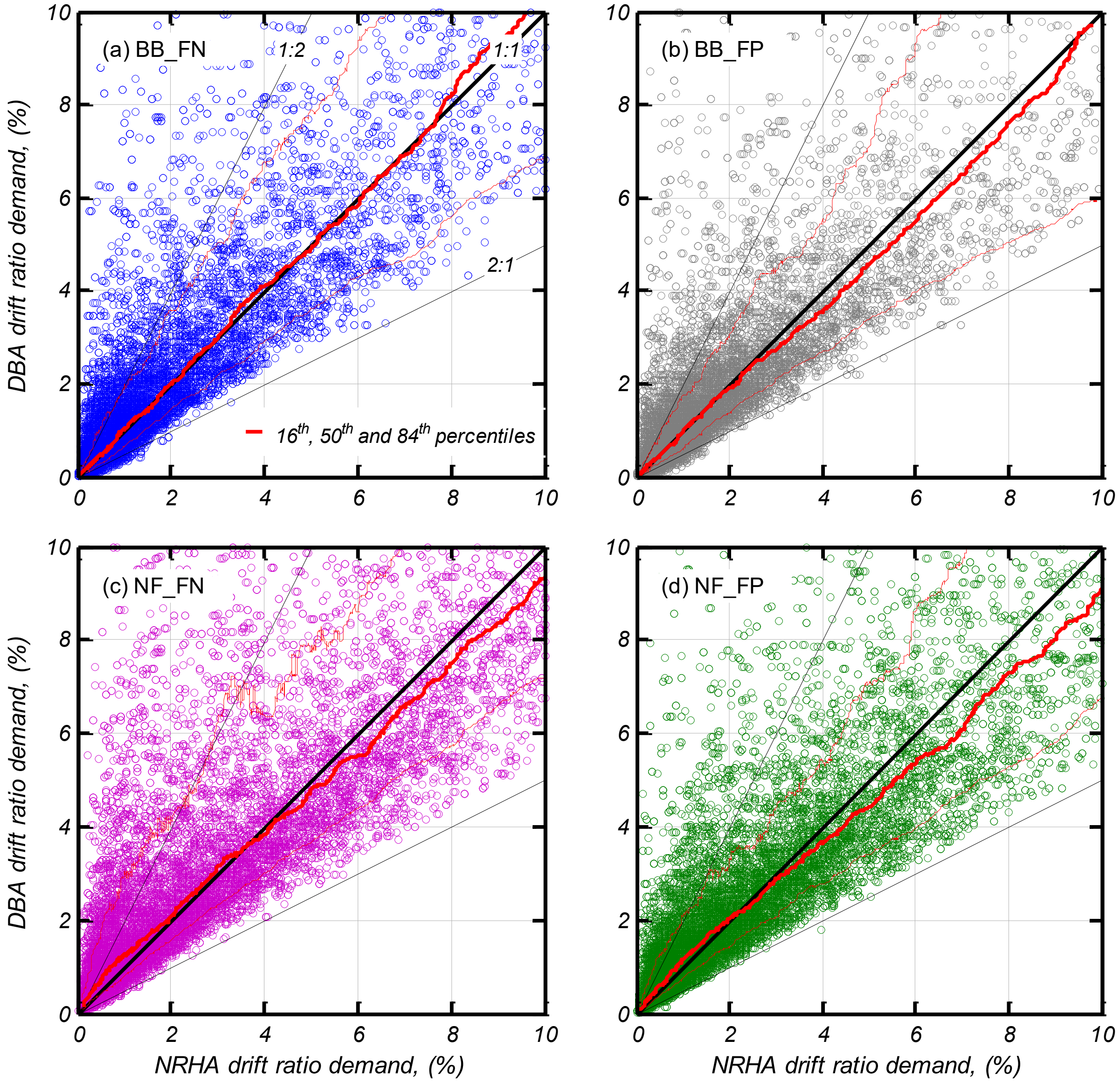

Figure 4.12 Comparison between the peak drift ratio demand computed from the nonlinear response history analyses and that predicted by the displacement-based analysis method using the BNWF area-based hysteretic damping ratio for cycle 1, for the rocking bridge piers with ρ_{ac} = 0.25: (a) broadband set – fault-normal components; (b) broadband set – fault-parallel components; (c) near-fault set – fault-normal components; and (d) near-fault set – fault-parallel components.

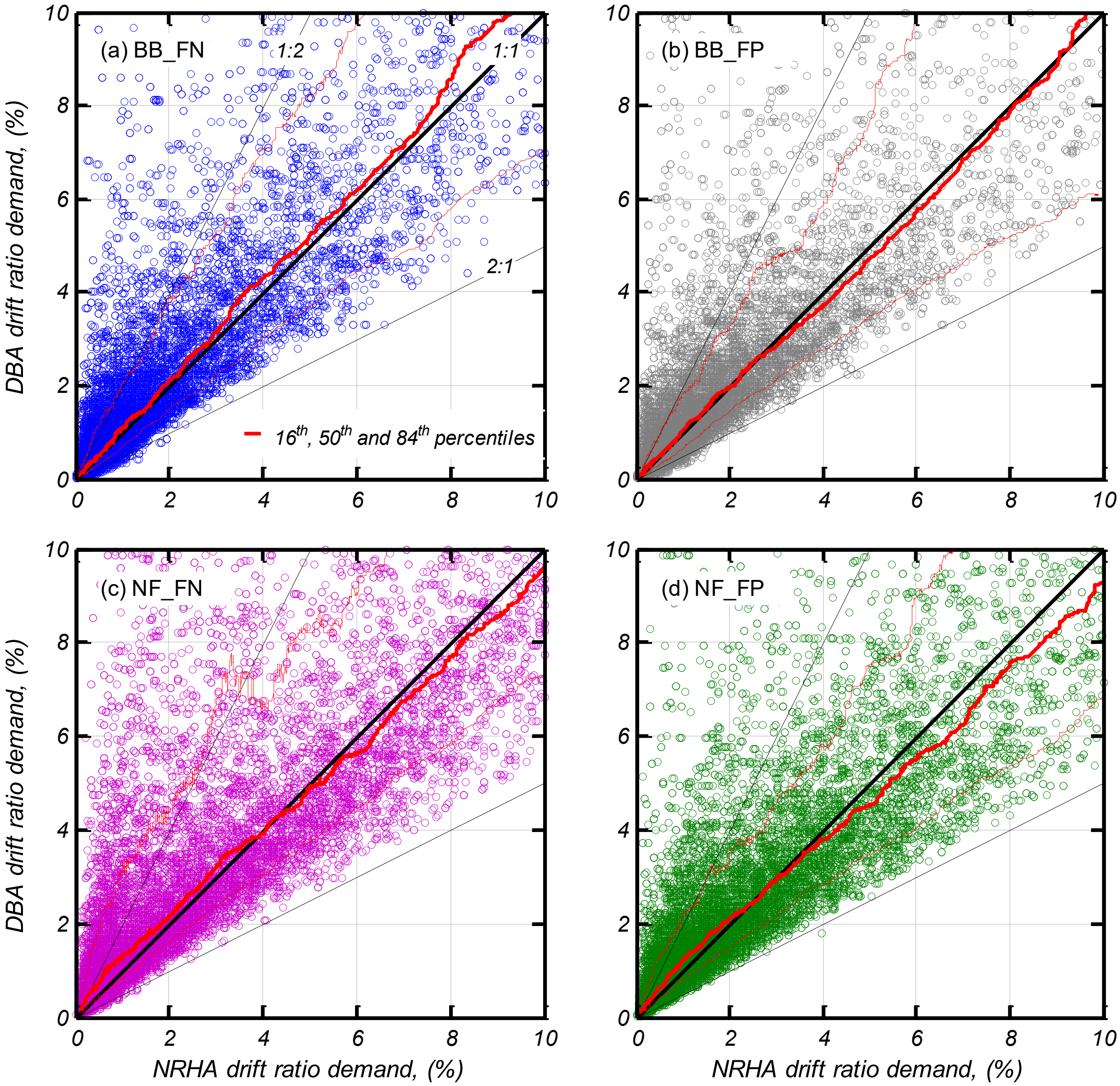

Figure 4.13 Comparison between the peak drift ratio demand computed from the nonlinear response history analyses and that predicted by the displacement-based analysis method using the BNWF area-based hysteretic damping ratio for cycle 1 corrected based on Eqn. 4.1, for the rocking bridge piers with ρ_{ac} = 0.25: (a) broadband set – fault-normal components; (b) broadband set – fault-parallel components; (c) near-fault set – fault-normal components; and (d) near-fault set – fault-parallel components.

4.6.3 Area-based Hysteretic Damping Ratio Correction as a Function of T_e

Grant et al. [2005] and Dwairi et al. [2007] demonstrated that as the effective period of an oscillator increases for the same displacement ductility, less damping becomes effective in reducing the displacement demand; therefore, the correction factor of the area-based hysteretic damping ratio needs to be lowered. They have shown that for hysteretic rules as the Takeda Thin (reinforced concrete columns) and Takeda Fat (reinforced concrete beams) the effective period dependency becomes negligible for values greater than approximately 1 second that cover the majority of cases, while for an elastic-perfectly-plastic hysteretic rule the period dependency extends up to approximately 2 seconds.

The area-based hysteretic damping ratio correction factor as a function of T_e ($C_{\xi a\_T|\mu}$) for rocking foundations is studied here, to assess if it can reduce the scatter in the peak demands computed by the displacement-based analysis method, as observed in Figure 4.13.

Procedure

The procedure used to obtain $C_{\xi a\_T|\mu}$ is as follows:

(i) Plot the equivalent hysteretic damping (ξ_{hys_eq}) versus actual footing rotation demand (θ_{f_NRHA}/b_f), obtained in Section 4.6.2 for various effective period (T_e) bins, and smooth the data by a moving median filter.

(ii) For each T_e bin, compute the area-based correction factor needed due to the combined effects of ductility and effective period ($C_{\xi a\_\mu \cap T}$), as the ratio between the first-cycle BNWF area-based hysteretic damping ratio and the median fit line for normalized footing rotations ranging from 1 to 8.

(iii) Compute the area-based correction factor due to the effective period ($C_{\xi a\_T|\mu}$), as the ratio between $C_{\xi a\_\mu \cap T}$ and $C_{\xi a\_\mu}$, where $C_{\xi a\_\mu}$ is shown in Figure 4.11.

Results

Figure 4.14 plots the area-based hysteretic damping ratio correction values due to effective period, as obtained by the above described process, for the studied ρ_{ac} values and ground motion sets. Based on these results, it is confirmed that the area-based hysteretic damping ratio becomes less effective with increasing effective period, and the following tentative expression is considered:

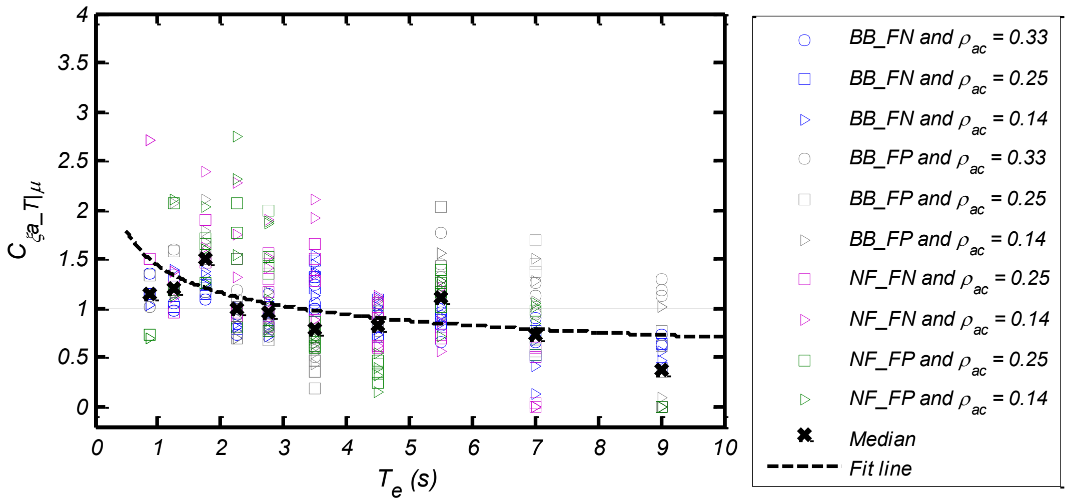

Figure 4.14 Correction factor ($C_{\xi a\_T|\mu}$) for area-based hysteretic damping ratios versus effective period (T_e) for rocking shallow foundations at normalized footing rotations (θ_f/b_f) between 1 and 8, for the studied ρ_{ac} cases.

$$C_{\xi a\_T|\mu} \approx \frac{1.44}{T_e^{0.31}} \tag{4.2}$$

Evaluation results

A forward evaluation procedure similar to the one described in Section 4.6.2, but with correcting the BNWF area-based hysteretic damping ratio of cycle 1 by the product of $C_{\xi a\_\mu}$ and $C_{\xi a\_\mu|T}$ is carried out to examine if the introduction of effective period dependency improves the prediction.

Figure 4.15 compares the peak drift ratio demand from the nonlinear response analyses and the displacement-based analysis method when T_e dependency is taken into account. Comparison of Figure 4.15 with Figure 4.14 reveals that the scatter in the prediction of the displacement-based analysis method does not improve to a noticeable extent when the effective period dependency is considered, while the median prediction for the near-fault set is shown to slightly improve at small drift ratios. Therefore, it is concluded that the effective period dependency can be neglected in the displacement-based analysis method.

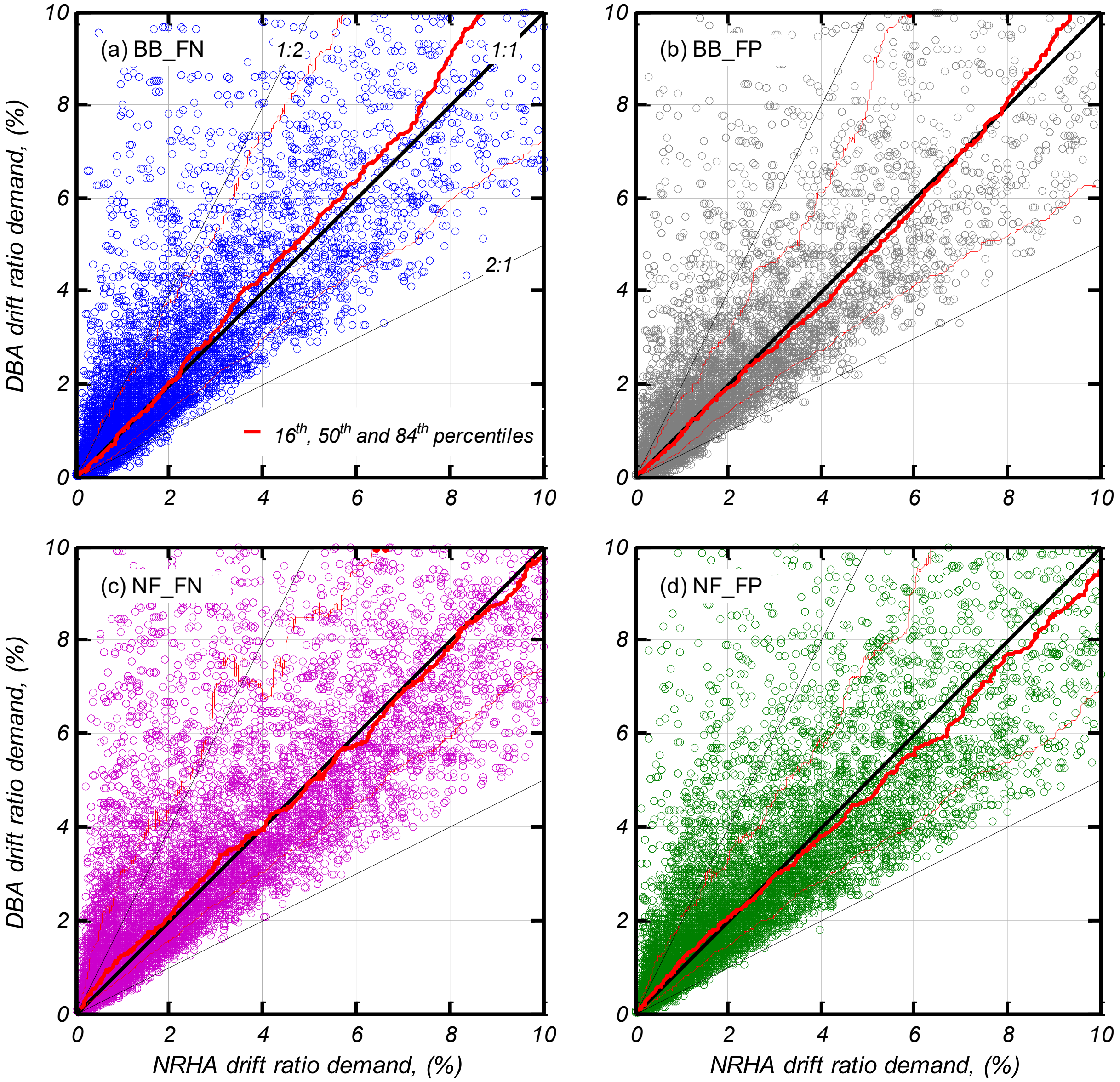

Figure 4.15 Comparison between the peak drift ratio demand computed from the nonlinear response analyses and that predicted by the displacement-based analysis method using the BNWF area-based hysteretic damping ratio for cycle 1 corrected based on Eqns. 4.1 and 4.2, for the rocking bridge piers with ρ_{ac} = 0.25: (a) broadband set – fault-normal components; (b) broadband set – fault-parallel components; (c) near-fault set – fault-normal components; and (d) near-fault set – fault-parallel components.

4.7 ALTERNATIVE HYSTERETIC DAMPING RATIO EXPRESSION

Experiments have shown that loose, cohensionless backfill soil falling into the gap under the rocking footing contributes to damping [Gajan and Kutter 2008; Deng et al. 2012a; Antonellis et al. 2015]. In this section, alternative lower-bound hysteretic damping ratio curves applicable to cases where the foundation is explicitly designed to prevent sand falling are derived from the BNWF models with ρ_{ac} equal to 0.25 and 0.14. These damping curves are proposed as secondary to the primary damping curves of Deng et al. [2014] modified by the correction factor of Eqn. 4.1, because of (i) the inherent limitations of BNWF models discussed in Section 3.3.2; (ii) the limited number of physical tests for which the BNWF models have been calibrated to, as opposed to the large number of tests that support the Deng et al. [2014] expressions; and (iii) the lack of accounting of the footing backfill hysteretic damping that an embedded rocking footing will induce even if sand falling under the footing is explicitly prevented.

Figure 4.16 plots the BNWF-derived median curves of hysteretic damping ratio versus footing normalized rotation for the four different ground motion sets. The median lines shown in Figure 4.16 are obtained from the median lines of Figure 4.9 (ρ_{ac} = 0.25) and Figure 4.10 (ρ_{ac} = 0.14), multiplied by $(T_e/T_{f\_pl})^2$. This correction is carried out because the alternative hysteretic damping curves will be used within the Deng et al. [2014] framework (see Section 2.4.2), that combines the different sources of damping as elements in series:

$$\xi_{eq} = \frac{T_c^{\,2}}{T_e^{\,2}} \cdot \xi_c + \frac{T_{f\_50}^{\;\;2}}{T_e^{\,2}} \cdot \xi_{rad} + \frac{T_{f\_pl}^{\;\;2}}{T_e^{\,2}} \cdot \xi_{f\_hys} \tag{4.3}$$

In the nonlinear response history analyses of the rocking bridge piers, ξ_{rad} = 0% and $\xi_c \approx$ 0%, leading to the $(T_e/T_{f\_pl})^2$ correction factor that varies between 1.39 and 1.04 for normalized footing rotations of 1 and 8, respectively.

The median lines for ρ_{ac} equal to 0.25 and 0.14 are fitted with the following expression

$$\xi_{f\_hys} = \frac{0.30}{2 \cdot \pi}\left(4 - \frac{3}{2.6 \cdot \rho_{ac} + 1} - \frac{b_f}{\theta_f}\right) \tag{4.4}$$

for $\theta_f/b_f \geq 1$. For normalized footing rotations between 0.139 and 1, hysteretic damping ratio is obtained by linear interpolation between zero and the value of Eqn. (4.4) for θ_f/b_f = 1. Eqn. (4.4) constitutes the proposed lower-bound hysteretic damping ratio curve applicable to cases with explicit prevention of sand falling under the rocking foundation for ρ_{ac} values between 0.14 and 0.25.

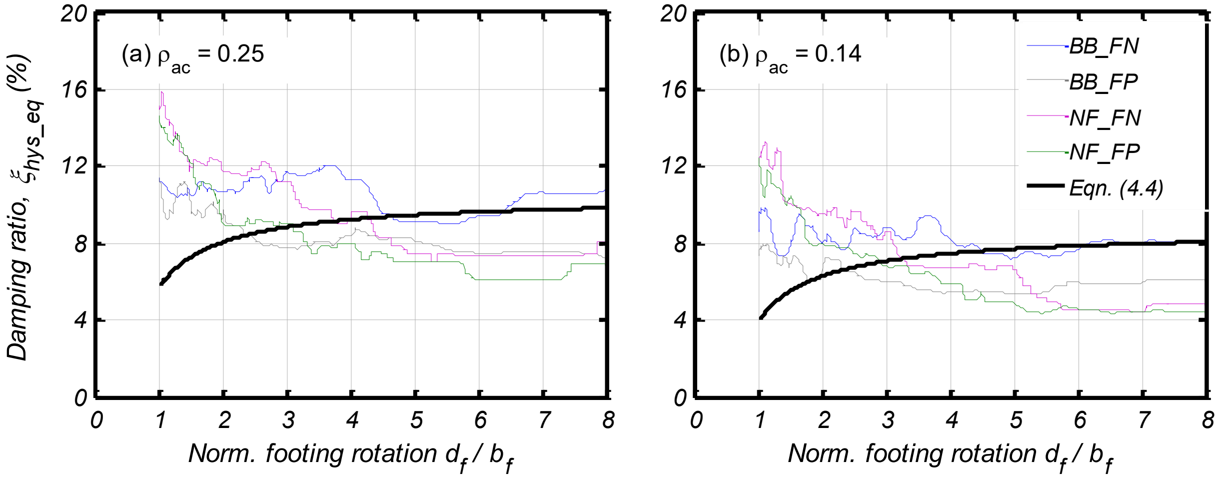

Figure 4.16 Alternative lower-bound hysteretic damping ratio curves directly derived from BNWF models for ρ_{ac} = 0.25 and 0.14, applicable to cases with explicit design to prevent soil falling under the rocking foundation.

4.8 IMPORTANCE OF P-Δ EFFECTS

Rocking foundations have a degrading post-peak lateral force capacity due to P-Δ effects, while such effects are not included in the linear design displacement spectra. Hence, this section investigates whether there is a need for the proposed displacement-based analysis method to consider P-Δ effects.

First, the drift ratio demand amplification due to P-Δ effects is studied by nonlinear response history analyses of the rocking bridge pier models with and without P-Δ effects. Figure 4.17 plots the ratio of the drift demand of a model with P-Δ to that of the respective model without P-Δ versus the instability ratio of the model without P-Δ effects. The instability ratio ($\theta_{P\text{-}\Delta}$) is the fraction of the moment capacity of the foundation that is due to the P-Δ moment. Cases of either model where the drift ratio demand exceeds that corresponding to static overturn are assigned a drift ratio value equal to 100%, resulting to two clouds of data observed at the top right and bottom right side of the plots. The median line remains fairly constant as the instability ratio increases, while the 84th percentile line gradually increases up to an instability ratio of 0.5, after which, P-Δ effects appear to rapidly amplify the drift demand of the models with P-Δ compared to those without. Figure 4.18 plots the same information with Figure 4.17, but with emphasis to cases with instability ratio values less than 0.6 and a linear y-axis. It is shown that for $\theta_{P\text{-}\Delta}$ equal to 0.3, 50% of the cases will have a drift ratio demand amplification due to P-Δ less than 1.04, while the corresponding value for the 84% of the cases is 1.25. It appears, therefore, that P-Δ effects could potentially be neglecting in the displacement-based method if P-Δ moment is bounded to 30% of the foundation moment capacity.

To further consolidate this argument, the prediction capability of the evaluation procedure explained in Section 4.6.2 that does not account for P-Δ effects, is used predict the drift ratio demand of the rocking bridge pier models with $\rho_{ac} = 0.25$ that include second-order effects. Figure 4.19 plots the ratio of the drift ratio demand computed from the nonlinear response history analyses (NRHA) with P-Δ effects to that predicted by the displacement-based analysis (DBA) method without P-Δ effects consideration versus the instability ratio corresponding to the peak demand predicted by DBA. It is shown that P-Δ effects are small (less than approximately 5% difference) when the predicted drift ratio demand corresponds to a P-Δ moment less than 30% of the footing rocking capacity.

4.9 STEP-BY-STEP ANALYSIS PROCEDURE

The proposed step-by-step displacement-based analysis method for the case of a single elastic cantilever column supported on rocking shallow foundation is provided in Table 4.3. With reference to Table 4.3, some additional notes are:

1. Two expressions are provided for determining the equivalent hysteretic damping of a rocking footing. The first is based on the Deng et al. [2014] modified by the correction factor of Eqn. (4.1), while the second is purely derived from the NRHA results of the BNWF models. The use of the first or the second expression is discussed in Section 4.7.
2. Radiation damping (ξ_{rad}) for a surface rocking footing ranges from 0% to 10% [Applied Technology Council (ATC) 2005] depending on the soil properties, the footing dimensions and the frequency of vibration. To ease calculations, a reasonable low value of 3% is suggested to be used in the case where radiation damping is not addressed explicitly using ATC [2005]. This value is fairly consistent with Paolucci et al. [2013] that suggested using $\xi_{rad} = 3.6\%$ as an alternative to analytical calculations.
3. It is suggested that iterations may be stopped when the new displacement value is no more than 2% different than the previous value. However, the final displacement demand

obtained from the 2% relative error criterion can be more than 2% different than that obtained by a stricter relative error criterion, e.g. 0.1% relative error. Thus, use of a stricter relative error criterion, or a criterion based on the rate of convergence (that is the relative error of the current iteration compared to the relative error of the previous iterations) is not discouraged.

It is noted that the above three comments, also apply to the displacement-based analysis methods presented in Chapters 5 and 6; nevertheless, they will not be iterated again.

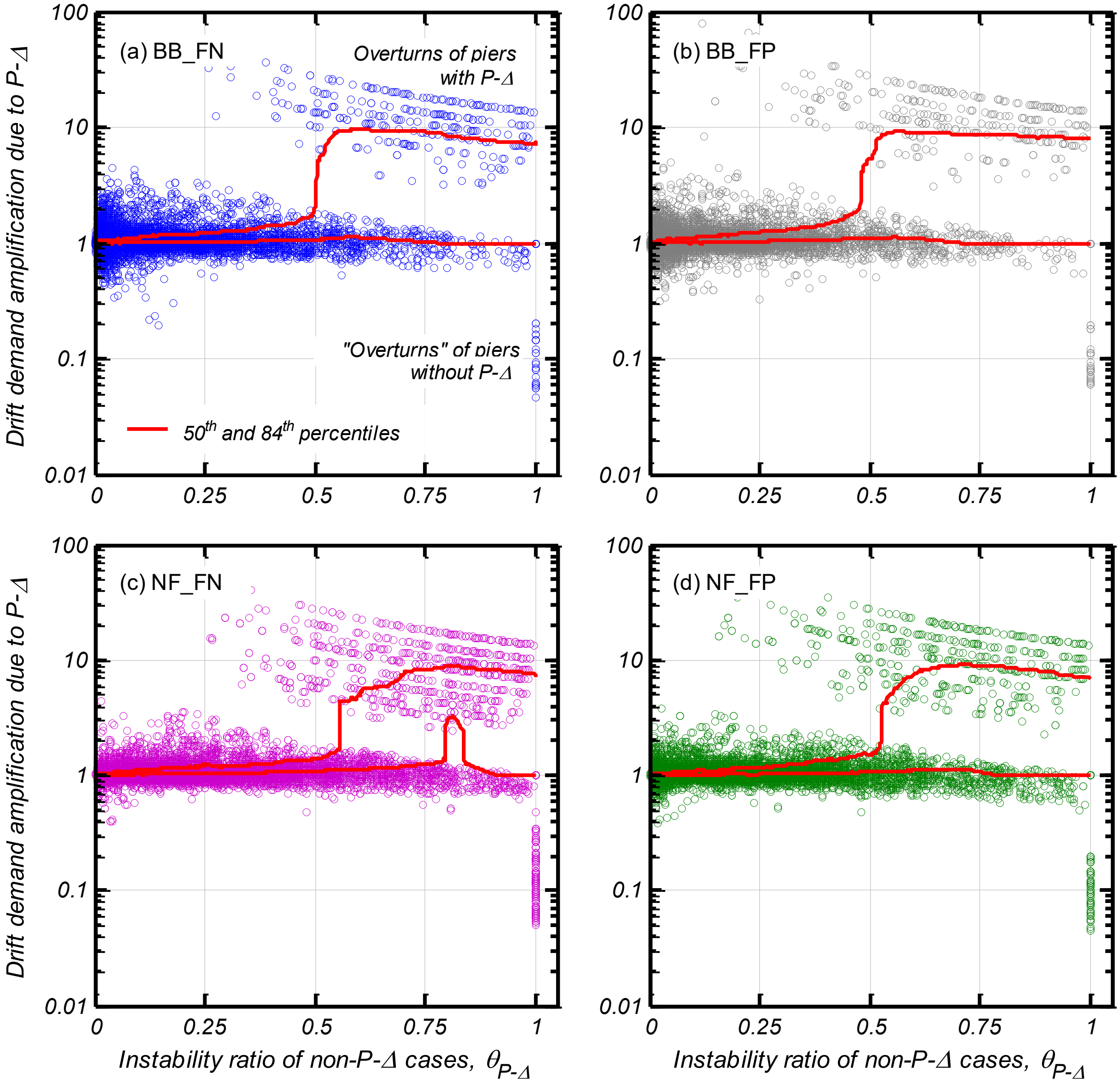

Figure 4.17 Drift ratio demand amplification due to P-Δ effects as computed from the nonlinear response history analyses for rocking bridge piers with and without P-Δ effects, for ρ_{ac} = 0.25, versus instability ratio of the piers without P-Δ.

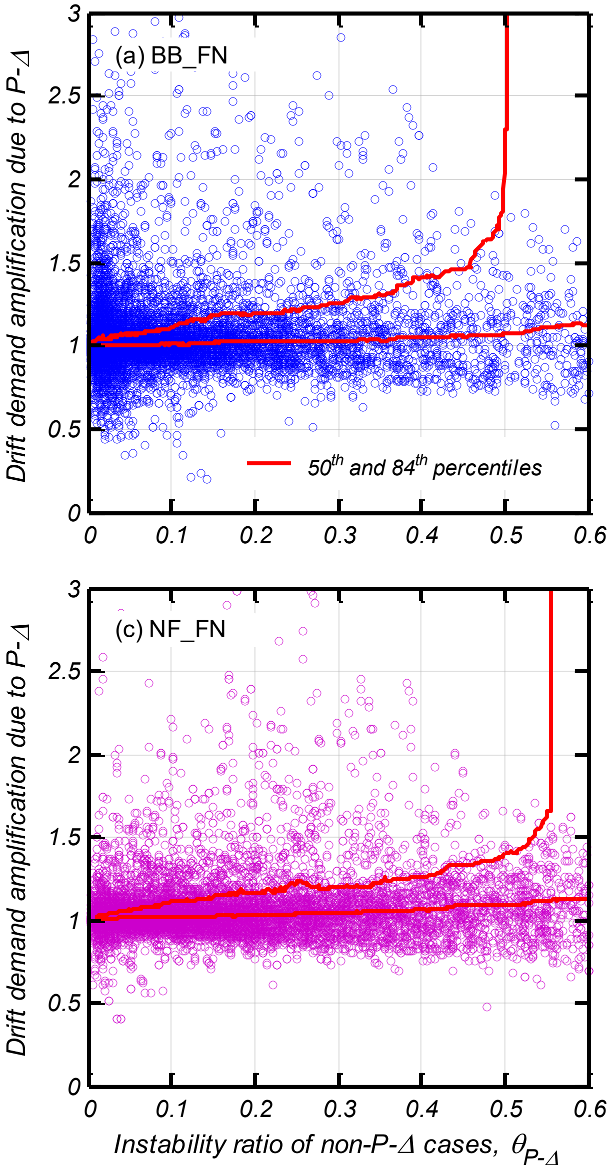

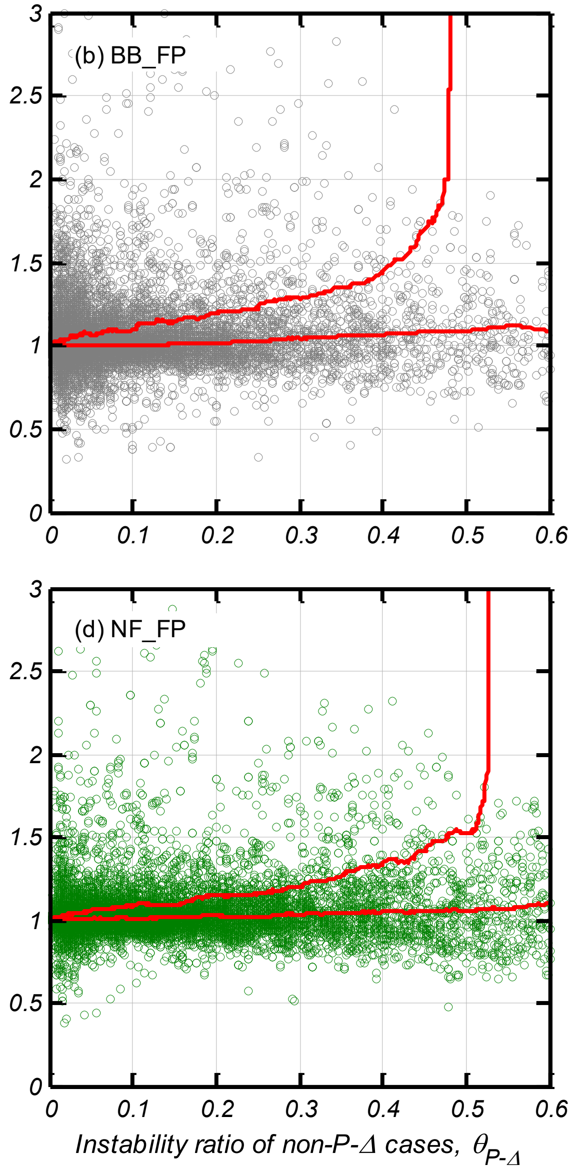

Figure 4.18 Drift ratio demand amplification due to P-Δ effects as computed from the nonlinear response history analyses for rocking bridge piers with and without P-Δ effects, for ρ_{ac} = 0.25, versus instability ratio of the piers without P-Δ.

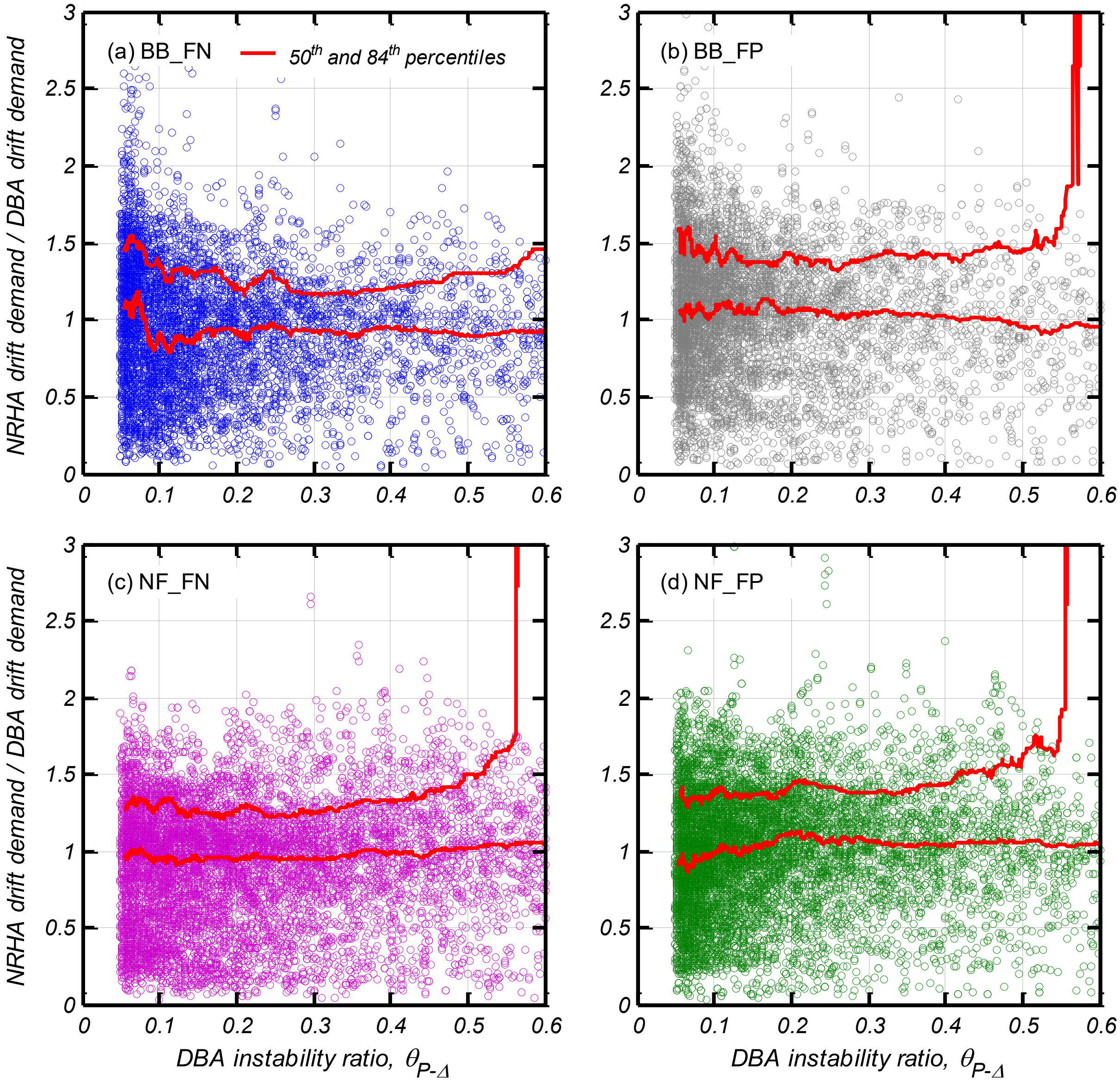

Figure 4.19 Ratio of the drift demand computed from the nonlinear response history analyses (NRHA) of the rocking bridge piers (ρ_{ac} = 0.25) with P-Δ effects to that predicted by the displacement-based analysis (DBA) method without P-Δ effects consideration, versus instability ratio corresponding to the peak demand of the DBA method.

Table 4.3 Proposed step-by-step displacement-based analysis method for a single elastic cantilever column supported on rocking shallow foundation.

1. Determine the dimensions of the foundation normal (L_f) and parallel (B_f) to the rocking axis and the cross-sectional dimensions of the column based on a preliminary design.

2. Iteratively calculate the critical contact area ratio (ρ_{ac}) such that

$$0.95 \cdot W_{f\_b} \leq q_{ult\_c} \cdot A_f \cdot \rho_{ac} \leq 1.05 \cdot W_{f\_b}$$

where q_c is the bearing capacity of the critical contact area, A_c, with plan dimensions of B_f and $L_f \cdot \rho_{ac}$, A_f is the plan area of the footing, and W_{f_b} is the total vertical force acting at the footing base.

3. Compute the foundation rocking capacity (M_{fc}) and the lateral seismic capacity (F_c):

$$M_{fc} = 0.5 \cdot W_{f\_b} \cdot L_f (1 - \rho_{ac})$$

$$F_c = M_{fc}/H$$

where H is the height of the deck from the footing base.

4. Determine the effective seismic weight:

$$W_s = W_d + 0.33 \cdot W_c$$

where W_d is the superstructural weight at the top of the column, and W_c is the column weight.

5. Compute the lateral displacement at the top of the column due to its flexibility when the foundation has mobilized its moment capacity (Δ_c) and the column fixed-base period (T_c):

$$\Delta_c = M_{fc}/(H \cdot K_c)$$

$$T_c = 2\pi \sqrt{\frac{W_s/g}{K_c}}$$

where H is the height of the deck centroid from the footing base, and K_c is an estimate of the column lateral stiffness with $I_{eff} \approx 0.5 \cdot I_g$.

6. Compute the elastic rotational stiffness of the foundation (K_{f_50}), and the corresponding translational period (T_{f_50}):

$$K_{f\_50} = 300 \cdot M_{fc}$$

$$T_{f\_50} = 2\pi \sqrt{\frac{W_s/g}{K_{f\_50}/H^2}}$$

7. Compute the lateral displacement corresponding to first yield of the rocking foundation (Δ_{y1}) and to the mobilization of the rocking footing capacity (Δ_{y2}):

$$\Delta_{y1} = 0.5\Delta_c + H \cdot \sin(0.5 \cdot h_f)$$

$$\Delta_{y2} = \Delta_c + H \cdot \sin(b_f)$$

where $h_f = 1/600$ rad, and $b_f = 0.012$ rad.

8. Assume a trial input system lateral displacement (Δ_{sys}). For first iteration, Δ_{sys}, can be set equal to Δ_{y2}.

9. Compute the lateral force (F):

Table 4.3 (Continued)

If $\Delta_{sys} \leq \Delta_{y1}$

$$F = F_c \cdot \Delta_{sys} / \Delta_{y1}$$

Else if $\Delta_{sys} \geq \Delta_{y2}$

$$F = F_c$$

Otherwise

$$F = 0.5 F_c \left(1 + \frac{\Delta_{sys} - \Delta_{y1}}{\Delta_{y2} - \Delta_{y1}} \right)$$

10. Compute the footing rotation (θ_f):

$$\theta_f = a\sin\left[\frac{\Delta_{sys} - (\Delta_c \cdot F)/F_c}{H} \right]$$

11. Compute the footing hysteretic damping ratio (ξ_{f_hys}), and the secant, at peak displacement, rotational stiffness (K_{f_pl}) and corresponding translational period (T_{f_pl}) of the rocking foundation that is associated to the footing hysteretic damping:

If $\theta_f \leq 0.5 \cdot h_f$

$$\xi_{f\_hys} = 0$$

$$T_{f\_pl} = 0$$

Else if $\theta_f \geq b_f$

$$\xi_{f\_hys} = \frac{0.90}{2\pi} \left(4 - \frac{3}{2.6 \cdot \rho_{ac} + 1} - \frac{b_f}{\theta_f} \right), \text{ or } \xi_{f\_hys} = \frac{0.30}{2\pi} \left(4 - \frac{3}{2.6 \cdot \rho_{ac} + 1} - \frac{b_f}{\theta_f} \right)$$

$$K_{f\_pl} = M_{fc} / (\theta_f - h_f), \text{ and } T_{f\_pl} = 2\pi \sqrt{\frac{W_s / g}{K_{f\_pl} / H^2}}$$

Otherwise

$$\xi_{f\_hys} = \frac{0.90}{2\pi} \left(4 - \frac{3}{2.6 \cdot \rho_{ac} + 1} - 1 \right) \cdot \left(\frac{\theta_f - 0.5 \cdot h_f}{b_f - 0.5 \cdot h_f} \right), \text{ or } \xi_{f\_hys} = \frac{0.30}{2\pi} \left(4 - \frac{3}{2.6 \cdot \rho_{ac} + 1} - 1 \right) \cdot \left(\frac{\theta_f - 0.5 \cdot h_f}{b_f - 0.5 \cdot h_f} \right)$$

$$K_{f\_pl} = F \cdot H / \left(\theta_f - F \cdot H / K_{f\_50} \right), \text{ and } T_{f\_pl} = 2\pi \sqrt{\frac{W_s / g}{K_{f\_pl} / H^2}}$$

Note that the use of the first or the second ξ_{f_hys} expression is discussed in Section 4.7.

12. Calculate the system effective period (T_{sys}) and equivalent viscous damping (ξ_{sys}):

$$T_{sys} = \sqrt{T_c^2 + T_{f\_50}^2 + T_{f\_pl}^2}$$

$$\xi_{sys} = \left(\frac{T_c}{T_{sys}} \right)^2 \xi_c + \left(\frac{T_{f\_50}}{T_{sys}} \right)^2 \xi_{rad} + \left(\frac{T_{f\_pl}}{T_{sys}} \right)^2 \xi_{f\_hys}$$

where ξ_c is the column elastic damping, and ξ_{rad} is the radiation damping of the footing rocking mode. Column elastic damping can be taken as 2%, while radiation damping can be assumed as approximately 3% if not addressed explicitly using the FEMA 440 document [ATC 2005].

Table 4.3 (Continued)

13. Compute the new lateral displacement at the top of the column (Δ_{sys}):

$$\Delta_{sys} = \left(\frac{0.07}{0.02 + \xi_{sys}} \right)^{\alpha} \cdot Sd\left(T_{sys}, 0.05\right)$$

where α = 0.5 for a site at which the elastic design spectrum (*Sd*) is dominated by broadband motions, or α = 0.25 for the case near-fault pulse-like motions.

14. Use Δ_{sys} as input value and repeat steps 8 to 13. Convergence occurs when computed system displacement at step 13 is no more than 2% different from the input displacement at step 8.

5 Analysis of Single Rocking Bent with Plastic Hinging at the Top of the Column

5.1 INTRODUCTION

This chapter presents the displacement-based seismic analysis of a single rocking bent in which the inelastic mode of response includes shallow foundation rocking and column-top plastic hinging. It is applicable to the response of single- or multi-column bridge bents in the longitudinal direction of bridges and to multi-column bridge bents in the transverse direction for the case where the strength and stiffness of the column-deck connection is substantial. The method is presented for the case of a single-column rocking bent, but can be directly extended for the cases of multi-column bents by considering the effective deck weight per each identical column. It should be noted that in the latter cases possible interaction between adjacent footings is not considered.

Figure 5.1 shows the deformed-state schematic of a single rocking bent with plastic hinging at the top of the column. For lateral displacement at the top of the column, Δ_{sys}, the behavior of the bent can be decomposed, based on the location of the inflection point, to two already studied problems: a rocking foundation with a flexible cantilever column on top, with total height equal to H_1 and lateral displacement equal to Δ_{ss1}, and an inelastic cantilever of total height H_2 and lateral displacement Δ_{ss2}. The equivalent viscous damping ratio of each subsystem can be readily determined based on available relationships; those presented in Chapter 4 for the rocking subsystem and those presented in Priestley et al. [2007] for the plastic hinging subsystem. Lastly, the equivalent viscous damping at the bent-level can be obtained by combining in series these two subsystems.

As a result of the different strength and flexibility characteristics of the two subsystems, the location of the inflection point varies as a function of lateral drift ratio. In the initial stage it is controlled by the ratio of the elastic flexibilities, while in the later stage it is controlled by the ratio of the capacities of the two inelastic mechanisms.

Two approaches are presented. First, a detailed method is presented based on a nonlinear monotonic analysis. This method accounts for the fluctuation of the inflection point. The second method avoids the use of a nonlinear monotonic pushover analysis, by assuming the inflection point is constant based on the ratio of the moment capacity of the footing to the nominal moment capacity of the column. In both methods, $P\text{-}\Delta$ effects are neglected but an upper limit to the allowable instability ratio ($\theta_{P\text{-}\Delta}$) is considered. The proposed limit varies linearly between 0.2 when the footing capacity contribution to the bent-level strength is negligible and 0.3 when it is dominant.

5.2 DESCRIPTION OF THE TWO METHODS

5.2.1 Method Based on Nonlinear Pushover Analysis

This method is summarized in Table 5.1 and accounts for the variation of the inflection point using nonlinear pushover analysis. The outcome of this method is a continuous calculation of the equivalent viscous damping ratio (ξ_{sys}), effective period (T_{sys}), column's top plastic hinge rotation (θ_{c_pl}) and instability ratio ($\theta_{P\text{-}\Delta}$) as a function of lateral drift ratio of the bent (Θ). The equivalent viscous damping ratio is computed based on the footing rotation, the column's critical section curvature and the location of the inflection point at a given lateral drift.

This method will be used below to validate the performance of the simplified method for some realistic bridge bent cases. It can also be used to analyze bridge bents that fall beyond the range of the cases examined here.

A single validation scenario is examined which involves a 24-ft tall column with 4-ft diameter, supporting a deck weight of 695 kips. The column has a pin connection to the footing that is considered to be fixed. The column has a 2.1% and 0.93% longitudinal and transverse reinforcement ratio, respectively, and a 7.4% axial load ratio at the top of the column. The expected unconfined and confined compressive strength of the concrete are equal to 5.2 and 6.9 ksi, respectively, while the expected yield and ultimate tensile strength of the #11 longitudinal

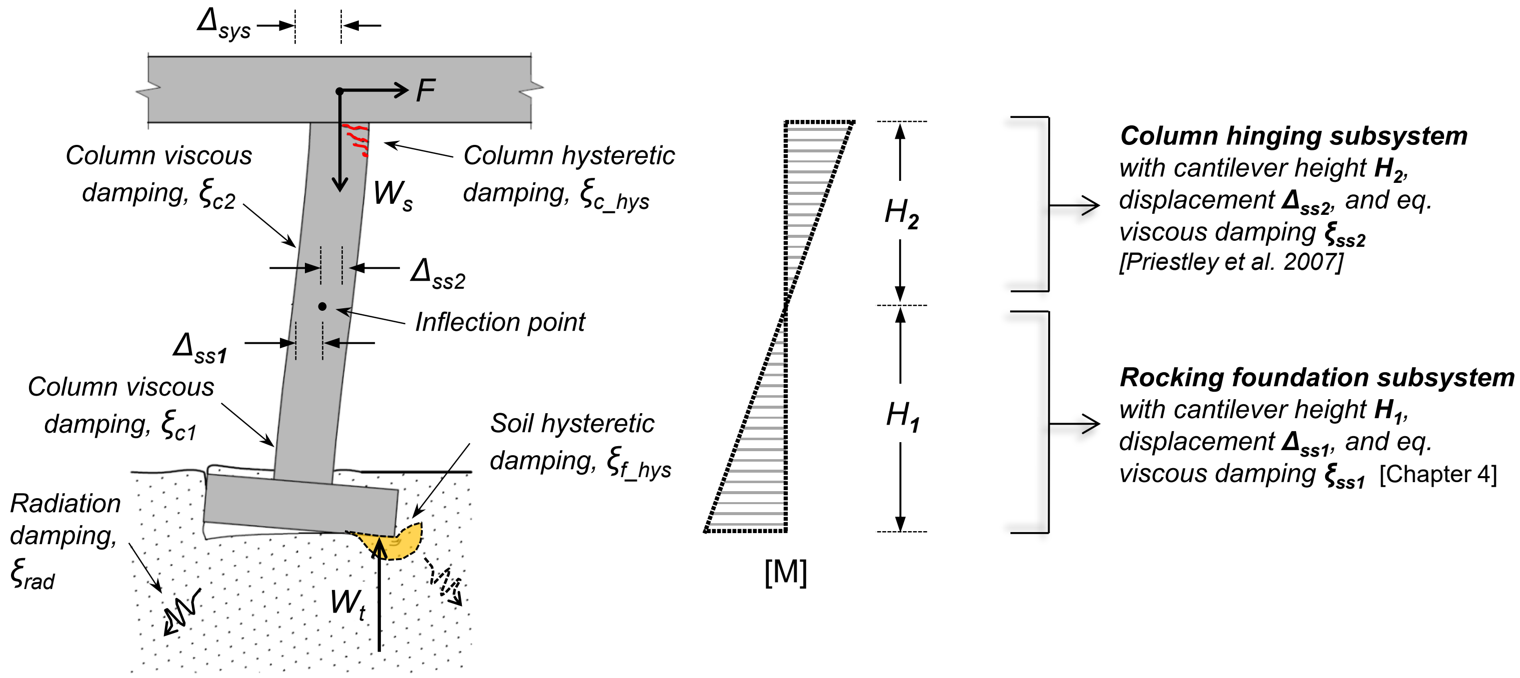

Figure 5.1 Decomposition approach for the analysis of a single-column rocking bent with plastic hinging at the top of the column.

reinforcing steel are equal to 68 and 95 ksi. A nonlinear pushover analysis is conducted to estimate the equivalent viscous damping and plastic rotation of the plastic hinge at the top of the column based on the procedure described in Table 5.1 with the modification that a pin connection is used at the base of the column.

Figure 5.3 shows: (a) the moment – curvature analysis of the section at the top of the column and the corresponding bilinear idealization; (b) the plastic rotation of the hinge at the top of the column; and (c) the equivalent viscous damping ratio. For the latter two, a comparison is shown between the nonlinear pushover based method and the Priestley et al. [2007] analytical expression for a hinging cantilever column. Priestley et al. [2007] estimate the equivalent viscous damping and plastic rotation as follows:

$$\Delta_y = \varphi_y \left(H + L_{SP}\right)^2 / 3 \tag{5.1}$$

$$\mu_\Delta = \Delta / \Delta_y \tag{5.2}$$

$$\xi_{eq} = 0.05 + 0.444\left(\frac{\mu_\Delta - 1}{\mu_\Delta \cdot \pi}\right) \tag{5.3}$$

$$\theta_{pl} = \left(\Delta - \Delta_y\right) / H \tag{5.4}$$

where *H* in this case is equal to 24 ft.

Based on the shown comparison, it is concluded that the nonlinear pushover analysis based method converges to the analytical expressions of Priestley et al. [2007].

5.2.2 Proposed Simplified Method

The proposed simplified method is summarized in Table 5.2. This method assumes that the inflection point remains constant with lateral drift.

Table 5.1 Step-by-step detailed method, based on nonlinear monotonic analysis, for a single rocking bent with plastic hinging at the top of the column.

1. Preliminary design of rocking foundation and column:

  a. Determine the dimensions of the foundation normal (L_f) and parallel (B_f) to the rocking axis and the cross-sectional dimensions of the column based on a preliminary design.

  b. Iteratively calculate the critical contact area ratio (ρ_{ac}) such that

$$0.95 \cdot W_{f\_b} \leq q_c \cdot A_f \cdot \rho_{ac} \leq 1.05 \cdot W_{f\_b}$$

  where q_c is the bearing capacity of the minimum possible soil-footing contact during rocking, A_c, with plan dimensions of B_f and $L_f \cdot \rho_{ac}$, A_f is the plan area of the footing, and W_{f_b} is the total vertical force acting at the footing base.

  c. Compute the foundation rocking capacity, M_{fc}:

$$M_{fc} = 0.5 \cdot W_{f\_b} \cdot L_f \left(1 - \rho_{ac}\right)$$

  d. Select the column longitudinal reinforcement ratio (ρ_l) to ensure that the column base yield moment (M_{cy_b}) is not smaller than the foundation rocking capacity.

2. Set-up calculations for the plastic hinge and column modeling:

  a. Based on a section analysis for an axial load equal to the superstructure weight (W_d), construct a bilinear idealization of the moment – curvature behavior and compute the nominal and ultimate moment capacities (M_{cN_t} and M_{cu_t}) of the column's top plastic hinge, the yield and ultimate curvatures (φ_{cy_t} and φ_{cu_t}), and the corresponding flexural rigidities:

$$EI_e = M_{cN\_t} / \varphi_{cy\_t}$$

$$EI_p = \left(M_{cu\_t} - M_{cN\_t}\right) / \left(\varphi_{cu\_t} - \varphi_{cy\_t}\right)$$

  b. Determine the distance of the critical column section to the point of contra-flexure based on the foundation moment capacity (M_{fc}) and the column's top nominal moment capacity (M_{cN_t}):

$$H_{2N} = \frac{M_{cN\_t}}{M_{fc} + M_{cN\_t}} \cdot H_s$$

  where H_s is the structural height, and is equal to the sum of the footing height (H_f) and the clear column height (H_c).

  c. Compute the strain penetration length (L_{SP}) and the column plastic hinge length (L_P):

$$L_{SP} = 0.15 \cdot \frac{f_{ye}}{ksi} \cdot d_{bl}$$

$$L_P = 0.2 \left(\frac{f_{ue}}{f_{ye}} - 1 \right) H_{2N} + L_{SP} \leq 0.08 \cdot H_2 + L_{SP}$$

  where f_{ye} and f_{ue} are the expected yield and ultimate strength of the reinforcing steel and d_{bl} is the nominal reinforcing bar diameter.

3. Conduct an inelastic monotonic pushover analysis of the considered bent based on Figure 5.2, and record the lateral force (F) and displacement at the top of the column (Δ), the footing rotation (θ_f) and moment (M_f), and the curvature (φ_{c_t}) and moment (M_{c_t}) at the critical section at the top

Table 5.1 (Continued)

of the column. Note that the length of the top nonlinear beam-column element should be chosen so that in conjunction with the number of integration points used, the weight of the integration point at the critical section matches the plastic hinge length, L_P.

4. For each time step of the pushover analysis determine the following critical parameters.

a. Compute the lateral drift ratio, Θ:

$$\Theta = \Delta / H_s$$

b. Determine the effective system period, T_{sys}:

$$T_{sys} = 2\pi \sqrt{\frac{W_s/g}{F/\Delta}}$$

where the effective seismic weight, W_s, is equal to the sum of the superstructural weight (W_d) at the top of the column and one-third of the column weight (W_c).

c. Determine the column's top plastic hinge rotation, θ_{c_pl}:

$$\theta_{c\_pl} = \langle \varphi_{c\_t} - \varphi_{cy\_t} \rangle L_P$$

where < > are MacCauley's brackets that set negative values to zero, i.e., $<x> = x$ if $x \geq 0$, otherwise $<x> = 0$.

d. Determine the instability ratio due to P-Δ effects, $\theta_{P\text{-}\Delta}$:

$$\theta_{P-\Delta} = \frac{W_s \cdot \Delta}{M_f + M_{c\_t}}$$

e. Determine the equivalent viscous damping ratio of the system period (ξ_{sys}) by analysis of the rocking (ξ_{ss1}) and hinging (ξ_{ss2}) subsystems and integration to the bent-level as element in series.

α. Compute the equivalent damping ratio of the rocking subsystem (ξ_{ss1}) and its contribution to the bent's lateral displacement (Δ_{ss1}) as follows:

i. Determine the height of the inflection point from the footing base, H_1:

$$H_1 = \frac{M_f}{M_f + M_{c\_t}} \cdot \left(H_f + H_c + L_{SP} \right)$$

ii. Compute the column elastic stiffness (K_{c1}) and period (T_{c1}):

$$K_{c1} = \frac{3(EI)_e}{\left(H_1 - H_f\right)^3}$$

$$T_{c1} = 2\pi \sqrt{\frac{W_s/g}{K_{c1}}}$$

iii. Compute the footing elastic rotational stiffness (K_{f_50}) and corresponding translational period (T_{f_50}):

$$K_{f\_50} = 300 \cdot M_{fc}$$

$$T_{f\_50} = 2\pi \sqrt{\frac{W_s/g}{K_{f\_50}/H_1^2}}$$

Table 5.1 (Continued)

iv. Compute the footing hysteretic damping ratio (ξ_{f_hys}), and the secant, at peak displacement, rotational stiffness (K_{f_pl}) and corresponding translational period (T_{f_pl}) of the rocking foundation that is associated to the footing hysteretic damping:

If $d_f \leq 0.5 \cdot h_f$ (h_f = 1/300 radians)

$$\xi_{f\_hys} = 0, \text{ and } T_{f\_pl} = 0$$

Else if $d_f \geq b_f$ (b_f = 0.012 radians)

$$\xi_{f\_hys} = \frac{0.90}{2\pi}\left(4 - \frac{3}{2.6 \cdot \rho_{ac} + 1} - \frac{b_f}{\theta_f}\right), \text{ or } \xi_{f\_hys} = \frac{0.30}{2\pi}\left(4 - \frac{3}{2.6 \cdot \rho_{ac} + 1} - \frac{b_f}{\theta_f}\right)$$

$$K_{f\_pl} = M_{fc} / \left(\theta_f - h_f\right), \text{ and } T_{f\_pl} = 2\pi\sqrt{\frac{W_s / g}{K_{f\_pl} / H_1^2}}$$

Otherwise

$$\xi_{f\_hys} = \frac{0.90}{2\pi}\left(4 - \frac{3}{2.6 \cdot \rho_{ac} + 1} - 1\right) \cdot \left(\frac{\theta_f - 0.5 \cdot h_f}{b_f - 0.5 \cdot h_f}\right), \text{ or}$$

$$\xi_{f\_hys} = \frac{0.30}{2\pi}\left(4 - \frac{3}{2.6 \cdot \rho_{ac} + 1} - 1\right) \cdot \left(\frac{\theta_f - 0.5 \cdot h_f}{b_f - 0.5 \cdot h_f}\right)$$

$$K_{f\_pl} = M_f / \left(\theta_f - M_f / K_{f\_50}\right), \text{ and } T_{f\_pl} = 2\pi\sqrt{\frac{W_s / g}{K_{f\_pl} / H_1^2}}$$

Note that the use of the first or the second ξ_{f_hys} expression is discussed in Section 4.7.

v. Compute the subsystem's effective period (T_{sys1}) and equivalent viscous damping (ξ_{sys1}):

$$T_{ss1} = \sqrt{T_{c1}^2 + T_{f\_50}^2 + T_{f\_pl}^2}$$

$$\xi_{ss1} = \left(\frac{T_{c1}}{T_{ss1}}\right)^2 \xi_{c1} + \left(\frac{T_{f\_50}}{T_{ss1}}\right)^2 \xi_{rad} + \left(\frac{T_{f\_pl}}{T_{ss1}}\right)^2 \xi_{f\_hys}$$

where ξ_{c1} is the column elastic damping, and ξ_{rad} is the radiation damping of the footing rocking mode. Column elastic damping can be taken as 2% as the column is designed to remain nominally elastic, while radiation damping can be assumed as approximately equal to 3% if not addressed explicitly using the FEMA 440 document [ATC 2005].

vi. Compute the subsystem's contribution to the lateral displacement of the bent (Δ_{ss1}):

$$\Delta_{ss1} = H_1 \cdot sin(\theta_f) + M_f / \left(H_1 \cdot K_{c1}\right)$$

β. Compute the equivalent damping ratio of the hinging subsystem (ξ_{ss2}) as follows:

i. Determine the distance of the inflection point the column critical section, H_2:

$$H_2 = \frac{M_{c\_t}}{M_f + M_{c\_t}} \cdot \left(H_f + H_c + L_{SP}\right)$$

Table 5.1 (Continued)

ii. Compute the subsystem's displacement ductility, $\mu_{\Delta 2}$:

$$\mu_{\Delta 2} = 1 + \frac{3\left(\varphi_{c\_t} - \varphi_{cy\_t}\right)L_P\left(H_2 - L_{SP}\right)}{\varphi_{cy\_t} \cdot H_2^{\,2}}$$

iii. Compute the subsystem's equivalent damping ratio, ξ_{sys2}:

If $\mu_{\Delta 2} \leq 1$

$$\xi_{ss2} = 0.05$$

Otherwise

$$\xi_{ss2} = 0.05 + 0.444 \cdot \left(\mu_{\Delta 2} - 1\right) / \left(\mu_{\Delta 2} \cdot \pi\right)$$

γ. Compute the equivalent damping ratio of the bent, ξ_{sys}:

$$\xi_{sys} = \frac{\xi_{ss1} \cdot \Delta_{ss1} + \xi_{ss2} \cdot \left(\Delta - \Delta_{ss1}\right)}{\Delta}$$

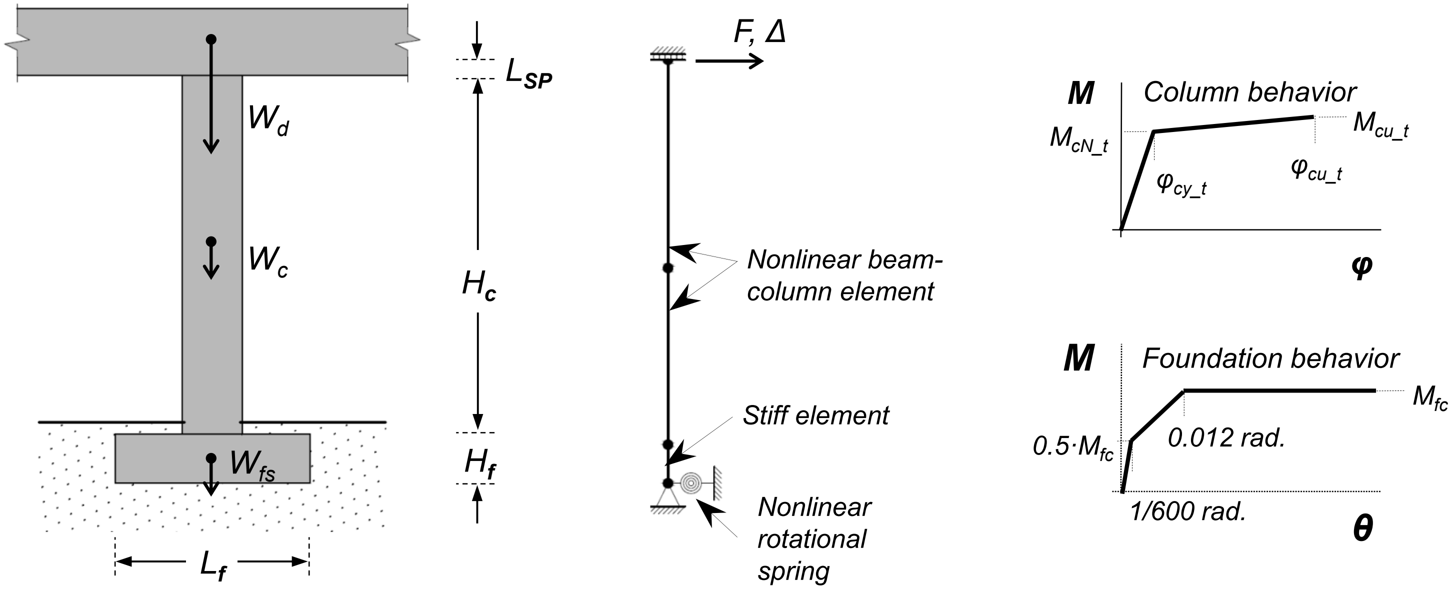

Figure 5.2 Idealized model for nonlinear pushover analysis of a single-column rocking bent with plastic hinging at the top of the column.

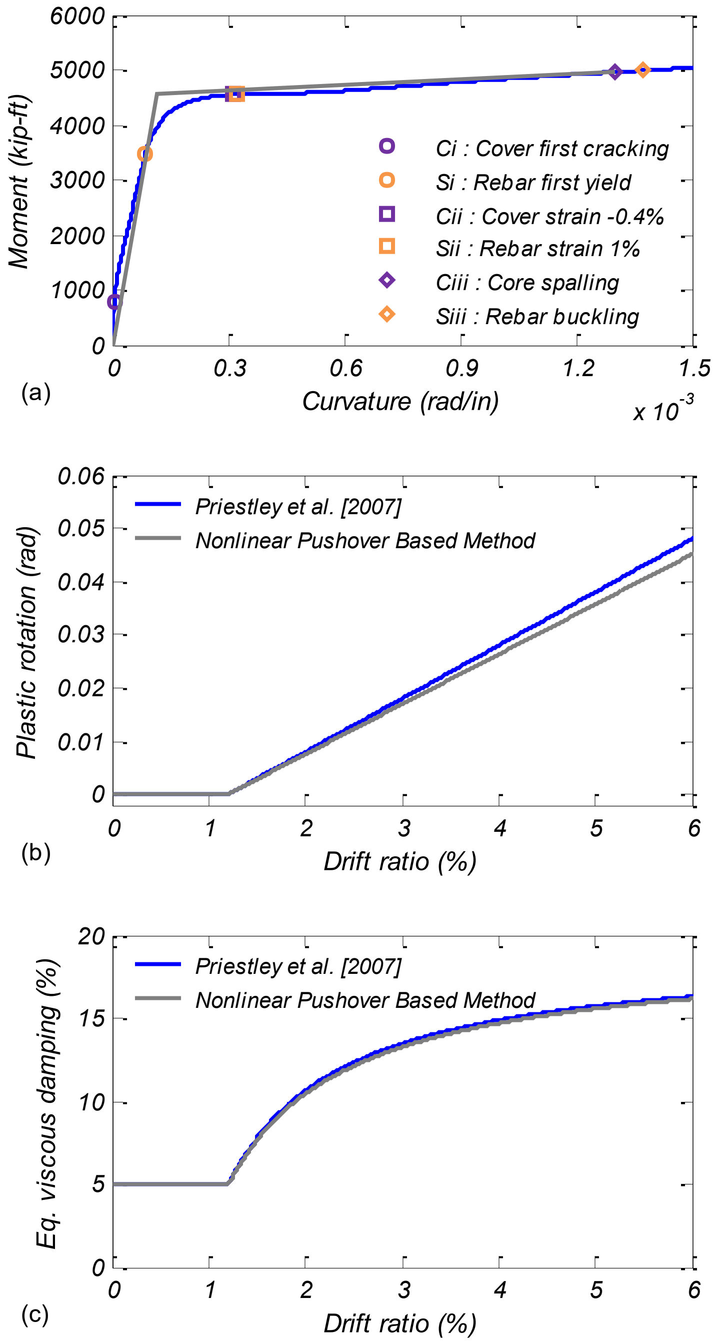

Figure 5.3 Validation of the nonlinear monotonic analysis based method for a column pinned at its base and with plastic hinging at its top against Priestley et al. [2007] analytical expressions: (a) section analysis of the top of the column; (b) column plastic hinge rotation; and (c) equivalent viscous damping ratio.

Table 5.2 Step-by-step simplified equivalent linear displacement-based method for the analysis of a single rocking bent with plastic hinging at the top of the column.

1. Preliminary design of rocking foundation and column:

- **a.** Determine the dimensions of the foundation normal (L_f) and parallel (B_f) to the rocking axis and the cross-sectional dimensions of the column based on a preliminary design.
- **b.** Iteratively calculate the critical contact area ratio (ρ_{ac}) such that

$$0.95 \cdot W_{f\_b} \leq q_c \cdot A_f \cdot \rho_{ac} \leq 1.05 \cdot W_{f\_b}$$

where q_c is the bearing capacity of the minimum possible soil-footing contact during rocking, A_c, with plan dimensions of B_f and $L_f \cdot \rho_{ac}$, A_f is the plan area of the footing, and W_{f_b} is the total vertical force acting at the footing base.

- **c.** Compute the foundation rocking capacity, M_{fc}:

$$M_{fc} = 0.5 \cdot W_{f\_b} \cdot L_f \left(1 - \rho_{ac}\right)$$

- **d.** Select the column longitudinal reinforcement ratio (ρ_l) to ensure that the column base yield moment (M_{cy_b}) is not smaller than the foundation rocking capacity.

2. Set-up calculations for the hinging subsystem:

- **a.** Based on a section analysis determine the yield curvature (φ_{cy_t}) and nominal moment capacity (M_{cN_t}) at the top of the column for an axial load equal to the superstructure weight(W_d). Alternatively, the yield curvature and nominal moment capacity can be estimated as:

$$\varphi_{cy\_t} = 2.25 \cdot \varepsilon_{ye} / D_c \text{ , or } \varphi_{cy\_t} = 2.10 \cdot \varepsilon_{ye} / h_c$$

$$M_{cN\_t} = (EI)_g \cdot \varphi_{cy\_t} \cdot \left\lfloor (EI)_e / (EI)_g \right\rfloor$$

where ε_{ye} is the expected yield strain of the reinforcing steel, D_c is the column diameter for circular columns, h_c is the section depth for rectangular columns, $(EI)_g$ is the gross flexural rigidity and $(EI)_e/(EI)_g$ is the elastic stiffness ratio that can be obtained from Caltrans SDC [2013a].

- **b.** Determine the cantilever height, H_2:

$$H_2 = \frac{M_{cN\_t}}{M_{fc} + M_{cN\_t}} \cdot \left(H_f + H_c\right)$$

where H_f is the footing height and H_c is the clear column height.

- **c.** Compute the strain penetration length, L_{SP}:

$$L_{SP} = 0.15 \cdot \frac{f_{ye}}{ksi} \cdot d_{bl}$$

where f_{ye} is the expected yield strength of the reinforcing steel and d_{bl} is the nominal reinforcing bar diameter .

- **d.** Calculate the yield displacements when 50% and 100% of the column-top nominal moment capacity is mobilized, Δ_{y2a} and Δ_{y2}, respectively:

$$\Delta_{y2a} = 0.5 \cdot \varphi_{cy\_t} \cdot \left(H_2 + L_{SP}\right)^2 / 3 \text{ , and } \Delta_{y2} = \varphi_{cy\_t} \cdot \left(H_2 + L_{SP}\right)^2 / 3$$

Table 5.2 (Continued)

3. Set-up calculations for the rocking subsystem:

- **a.** Determine the effective seismic weight, W_s:

$$W_s = W_d + 0.33 \cdot W_c$$

where W_d is the superstructural weight at the top of the column, and W_c is the column weight.

- **b.** Determine the cantilever height, H_1:

$$H_1 = H_f + H_c - H_2$$

- **c.** Determine the footing elastic rotational stiffness (K_{f_50}) and corresponding translational period (T_{f_50}):

$$K_{f\_50} = 300 \cdot M_{fc}\ , \text{ and } \ T_{f\_50} = 2\pi\sqrt{\frac{W_s/g}{K_{f\_50}/H_1^2}}$$

- **d.** Determine the fixed base stiffness (K_{c1}) and period (T_{c1}) of the flexible column:

$$K_{c1} = \frac{3 \cdot (EI)_e}{(H_1 - H_f)^3}\ , \text{ and } \ T_{c1} = 2\pi\sqrt{\frac{W_s/g}{K_{c1}}}$$

where for simplicity the effective flexural rigidity, $(EI)_e$, can be taken equal to that of the top column section determined previously, for a uniform section column.

- **e.** Calculate the lateral displacement due to the column flexibility that corresponds to the mobilization of the footing rocking moment capacity, Δ_{c1}:

$$\Delta_{c1} = M_{fc}/(H_1 \cdot K_{c1})$$

- **f.** Calculate the yield displacements when 50% and 100% of the footing rocking moment capacity is mobilized, Δ_{y1a} and Δ_{y1}, respectively:

$$\Delta_{y1a} = 0.5 \cdot \Delta_{c1} + H_1 \cdot sin(0.5 \cdot h_f),\ \text{ and } \ \Delta_{y1} = \Delta_{c1} + H_1 \cdot sin(b_f)$$

where h_f and b_f are equal to 1/300 and 0.012 radians, respectively.

4. Set-up calculations at the bent-level:

- **a.** Determine the nominal lateral capacity (F_c) and the yield displacements at 50% (Δ_{ya}) and 100% (Δ_y) of the lateral capacity:

$$F_c = (M_{fc} + M_{cN\_t})/(H_f + H_c)\ ,\ \Delta_{ya} = \Delta_{y1a} + \Delta_{y2a}\ , \text{ and } \ \Delta_y = \Delta_{y1} + \Delta_{y2}$$

5. Assume a trial input system lateral displacement, Δ_{sys}. For first iteration only, set Δ_{sys} equal to Δ_y.

6. Compute the lateral force (F):

If $\Delta_{sys} < \Delta_{ya}$

$$F = 0.5 \cdot F_c \cdot \Delta_{sys}/\Delta_{ya}$$

Else if $\Delta_{sys} > \Delta_y$

$$F = F_c$$

Otherwise

$$F = 0.5 \cdot F_c\left[1 + (\Delta_{sys} - \Delta_{ya})/(\Delta_{sys} - \Delta_y)\right]$$

Table 5.2 (Continued)

7. Calculations to determine equivalent viscous damping for the hinging subsystem:

a. Determine the total displacement of the subsystem (Δ_{ss2}):

If $\Delta_{sys} < \Delta_{ya}$

$$\Delta_{ss2} = \left(\Delta_{y2a} \cdot F\right) / \left(0.5 \cdot F_c\right)$$

Else if $\Delta_{sys} > \Delta_y$

$$\Delta_{ss2} = \Delta_{y2} + \left(\Delta_{sys} - \Delta_y\right) \cdot \frac{H_2}{H_1 + H_2}$$

Otherwise

$$\Delta_{ss2} = \Delta_{y2a} + \left(\Delta_{y2} - \Delta_{y2a}\right) \cdot \frac{F - 0.5 \cdot F_c}{0.5 \cdot F_c}$$

b. Determine the displacement ductility ($\mu_{\Delta 2}$):

$$\mu_{\Delta 2} = \frac{\Delta_{ss2}}{\Delta_{y2}}$$

c. Calculate the equivalent viscous damping of the subsystem (ξ_{ss2}):

If $\mu_{\Delta 2} < 1$

$$\xi_{ss2} = 0.05$$

Otherwise

$$\xi_{ss2} = 0.05 + 0.444 \cdot \left(\mu_{\Delta 2} - 1\right) / \left(\mu_{\Delta 2} \cdot \pi\right)$$

8. Calculations to determine equivalent viscous damping for the rocking subsystem:

a. Determine the total displacement of the subsystem (Δ_{ss1}):

If $\Delta_{sys} < \Delta_{ya}$

$$\Delta_{ss1} = \left(\Delta_{y1a} \cdot F\right) / \left(0.5 \cdot F_c\right)$$

Else if $\Delta_{sys} > \Delta_y$

$$\Delta_{ss1} = \Delta_{y1} + \left(\Delta_{sys} - \Delta_y\right) \cdot \frac{H_1}{H_1 + H_2}$$

Otherwise

$$\Delta_{ss1} = \Delta_{y1a} + \left(\Delta_{y1} - \Delta_{y1a}\right) \cdot \frac{F - 0.5 \cdot F_c}{0.5 \cdot F_c}$$

b. Determine the footing rotation (θ_f):

$$\theta_f = a\sin\left[\frac{\Delta_{ss1} - \Delta_{c1} \cdot F/F_c}{H_1}\right]$$

c. Compute the footing hysteretic damping ratio (ξ_{f_hys}), and the secant, at peak displacement, rotational stiffness (K_{f_pl}) and corresponding translational period (T_{f_pl}) of the rocking foundation that is associated to the footing hysteretic damping:

Table 5.2 (Continued)

If $\theta_f \leq 0.5 \cdot h_f$ (h_f = 1/300 radians)

$$\xi_{f\_hys} = 0, \text{ and } T_{f\_pl} = 0$$

Else if $\theta_f \geq b_f$ (b_f = 0.012 radians)

$$\xi_{f\_hys} = \frac{0.90}{2\pi}\left(4 - \frac{3}{2.6 \cdot \rho_{ac} + 1} - \frac{b_f}{\theta_f}\right), \text{ or } \xi_{f\_hys} = \frac{0.30}{2\pi}\left(4 - \frac{3}{2.6 \cdot \rho_{ac} + 1} - \frac{b_f}{\theta_f}\right)$$

$$K_{f\_pl} = M_{fc} / \left(\theta_f - h_f\right), \text{ and } T_{f\_pl} = 2\pi\sqrt{\frac{W_s/g}{K_{f\_pl}/H_1^2}}$$

Otherwise

$$\xi_{f\_hys} = \frac{0.90}{2\pi}\left(4 - \frac{3}{2.6 \cdot \rho_{ac} + 1} - 1\right) \cdot \left(\frac{\theta_f - 0.5 \cdot h_f}{b_f - 0.5 \cdot h_f}\right), \text{ or}$$

$$\xi_{f\_hys} = \frac{0.28}{2\pi}\left(4 - \frac{3}{2.6 \cdot \rho_{ac} + 1} - 1\right) \cdot \left(\frac{\theta_f - 0.5 \cdot h_f}{b_f - 0.5 \cdot h_f}\right)$$

$$K_{f\_pl} = F \cdot H_1 / \left(\theta_f - F \cdot H_1 / K_{f\_50}\right), \text{ and } T_{f\_pl} = 2\pi\sqrt{\frac{W_s/g}{K_{f\_pl}/H_1^2}}$$

Note that the use of the first or the second ξ_{f_hys} expression is discussed in Section 4.7.

d. Calculate the subsystem's effective period (T_{ss1}) and equivalent viscous damping (ξ_{ss1}):

$$T_{ss1} = \sqrt{T_{c1}^2 + T_{f\_50}^2 + T_{f\_pl}^2}$$

$$\xi_{ss1} = \left(\frac{T_{c1}}{T_{ss1}}\right)^2 \xi_{c1} + \left(\frac{T_{f\_50}}{T_{ss1}}\right)^2 \xi_{rad} + \left(\frac{T_{f\_pl}}{T_{ss1}}\right)^2 \xi_{f\_hys}$$

where ξ_{c1} is the column elastic damping, and ξ_{rad} is the radiation damping of the footing rocking mode. Column elastic damping can be taken as 2% as the column is designed to remain nominally elastic, while radiation damping can be assumed as approximately equal to 3% if not addressed explicitly; e.g. using the FEMA 440 document [ATC 2005].

9. Determine the system equivalent viscous damping (ξ_{sys}) and effective period (T_{sys}) at the bent-level:

$$\xi_{sys} = \frac{\xi_{ss1} \cdot \Delta_{ss1} + \xi_{ss2} \cdot \Delta_{ss2}}{\Delta_{sys}}$$

$$T_{sys} = 2\pi\sqrt{\frac{W_s/g}{F/\Delta_{sys}}}$$

10. Compute the new lateral displacement at the top of the column (Δ_{sys}):

$$\Delta_{sys} = \left(\frac{0.07}{0.02 + \xi_{sys}}\right)^{\alpha} \cdot Sd\left(T_{sys}, 0.05\right)$$

where α = 0.5 for a site at which the elastic design spectrum (*Sd*) is dominated by broadband motions, or α = 0.25 for the case near-fault pulse-like motions.

Table 5.2 (Continued)

11. Use Δ_{sys} as input value and repeat steps 5 to 10. Convergence occurs when computed system displacement at step 10 is no more than 2% different from the input displacement used in step 5.

12. When convergence has been achieved and if Δ_{sys} is larger than Δ_y, estimate the column hinge's plastic rotation (θ_{c_pl}) and check if P-Δ instability ratio ($\theta_{P\text{-}\Delta}$) exceeds the allowable limit:

$$\theta_{c\_pl} = \frac{\left\langle \Delta_{ss2} - \Delta_{y2} \right\rangle}{H_2}, \text{ and } \theta_{P-\Delta} = \frac{W_s \cdot \Delta_{sys}}{M_{fc} + M_{cN\_t}} \le \frac{0.2 \cdot M_{cN\_t} + 0.3 \cdot M_{fc}}{M_{fc} + M_{cN\_t}}$$

where < > set negative values to zero, i.e., $\langle x \rangle = x$ if $x \geq 0$, otherwise $\langle x \rangle = 0$.

5.3 COMPARISON OF NONLINEAR PUSHOVER ANALYSIS BASED METHOD AND SIMPLIFIED METHOD

5.3.1 Considered Cases

A set of 16 bridge bents are examined here to compare the simplified and the detailed method. The bridge bents studied here include a square foundation and a single circular column supporting the deck weight. The bridge bents are expected to resist seismic action with plastic hinging at the top of the column in the longitudinal direction, while no plastic hinging develops in the transverse direction. The main characteristics of each case are shown in Table 5.3. The key parameters altered were: (i) the critical contact area ratio of the rocking foundation (ρ_{ac}); (ii) the clear column height (H_c); (iii) the longitudinal reinforcement ratio of the column (ρ_l); and (iv) the deck weight (W_d). For simplicity, the footing height and embedment were equal to 6 and 9 ft, respectively, for all cases. In addition, the concrete and reinforcing steel strength characteristics, and the rebar diameter were as described in Section 5.2.2.

For the first four models, the critical contact area ratio is equal to 0.125, the clear column height is equal to 25 or 50 ft, the longitudinal reinforcing steel ratio is equal to 1% or 2.5%, and the deck weight is equal to 1500 kip, while the ratio between the yield moment at the base of the column (M_{cy_b}) and the footing moment capacity (M_{fc}) is approximately equal to 1 to prevent damage at the bottom of the column. Hence, models 1 to 4 are characterized by: (i) a fairly constant lower-bound strength ratio between the nominal moment capacity at the top of the column (M_{cN_t}) and the foundation moment capacity (M_{fc}) that has a value between 1.26 and 1.36; and (ii) a wider-range increasing column-to-footing elastic flexibility ratio (T_c/T_{f_50}), where T_c is the double-bending fixed-base period of the column and T_{f_50} is the single bending period due to the initial rotational stiffness of the rocking foundation, that has a value between 0.47 and 0.78. Models 5 to 8 are similar to models 1 to 4, but the critical contact area ratio is equal to 0.071 instead of 0.125.

Models 9 to 16 represent a scenario where the column-to-footing strength ratio is not near to 1 as it was in models 1 to 8. This could be a common case for the non-critical bents of a bridge with different span lengths and/or column heights where the same foundation size and column size/reinforcement is selected. With constructability in mind, each model in this second set has the same foundation size and column size/reinforcement with the corresponding model from the first set, but the deck weight is reduced to 1000 kip. The result is that models 9 to 12, for example, have a strength ratio between 1.46 and 1.71, compared to models 1 to 4 where this ratio ranged between 1.26 and 1.36, while the column-to-footing flexibility ratios are similar between the two sets.

Lastly, it is noted that all models are developed so that: (i) the strength ratio of the bents in the transverse direction is between 0.2 and 0.25; (ii) the normalized moment-to-shear ratios are large enough to ensure that column is flexure (not shear) dominated and the footing is rocking (not sliding) dominated; and (iii) the required soil bearing capacity at the critical contact area is less than about 150 ksf.

5.3.2 Comparison Results

Figures 5.4 to 5.7 compare the simplified method to the more detailed nonlinear pushover based method for the examined cases. Figure 5.4 compares the monotonic pushover curves as obtained from the two methods, with the successive yield points being identified. In all cases the results of the simplified method agree fairly well with these of the detailed method. More specifically, the drift ratio at the bent's nominal lateral capacity for the simplified method falls in between the drift ratios at which the nominal capacity at the top of the column and the footing capacity are mobilized, while the drift ratio corresponding to the ultimate curvature of the plastic hinge is only slightly overestimated. Figure 5.5 plots the height of the inflection point from the footing base normalized by the structural height as a function of the drift ratio. The variation of the inflection point location is relatively narrow and close to the location assumed by the column-to-footing strength ratio.

Figure 5.6 compares the footing rotation and the column hinge plastic rotation as a function of the drift ratio. For stiff columns (e.g., models 1, 5, 9 and 13) the simplified method results in overestimation of the footing rotation and underestimation of the column plastic rotation. With increasing column flexibility (e.g., models 4, 8, 12 and 16), the trend appears to reverse. Comparison of the models with ρ_{ac} = 0.125 and 0.071 shows that the accuracy of the simplified method is not sensitive to variations in critical contact area ratio or the column/footing strength ratio.

Figure 5.7 compares the equivalent viscous damping ratio of the two subsystems as well as of the entire system versus the lateral drift ratio. The equivalent viscous damping ratio at the bent-level is well predicted by the simplified method, particularly for the cases of flexible columns. For stiff columns, an underestimation is observed at small drift ratios; nevertheless, the difference is practically negligible for drift ratios larger than approximately 1.5%.

Overall, the simplified method is found sufficient and practical to calculate the equivalent viscous damping ratio and plastic rotation at the top of the column. It is also shown that the critical contact area ratio and the strength ratio between the column plastic hinge and the rocking footing do not affect the efficiency of the simplified method, as opposed to the column-to-footing elastic flexibility ratio. Hence, the detailed method presented in Table 5.1 may be used for cases that fall beyond the column-to-footing elastic flexibility ratio range examined here, in particular for very stiff/short columns.

Table 5.3 Model parameters of single-column rocking bents with plastic hinging at the top of the column.

No.	ρ_{ac}	H_c (ft)	ρ_l (%)	W_d (kip)	L_f (ft)	D_c (ft)	W_s (kip)	W_{f_b} (kip)	M_{fc} (kip-ft)	M_{cy_b} / M_{fN}	M_{cN_t} / M_{fc}	C_N	C_{r_T}	W_d / $(f_{ce}\cdot A_g)$	M_{cN_t} / $(V_N\cdot D_c)$	M_{fc} / $(V_N\cdot L_f)$	q_c (ksf)	T_{f_50} (s)	T_c (s)	T_c / T_{f_50}
1	0.125	25	1	1500	12.5	6.67	1543	1813	9913	1.03	1.29	0.47	0.21	0.057	2.6	1.1	93	0.78	0.37	0.47
2	0.125	25	2.5	1500	12.5	5.33	1528	1770	9681	1.03	1.35	0.48	0.20	0.090	3.3	1.1	91	0.79	0.44	0.56
3	0.125	50	1	1500	18.0	8.33	1635	2290	18037	1.01	1.26	0.44	0.20	0.037	3.7	1.4	57	1.08	0.72	0.66
4	0.125	50	2.5	1500	18.0	6.50	1582	2140	16851	1.02	1.36	0.45	0.19	0.060	5.0	1.3	53	1.10	0.86	0.78
5	0.071	25	1	1500	13.0	6.90	1546	1837	11086	1.00	1.25	0.52	0.23	0.054	2.5	1.1	152	0.74	0.35	0.47
6	0.071	25	2.5	1500	13.0	5.50	1529	1791	10810	1.00	1.32	0.53	0.23	0.084	3.2	1.0	148	0.75	0.42	0.56
7	0.071	50	1	1500	18.5	8.67	1646	2345	20144	1.00	1.25	0.49	0.22	0.034	3.6	1.3	96	1.02	0.67	0.65
8	0.071	50	2.5	1500	18.5	6.75	1589	2181	18733	1.01	1.36	0.50	0.21	0.056	4.8	1.3	89	1.04	0.80	0.77
9	0.091	25	1	1000	12.5	6.67	1043	1313	7461	1.22	1.56	0.59	0.23	0.038	2.8	1.0	93	0.74	0.32	0.43
10	0.090	25	2.5	1000	12.5	5.33	1028	1270	7227	1.28	1.71	0.62	0.23	0.060	3.7	0.9	91	0.75	0.37	0.49
11	0.098	50	1	1000	18.0	8.33	1135	1790	14539	1.16	1.46	0.56	0.23	0.025	4.0	1.3	57	1.00	0.62	0.62
12	0.096	50	2.5	1000	18.0	6.50	1082	1640	13344	1.21	1.64	0.58	0.22	0.040	5.4	1.2	53	1.02	0.72	0.71
13	0.052	25	1	1000	13.0	6.90	1046	1337	8237	1.22	1.55	0.65	0.25	0.036	2.7	0.9	152	0.71	0.30	0.42
14	0.051	25	2.5	1000	13.0	5.50	1029	1291	7960	1.26	1.70	0.67	0.25	0.056	3.6	0.9	148	0.71	0.35	0.49
15	0.056	50	1	1000	18.5	8.67	1146	1845	16109	1.18	1.47	0.62	0.25	0.023	3.8	1.2	96	0.96	0.57	0.60
16	0.055	50	2.5	1000	18.5	6.75	1089	1681	14693	1.23	1.67	0.64	0.24	0.037	5.2	1.1	89	0.97	0.67	0.69

Notation : ρ_{ac} = critical contact area ratio; H_c = clear column height; ρ_l = longitudinal steel reinforcement ratio; W_d = deck weight; W_s = seismic weight; W_{f_b} = total weight; M_{fc} = footing moment capacity neglecting soil passive resistance; M_{cy_b} = yield moment at the base of the column; M_{cN_t} = nominal moment capacity at the top of the column; C_N = strength ratio in the longitudinal direction = $(M_{fc} + M_{cN\_t})/(W_s\cdot H_t)$, where $H_t = H_c + 6$ft; C_{r_T} = strength ratio in the transverse direction = $M_{fc}/(W_s\cdot H_t)$; V_N = lateral strength corresponding to C_N; q_c = required soil bearing capacity at the critical contact area; T_{f_50} = single-bending period due to the initial rotational stiffness of the foundation; T_c = double-bending fixed-base period of the column.

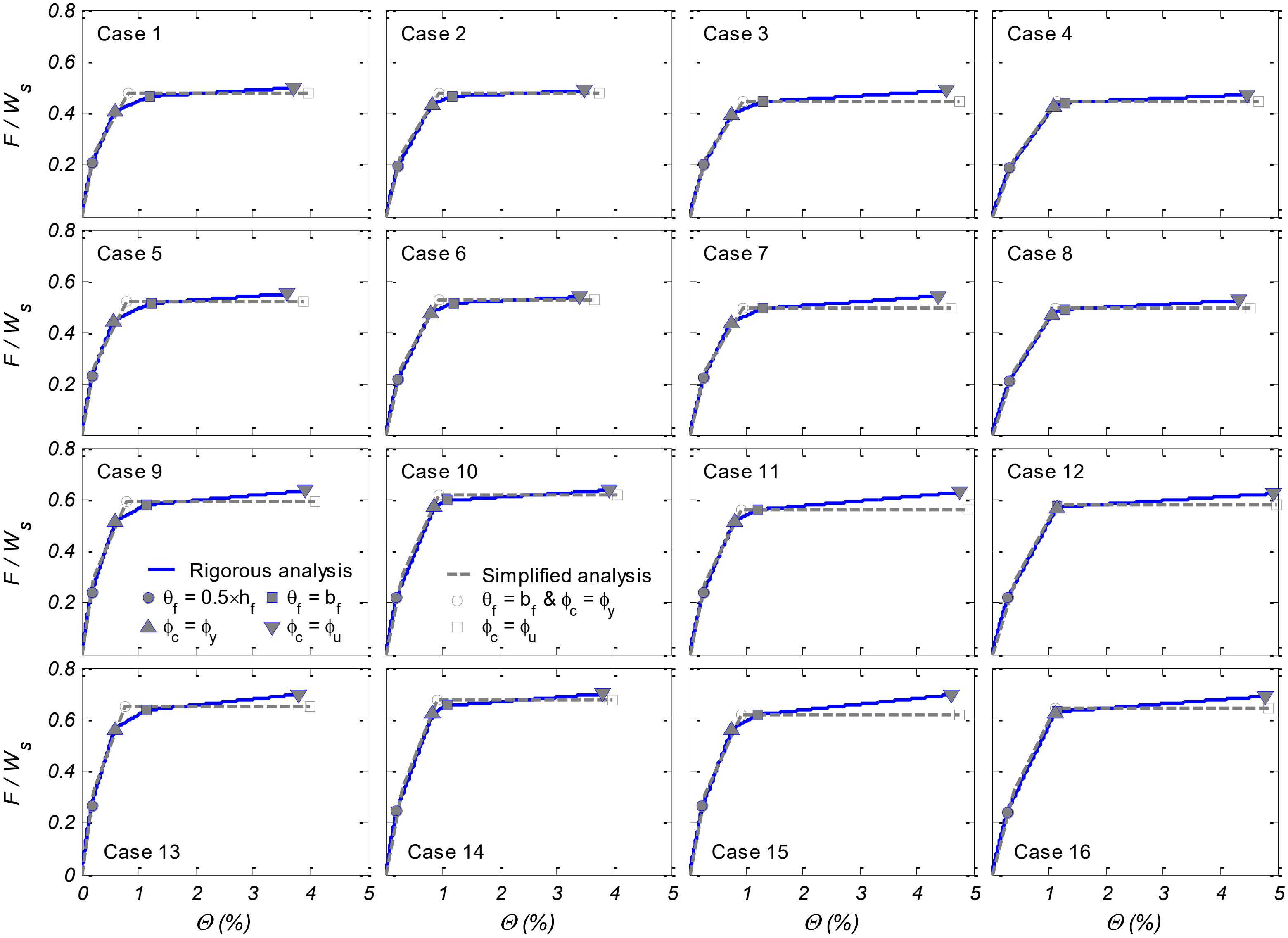

Figure 5.4 Monotonic analysis results for the two methods; lateral force (*F*) normalized by the seismic weight (W_s) versus drift ratio (*Θ*).

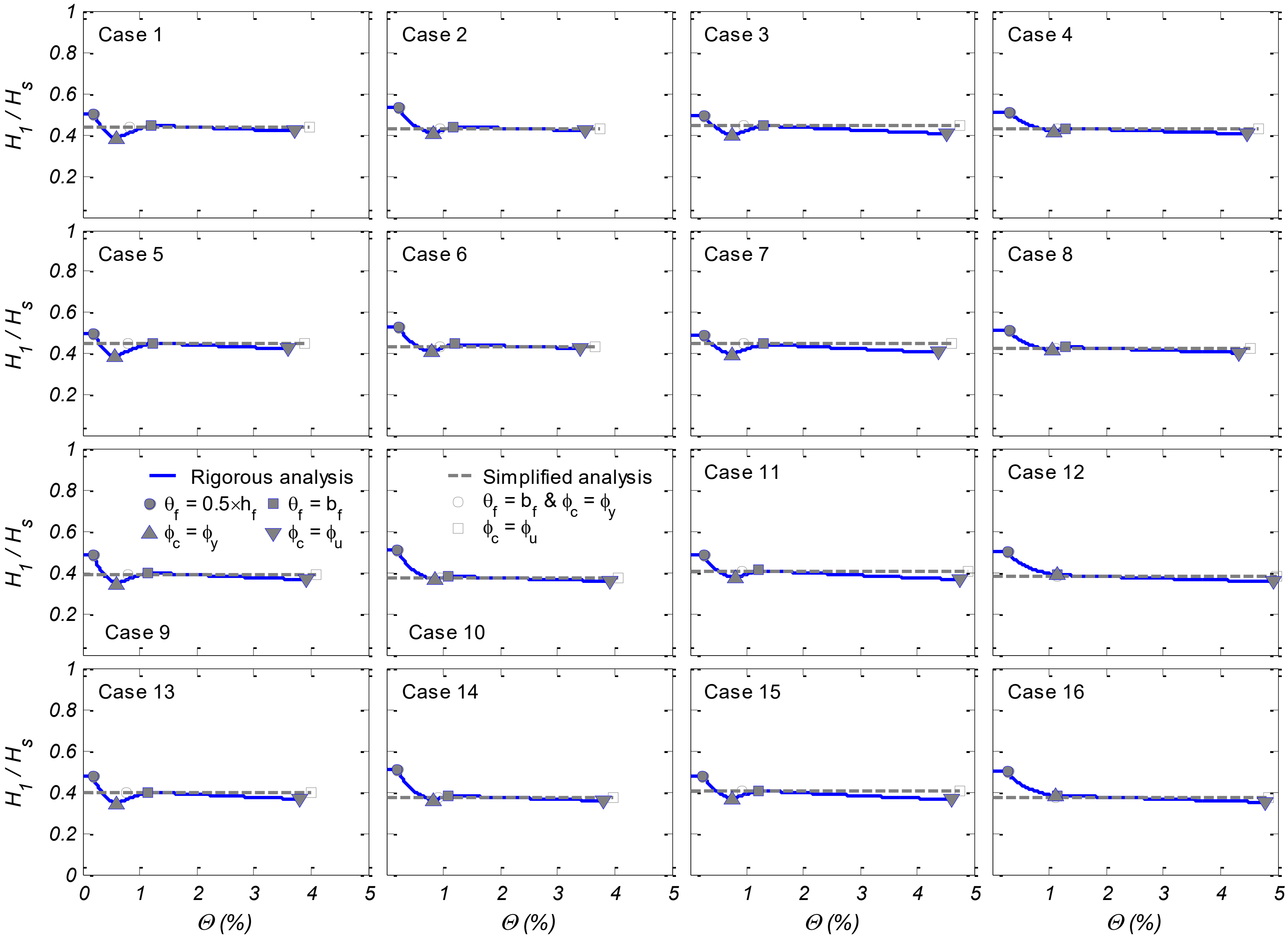

Figure 5.5 Monotonic analysis results for the two methods; height of inflection point from the footing base (H_1) normalized by the structural height (H_s) versus drift ratio (Θ).

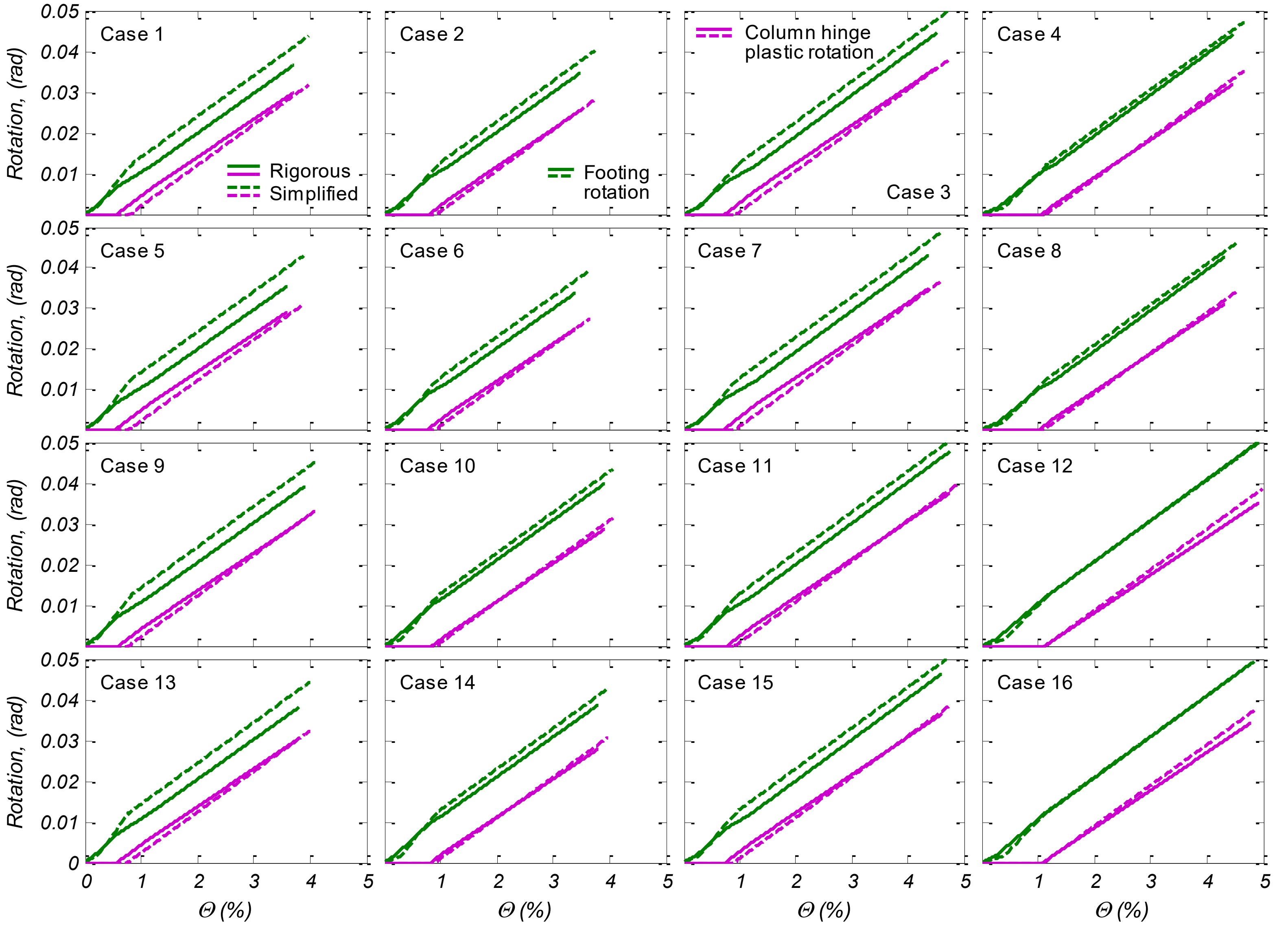

Figure 5.6 Monotonic analysis results for the two methods; footing rotation and column's top hinge plastic rotation versus drift ratio (*Θ*).

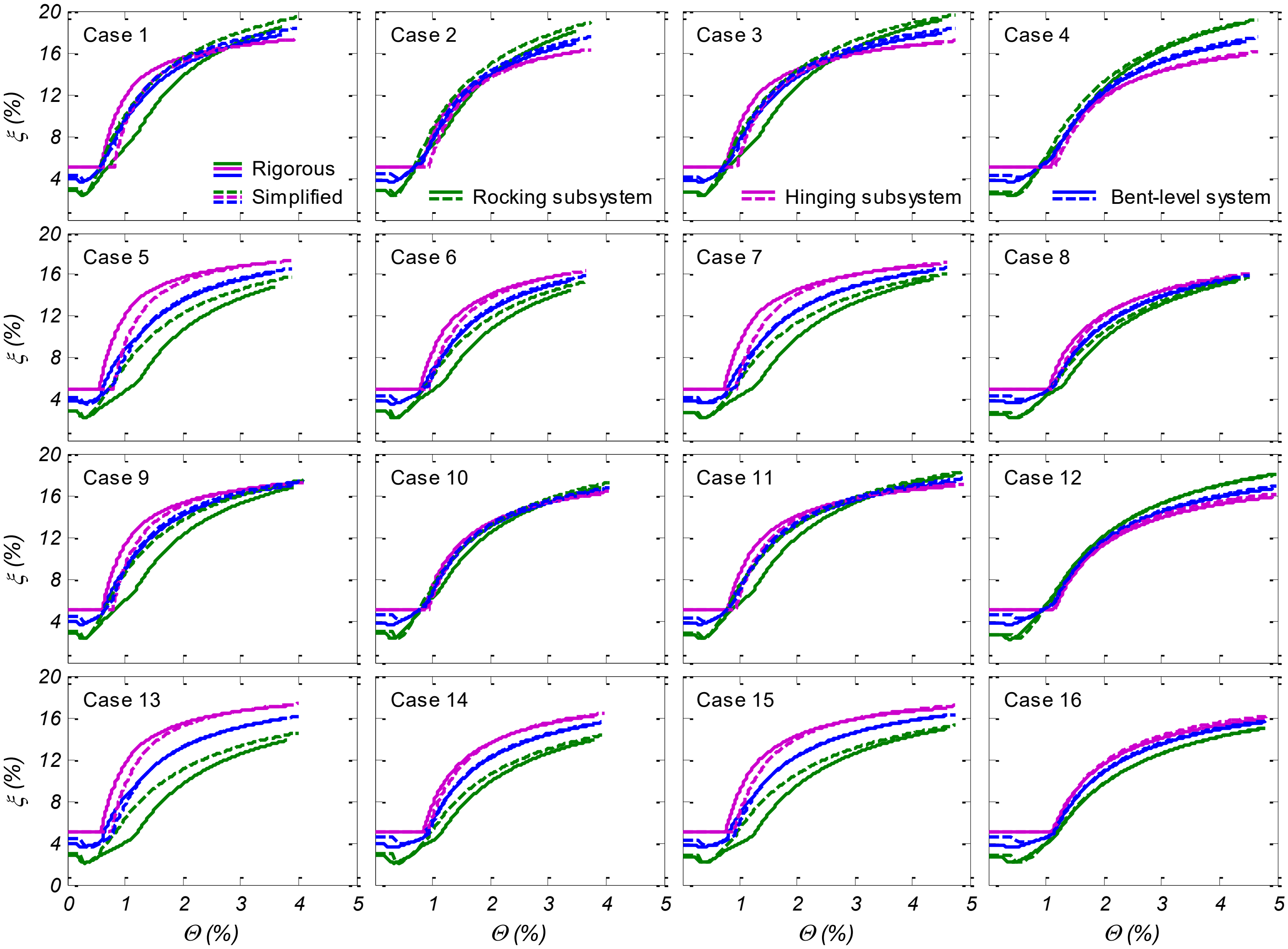

Figure 5.7 Monotonic analysis results for the two methods; equivalent viscous damping ratio (ξ) versus drift ratio (Θ) at the bent-level as well as for the rocking and hinging sub-systems.

6 Bridge System Level Analysis

6.1 TRANSVERSE DIRECTION

Figure 6.1 shows at deformed state the plan view of a single-column bent bridge excited in the transverse direction. Typically, the lateral displacement pattern of the deck is affected by multiple modes of response; it depends on the bridge geometry, the relative stiffness between the superstructure and the bents, the lateral restraint of the abutments, and the level of inelasticity of response. Previous researchers [e.g. Dwairi and Kowalsky 2006; Priestley et al. 2007; Sadan et al. 2012] have analyzed this problem through an iterative eigenvalue analysis that uses the effective (secant) lateral stiffness for the abutments and bents to determine the lateral displacement pattern of the deck and the corresponding SDOF idealization. This section presents a more practical approach to account for the important abutment and modal participation effects in the displacement-based analysis method for bridge systems with rocking foundations. Two modification factors, explained below, are introduced to partially account for the bent-to-bent interaction and the restraint of the abutments.

6.1.1 Mass Participation Correction Factor

The mass participation correction factor (C_m) is used to reduce the tributary seismic mass at the top of the each bent to account for the effective mass that participates to the transverse response of the bridge. The mass participation correction factor depends on the modal properties of the bridge at different levels of lateral response. Here the same mass participation factor is used for all bents of a bridge for simplicity. C_m ranges between 0.7 – 0.9 based on previous studies [Dwairi and Kowalsky 2006; Sadan et al. 2012] that have analyzed many different bridge configurations through modal analysis with effective (secant) stiffness properties for the abutments and bents.

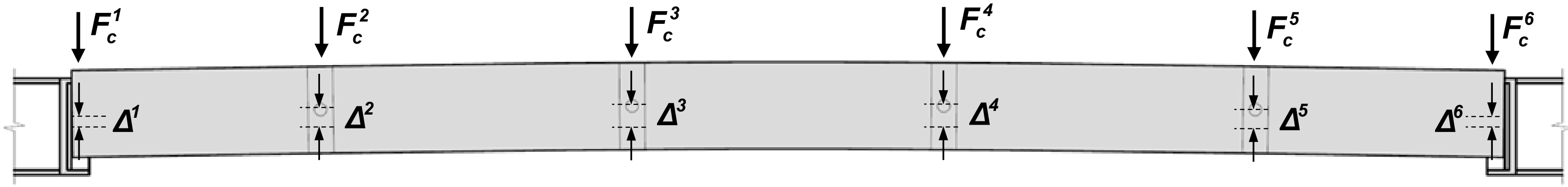

Figure 6.1 Deformed state plan view schematic of a single-column bent bridge excited in the transverse direction.

6.1.2 Abutment Strength Correction Factor

The abutment strength correction factor (C_a) is used to account for the effect of the abutment on the lateral displacement of the bents by uniformly lumping the relative abutment strength surplus or deficit to the individual bents. The abutment strength correction factor is obtained as:

$$C_a = \frac{1 + \sum_{i=1,n} F_c \Big/ \sum_{i=2 \ldots n-1} F_c}{1 + \sum_{i=1,n} W_s \Big/ \sum_{i=2 \ldots n-1} W_s} \tag{6.1}$$

where F_c is the lateral capacity of each bent or abutment, W_s is the corresponding tributary seismic weight that for the bents also includes one-third of the column weight, and n is the total number of the bents and abutments. The numerator of Eqn. (6.1) is equal to the increase of the bridge lateral capacity when the abutment strength is considered, while the denominator is equal to the corresponding increase of the bridge seismic weight. Hence, C_a can be greater or smaller than one.

Within the displacement-based analysis of each individual bent presented here, the abutment strength correction factor is used to modify both the bent strength and stiffness keeping the yield displacement unchanged. Sensitivity of the bent's response to the exact value of C_a can be assessed by an upper bound estimate in which the abutment lateral capacity includes non-ductile resisting mechanisms such as shear keys, and a lower bound estimate where such mechanisms are neglected.

6.1.3 Step-by-Step Procedure

Table 6.1 presents the step-by-step displacement-based method for the analysis of a single-column bent bridge in the transverse direction with columns on rocking shallow foundations at the base. Table 6.1 would also be applicable to multi-column bent bridges if a pin connection is used between the top of the columns and the deck, by using from step 4 onwards the seismic weight corresponding to a single column of the bent.

6.2 LONGITUDINAL DIRECTION

Figure 6.2(a,b) shows at deformed state an elevation view of the entire bridge as well as of a single bent for uniaxial excitation in the longitudinal direction. Figure 6.2(c,d,e) shows a schematic representation of the bridge with a system of nonlinear spring-dashpot elements. It also shows the various stages of the proposed displacement-based method of analysis that replaces nonlinear force resisting mechanisms with equivalent linear elements. First, the rocking foundation and plastic hinge at the top of the column within each bent are integrated (as elements in series) into an equivalent linear viscoelastic element, while in the final stage, the equivalent linear elements representing the bents and the abutments are integrated into an equivalent linear viscoelastic element for the whole bridge.

Table 6.2 presents the step-by-step displacement-based method for the analysis of a single-column bent bridge in the longitudinal direction with columns on rocking shallow foundations and plastic hinging at their top. The entire mass is considered effective in the longitudinal response.

Table 6.1 Step-by-step displacement-based method for the analysis of a single-column bent bridge in the transverse direction with columns on rocking shallow foundations at the base.

Abutment strength correction factor, C_a

1. For each bridge bent:

  a. Determine the dimensions of the foundation normal (L_f) and parallel (B_f) to the rocking axis and the cross-sectional dimensions of the column based on a preliminary design.

  b. Iteratively calculate the critical contact area ratio (ρ_{ac}) such that

$$0.95 \cdot W_{f\_b} \leq q_c \cdot A_f \cdot \rho_{ac} \leq 1.05 \cdot W_{f\_b}$$

  where q_c is the bearing capacity of the minimum possible soil-footing contact during rocking, A_c, with plan dimensions of B_f and $L_f \cdot \rho_{ac}$, A_f is the plan area of the footing, and W_{f_b} is the total vertical force acting at the footing base.

  c. Compute the foundation rocking capacity, M_{fc}:

$$M_{fc} = 0.5 \cdot W_{f\_b} \cdot L_f \left(1 - \rho_{ac}\right)$$

  d. Select the column longitudinal reinforcement ratio (ρ_l) to ensure that the column base yield moment (M_{cy_b}) is not smaller than the foundation rocking capacity.

  e. Determine the lateral seismic capacity, F_c:

$$F_c = M_{fc}/H$$

  where H is equal to the height of the deck centroid from the footing base.

  f. Determine the effective seismic weight, W_s:

$$W_s = W_d + 0.33 \cdot W_c$$

  where W_d is the tributary superstructural weight at the top of the column, and W_c is the column weight.

2. For each bridge abutment:

  a. Based on a preliminary design, determine the lateral seismic capacity (F_c) provided by the abutment.

  b. Determine the effective seismic weight (W_s) at the abutment.

3. Calculate the abutment strength correction factor (C_a):

$$C_a = \frac{1 + \sum_{i=1,n} F_c \Big/ \sum_{i=2 \ldots n-1} F_c}{1 + \sum_{i=1,n} W_s \Big/ \sum_{i=2 \ldots n-1} W_s}$$

where n is equal to the sum of the abutments and bents of the bridge.

Iterative analysis of bent *i*

4. Compute the lateral displacement at the top of the column due to its flexibility when the foundation has mobilized its moment capacity (Δ_c) and the column fixed-base period (T_c):

$$\Delta_c = M_{fc}/\left(H \cdot K_c\right), \text{ and } T_c = 2\pi \sqrt{\frac{\left(C_m \cdot W_s\right)/g}{C_a \cdot K_c}}$$

where K_c is an estimate of the column lateral stiffness with $I_{eff} \approx 0.5 \cdot I_g$, and C_m is the mass

Table 6.1 (Continued)

participation factor that can be bounded between 0.7 and 0.9.

5. Compute the elastic rotational stiffness of the foundation (K_{f_50}), and the corresponding translational period (T_{f_50}):

$$K_{f\_50} = 300 \cdot M_{fc}\text{, and } T_{f\_50} = 2\pi\sqrt{\frac{(C_m \cdot W_s)/g}{(C_a \cdot K_{f\_50})/H^2}}$$

6. Compute the lateral displacement corresponding to first yield of the rocking foundation (Δ_{y1}) and to the mobilization of the rocking footing capacity (Δ_{y2}):

$$\Delta_{y1} = 0.5\Delta_c + H \cdot sin(0.5 \cdot h_f)\text{, and } \Delta_{y2} = \Delta_c + H \cdot sin(b_f)$$

where $h_f = 1/300$ rad and $b_f = 0.012$ rad.

7. Assume a trial input system lateral displacement (Δ_{sys}). For first iteration, Δ_{sys} can be set equal to Δ_{y2}.

8. Compute the lateral force, F:

If $\Delta_{sys} \leq \Delta_{y1}$

$$F = F_c \cdot \Delta_{sys}/\Delta_{y1}$$

Else if $\Delta_{sys} \geq \Delta_{y2}$

$$F = F_c$$

Otherwise

$$F = 0.5F_c\left(1 + \frac{\Delta_{sys} - \Delta_{y1}}{\Delta_{y2} - \Delta_{y1}}\right)$$

9. Compute the footing rotation (θ_f):

$$\theta_f = a\,sin\left[\frac{\Delta_{sys} - (\Delta_c \cdot F)/F_c}{H}\right]$$

10. Compute the footing hysteretic damping ratio (ξ_{f_hys}), and the secant, at peak displacement, rotational stiffness (K_{f_pl}) and corresponding translational period (T_{f_pl}) of the rocking foundation that is associated to the footing hysteretic damping:

If $\theta_f \leq 0.5 \cdot h_f$

$$\xi_{f\_hys} = 0\text{, and } T_{f\_pl} = 0$$

Else if $\theta_f \geq b_f$

$$\xi_{f\_hys} = \frac{0.90}{2\pi}\left(4 - \frac{3}{2.6 \cdot \rho_{ac} + 1} - \frac{b_f}{\theta_f}\right)\text{, or } \xi_{f\_hys} = \frac{0.30}{2\pi}\left(4 - \frac{3}{2.6 \cdot \rho_{ac} + 1} - \frac{b_f}{\theta_f}\right)$$

$$K_{f\_pl} = M_{fc}/(\theta_f - h_f)\text{, and } T_{f\_pl} = 2\pi\sqrt{\frac{(C_m \cdot W_s)/g}{(C_a \cdot K_{f\_pl})/H^2}}$$

Otherwise

Table 6.1 (Continued)

$$\xi_{f\_hys} = \frac{0.90}{2\pi}\left(4-\frac{3}{2.6\cdot\rho_{ac}+1}-1\right)\cdot\left(\frac{\theta_f-0.5\cdot h_f}{b_f-0.5\cdot h_f}\right), \text{ or } \xi_{f\_hys} = \frac{0.30}{2\pi}\left(4-\frac{3}{2.6\cdot\rho_{ac}+1}-1\right)\cdot\left(\frac{\theta_f-0.5\cdot h_f}{b_f-0.5\cdot h_f}\right)$$

$$K_{f\_pl} = F\cdot H/\left(\theta_f - F\cdot H/K_{f\_50}\right), \text{ and } T_{f\_pl} = 2\pi\sqrt{\frac{\left(C_m\cdot W_s\right)/g}{\left(C_a\cdot K_{f\_pl}\right)/H^2}}$$

Note that the use of the first or the second ξ_{f_hys} expression is discussed in Section 4.7.

11. Calculate the system's effective period (T_{sys}) and equivalent viscous damping (ξ_{sys}):

$$T_{sys} = \sqrt{T_c^{\,2} + T_{f\_50}^{\,2} + T_{f\_pl}^{\,2}}$$

$$\xi_{sys} = \left(\frac{T_c}{T_{sys}}\right)^2 \xi_c + \left(\frac{T_{f\_50}}{T_{sys}}\right)^2 \xi_{rad} + \left(\frac{T_{f\_pl}}{T_{sys}}\right)^2 \xi_{f\_hys}$$

where ξ_c is the column "elastic" damping, and ξ_{rad} is the radiation damping of the footing rocking mode. Column "elastic" damping can be taken as 2% as the column is designed to remain nominally elastic, while radiation damping can be assumed as approximately equal to 3% if not addressed explicitly; e.g. using the FEMA 440 document [ATC 2005].

12. Compute the new lateral displacement of the system (Δ_{sys}):

$$\Delta_{sys} = \left(\frac{0.07}{0.02+\xi_{sys}}\right)^{\alpha}\cdot Sd\left(T_{sys}, 0.05\right)$$

where α = 0.5 for a site at which the elastic design spectrum (*Sd*) is dominated by broadband motions, or α = 0.25 for the case of near-fault pulse-like motions.

13. Use new Δ_{sys} as input value and repeat steps 8 to 13. Convergence occurs when computed system displacement at step 13 is no more than 2% different from the input displacement at step 8.

14. For the converged displacement, check if P-Δ instability ratio ($\theta_{P\text{-}\Delta}$) exceeds the allowable limit:

$$\theta_{P-\Delta} = \frac{W_s\cdot\Delta_{sys}}{F\cdot H} \le 0.3$$

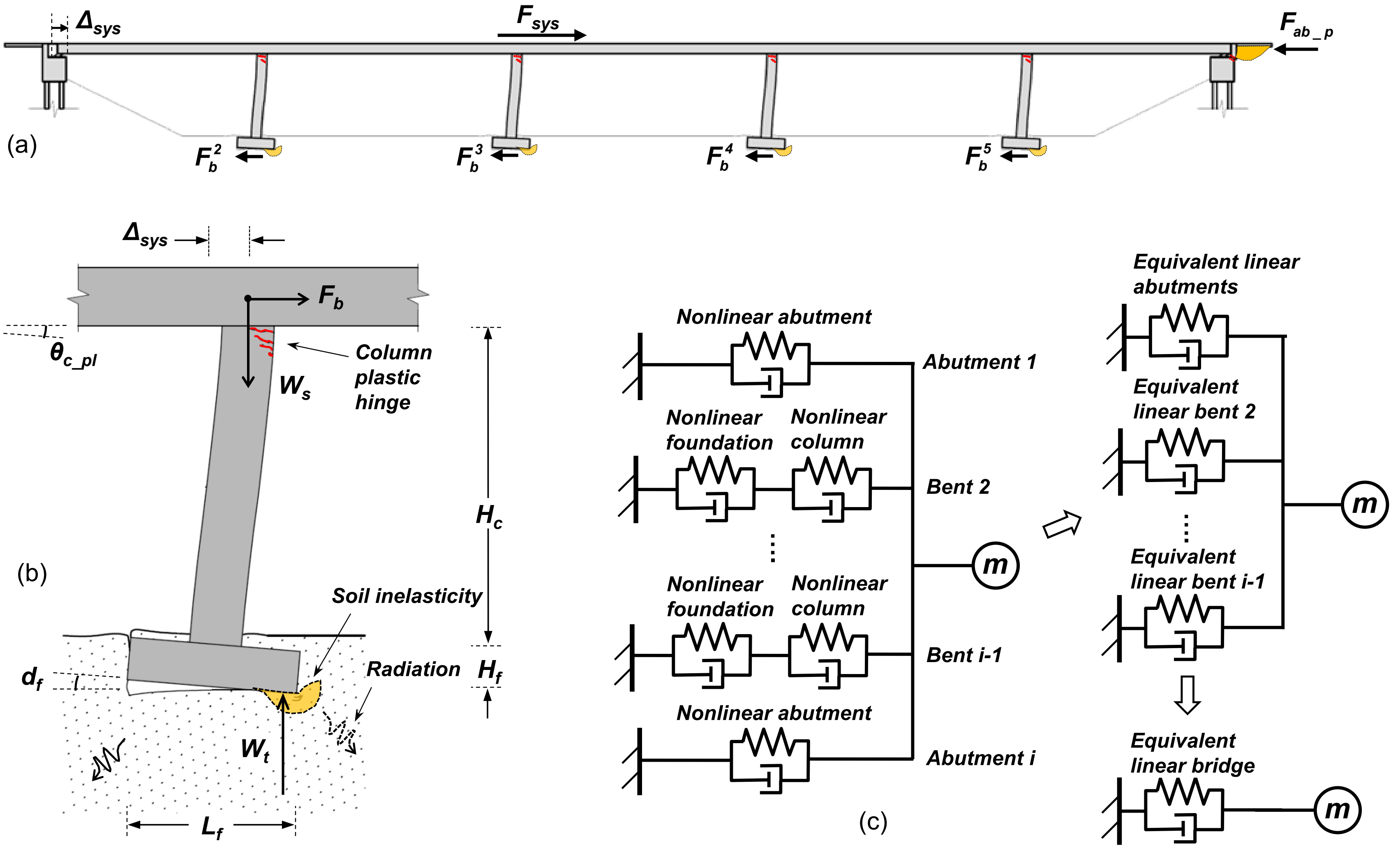

Figure 6.2 Summary of the displacement-based method for the analysis of a single-column bent bridge in the longitudinal direction with columns on rocking shallow foundations and plastic hinging at their top: (a) Elevation view of the bridge at deformed state; (b) elevation view of a bent at deformed state; (c) representation of the bridge response coupling in parallel pairs of viscoelastic elements that represent bents and abutments and integration to a single viscoelastic element.

Table 6.2 Step-by-step displacement-based method for the analysis of a single-column bent bridge in the longitudinal direction with columns on rocking shallow foundations and plastic hinging at their top.

Set-up procedure for bent *i*

1. Preliminary design of rocking foundation and column:

a. Determine the dimensions of the foundation normal (L_f) and parallel (B_f) to the rocking axis and the cross-sectional dimensions of the column based on a preliminary design.

b. Iteratively calculate the critical contact area ratio (ρ_{ac}) such that

$$0.95 \cdot W_{f\_b} \leq q_c \cdot A_f \cdot \rho_{ac} \leq 1.05 \cdot W_{f\_b}$$

where q_c is the bearing capacity of the minimum possible soil-footing contact during rocking, A_c, with plan dimensions of B_f and $L_f \cdot \rho_{ac}$, A_f is the plan area of the footing, and W_{f_b} is the total vertical force acting at the footing base.

c. Compute the foundation rocking capacity, M_{fc}:

$$M_{fc} = 0.5 \cdot W_{f\_b} \cdot L_f \left(1 - \rho_{ac}\right)$$

d. Select the column longitudinal reinforcement ratio (ρ_l) to ensure that the column base yield moment (M_{cy_b}) is not smaller than the foundation rocking capacity.

2. Determine the effective seismic weight, W_s:

$$W_s = W_d + 0.33 \cdot W_c$$

where W_d is the tributary superstructural weight at the top of the column, and W_c is the column weight.

3. Initial calculations for the hinging subsystem:

a. Based on a section analysis determine the yield curvature (φ_{cy_t}) and nominal moment capacity (M_{cN_t}) at the top of the column for an axial load equal to the superstructure weight (W_d). Alternatively, the yield curvature and nominal moment capacity can be estimated as:

$$\varphi_{cy\_t} = 2.25 \cdot \varepsilon_{ye} / D_c \text{ , or } \varphi_{cy\_t} = 2.10 \cdot \varepsilon_{ye} / h_c$$

$$M_{cN\_t} = (EI)_g \cdot \varphi_{cy\_t} \cdot \left\lfloor (EI)_e / (EI)_g \right\rfloor$$

where ε_{ye} is the expected yield strain of the reinforcing steel, D_c is the column diameter for circular columns, h_c is the section depth for rectangular columns, $(EI)_g$ is the gross flexural rigidity and $(EI)_e/(EI)_g$ is the elastic stiffness ratio that can be obtained from Caltrans SDC [2013a].

b. Determine the equivalent cantilever height (i.e. distance to inflection point), H_2:

$$H_2 = \frac{M_{cN\_t}}{M_{fc} + M_{cN\_t}} \cdot \left(H_f + H_c\right)$$

where H_f is the footing height and H_c is the clear column height.

c. Compute the strain penetration length, L_{SP}:

$$L_{SP} = 0.15 \cdot \frac{f_{ye}}{ksi} \cdot d_{bl}$$

where f_{ye} is the expected yield strength of the reinforcing steel and d_{bl} is the nominal

Table 6.2 (Continued)

reinforcing bar diameter.

d. Calculate the yield displacements when 50% and 100% of the column-top nominal moment capacity is mobilized, Δ_{y2a} and Δ_{y2}, respectively:

$$\Delta_{y2a} = 0.5 \cdot \varphi_{cy\_t} \cdot (H_2 + L_{SP})^2 / 3, \text{ and } \Delta_{y2} = \varphi_{cy\_t} \cdot (H_2 + L_{SP})^2 / 3$$

4. Initial calculations for the rocking subsystem:

a. Determine the equivalent cantilever height (i.e. distance to inflection point), H_1:

$$H_1 = H_f + H_c - H_2$$

b. Determine the footing elastic rotational stiffness (K_{f_50}) and corresponding translational period (T_{f_50}):

$$K_{f\_50} = 300 \cdot M_{fc}, \text{ and } T_{f\_50} = 2\pi \sqrt{\frac{W_s/g}{K_{f\_50}/H_1^2}}$$

c. Determine the fixed base stiffness (K_{c1}) and period (T_{c1}) of the flexible column:

$$K_{c1} = \frac{3 \cdot (EI)_e}{(H_1 - H_f)^3}, \text{ and } T_{c1} = 2\pi \sqrt{\frac{W_s/g}{K_{c1}}}$$

where for simplicity the effective flexural rigidity, $(EI)_e$, can be taken equal to that of the top column section determined previously, for a uniform section column.

d. Calculate the lateral displacement due to the column flexibility that corresponds to the mobilization of the footing rocking moment capacity, Δ_{c1}:

$$\Delta_{c1} = M_{fc} / (H_1 \cdot K_{c1})$$

e. Calculate the yield displacements when 50% and 100% of the footing rocking moment capacity is mobilized, Δ_{y1a} and Δ_{y1}, respectively:

$$\Delta_{y1a} = 0.5 \cdot \Delta_{c1} + H_1 \cdot \sin(0.5 \cdot h_f), \text{ and } \Delta_{y1} = \Delta_{c1} + H_1 \cdot \sin(b_f)$$

where h_f and b_f are equal to 1/300 and 0.012 radians, respectively.

5. Determine the nominal bent lateral capacity (F_{bc}) and the yield displacements at 50% (Δ_{ya}) and 100% (Δ_y) of the bent's lateral capacity:

$$F_{bc} = (M_{fc} + M_{cN\_t}) / (H_f + H_c), \quad \Delta_{ya} = \Delta_{y1a} + \Delta_{y2a}, \text{ and } \Delta_y = \Delta_{y1} + \Delta_{y2}$$

Set-up procedure for the abutments

6. Determine the effective seismic weight (W_s) at each abutment.

7. Compute the average backfill passive pressure capacity (F_{ab_pc}) and effective stiffness (K_{ab_p}) at the two abutments based on Caltrans SDC [2013a].

8. If appropriate (e.g. PTFE slider bearings, simply supported abutment diaphragm on spread footing), calculate the seismic resisting friction capacity at each abutment (F_{ab_fc}) and the corresponding yield displacement (Δ_y):

$$F_{ab\_fc} = \mu_f \cdot P_{ab}$$

where P_{ab} is the static axial load on the sliding interface and μ_f is the appropriate dynamic friction

Table 6.2 (Continued)

coefficient.

Initiation of iterative procedure for bridge-level analysis

9. Assume a trial input system lateral displacement (Δ_{sys}). For first iteration, Δ_{sys} should be sufficient to mobilize the rocking foundations and the plastic hinges at the top of the columns at all bents

$$\Delta_{sys} = max\left(\Delta_y^{i=2\ \dots\ n-1}\right)$$

where *n* is the total number of bents and abutments for the bridge.

Equivalent viscous damping at bent *i*

10. Compute the lateral force at the bent (F_b):

If $\Delta_{sys} < \Delta_{ya}$

$$F_b = 0.5 \cdot F_{bc} \cdot \Delta_{sys} / \Delta_{ya}$$

Else if $\Delta_{sys} > \Delta_y$

$$F_b = F_{bc}$$

Otherwise

$$F_b = 0.5 \cdot F_{bc}\left[1 + \left(\Delta_{sys} - \Delta_{ya}\right) / \left(\Delta_{sys} - \Delta_y\right)\right]$$

11. Calculations to determine equivalent viscous damping for the hinging subsystem of the bent:

a. Determine the total displacement of the subsystem (Δ_{ss2}):

If $\Delta_{sys} < \Delta_{ya}$

$$\Delta_{ss2} = \left(\Delta_{y2a} \cdot F_b\right) / \left(0.5 \cdot F_{bc}\right)$$

Else if $\Delta_{sys} > \Delta_y$

$$\Delta_{ss2} = \Delta_{y2} + \left(\Delta_{sys} - \Delta_y\right) \cdot \frac{H_2}{H_1 + H_2}$$

Otherwise

$$\Delta_{ss2} = \Delta_{y2a} + \left(\Delta_{y2} - \Delta_{y2a}\right) \cdot \frac{F_b - 0.5 \cdot F_{bc}}{0.5 \cdot F_{bc}}$$

b. Determine the displacement ductility ($\mu_{\Delta 2}$):

$$\mu_{\Delta 2} = \Delta_{ss2} / \Delta_{y2}$$

c. Calculate the equivalent viscous damping of the subsystem (ξ_{ss2}):

If $\mu_{\Delta 2} < 1$

$$\xi_{ss2} = 0.05$$

Otherwise

$$\xi_{ss2} = 0.05 + 0.444 \cdot \left(\mu_{\Delta 2} - 1\right) / \left(\mu_{\Delta 2} \cdot \pi\right)$$

12. Calculations to determine equivalent viscous damping for the rocking subsystem of the bent:

Table 6.2 (Continued)

a. Determine the total displacement of the subsystem (Δ_{ss1}):

If $\Delta_{sys} < \Delta_{ya}$

$$\Delta_{ss1} = \left(\Delta_{y1a} \cdot F_b\right) / \left(0.5 \cdot F_{bc}\right)$$

Else if $\Delta_{sys} > \Delta_y$

$$\Delta_{ss1} = \Delta_{y1} + \left(\Delta_{sys} - \Delta_y\right) \cdot \frac{H_1}{H_1 + H_2}$$

Otherwise

$$\Delta_{ss1} = \Delta_{y1a} + \left(\Delta_{y1} - \Delta_{y1a}\right) \cdot \frac{F_b - 0.5 \cdot F_{bc}}{0.5 \cdot F_{bc}}$$

b. Determine the footing rotation (θ_f):

$$\theta_f = a\,sin\left[\frac{\Delta_{ss1} - \Delta_{c1} \cdot F_b / F_{bc}}{H_1}\right]$$

c. Compute the footing hysteretic damping ratio (ξ_{f_hys}), and the secant, at peak displacement, rotational stiffness (K_{f_pl}) and corresponding translational period (T_{f_pl}) of the rocking foundation that is associated to the footing hysteretic damping:

If $\theta_f \leq 0.5 \cdot h_f$ ($h_f = 1/300$ radians)

$$\xi_{f\_hys} = 0 \text{, and } T_{f\_pl} = 0$$

Else if $\theta_f \geq b_f$ ($b_f = 0.012$ radians)

$$\xi_{f\_hys} = \frac{0.90}{2\pi}\left(4 - \frac{3}{2.6 \cdot \rho_{ac} + 1} - \frac{b_f}{\theta_f}\right) \text{, or } \xi_{f\_hys} = \frac{0.30}{2\pi}\left(4 - \frac{3}{2.6 \cdot \rho_{ac} + 1} - \frac{b_f}{\theta_f}\right)$$

$$K_{f\_pl} = M_{fc} / \left(\theta_f - h_f\right) \text{, and } T_{f\_pl} = 2\pi\sqrt{\frac{W_s / g}{K_{f\_pl} / H_1^2}}$$

Otherwise

$$\xi_{f\_hys} = \frac{0.90}{2\pi}\left(4 - \frac{3}{2.6 \cdot \rho_{ac} + 1} - 1\right) \cdot \left(\frac{\theta_f - 0.5 \cdot h_f}{b_f - 0.5 \cdot h_f}\right) \text{, or}$$

$$\xi_{f\_hys} = \frac{0.30}{2\pi}\left(4 - \frac{3}{2.6 \cdot \rho_{ac} + 1} - 1\right) \cdot \left(\frac{\theta_f - 0.5 \cdot h_f}{b_f - 0.5 \cdot h_f}\right)$$

$$K_{f\_pl} = F_b \cdot H_1 / \left(\theta_f - F_b \cdot H_1 / K_{f\_50}\right) \text{, and } T_{f\_pl} = 2\pi\sqrt{\frac{W_s / g}{K_{f\_pl} / H_1^2}}$$

Note that the use of the first or the second ξ_{f_hys} expression is discussed in Section 4.7.

d. Calculate the subsystem's effective period (T_{ss1}) and equivalent viscous damping (ξ_{ss1}):

$$T_{ss1} = \sqrt{T_{c1}^{\ 2} + T_{f\_50}^{\ 2} + T_{f\_pl}^{\ 2}}$$

$$\xi_{ss1} = \left(\frac{T_{c1}}{T_{ss1}}\right)^2 \xi_{c1} + \left(\frac{T_{f\_50}}{T_{ss1}}\right)^2 \xi_{rad} + \left(\frac{T_{f\_pl}}{T_{ss1}}\right)^2 \xi_{f\_hys}$$

Table 6.2 (Continued)

where ξ_{c1} is the column "elastic" damping, and ξ_{rad} is the radiation damping of the footing rocking mode. Column "elastic" damping can be taken as 2% as the column is designed to remain nominally elastic, while radiation damping can be assumed as approximately equal to 3% if not addressed explicitly; e.g. using the FEMA 440 document [ATC 2005].

e. Determine the equivalent viscous damping (ξ_b) at the bent-level:

$$\xi_b = \frac{\xi_{ss1} \cdot \Delta_{ss1} + \xi_{ss2} \cdot \Delta_{ss2}}{\Delta_{sys}}$$

Equivalent viscous damping at the abutments

13. For the abutments' passive pressure seismic resisting mechanism, compute the displacement ductility demand (μ_Δ), the resisting lateral force (F_{ab_p}), and the equivalent viscous damping (ξ_{ab_p}):

$$\mu_\Delta = \Delta_{sys} / \Delta_y$$

If $\mu_\Delta < 1$

$$F_{ab\_p} = K_{ab\_p} \cdot \Delta_{sys}$$

$$\xi_{ab\_p} = \xi_{ab\_p\_el}$$

Otherwise

$$F_{ab\_p} = F_{ab\_pc}$$

$$\xi_{ab\_p} = 0.5 \left[\mu_\Delta^{0.127} \cdot \xi_{ab\_p\_el} + 0.224 \cdot \left(1 - \frac{1}{\mu_\Delta^{0.336}} \right) \right]$$

where $\xi_{ab\_p\_el}$ is the "elastic" damping that can be taken as approximately equal to 2%. Note that the ξ_{ab_p} is obtained from an elastic-perfectly-plastic hysteresis rule, corrected by the 0.5 factor to account for the fact that during a full cycle the abutment passive resistance will dissipate energy in the first and third quadrant.

14. For the abutments' frictional seismic resisting mechanism, compute the displacement ductility demand (μ_Δ), the resisting lateral force (F_{ab_f}), and the equivalent viscous damping (ξ_{ab_f}):

$$\mu_\Delta = \Delta_{sys} / \Delta_y$$

If $\mu_\Delta < 1$

$$F_{ab\_f} = F_{ab\_fc} \cdot \Delta_{sys} / \Delta_y$$

$$\xi_{ab\_f} = \xi_{ab\_f\_el}$$

Otherwise

$$F_{ab\_f} = F_{ab\_fc}$$

$$\xi_{ab\_f} = \mu_\Delta^{0.127} \cdot \xi_{ab\_f\_el} + 0.224 \cdot \left(1 - \frac{1}{\mu_\Delta^{0.336}} \right)$$

where $\xi_{ab\_f\_el}$ is the elastic damping that can be taken as 2%.

Table 6.2 (Continued)

Integration to the bridge-level

15. Calculate the secant stiffness (K_{sys}) and period (T_{sys}) of the bridge:

$$K_{sys} = \frac{F_{ab\_p} + \sum\limits_{i=1,\,n} F_{ab\_f} + \sum\limits_{i=2 \ldots n-1} F_b}{\Delta_{sys}}$$

$$T_{sys} = 2\pi \sqrt{\frac{\sum\limits_{i=1 \ldots n} W_s \big/ g}{K_{sys}}}$$

16. Calculate the equivalent viscous damping ratio of the bridge (ξ_{sys}):

$$\xi_{sys} = \frac{F_{ab\_p} \cdot \xi_{ab\_p} + \sum\limits_{i=1,\,n} F_{ab\_f} \cdot \xi_{ab\_f} + \sum\limits_{i=2 \ldots n-1} F_b \cdot \xi_b}{F_{ab\_p} + \sum\limits_{i=1,\,n} F_{ab\_f} + \sum\limits_{i=2 \ldots n-1} F_b}$$

17. Compute the new lateral displacement of the bridge (Δ_{sys}):

$$\Delta_{sys} = \left(\frac{0.07}{0.02 + \xi_{sys}} \right)^{\alpha} \cdot Sd\left(T_{sys}, 0.05\right).$$

where $\alpha = 0.5$ for a site at which the elastic design spectrum (Sd) is dominated by broadband motions, or $\alpha = 0.25$ for the case of near-fault pulse-like motions.

18. Check for convergence:

a. If new Δ_{sys} is no more than 2% different from the input displacement used in step 9 end iterations.

b. Else use Δ_{sys} as input value and repeat steps 9 to 18.

19. Estimate at each bent the column hinges' plastic rotation (θ_{c_pl}) and check if P-Δ instability ratio ($\theta_{P\text{-}\Delta}$) exceeds the allowable limit:

$$\theta_{c\_pl} = \left\langle \Delta_{ss2} - \Delta_{y2} \right\rangle \big/ H_2 , \text{ and } \theta_{P-\Delta} = \frac{W_s \cdot \Delta_{sys}}{F_b \left(H_c + H_f \right)} \le \frac{0.2 \cdot M_{cN\_t} + 0.3 \cdot M_{fc}}{M_{fc} + M_{cN\_t}}$$

where < > set negative values to zero, i.e., $\langle x \rangle = x$ if $x \ge 0$, otherwise $\langle x \rangle = 0$.

7 System Level Design and Validation based on Two Bridges Case Studies

Two existing bridges of Caltrans are hypothetically re-designed, for a site in San Bernardino, California of very high seismic hazard (1.6 ft/s slope of the design displacement spectrum up to a period of 5 seconds), using columns with rocking shallow foundations at the base and moment resistant connections between the columns and the deck. The designs aim at limited post-earthquake structural damage and residual deformations and thus to prompt post-earthquake functionality. Three-dimensional nonlinear response history analyses (NRHA) of the two bridges using a suite of 14 ground motions are performed to validate the design concepts as well as the displacement-based analysis method of Chapter 6.

7.1 DESCRIPTION OF SELECTED REAL BRIDGES

The first bridge, referred to herein as Mono Way Bridge, is shown in plan, elevation and typical section view in Figure 7.1. It has four spans of similar length and a total length of 744 ft. The weight of the superstructure is 13,444 kip, while the weight of the columns is 4,634 kip. Horizontal curvature of the bridge and abutment skewness is small. The pre-stressed box girder deck has a width of 46.83 ft, and depth of 8.75 ft. It is supported on three single-column bents of increasing column height varying from 75.1 ft near the left abutment to 110.2 ft near the right abutment. The columns are octagonal in shape with dimensions of 8 ft and 12 ft in the longitudinal and transverse directions, respectively; their longitudinal reinforcement ratio is 1%. The concrete has nominal unconfined compressive strength of 3.6 ksi, while the reinforcing steel has nominal yield strength of 60 ksi. The bridge is supported on shallow foundations with plan dimensions of 25 ft and 30 ft in the longitudinal and transverse directions, respectively. Tie down anchors near the edges of the footings are used to prevent uplift. The abutments of the bridge are seat-type abutments with 2.5 in. expansion joints and three spherical PTFE bearings placed between the soffit of the deck and the abutment stem. Two exterior sacrificial shear keys are placed at each abutment. Hence, the capacity of the Mono Way Bridge abutments is relatively small in the longitudinal and the transverse directions.

The second bridge, referred to herein as Murray Ridge Bridge, is shown in plan, elevation and typical section view in Figure 7.2. It has four spans of different length and a total length of 350 ft. The weight of the superstructure is 10,673 kip, while the mass of the columns is 2,110 kip. In-plan curvature of the bridge is small while the abutments and bents are 16.9 degrees askew. The post-tensioned box girder deck has a width of 80 ft, depth of 6 ft and 10 girders in total. It is supported on three "Y-shaped" columns of clear height varying from 46.9 ft to 60.7 ft. The base section of the columns is rectangular with dimensions of 6 ft and 18 ft in the local longitudinal and transverse direction, respectively, and has a longitudinal reinforcement ratio of 0.7%. The concrete has nominal unconfined compressive strength of 1.2 ksi, while the reinforcing steel has nominal yield strength of 20 ksi. The bridge is supported on shallow foundations with plan dimensions of 16 ft and 34 ft in the local longitudinal and transverse directions, respectively. Integral diaphragm-type abutments are used at the ends of the bridge with a height of 12 ft at the middle of the deck and 7% out-of-plane slope. The abutments' diaphragms are simply supported on shallow spread footings with a continuous shear key along the local transverse direction. Hence, Murray Ridge Bridge has relatively strong abutments, particularly in the longitudinal direction. It is also noted that the bridge has been retrofitted by means of column casing and footings enlargement.

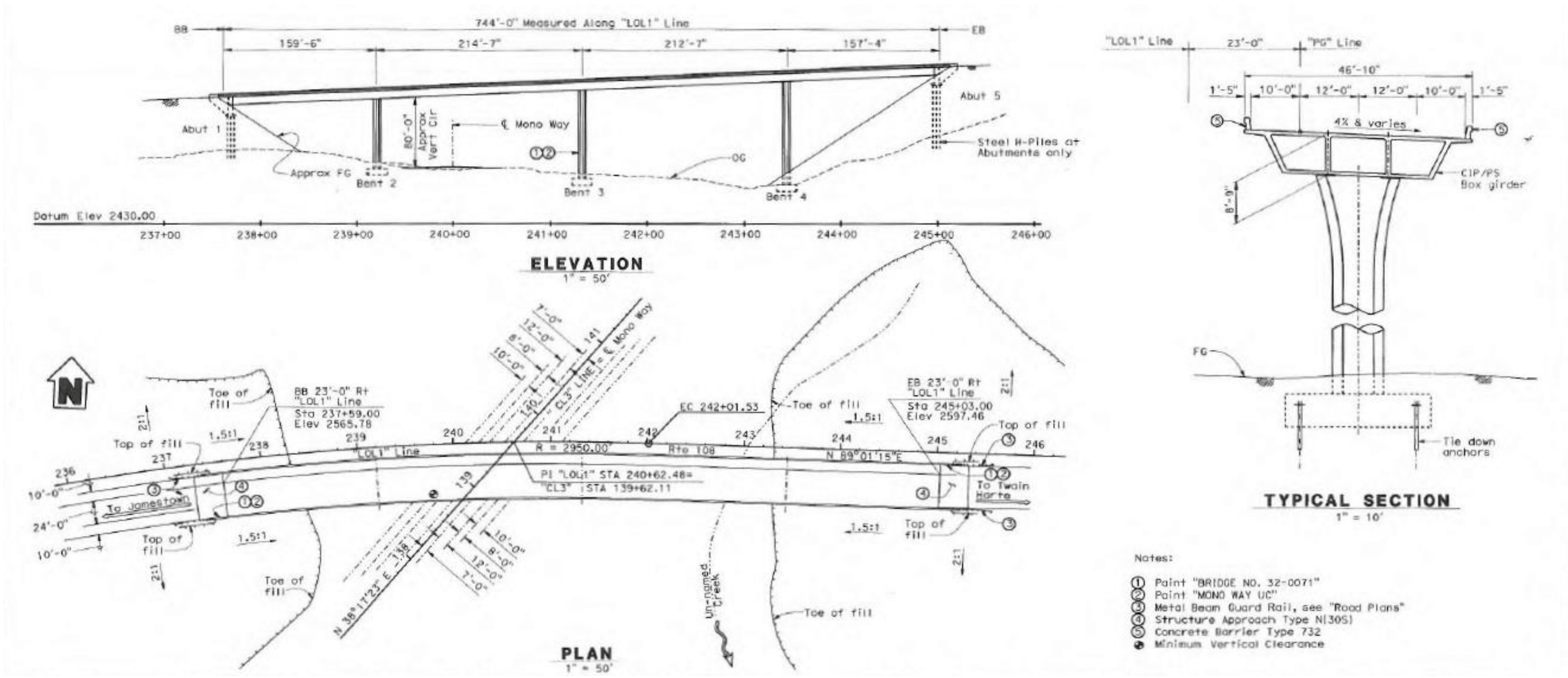

Notes:

① Paint "BRIDGE NO. 32-0071"
② Paint "MONO WAY UC"
③ Metal Beam Guard Rail, see "Road Plans"
④ Structure Approach Type N(30S)
⑤ Concrete Barrier Type 732
● Minimum Vertical Clearance

Figure 7.1 Plan, elevation and typical section view of the Mono Way Bridge [Caltran's drawings].

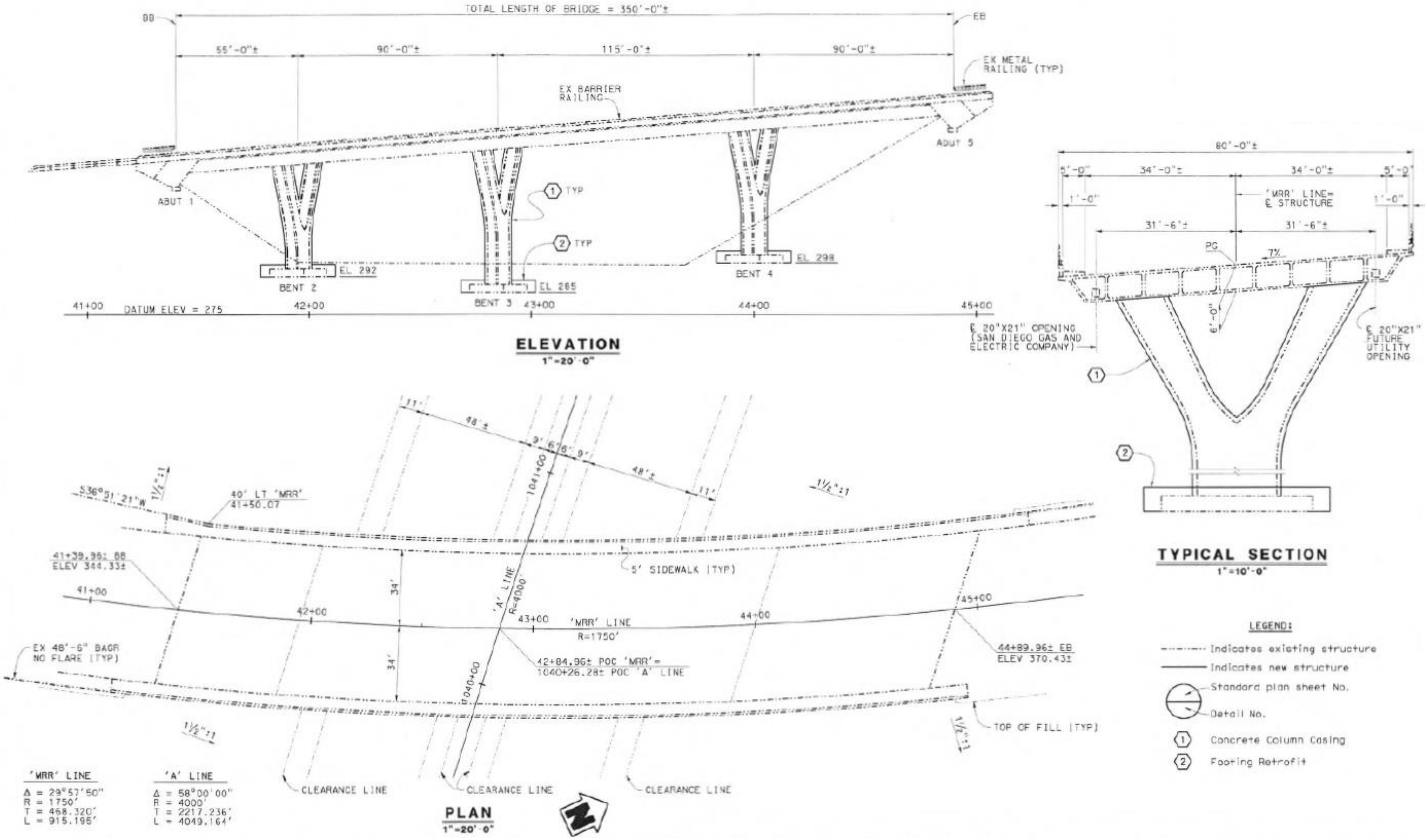

Figure 7.2 Plan, elevation and typical section view of the Murray Ridge Bridge [Caltran's drawings].

7.2 SEISMIC HAZARD DESCRIPTION

The two considered bridges have been hypothetically redesigned with rocking shallow foundations at the base of the columns for a site located at a latitude of 34.2367 and longitude of 117.425, approximately 1.5 km from the San Andreas Fault, North-West of San Bernardino, CA, with V_{s30} = 400 m/s. The 5% damped displacement spectrum for the design earthquake (DE) that has a 5% probability of exceedance in 50 years is shown in Figure 7.3. Figure 7.3 also shows that the hypothetical redesign DE spectrum is much stronger (by a factor of 5 to 9) than the DE spectra used for the design of the real conventionally designed bridges. The actual DE displacement spectrum for the Mono Way Bridge was obtained from the bridge drawings and that for the Murray Ridge Bridge site was obtained from Caltrans online ARS tool [Caltrans 2013b].

A set of 14 ground motions were used for the Nonlinear Response History Analysis (NRHA) of the two redesigned bridges. For each of the motions, both the fault-normal (FN) and fault-parallel (FP) horizontal components were used in the NRHA. The motions were scaled in amplitude such that the mean linear spectra of the fault-normal components at 5% damping match the target DE spectrum. Table 7.1 summarizes the set of the 14 ground motions used, along with the amplitude scale factor used to match the DE target spectrum. It is noted that out of the 14 ground motions, 3 motions are included in the broadband set used in Chapter 4, while 10 motions are included in the corresponding near-fault pulse-like set. Figure 7.4 plots the linear acceleration and displacement spectra of the fault-normal and fault parallel components of the 14 motions, scaled to the DE target spectrum. Figure 7.5 compares the mean linear acceleration and displacement spectra of the fault-normal and fault-parallel components of the 14 ground motions, scaled to the DE seismic hazard level, to the target DE spectrum.

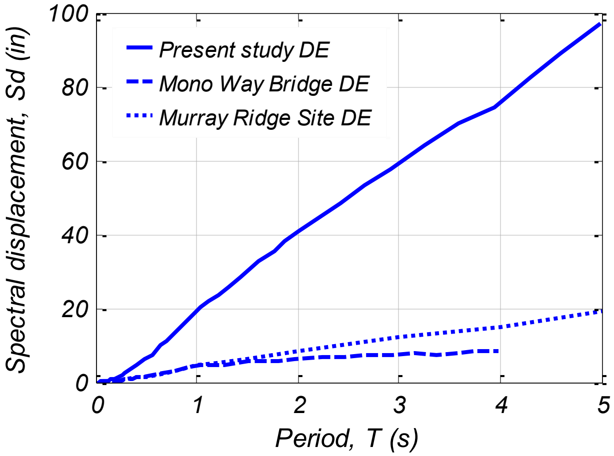

Figure 7.3 Linear displacement spectrum (ξ = 5%) used in the present study at the DE seismic hazard level, and corresponding DE spectra of the Mono Way Bridge (Caltrans' drawings) and of the Murray Ridge Bridge site (Caltrans online ARS tool).

Table 7.1 Set of ground motions used in the numerical analyses of the two bridges.

No.	Earthquake Location	Year	M_w	Station Name	R_{rup} (km)	Motion Characterization	Scale Factor to DE Level
1	Loma Prieta, CA	1989	6.9	LGPC	3.9	Pulse-like	2.58
2	Northridge, CA	1994	6.7	Jensen Filter Plant.	5.4	Broadband	3.00
3	Coalinga, CA	1983	6.4	Pleasant Valley P.P. – Yard	8.4	Pulse-like	3.00
4	San Fernando, CA	1971	6.6	Pacoima Dam	1.8	Pulse-like	1.60
5	Chi-Chi, Taiwan	1999	7.6	TCU068	0.3	Pulse-like	1.22
6	Cape Mendocino, CA	1992	7.0	Cape Mendocino	7.0	Pulse-like	2.54
7	Duzce, Turkey	1999	7.1	Duzce	6.6	Pulse-like	0.80
8	Tabas, Iran	1978	7.4	Tabas	2.1	Pulse-like	0.80
9	Christchurch, NZ	2011	6.3	PRPC	2.5	Pulse-like	3.00
10	Chi-Chi, Taiwan	1999	7.6	TCU074	13.5	--	2.92
11	Chi-Chi, Taiwan	1999	7.6	TCU102	1.5	Pulse-like	3.00
12	Landers, CA	1992	7.3	Lucerne	2.2	Pulse-like	2.23
13	Kocaeli, Turkey	1999	7.5	Yarimca	4.8	Broadband	2.72
14	Imperial Valley, CA	1979	6.5	El Centro Array #4	7.1	Broadband	2.40

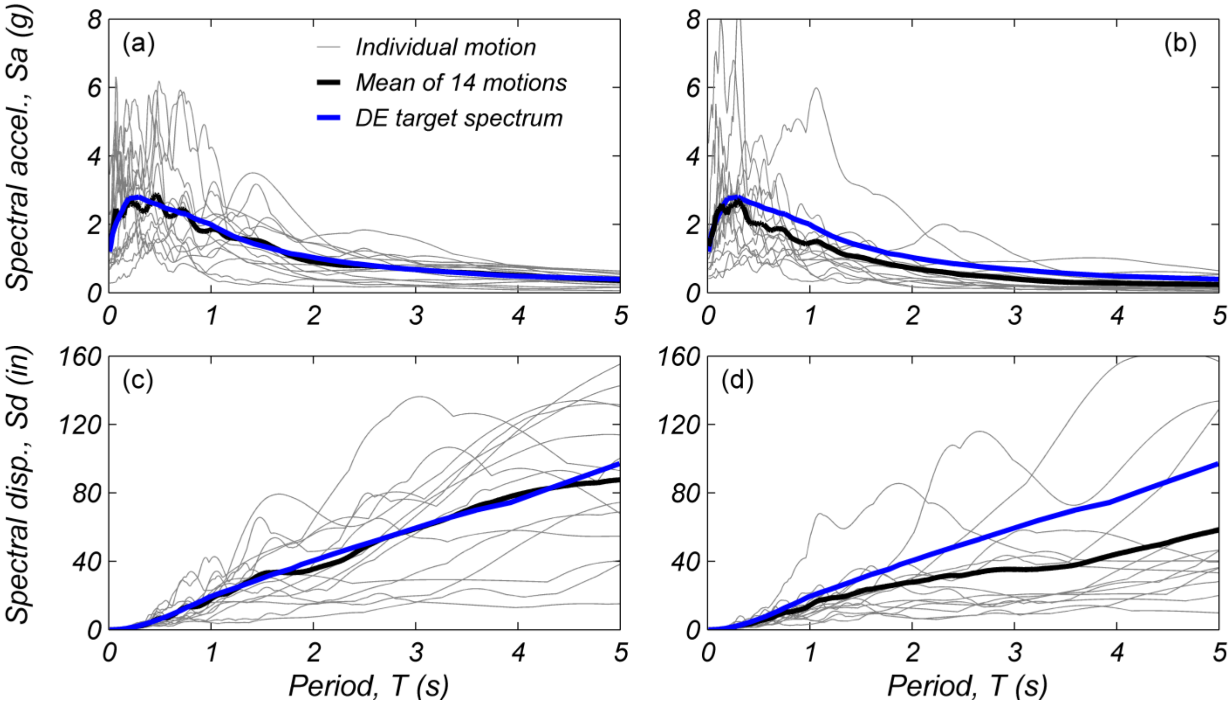

Figure 7.4 Linear acceleration and displacement spectra for 5% damping for the (a, c) fault-normal and (b, d) fault-parallel components of the 14 ground motions, with the fault-normal components scaled at the DE target spectrum.

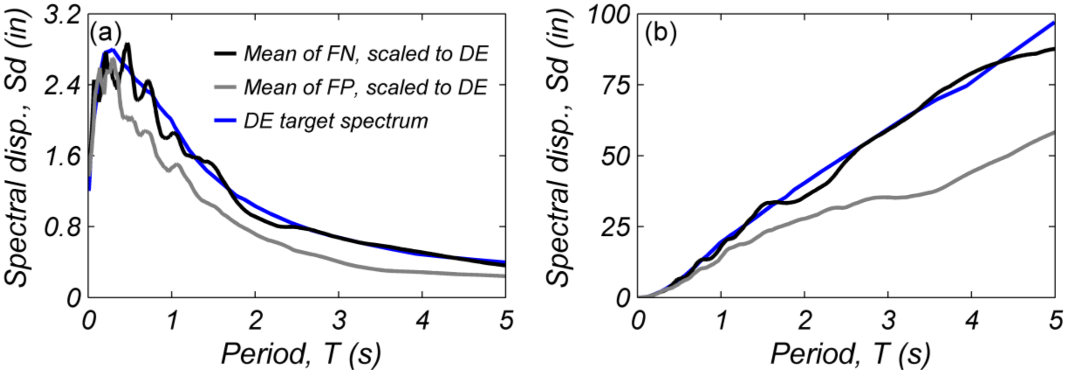

Figure 7.5 (a) Linear acceleration and (b) displacement spectra for the DE seismic hazard level, compared to the mean spectra at 5% damping ratio of the fault-normal and fault-parallel components of the 14 ground motions scaled to the DE hazard level.

7.3 DISPLACEMENT-BASED SEISMIC DESIGN

7.3.1 Design Objectives

The design objectives for the two re-designed bridges, with columns on rocking shallow foundations and moment-resistant connections with the deck, at the design level earthquake (DE) with 5% probability of exceedance in 50 years, were aiming at prompt post-earthquake functionality of the bridge and limited structural and foundation damage as well as limited residual displacements. More specifically, they were as follows:

(1) The peak drift ratio demand for the mean DE ground motion was required to be less than 6% to avoid damage due to kinematics.

(2) The residual drift ratio for the mean DE ground motion was required to be less than 1%.

(3) The tensile strain in the columns for the mean DE ground motion was required to be less than 3% on the assumption that such strains would facilitate repair of the plastic hinge regions of the columns after a DE event.

(4) Elastic response of the post-tensioned strands of the deck.

For systems responding with plastic hinging, Caltrans currently limits the allowable P-Δ moment to 20% of the idealized plastic moment capacity of the hinge [Caltrans 2013a]. In recognition of the improved overturning stability of rocking foundations [Deng et al. 2012b], the allowable instability ratio is increased to 0.3 in the transverse direction (see Chapter 4), while a weighted average between 0.2 and 0.3 is used in the longitudinal direction depending on the relative contribution of the plastic hinge at the top of the column and of the rocking foundation to the strength of the considered bent (see Chapter 5).

7.3.2 Redesign of Bridges with Rocking Shallow Foundations

Design assumptions

The two bridges are redesigned with rocking shallow foundations for the DE seismic hazard level considering the following two scenarios: (i) the FN component is applied in the transverse direction; and (ii) the FN component is applied in the longitudinal direction. In each of these two cases, the effect of biaxial loading due to the fault-parallel components is neglected.

As noted in Chapters 2 and 4 – 6, the design linear displacement spectrum at 5% damping would be adjusted at different damping levels through the displacement reduction factor, R_D, with different values of the power α depending on the characteristics of the ground motions expected to dominate the design spectrum. Despite that, the displacement-based analysis of the bridges in the present study is conducted by re-computing the mean linear displacement spectrum of the 14 fault-normal ground motions at different damping ratio values. This approach is followed for the following reasons: (i) it ensures a consistent comparison between the predicted and numerically computed displacement demands; (ii) the set of 14 motions used in the present study is a mix of pulse-like and broadband motions; (iii) it was found that a single value of the power α could not adequately represent the mean linear displacement spectrum of the selected 14 fault-normal motions across the whole range of periods of interest; and (iv) evaluation of the appropriate displacement reduction factor due to increased damping (R_D) is not within the scope of this study.

Lastly, two expressions have been discussed in Chapter 4 for the equivalent viscous damping of a rocking shallow foundation. The first expression is the Deng et al. [2014] area-based hysteretic damping equation multiplied by the 0.45 area-based correction factor of Eqn. (4.1). The second expression, Eqn. (4.4), is purely based on the BNWF models and yields 33% smaller damping compared to the first expression, consistent with findings from Chapter 3. Among the two, the first one is the main expression proposed to be used in design, while the second one may be used as a conservative lower bound estimate of equivalent viscous damping in cases with explicit prevention of sand falling mechanism. Nevertheless, Eqn. (4.4) is representative of the expected damping in the numerical model of the bridges. Thus, Eqn. (4.4) has also been used in the displacement-based analysis of the bridges to ensure consistent comparison with the NRHA results.

Material properties

The redesign of the two bridges with rocking shallow foundations is based on the following properties for the soil, concrete, and reinforcing steel. The foundation soil for both bridges is assumed to be a clean dry sand with constant volume friction angle φ_{cv} = 30°, minimum and maximum void ratios e_{min} = 0.478 and e_{max} = 0.818, respectively, relative density D_R = 90%, dry unit weight γ_d = 110 pcf and Poisson's ratio ν = 0.33. The concrete for the Mono Way Bridge and the Murray Ridge Bridge (in parenthesis) has an expected unconfined compressive strength f_{ce}' = 6 (5.2) ksi and an expected confined compressive strength f_{cc}' = 8 (7.2) ksi. For both bridges, the reinforcing steel has been considered to have an expected yield strength f_{ye} = 68 ksi and 1% hardening ratio.

Design for excitation in the transverse direction

Table 7.2 summarizes the geometry and sizing of the redesigned bridges: the footing dimension in the local transverse (B_f) and longitudinal direction (L_f), the footing height (H_f) and embedment (D_f), the column base dimension in the transverse (B_{cl}) and longitudinal direction (L_{cl}), the longitudinal reinforcement ratio (ρ_l) and the clear column height (H_c). It also shows the corresponding values of the built bridges if different from the redesigned. Note that apart from changes to the footing and column sizing for the redesigned bridges, square footings and circular columns have been used in the Mono Way Bridge, while the column height of bent 2 for the Murray Ridge Bridge has been increased by 6 ft. These changes were dictated by the more than five times greater seismic hazard used here compared with that of the as-built bridges.

Table 7.3 provides a summary of key design characteristics of the redesigned bridges for response in the transverse direction. The critical contact area ratio (ρ_{ac}) for all rocking foundations in the transverse direction is less than 0.125 to ensure limited soil inelasticity due to rocking. The acceleration coefficient at the deck centroid that would mobilize the footings' moment capacity (C_N) is in the 0.2 – 0.3 range for all bents at both bridges. The corresponding C_N at the bridge level has a peak value of 0.26 and 0.57 for the Mono Way Bridge and Murray Ridge Bridge, respectively, while C_N drops to a residual value of 0.2 and 0.42 for large drifts that exceed the displacement capacity of the exterior shear keys of the Mono Way Bridge and of the wing walls for the Murray Ridge Bridge, respectively. The percentage contribution of the sliding resisting mechanisms at the abutments to the overall residual lateral strength of the bridge (assumes complete damage of the shear keys and wing walls) is 9.8% and 24.2% for the Mono Way and Murray Ridge bridges, respectively. This parameter is of particular importance for the prediction of drift demand in the transverse direction, as it is associated with a high energy dissipation that is neglected in the procedure outlined in Table 6.1. The normalized moment-to-shear ratio of the foundations [$M_{fc}/(F_c \times B_f)$] is larger than 1, indicating a rocking dominated response and small sliding. Nominally elastic response at the base of the columns is also satisfied as the yield moment of the columns in the transverse direction exceeds the foundation moment capacity by approximately 25% for the Mono Way Bridge and 130% for the Murray Ridge Bridge. Lastly, the end column of Table 7.3 provides the abutment strength correction (C_a), as determined by Eqn. (6.1). For each bridge two values are provided; the lower bound value neglects strength contribution from resisting mechanisms with small to moderate ductility (i.e. shear keys or wing walls), while the upper bound value includes such mechanisms. For the Mono Way Bridge C_a is found to be between 0.89 and 1.15, while for the Murray Ridge Bridge C_a = 1.23 – 1.60.

Table 7.4 summarizes the displacement-based analysis results of the redesigned bridges in the transverse direction, based on the procedure outlined in Table 6.1, for a mass participation factor $C_m = 0.7$. The predicted transverse drift ratio demand of the Mono Way Bridge is between 5.8% and 7.4%, while for the Murray Ridge Bridge it is between 6.2% and 7.3%. A maximum instability ratio $\theta_{P\text{-}\Delta} = 0.32$ is predicted at bent 2 of Murray Ridge Bridge. This value is close enough to the suggested limit value of 0.3 and it is considered acceptable. It is also worth noting the small equivalent viscous damping ratio of the bents (ξ_{sys}) having an average value of 5% for the Mono Way Bridge where the critical contact area ratio (ρ_{ac}) is in the order of 0.05, and a value of 6.5% for the Murray Ridge Bridge where $\rho_{ac} \approx 0.1$. These values are substantially smaller than the 15 – 25% damping expected for abutments that deform by frictional sliding.

Table 7.2 Geometry/sizing and column longitudinal reinforcement ratio of the two bridges.

Bridge	Bent	B_f (ft)	L_f (ft)	H_f (ft)	D_f (ft)	B_{cl} (ft)	L_{cl} (ft)	ρ_l (%)	H_c (ft)
Mono Way	2	33 (30)[*]	33 (25)	6	13.4	12 dia. (12×8)		2.5 (1.5)	75.3
	3	33 (30)	33 (25)	6	13.4	12 dia. (12×8)		2.5 (1.5)	93.3
	4	33 (30)	33 (25)	6	19.4	12 dia. (12×8)		2.5 (1.5)	110.0
Murray Ridge	2	25 (34)	14 (16)	3.5	12.9 (6.9)	18	5	1.8 (0.7)	52.9 (46.9)
	3	25 (34)	14 (16)	3.5	12.8	18	5	1.8 (0.7)	60.7
	4	25 (34)	14 (16)	3.5	16.9	18	5	1.8 (0.7)	56.2

[*] In parenthesis values are the as-built values of the two bridges if different from the redesigned.

Table 7.3 Design summary for excitation in the transverse direction.

Bridge	Location	H (ft)	W_d (kip)	W_c (kip)	W_s (kip)	W_{c_b} (kip)	W_{f_b} (kip)	ρ_{ac}	M_{fc} (kip-ft)	F_c (kip)	F_c / F_{c_bridge} (%)	C_N[1]	$M_{fc} / (F_c \cdot B_f)$	M_{cy_b} / M_{fc}	C_a
Mono Way	A1	--	1500	--	1500	--	--	--	--	150[2] (600[3])	4.9[2] (15.1[3])	0.1[2] (0.4[3])	--	--	0.89[2] (1.15[3])
	B2	86.7	3454	1303	3888	4757	5281	0.041	88670	1023	33.4[2] (25.8[3])	0.26	2.6	1.29	
	B3	104.7	3831	1615	4369	5446	5940	0.046	98670	943	30.8[3] (23.8[4])	0.22	3.2	1.22	
	B4	122.0	3274	1914	3912	5188	5586	0.033	97570	800	26.1[2] (20.2[3])	0.20	3.7	1.22	
	A5	--	1500	--	1500	--	--	--	--	150[2] (600[3])	4.9[2] (15.1[3])	0.1[2] (0.4[3])	--	--	
	Bridge	--	13559	4832	15170	--	--	--	--	3066[2] (3966[3])	--	0.2[2] (0.26[3])	--	--	
Murray Ridge	A1	--	957	--	957	--	--	--	--	479[4] (1007[5])	9.4[4] (14.7[5])	0.5[4] (1.05[5])	--	--	1.23[4] (1.60[5])
	B2	59.7	2159	681	2386	2840	3291	0.080	38680	648	12.7[4] (9.5[5])	0.27	2.4	2.67	
	B3	67.4	3299	784	3560	4083	4530	0.113	51070	758	14.9[3] (11.1[4])	0.21	2.7	2.25	
	B4	62.9	3327	725	3569	4052	4618	0.093	53500	850	16.7[4] (12.4[5])	0.24	2.5	2.06	
	A5	--	1501	--	1501	--	--	--	--	751[4] (1279[5])	14.8[4] (18.7[5])	0.5[4] (0.85[5])	--	--	
	Bridge	--	11243	2190	11973	--	--	--	--	5081[4] (6857[5])	--	0.42[4] (0.57[5])	--	--	

[1] Defined as the lateral force capacity (F_c) normalized by the corresponding seismic weight (W_s); [2] Due to PTFE bearings ($\mu = 0.1$); [3] Due to PTFE bearings and one exterior shear key; [4] Due to diaphragm-spread footing sliding ($\mu = 0.5$); [5] Due to diaphragm-spread footing sliding and the two wing walls.

Table 7.4 Summary of the displacement-based analysis for excitation in the transverse direction for C_m = 0.7, and C_a the upper-bound value of Table 7.3.

	Mono Way Bridge			Murray Ridge Bridge		
Parameter[1]	Bent 2	Bent 3	Bent 4	Bent 2	Bent 3	Bent 4
H (ft)	86.7	104.7	122.0	59.7	67.4	62.9
W_s (kip)	3888	4369	3912	2386	3560	3569
ρ_{ac}	0.041	0.046	0.033	0.080	0.113	0.093
M_{fc} (kip-ft)	88670	98670	97570	38680	51070	53500
F_c (kip)	1023	943	800	648	758	850
K_c (kip/in)	318	175	111	1181	754	966
Δ_c (in)	3.2	5.4	7.2	0.5	1.0	0.9
T_c (s)	0.82	1.17	1.36	0.28	0.43	0.39
K_{f_50} (kip-ft/rad × 10^3)	26601	29601	29271	11604	15321	16050
T_{f_50} (s)	0.85	1.03	1.12	0.59	0.71	0.65
Δ_{y1} (in)	3.3	4.8	6.0	1.5	1.9	1.7
Δ_{y2} (in)	15.7	20.5	24.8	9.1	10.7	9.9
Δ_{sys_input} (in)	76.1	81.5	84.3	43.4	57.8	53.3
F (kip)	1023	942	800	648	758	851
d_f (rad)	0.070	0.061	0.053	0.060	0.070	0.069
K_{f_pl} (kip-ft/rad × 10^3)	1328	1722	1976	684	762	809
T_{f_pl} (s)	3.82	4.27	4.30	2.41	3.19	2.90
ξ_{f_pl} (%)	5.4	5.4	4.8	6.3	7.2	6.7
T_{sys} (s)	4.00	4.55	4.64	2.50	3.30	3.00
ξ_{sys} (%)	5.1	5.0	4.5	6.0	6.9	6.5
Δ_{sys_output} (in)	76.7	82.4	84.7	44.1	58.8	54.1
Θ (%)	7.4	6.6	5.8	6.2	7.3	7.2
$\theta_{P\text{-}\Delta}$	0.25	0.27	0.24	0.21	0.32	0.28

[1] Symbols defined in Table 6.1.

Design for excitation in the longitudinal direction

Table 7.5 provides the design summary of the redesigned bridges for response in the longitudinal direction. The acceleration coefficient at the deck centroid that would mobilize the longitudinal force capacity of the bridges (C_N) is 0.64 for the Mono Way Bridge and 1.18 for the Murray Ridge Bridge. The abutment passive, abutment sliding and bents' foundation rocking and column top plastic hinging contributions to the total strength of the Mono Way Bridge are 16%, 3% and 81%, respectively; hence, most of the longitudinal strength of the bridge is provided from the bents. For the Mono Way Bridge, the corresponding contributions are 65%, 9% and 26%; thus, it is the abutment passive resistance that contributes the most to the longitudinal strength of the bridge.

The critical contact area ratio (ρ_{ac}) for all rocking foundations in the longitudinal direction is less than 0.125. The normalized moment-to-shear ratio of the foundations [$M_{fc}/(F_c \times L_f)$] is roughly larger than 1, indicating a rocking dominated response and small sliding. Nominally elastic response at the base of the columns is also satisfied, as the yield moment of the columns' base in the longitudinal direction exceeds the corresponding foundation moment capacity by approximately 25% for the Mono Way Bridge and 30% for the Murray Ridge Bridge. Lastly, the ratio between the nominal moment capacity at the top of the columns and the foundation moment capacity is in the 1.6 – 1.8 range for the Mono Way Bridge, and in the 1.5 – 2 range for the Murray Ridge Bridge.

Tables 7.6 and 7.7 summarize the displacement-based analysis of the Mono Way Bridge and the Murray Ridge Bridge, respectively, in the longitudinal direction, based on the procedure outlined in Table 6.2 for $C_m = 1$.

The predicted longitudinal drift ratio demand at the bents of the Mono Way Bridge [and the Murray Ridge Bridge] is between 2.4% [2.3%] and 3.5% [2.7%], while the plastic rotation at the top of the columns is in the 1.4 – 2.7% [1 – 1.4%] range satisfying the relevant design objective. Also, for both bridges the predicted instability ratio ($\theta_{P\text{-}\Delta}$) is within the allowable limits. For the Mono Way Bridge, the ξ_{eq} at the bents due to foundation rocking and due to column plastic hinging is approximately 4% and 14%, respectively, resulting in a bent-level ξ_{eq} in the order of 10%. At the abutments, ξ_{eq} is 7.5% due to the backfill passive resistance and 23.4% due to sliding at the PTFE bearings. Integration at the bridge level results to a ξ_{eq} of 10.6%. For the Murray Ridge Bridge similar observations can be made.

Table 7.5 Design summary for excitation in the longitudinal direction.

Bridge	Resisting Mechanism	Location	H (ft)	W_d (kip)	W_c (kip)	W_s (kip)	W_{c_b} (kip)	W_{f_b} (kip)	ρ_{ac}	M_{fc} (kip-ft)	M_{cN_t} (kip-ft)	F_c (kip)	F_c/F_{c_bridge} (%)	C_N[1]	M_{fc} / $(F_c \cdot L_f)$	M_{cy_b} / M_{fc}	M_{cN_t} / M_{fc}
Mono Way	Abut. Passive	A1 & A5 (ave.)	--	--	--	--	--	--	--	--	--	1543	15.9	0.10	--	--	--
	Abut. Sliding	A1	--	1500	--	1500	--	--	--	--	--	150	1.5	0.01	--	--	--
		A5	--	1500	--	1500	--	--	--	--	--	150	1.5	0.01	--	--	--
	Foundation Rocking & Column Top Plastic Hinging	B2	81.3	3454	1303	3888	4757	5281	0.047	88181	158853	3040	31.4	0.20	0.9	1.3	1.8
		B3	99.3	3831	1615	4369	5446	5940	0.050	98238	160253	2604	26.9	0.17	1.1	1.2	1.6
		B4	116.6	3274	1914	3912	5188	5586	0.035	97345	158180	2192	22.6	0.14	1.3	1.2	1.6
	Bridge	--	--	13559	4832	15170	--	--	--	--	--	9680	--	0.64	--	--	--
Murray Ridge	Abut. Passive	A1 & A5 (ave.)	--	--	--	--	--	--	--	--	--	9254	65.4	0.77	--	--	--
	Abut. Sliding	A1	--	957	--	957	--	--	--	--	--	479	3.4	0.04	--	--	--
		A5	--	1501	--	1501	--	--	--	--	--	751	5.3	0.06	--	--	--
	Foundation Rocking & Column Top Plastic Hinging	B2	56.4	2159	681	2386	2840	3291	0.086	22550	45321	1203	8.5	0.10	1.3	1.5	2.0
		B3	64.1	3299	784	3560	4083	4530	0.115	29530	45802	1174	8.3	0.10	1.8	1.2	1.6
		B4	59.7	3327	725	3569	4052	4618	0.098	31220	45731	1289	9.1	0.11	1.7	1.2	1.5
	Bridge	--	--	11243	2190	11973	--	--	--	--	--	14150	--	1.18	--	--	--

[1] Defined as the lateral force capacity (F_c) normalized by the total bridge seismic weight (W_s).

Table 7.6 Summary of the displacement-based analysis for excitation in the longitudinal direction of the Mono Way Bridge for C_m = 1.

Resisting Mechanism	Abut. Passive	Abut. Sliding		Rocking & Plastic Hinging		
Parameter[1] | Location	A1 & A5 (ave.)	A1	A5	B2	B3	B4
H (ft)	--	--	--	81.3	99.3	116.6
ρ_{ac}	--	--	--	0.047	0.050	0.035
M_{fc} (kip-ft)	--	--	--	88181	98238	97345
M_{cN_t} (kip-ft)	--	--	--	158853	160253	158180
H_1 (ft)	--	--	--	29.0	37.8	44.3
H_2 (ft)	--	--	--	52.2	61.6	72.0
L_{SP} (ft)	--	--	--	1.2	1.2	1.2
φ_{cy_t} (rad/in × 10^{-5})	--	--	--	3.6	3.6	3.6
Δ_{c1} (in)	--	--	--	0.4	0.9	1.3
Δ_{y1} (in)	--	--	--	4.6	6.3	7.7
Δ_{y2} (in)	--	--	--	4.9	6.8	9.2
Δ_y (in)	3.2[2]	0.1	0.1	9.5	13.1	17.0
F_c (kip)	1543	150	150	3040	2604	2192
T_{f_50} (s)	--	--	--	0.77	0.95	1.12
T_{c1} (s)	--	--	--	0.45	0.73	0.98
Δ_{sys_input} (in)	34.1					
F (kip)	1543	150	150	3040	2604	2192
Δ_{ss2} (in)	--	--	--	21.9	21.1	21.1
μ_Δ or $\mu_{\Delta 2}$	10.5	341	341	4.4	3.1	2.3
ξ_{ss2} (%)	--	--	--	16.0	14.6	12.9
Δ_{ss1} (in)	--	--	--	12.2	13.0	13.0
d_f (rad)	--	--	--	0.034	0.027	0.022
T_{f_pl} (s)	--	--	--	2.33	2.51	2.64
ξ_{f_pl} (%)	--	--	--	4.6	4.3	3.4
T_{ss1} (s)	--	--	--	2.49	2.78	3.03
ξ_{ss1} (%)	--	--	--	4.4	4.0	3.2
ξ_b or ξ_{ab_p} or ξ_{ab_f} (%)	7.5	23.4	23.4	11.8	10.5	9.2
W_s (kip)	15170					
K_{sys} (kip/in)	284					
T_{sys} (s)	2.34					
ξ_{sys} (%)	10.6					
Δ_{sys_output} (in)	34.3					
Θ (%)	--	--	--	3.5	2.9	2.4
θ_{c_pl} (%)	--	--	--	2.7	1.9	1.4
$\theta_{P\text{-}\Delta}$[3]	--	--	--	0.05	0.05	0.04
$\theta_{P\text{-}\Delta\_limit}$	--	--	--	0.24	0.24	0.24

[1] Symbols defined in Table 6.2; [2] Includes 2.5 in expansion joint; [3] Defined with respect to the tributary seismic weight (W_s) of each bent.

Table 7.7 Summary of the displacement-based analysis for excitation in the longitudinal direction of the Murray Ridge Bridge for $C_m = 1$.

Resisting Mechanism	Abut. Passive	Abut. Sliding		Rocking & Plastic Hinging		
Parameter[1] | Location	A1 & A5 (ave.)	A1	A5	B2	B3	B4
H (ft)	--	--	--	56.4	64.1	59.7
ρ_{ac}	--	--	--	0.086	0.115	0.098
M_{fc} (kip-ft)	--	--	--	22550	29530	31220
M_{cN_t} (kip-ft)	--	--	--	45321	45802	45731
H_1 (ft)	--	--	--	18.8	25.1	24.2
H_2 (ft)	--	--	--	37.7	39.0	35.5
L_{SP} (ft)	--	--	--	1.2	1.2	1.2
φ_{cy_t} (rad/in × 10^{-5})	--	--	--	8.1	8.1	8.1
Δ_{c1} (in)	--	--	--	0.4	1.0	1.0
Δ_{y1} (in)	--	--	--	3.1	4.6	4.5
Δ_{y2} (in)	--	--	--	5.8	6.2	5.2
Δ_y (in)	1.1	0.1	0.1	8.9	10.9	9.7
F_c (kip)	9254	479	751	1203	1174	1289
T_{f_50} (s)	--	--	--	0.87	1.02	0.96
T_{c1} (s)	--	--	--	0.61	1.02	0.96
Δ_{sys_input} (in)	18.0					
F (kip)	9254	479	751	1203	1174	1289
Δ_{ss2} (in)	--	--	--	12.0	10.9	10.7
μ_Δ or $\mu_{\Delta 2}$	16.4	180	180	2.1	1.8	2.1
ξ_{ss2} (%)	--	--	--	12.3	11.1	12.3
Δ_{ss1} (in)	--	--	--	6.0	7.1	7.3
d_f (rad)	--	--	--	0.025	0.020	0.022
T_{f_pl} (s)	--	--	--	2.23	2.29	2.26
ξ_{f_pl} (%)	--	--	--	5.1	5.2	5.1
T_{ss1} (s)	--	--	--	2.47	2.71	2.63
ξ_{ss1} (%)	--	--	--	4.6	4.4	4.4
ξ_b or ξ_{ab_p} or ξ_{ab_f} (%)	8.2	22.4	22.4	9.7	8.5	9.1
W_s (kip)	11973					
K_{sys} (kip/in)	786					
T_{sys} (s)	1.24					
ξ_{sys} (%)	9.7					
Δ_{sys_output} (in)	18.8					
Θ (%)	--	--	--	2.7	2.3	2.5
θ_{c_pl} (%)	--	--	--	1.4	1.0	1.3
$\theta_{P\text{-}\Delta}$[2]	--	--	--	0.06	0.07	0.07
$\theta_{P\text{-}\Delta\_limit}$	--	--	--	0.23	0.24	0.24

[1] Symbols defined in Table 6.2; [2] Defined with respect to the tributary seismic weight (W_s) of each bent.

7.4 NUMERICAL MODELS

The analyses were conducted using the Open System for Earthquake Engineering Simulation (*OpenSees*) [Mazzoni et al. 2014] computer software using numerical models similar to the ones described by Antonellis and Panagiotou [2013]. Figures 7.6 and 7.7 describe the numerical models for the Mono Way Bridge and the Murray Ridge Bridge, respectively.

Fiber-section nonlinear Euler Bernoulli beam-column (frame) elements were used to model the columns and the deck with 5 integration points per element. The *Concrete03* and *Steel02*, material models, were used to model the concrete and steel, respectively. A zero-length fiber-section, with concrete and steel tangent modulus properties reduced by 14 times, compared to these used in the column elements, was used between the columns' top and the superstructure to model strain penetration into the superstructure. Post-tensioning of the deck was modeled using an initial strain elastic material (*InitStrainMaterial*). Linear elastic stiff elements were used to connect the top of the columns with the centroid of the deck for the Mono Way Bridge and to model the column-to-bent cap joints for the Murray Ridge Bridge. Linear elastic elements were used to model the bent caps in the transverse direction. Linear elastic stiff elements were also used to: (i) connect the bottom of the column with the foundation centroid and the bottom of the foundation; and (ii) to model the abutment caps (Mono Way Bridge) and the abutment diaphragms (Murray Ridge Bridge).

The soil underneath each shallow foundation was modeled using 289 zero length springs distributed in a non-uniform 17 × 17 grid. The vertical force-displacement relation was modeled using the *QzSimple1* F-Δ relation. The initial stiffness, capacity and distribution of the vertical springs are based on Chapter 3. Horizontal springs at the periphery of the footings were used to model the base friction (*TzSimple1*) and passive reaction of the surrounding soil (*PySimple1*), similarly with Antonellis and Panagiotou [2013]. The foundation nodes connected with the passive soil springs were placed at a height above the footing base, based on the centroid of the expected passive earth pressure distribution, and were connected to the nodes at the footing base with vertical linear elastic stiff elements. The total frictional capacity of the footings was assumed to be 60% of the total axial load at the base of the footings.

The bearings at the abutments of the Mono Way Bridge were modeled with zero-length spring elements, with an elastic-perfectly-plastic force-displacement behavior in the two horizontal directions, while in the vertical direction the bearings were modeled to have zero tensile strength and a linear elastic stiff behavior in compression. The abutment diaphragm – spread footing sliding behavior for the Murray Ridge Bridge was modeled with a series of *Flat Slider Bearing Elements* that couple the sliding resistance in any horizontal direction with the axial compression force and have zero tensile strength. The abutment backfill soil was modeled according to Caltrans Seismic Design Criteria [2013a] using a series of zero-length springs with zero tensile strength and an elastic-perfectly plastic behavior in compression (*ElasticPPGap*). An initial gap was used only for the Mono Way Bridge to model the expansion joint. The shear keys of the Mono Way Bridge were modeled using zero-length spring elements with the tri-linear force-displacement relationship of Aviram et al. [2008]. The wing walls' response of the Murray Ridge Bridge was approximately modeled with zero-length spring elements with pinching and deteriorating force-displacement behavior using the *Hysteretic* uniaxial material in OpenSees.

The mass was assigned at the centroid of the abutments, the deck nodes, the column nodes and at the centroid of the foundations. The corresponding mass moments of inertia at each of these locations were also assigned. The gravity load was assigned as point loads in the above locations. A tangent stiffness Rayleigh damping of 2% was used at the frequencies of modes 1 and 10, determined by an elastic modal analysis after application of gravity loads (i.e. initial bridge stiffness). The corresponding frequencies were 0.5 Hz and 1.6 Hz for the Mono Way Bridge, and 2.0 Hz and 6.5 Hz for the Murray Ridge Bridge.

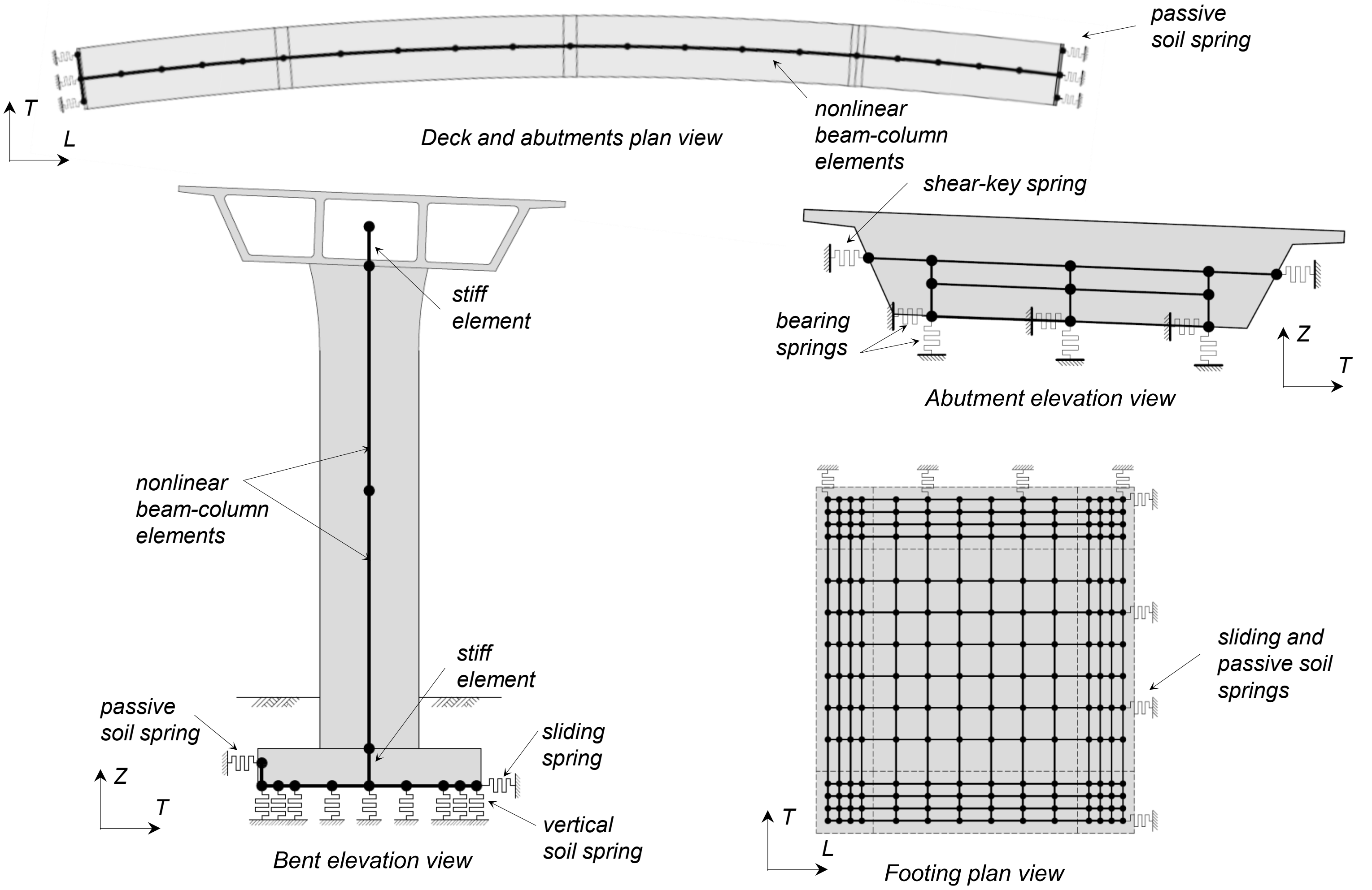

Figure 7.6 Description of the Mono Way Bridge numerical model (not all springs are shown).

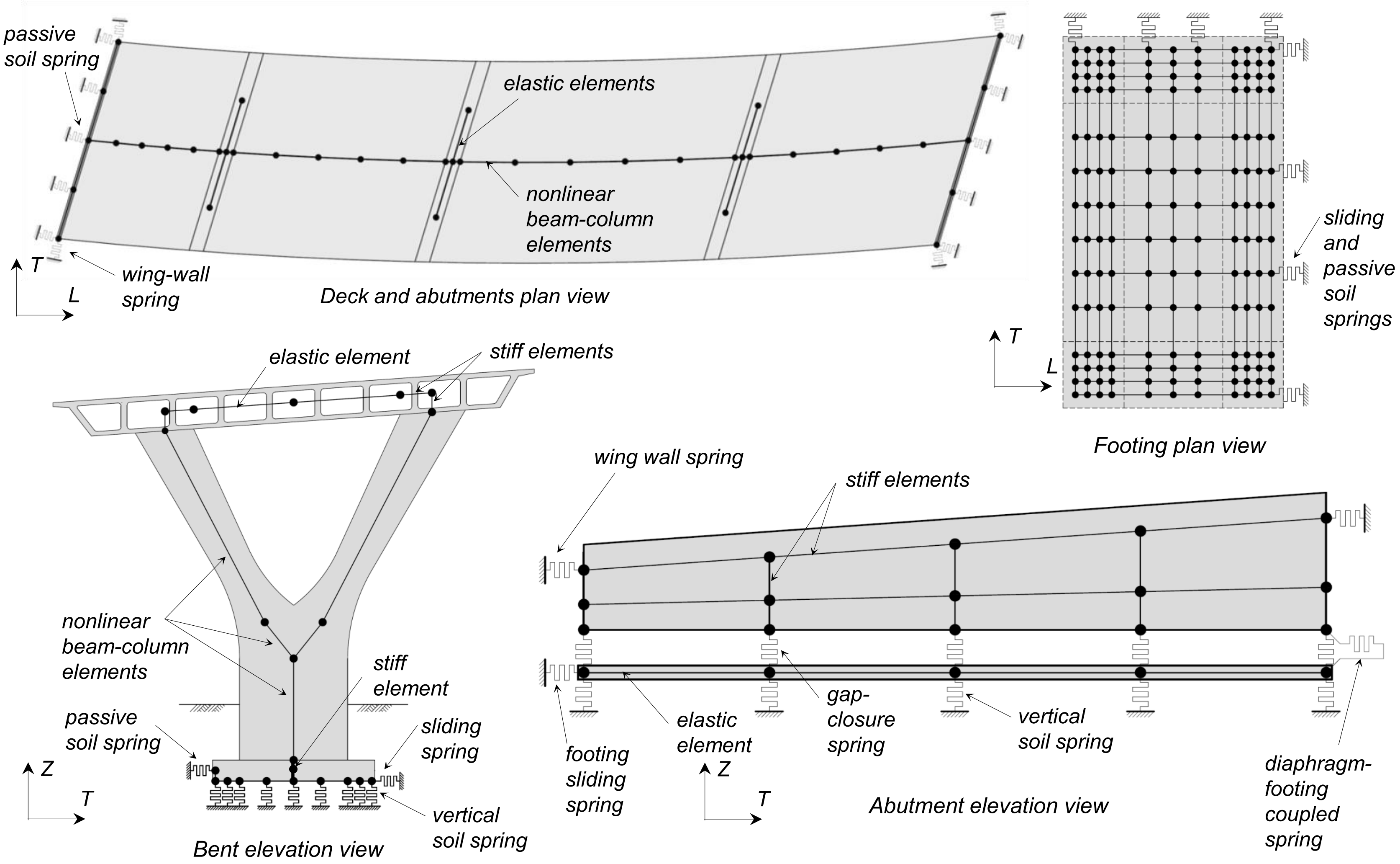

Figure 7.7 Description of the Murray Ridge Bridge numerical model (not all springs are shown).

7.5 NONLINEAR RESPONSE HISTORY ANALYSIS RESULTS

7.5.1 Response Summary

Table 7.8 summarizes the mean values of responses of the redesigned bridges at the DE level of shaking. The Mono Way Bridge develops peak drift ratios in the transverse direction between 5.1% and 6.0% for the FNT loading scenario, and peak drift ratios of 2.5% – 3.4% in the longitudinal direction for the FNL case. The corresponding drift ratios for the Murray Ridge Bridge are smaller as it is stronger than the Mono Way Bridge in both directions. Namely, Murray Ridge Bridge sustains peak transverse and longitudinal drift ratios of 3.3% – 3.6% and 1.8% – 2.0% for the FNT and FNL cases, respectively. The residual drift ratios are less than 0.5% for both bridges, whereas the residual foundation settlements are less than 1.5 and 0.5 inches for the Mono Way Bridge and the Murray Ridge Bridge, respectively. The peak plastic rotation at the top of the columns in the FNL scenario is 1% – 1.2% for the Mono Way Bridge, and 0.4% – 0.6% for the Murray Ridge Bridge. The corresponding peak tensile strains of the longitudinal reinforcement are 1.6% – 2.2% and 1.1% – 1.5% indicating acceptable levels of inelasticity. The longitudinal reinforcement at the base of the columns remains in the elastic range (less than 0.2% tensile strain), as is also the case for the deck pre-stressing strands since the mean peak incremental tensile strain of the strands (with respect to the initial tension) does not exceed a value 0.2% for either bridge. Lastly, it is worth noticing that significant axial load variation takes place at the abutments and the nearest bents of the Murray Ridge Bridge at both the FNT and FNL cases. The implication of this axial load variation in the case of the Murray Ridge Bridge is discussed below in more detail. Significant axial load variation is also observed for the Mono Way Bridge, but to a lesser extent.

Table 7.8 Mean values for different response parameters for the DE level of shaking.

Response parameter	Location	Mono Way Bridge FNT	Mono Way Bridge FNL	Murray Ridge Bridge FNT	Murray Ridge Bridge FNL
Peak column transverse drift ratio[1] (%)	B2	6.0	3.2	3.6	2.4
	B3	5.3	2.8	3.3	2.1
	B4	5.1	2.6	3.6	2.3
Peak column longitudinal drift ratio[1] (%)	B2	2.2	3.4	1.3	2.0
	B3	1.9	2.9	1.2	1.8
	B4	1.6	2.5	1.3	1.9
Residual column transverse drift ratio[1] (%)	B2	0.1	0.0	0.1	0.1
	B3	0.0	0.0	0.1	0.1
	B4	0.0	0.0	0.1	0.1
Residual column longitudinal drift ratio[1] (%)	B2	0.2	0.1	0.1	0.2
	B3	0.1	0.0	0.0	0.2
	B4	0.1	0.0	0.1	0.2
Residual footing settlement (in)	B2	1.2	0.8	0.2	0.2
	B3	0.8	0.5	0.4	0.3
	B4	0.7	0.4	0.2	0.2
Column base longitudinal reinforcement peak tensile strain (%)	B2	0.2	0.2	0.1	0.1
	B3	0.2	0.2	0.1	0.1
	B4	0.2	0.2	0.1	0.1
Column top longitudinal reinforcement peak tensile strain (%)	B2	1.4	2.2	0.7	1.4
	B3	1.1	2.0	0.7	1.1
	B4	0.7	1.6	0.9	1.5
Column top peak plastic rotation (%)	B2	0.6	1.1	0.3	0.6
	B3	0.6	1.2	0.2	0.4
	B4	0.3	1.0	0.3	0.5
Pre-stressing strands tensile strain[2] (%)		0.11	0.14	0.04	0.04
Minimum and maximum (in parentheses) normalized axial compression force[3]	A1	0.49 (1.51)	0.48 (1.62)	0.56 (2.19)	0.47 (2.17)
	B2	0.68 (1.47)	0.62 (1.61)	0.24 (1.77)	0.33 (1.70)
	B3	0.71 (1.38)	0.63 (1.48)	0.59 (1.46)	0.56 (1.42)
	B4	0.74 (1.36)	0.72 (1.43)	0.46 (1.57)	0.50 (1.54)
	A5	0.61 (1.35)	0.58 (1.39)	0.44 (2.06)	0.42 (1.94)
	Bridge	0.78 (1.32)	0.74 (1.40)	0.71 (1.42)	0.70 (1.40)

[1] In the local transverse and longitudinal direction for the Murray Ridge Bridge; [2] Additional to the initial tensile strain of the deck pre-stressing strands; [3] Low-pass filtered at 5 Hz.

7.5.2 Validation of the Displacement Based Method of Analysis

Transverse direction response

Figure 7.8 plots the mean transverse drift ratio demand of the 14 nonlinear response history analyses for the DE level of shaking and the FNT case, as well as the corresponding predictions from the displacement-based assessment for three cases: (i) $C_m = 1$ and $C_a = 1$; (ii) $C_m = 0.7$ and $C_a = 1$; and (ii) $C_m = 0.7$ and C_a the upper bound value of Table 7.3. Case (i) represents the scenario where the bents are analyzed independently, without correcting for the mass participation factor in the main translational mode in the transverse direction being less than 1 and without also accounting for the possible restrain effect of the abutments. Case (ii) differs from case (i) by accounting only for the reduced effective seismic mass, while case (iii), compared to case (ii), also accounts for the possible restrain at the abutments through the abutment strength correction factor being different than 1.

It is observed that in all three cases the drift ratio demand predicted by the displacement-based analysis method overestimates the mean drift ratio demand obtained by the nonlinear dynamic analyses. The overestimation is greatest (14% – 35% for the Mono Way Bridge, and 192% – 206% for the Murray Ridge Bridge) for case (i) when neither the reduced effective seismic mass, nor the abutment strength characteristics are considered. Consideration of the minimum suggested mass participation factor ($C_m = 0.7$) alone, marginally improves the prediction of the displacement-based method (overestimation of 16% – 29% for the Mono Way Bridge, and 185% – 190% for the Murray Ridge Bridge). This is expected since a C_m value of 0.7, instead of 1, will only stiffen the response of the independent bents by approximately 16%. Extending this observation, it can be concluded that the exact C_m value in the suggested range of 0.7 – 0.9 is of little significance. Case (iii), where the upper bound C_a value is used in addition to $C_m = 0.7$ further improves the results. This improvement is more noticeable for the Murray Ridge Bridge where $C_a = 1.6$, as opposed to the Mono Way Bridge where $C_a = 1.15$. For this case, the displacement-based assessment method overestimates the peak drift ratio demand by 13% – 24% for the Mono Way Bridge, and by 70% – 122% for the Murray Ridge Bridge. The reasonable drift demand overestimation for the Mono Way Bridge and the respective significant overestimation for the Murray Ridge Bridge may be explained by the reasons discussed below.

Firstly, the single source of hysteretic damping considered in the analysis of the bents in

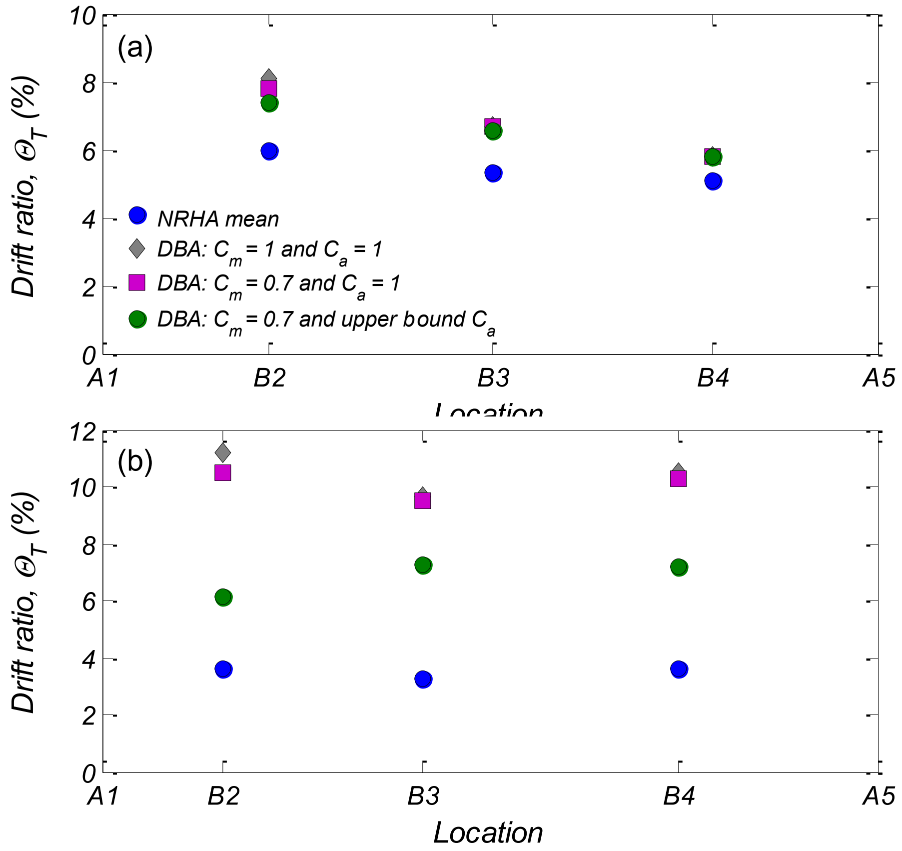

Figure 7.8 Comparison between the mean transverse drift ratio demands from NRHA and DBA for the DE-FNT case: (a) Mono Way Bridge; and (b) Murray Ridge Bridge.

the transverse direction comes from the soil inelastic action during rocking. As discussed in Chapter 4, the proposed equations for the equivalent viscous damping due to rocking have a built-in conservatism as they are calibrated to match the median drift ratio demand computed by the NRHAs, and hence, they typically overestimate the mean response (see Figure 4.13).

Secondly, the effect of the abutments on the response of the bents is considered only through the abutment strength correction factor (C_a) that would typically result to a stiffened response of the analyzed bents. For example, the used $C_a = 1.15$ and $C_a = 1.6$ stiffen the bents of the Mono Way and the Murray Ridge Bridge by about 7% and 20%. However, the effect of the increased energy dissipation at the abutments, especially due to high frictional resistance mechanisms, is neglected. The equivalent viscous damping at the bents is solely that of foundation rocking that is a low level energy dissipation mechanism (ξ_{eq} smaller than approximately 8%) due to the controlled soil inelasticity ($\rho_{ac} < 0.125$), while ξ_{eq} at the abutments that deform by frictional sliding can be in the 15 – 25% range. This simplification has a greater impact on the drift ratio demand prediction of the Murray Ridge Bridge where the high dissipation abutment diaphragm – spread footing sliding mechanism accounts for 25% of the total lateral capacity of the bridge (after wing walls' damage), as opposed to the Mono Way Bridge where the high dissipation at the PTFE bearings provides only 10% of the total lateral capacity of the bridge (after shearing off of the shear keys). An approximate method for the quantification of the abutments' energy dissipation effects in the displacement-based analysis method is discussed in the following section.

Third, because the abutment diaphragm of the Murray Ridge Bridge is significantly wider than the bents' footings (approximately 2.5 times wider), there is significant dynamic framing action between the abutments and the nearest bents during transverse response that is not included in the simplified displacement-based analysis method. The result of this framing action is axial load transfer to the abutments that are more robust, both in terms of energy dissipation and strength (sliding coefficient, $\mu = 0.5$), compared to the rocking bents. Figure 7.9 illustrates this mechanism; the similar rotation at the footing and deck centroid of bent 2, as well as at the deck centroid at abutment 1, results to a partial "lift up" of bent 2 and thus, to a decrease in axial load at the bent and an increase in axial load at the abutment. To further examine whether this mechanism can explain the significant overestimation of drift demands for the Murray Ridge Bridge, Figure 7.10 plots the axial load at the abutments, bents and the bridge, as well as the corresponding resisting lateral force in the transverse direction. Figure 7.10 shows significant dynamic oscillation of the axial load and lateral resisting force at the abutments and the bents; however, the total shear in the transverse direction compares well with the predicted capacity used in design. Thus, this mechanism alone, cannot explain the significant overestimation of drift demands for the Murray Ridge Bridge.

It is concluded that the displacement-based analysis method, as presented in Section 6.1, provides a reasonably conservative estimate of drift ratio demands in cases where high energy dissipation mechanisms at the abutments do not significantly contribute to the transverse strength of the bridge (Mono Way Bridge). In the Murray Ridge Bridge, such mechanisms do contribute significantly to the transverse bridge strength, and the proposed approach was found to yield too conservative estimates. In this case, a complete bridge-level approach that directly accounts for the different damping sources may be preferable. In addition, significant dynamic framing action in the transverse direction of the Murray Ridge Bridge may have further worsened the prediction of the displacement-based analysis method.

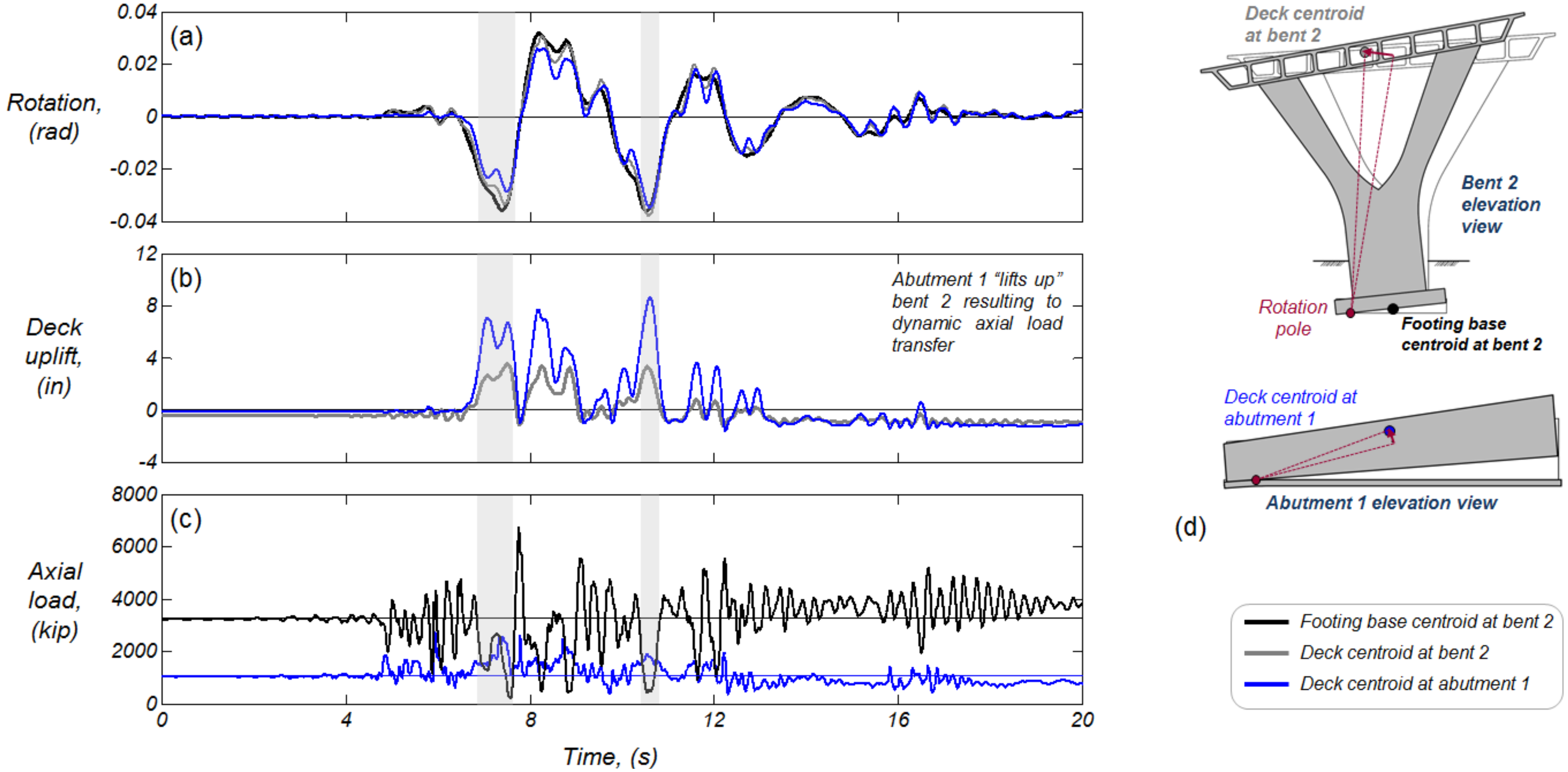

Figure 7.9 Abutment to bent dynamic interaction mechanisms for Murray Ridge Bridge under a ground motion with the fault-normal component in the transverse direction demonstrating a limitation of the simplified displacement-based analysis method: (a) rotation about the longitudinal axis for abutment 1 and bent 2; (b) deck uplift at abutment 1 and bent 2; (c) dynamic axial load at abutment 1 and bent 2; (d) schematic illustration of kinematic interaction.

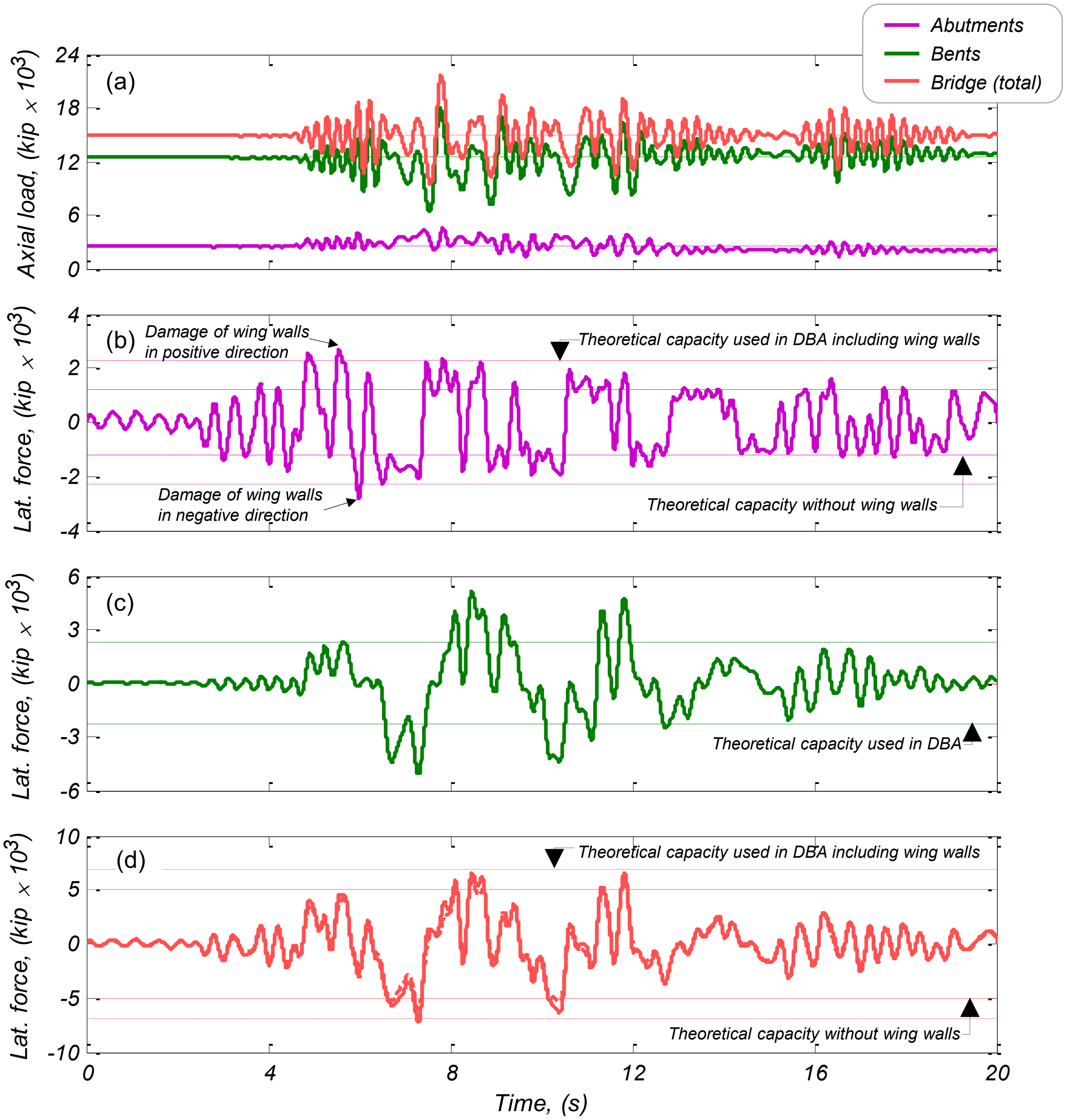

Figure 7.10 Effect of the abutment to bent dynamic interaction mechanisms for Murray Ridge Bridge, under a ground motion with the fault-normal component in the transverse direction, to the total transverse load carrying capacity of the bridge: (a) axial load at abutments, bents and bridge; and lateral force resisted by the (b) abutments, (c) bents and (d) bridge. Note: response histories are low-pass filtered at 5 Hz.

Approximate quantification of abutments' energy dissipation effects for excitation in the transverse direction

This section presents an approximate quantification of the abutments' energy dissipation effects for excitation in the transverse direction so that the gross overestimation of drift demands for the Murray Ridge Bridge can be better understood and explained. Since the equivalent viscous damping at the individual bents is solely that of foundation rocking and energy dissipation at the abutments is neglected, an energy dissipation correction factor (C_{ξ_ab}) can be introduced to scale-up the equivalent damping of the rocking footings. This correction factor can be estimated as

$$C_{\xi\_ab} = 1 + \frac{E_{diss\_ab}}{E_{diss\_b}} \tag{7.1}$$

where E_{diss_ab} is the energy dissipated at the two abutments and E_{diss_b} is the energy dissipated at the bents. Eqn. (7.1) can be rewritten as

$$C_{\xi\_ab} = 1 + \frac{\sum\limits_{i=1,\,n} \xi_{ab} \cdot F_{ab} \cdot \Delta_{ab}}{\sum\limits_{i=2\ldots n-1} \xi_{b} \cdot F_{b} \cdot \Delta_{b}} \tag{7.2}$$

where ξ_{ab} (or ξ_b) is the equivalent viscous damping at the abutments (or bents), F_{ab} (or F_b) is the lateral force at the abutments (or bents), Δ_{ab} (or Δ_b) is the deck transverse displacement at the abutments (or bents), and n is the total number of abutments and bents combined.

Since the DBA method presented in Section 6.1 does not provide an estimate of the deck displacement at the abutments (Δ_{ab}) due to the individual bents' analysis approach, Eqn. (7.2) may be further simplified as

$$C_{\xi\_ab} = 1 + \frac{\sum\limits_{i=1,\,n} \xi_{ab\_f} \cdot F_{ab\_f}}{\sum\limits_{i=2\ldots n-1} \xi_{b} \cdot F_{b}} \tag{7.3}$$

where ξ_b and F_b are the equivalent viscous damping and lateral force at each bent as estimated by the initial individual bent approach assuming $C_{\xi\_\mathrm{ab}} = 1$ (e.g. from Table 7.4 for this case), and ξ_{ab_f} and F_{ab_f} are the equivalent viscous damping and lateral force at each abutment due to the sliding resistance mechanisms for a lateral displacement that is the average of the lateral displacement of the bents. C_{ξ_ab} estimated by Eqn. (7.3) and the procedure described above may or may not be larger than that estimated by Eqn. (7.2); while the abutments typically displace less than the bents of a bridge, Eqn. (7.3) neglects energy dissipation at the abutments due to other force resisting mechanisms such as shear keys or wing walls.

Once C_{ξ_ab} has been estimated, the DBA method described in Section 6.1 can be repeated by scaling-up the equivalent viscous damping of the rocking footings through C_{ξ_ab}. This procedure will provide a one-time updated drift demand prediction that approximately accounts for the abutments' energy dissipation effects. Alternatively, a double-iterative procedure can be used until C_{ξ_ab} stabilizes. The described procedure results to a one-time correction C_{ξ_ab} value of 1.55 for the Mono Way Bridge which is also the stable C_{ξ_ab} value, while for the Murray Ridge Bridge the one-time correction for the abutments' energy dissipation effects yields $C_{\xi\_ab} = 3.02$ with the converged C_{ξ_ab} value found to be 3.25 after an additional iteration.

Figure 7.11 compares the mean transverse drift ratio demand of the 14 NRHA for the DE level of shaking and the FNT case, the DBA prediction for the case with $C_m = 0.7$, C_a equal to the upper bound value of Table 7.3 and $C_{\xi\_ab} = 1$ (also shown in Figure 7.8), and the DBA prediction for the case with $C_m = 0.7$, C_a equal to the upper bound value of Table 7.3 and $C_{\xi\_ab} > 1$ (i.e. case with approximate quantification of the abutments' energy dissipation effects). It is observed that the described procedure for quantifying the energy dissipation at the abutments greatly improves the DBA prediction for the Murray Ridge Bridge, without jeopardizing the corresponding prediction for the Mono Way Bridge. More specifically, the drift demand overestimation for the Mono Way Bridge reduces from the 13 – 24% range to less than 9%, whereas the drift demand comparison for the Murray Ridge Bridge reduces from an overestimation in the 70 – 122% range to a relative error of less than 7%.

It is noted that although the approximate quantification of abutments' energy dissipation effects for excitation in the transverse direction has improved the DBA prediction for the considered bridges, it should not be generalized to other cases without caution. Since Eqn. (7.1) assumes that the abutments' energy dissipation correction factor (C_{ξ_ab}) is no smaller than one, and the equivalent viscous damping ratio of the rocking bents is associated to an enhanced lateral secant stiffness through the abutment strength correction factor (C_a), the approximate method can yield unconservative results when the damping ratio at the abutments (ξ_{ab}) is smaller than that at the rocking bents (ξ_b). Unconservative estimates can also be produced for short bridges and/or strong abutments that do not displace laterally due to the simplification of Eqn. (7.3). In such cases, the iterative eigenvalue approach, briefly mentioned in Section 6.1, shall be used as a more complete and accurate approach that has been tested more extensively, with equivalent linear properties of the rocking bents as provided in Chapters 4 and 5.

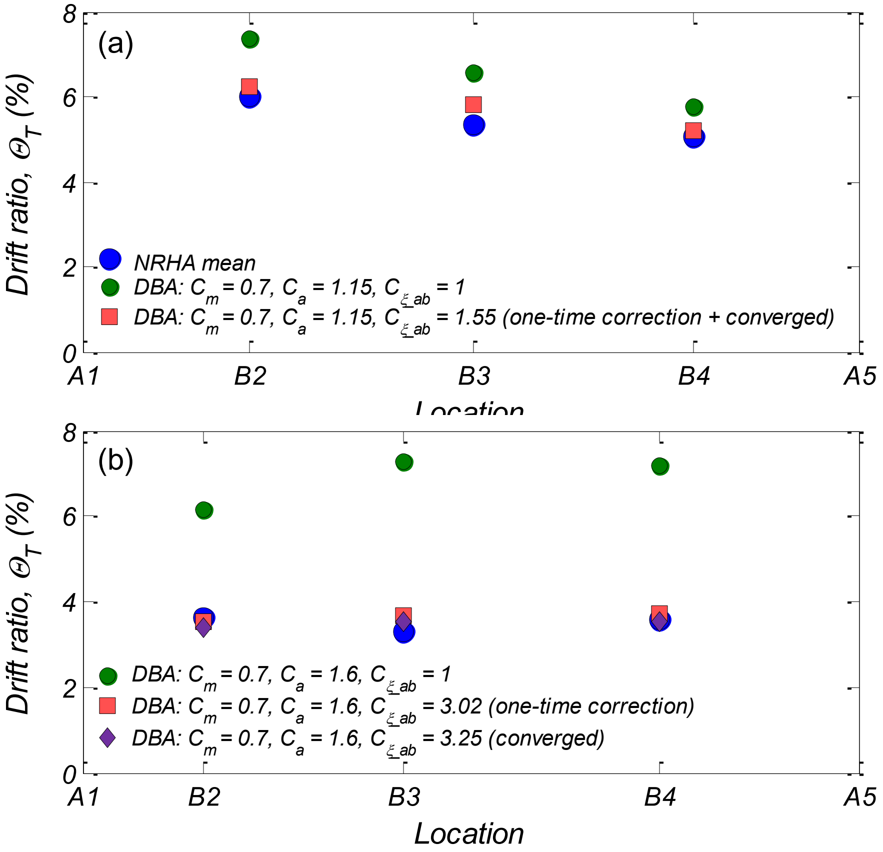

Figure 7.11 Comparison between the mean transverse drift ratio demands from NRHA and DBA with approximate quantification of the abutments' energy dissipation effects for the DE-FNT case: (a) Mono Way Bridge; and (b) Murray Ridge Bridge.

Longitudinal direction response

Figure 7.12 plots the mean longitudinal drift ratio for the DE level FNT case, as well as the corresponding predictions from the displacement-based analysis method for $C_m = 1$. For both bridges DBA predicts well the drift ratio; the prediction for the Mono Way Bridge is within 3% for all bents, while that for the Murray Ridge Bridge is approximately 30% larger.

The good prediction for the longitudinal direction is expected since: (i) the bridge-level approach directly accounts for the energy dissipation from all sources; (ii) the effect of the built-in conservatism of the equivalent viscous damping of foundation rocking is reduced as it is not the only source of hysteretic damping that affects the system-level damping; and (iii) framing action in the longitudinal direction does not bias the results as it does in the transverse direction.

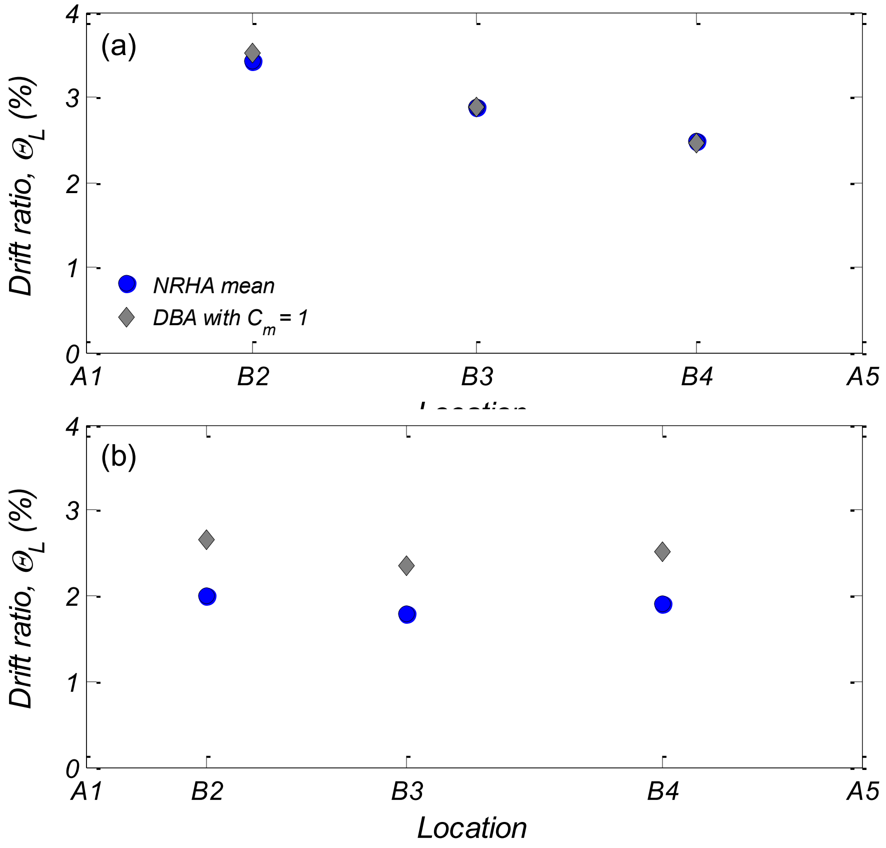

Figure 7.12 Comparison between the mean longitudinal drift ratio demands from NRHA and DBA for the DE-FNL case: (a) Mono Way Bridge; and (b) Murray Ridge Bridge.

7.6 SUMMARY

In this chapter, two existing bridges of Caltrans were hypothetically re-designed, using columns on rocking shallow foundations and moment-resistant connections with the deck, for a site of very high seismic hazard in San Bernardino, California. The objective of the designs was limited post-earthquake structural damage and residual deformations in order to achieve prompt post-earthquake functionality. Three-dimensional nonlinear response history analyses (NRHA) of the full bridges were used to validate the seismic designs. Moreover, the NRHA results are used to validate the system level DBA method (Chapter 6) used to estimate displacement demands and thus to design the bridges. Findings can be summarized as follows:

1. The performed three-dimensional NRHA of the two redesigned bridges demonstrated their excellent seismic performance at a very severe site. Mono Way Bridge developed mean peak drift ratios of up to 6% in the transverse direction and up to 3.2% in the longitudinal direction, whereas the corresponding mean peak drift ratios for the Murray

Ridge Bridge were 3.6% and 2.4%. The mean peak tensile strain of the longitudinal reinforcement at the top of the columns was 2.2% for the Mono Way Bridge and 1.5% for the Murray Ridge Bridge. The mean residual drift ratios for both bridges were limited to less than 0.5%.

2. The displacement-based method of analysis in the transverse direction provides a reasonable, but somewhat conservative (20% overestimation for the Mono Way Bridge and 100% overestimation for the Murray Ridge Bridge) estimate of the mean peak drift demand computed from the 14 nonlinear response history analyses.
3. The conservatism of the method depends on the relative contribution of high energy dissipation mechanisms at the abutments to the overall strength of the bridge, since the proposed method neglects such effects. For the Murray Ridge Bridge, the amount of equivalent viscous damping due to the frictional energy dissipation at the abutments in the transverse direction was 2 times that of all the bents together, while the corresponding value for the Mono Way Bridge was only 0.5.
4. Approximate quantification of abutments' energy dissipation effects in the transverse direction, through a scale-up factor used to enhance energy dissipation of the rocking footings at individual bents, significantly improved DBA prediction for the Murray Ridge Bridge resulting to an error of less than 10% compared to the NRHA results.
5. Peak drift demand in the longitudinal direction were well predicted by the displacement-based analysis due to the used bridge-level approach that directly accounts for the strength and energy dissipation characteristics of all components.
6. For the very wide deck Murray Ridge Bridge, using single-column bents produces quite significant uplift displacements at the abutments and the nearest bents. The uplift causes a significant variation in axial loads at the abutments and the nearest bents, which is not considered in the DBA method. Despite that, the increase of lateral strength of the bridge in the transverse direction due to the increased axial compression at the abutments was up to 10%.
7. Use of two-column bents with pins at the top of the columns and rocking foundations at the base of the columns could alleviate the variation of axial load on columns due to uplift forces at the abutments.

8 Response Spectrum Analysis of the Bridges with Rocking Foundations

8.1 INTRODUCTION

This chapter presents the results of a response spectrum analysis of the two re-designed bridges, with rocking shallow foundations. This method is commonly used for estimating displacement demands of ordinary reinforced-concrete fixed-base bridges by Caltrans engineers. The results from the response spectrum analysis (RSA) method are compared to the results of the displacement-based analysis (DBA) method, and the three-dimensional nonlinear response history analysis (NRHA).

8.2 NUMERICAL MODEL

The response spectrum analysis was performed using the software SAP2000. A numerical model for each bridge was developed; the model assumptions and the stiffness of the elastic elements and springs are described below. Three elements were used to model each column, whereas four elements were used for each deck span, and one element for each footing. Stiff elements connected the top of the columns and the centroid of the deck for the Mono Way Bridge and to model the column-to-bent cap joints for the Murray Ridge Bridge. Two additional elements were used to model the bent caps of the second bridge in the transverse direction. The rocking foundations were modeled using rotational springs with stiffness equal to the Deng et al. [2014] secant rotational stiffness at first mobilization of the rocking moment capacity (i.e. footing rotation of 0.012 rad). The footing and the column elements were modeled using 50% of their gross flexural rigidity, whereas 100% of the gross flexural rigidity was used for the post-tensioned deck elements and the transverse bent cap elements of Murray Ridge Bridge. The abutments were modeled using linear elastic horizontal springs in the transverse and longitudinal direction. Two different cases were assumed: (a) a "locked" abutment case; and (b) an "unlocked" abutment case. For the "locked" abutment case, the stiffness of each longitudinal abutment spring was equal to the initial stiffness of the PTFE bearings for the Mono Way Bridge and of the abutment diaphragm to spread footing sliding for the Murray Ridge Bridge, and half of the initial stiffness provided by backfill passive resistance. For the transverse spring, the frictional stiffness was used, ignoring for simplicity the shear keys of the Mono Way Bridge and the wing walls of the Murray Ridge Bridge. For the "unlocked" abutment case, both the longitudinal and the transverse springs were modeled using 10% of the initial frictional stiffness. These two cases were analyzed in an attempt to bound the expected response of the bridges. Translational and rotatory masses were assigned at each node, whereas point loads were used for the analysis under gravity loads. Figure 8.1 shows an isometric view of the Mono Way Bridge model in SAP2000.

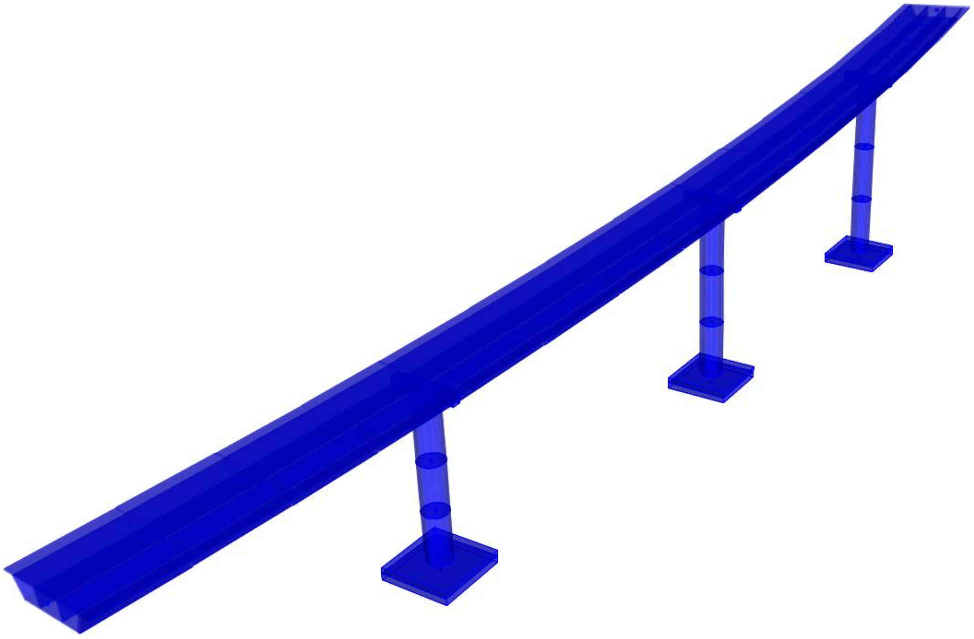

Figure 8.1 Isometric view of the Mono Way Bridge model in SAP2000.

8.3 MODAL ANALYSIS RESULTS

Table 8.1 summarizes the modal analysis results of the two re-designed bridges for the “locked” and “unlocked” abutment models. It shows the periods and modal masses (as percentage of the total bridge mass) that correspond to the first four modes in the transverse direction and the first mode in the longitudinal direction. The effective horizontal seismic mass is approximately 70% and 85% of the total bridge mass for the Mono Way Bridge and the Murray Ridge Bridge, respectively, irrespective of excitation direction and abutment modeling. The fundamental vibration period in the longitudinal direction is shown to increase significantly for both bridges, by 180% for the Mono Way Bridge and by 120% for the Murray Ridge Bridge, when the abutments are “unlocked”. In the transverse direction, the corresponding increase is 100% for the wide-deck Murray Ridge Bridge, while an only 22% increase is observed for the Mono Way Bridge that has a more flexible deck.

Table 8.1 Modal analysis results for the two bridges.

Bridge	Abutment	Mode Type	Period, T (s)	Modal Mass, M* (%)[1]
Mono Way	"Locked"	Transverse 1	2.17	59.3
		Transverse 2	0.86	--[2]
		Transverse 3	0.48	8.9
		Transverse 4	0.31	--[2]
		Longitudinal 1	0.62	70.5
	"Unlocked"	Transverse 1	2.65	65.8
		Transverse 2	1.48	--[2]
		Transverse 3	0.90	3.0
		Transverse 4	0.47	--[2]
		Longitudinal 1	1.74	71.9
Murray Ridge	"Locked"	Transverse 1	0.51	61.5
		Transverse 2	0.35	17.7
		Transverse 3	0.27	--[2]
		Transverse 4	0.23	--[2]
		Longitudinal 1	0.45	85.4
	"Unlocked"	Transverse 1	1.00	78.9
		Transverse 2	0.67	--[2]
		Transverse 3	0.36	5.5
		Transverse 4	0.26	--[2]
		Longitudinal 1	0.98	86.4

[1] Percentage of total bridge mass; [2] Anti-symmetric mode.

8.4 RESPONSE SPECTRUM ANALYSIS RESULTS

The response spectrum analysis used the 5% damped mean response spectrum of the DE-level ground motions. For each bridge and abutment model, two analyses were conducted. In the first analysis, the mean response spectrum of the fault-normal (FN) components was imposed in the transverse bridge direction whereas that of the fault-parallel (FP) components was imposed in the longitudinal bridge direction (DE-FNT case). In the second analysis, the orientation of the FN and FP mean response spectra was reversed (DE-FNL case). The nodal displacements from each mode were summed together using the Complete Quadratic Combination 3 (*CQC3*) method [Menun and Kiureghian 1998].

Tables 8.2 and 8.3 summarize the response spectrum analysis (RSA) drift ratio results of the bridge bents in the transverse and longitudinal direction, in comparison to the nonlinear response history analysis (NRHA) and the displacement-based analysis (DBA) results, for the DE-FNT and DE-FNL cases, respectively.

8.4.1 Transverse Direction Response

For the “locked” abutment model, RSA method predicts drift ratio demands in the transverse direction that are in the 2.7% – 3.6% range for the Mono Way Bridge and in the 0.6% – 0.8% range for the Murray Ridge Bridge, whereas the corresponding mean drift ratio demands from the NRHA are 5.1% – 6.0% and 3.3% – 3.6%, respectively. Hence, the “locked” abutment RSA model results to an underestimation of drift demand, compared to NRHA, in the order of 10 – 55% for the Mono Way Bridge and in the order of 75% – 85% for the Murray Ridge Bridge. The serious underestimation of the Mono Way Bridge transverse response is due to the stiff deck that does not allow significant displacements to develop at the bridge bents if deck translation at the abutments is restricted. The observed underestimation is expected as the “locked” abutment model intends to provide the lower bound estimate of the expected seismic response.

For the “unlocked” abutment model, RSA method predicts transverse drift ratio demands in the 3.9% – 5.4% range for the Mono Way Bridge and in the 2.4% – 2.6% range for the Murray Ridge Bridge. Although these results are closer to the NRHA, the “unlocked” abutment model did not bound the bridge response as determined by the NRHA and is unconservative. The drift demand underestimation is up to 24% for the Mono Way Bridge, and about 30% for the Murray

Ridge Bridge. As discussed in Chapter 7, DBA method provides conservative estimates of the peak transverse response when abutments' energy dissipation effects are not considered; the overestimation is between 13% and 23% for the Mono Way Bridge, and between 70% and 120% for the Murray Ridge Bridge. When energy dissipation at the abutments is approximately quantified, the DBA drift demand prediction error reduces to less than 10% for the Murray Ridge Bridge.

8.4.2 Longitudinal Direction Response

For the "locked" abutment model, RSA method predicts small drift ratio demands in the longitudinal direction; the range is 0.6% – 0.9% for the Mono Way Bridge and 0.6% – 0.7% for the Murray Ridge Bridge. These drifts are approximately 75% and 65% smaller than those computed by NRHA for the Mono Way and the Murray Ridge Bridge, respectively. When the abutments are "unlocked", RSA method results overestimate those from the NRHA by 13% for the Mono Way Bridge and by 35% for the Murray Ridge Bridge. Therefore, the considered abutment models were successful in enveloping the NRHA response.

The DBA method in the longitudinal direction provides an almost exact estimation of the Mono Way Bridge response, and an approximately 35% conservative estimate of the Murray Ridge Bridge response. Thus, the DBA method proves to be more successful in estimating the peak longitudinal response for both bridges, compared to the RSA method.

Table 8.2 Response spectrum analysis (RSA) drift ratio (%) results in the transverse direction, in comparison to the nonlinear response history analysis (NRHA) and the displacement-based analysis (DBA) results, for the DE-FNT case.

		RSA			
Bridge	Location	"Locked" Abutment	"Unlocked" Abutment	NRHA	DBA[1]
Mono Way	Bent 2	3.6	4.6	6.0	7.3
	Bent 3	4.8	5.3	5.3	6.5
	Bent 4	2.7	3.9	5.1	5.7
Murray Ridge	Bent 2	0.6	2.5	3.6	6.1
	Bent 3	0.8	2.4	3.3	7.2
	Bent 4	0.7	2.6	3.6	7.1

[1] DBA results are for $C_m = 0.7$, the upper bound C_a value of Table 7.3 and $C_{\xi\_ab} = 1$.

Table 8.3 Response spectrum analysis (RSA) drift ratio (%) results in the longitudinal direction, compared to the nonlinear response history analysis (NRHA) and the displacement-based analysis (DBA) results, for the DE-FNL case.

		RSA			
Bridge	Location	"Locked" Abutment	"Unlocked" Abutment	NRHA	DBA
Mono Way	Bent 2	0.9	3.9	3.4	3.5
	Bent 3	0.7	3.2	2.9	2.9
	Bent 4	0.6	2.8	2.5	2.5
Murray Ridge	Bent 2	0.7	2.7	2.0	2.7
	Bent 3	0.6	2.4	1.8	2.3
	Bent 4	0.6	2.6	1.9	2.5

8.5 SUMMARY

In this chapter, the results of a response spectrum analysis of the two re-designed bridges with rocking shallow foundations have been presented. For each bridge, two abutment models have been considered: (a) a “locked” abutment case; and (b) an “unlocked” abutment case. These two models were intended to bound the seismic response as obtained by the NRHA in Chapter 7. Findings can be summarized as follows:

1. For seismic response in the transverse direction, the RSA method was found to be unsuccessful in bounding the bridge response in the design earthquake as obtained by the NRHA. RSA predictions assuming unlocked abutments greatly underpredicted the NRHA displacements for these two bridges subjected to the design earthquake. The underestimation was up to 55% for the Mono Way Bridge, and up to 85% for the Murray Ridge Bridge. The “unlocked” abutment RSA models yielded more reasonable, but unconservative estimates of peak displacement response. The underestimation was up to 24% for the Mono Way Bridge and up to 30% for the Murray Ridge Bridge.
2. For seismic response in the longitudinal direction, the RSA method was successful in bounding the bridge response as obtained by the NRHA. The “locked” abutment RSA models underestimated the NRHA peak displacement demands by approximately 75% for the Mono Way Bridge and 65% for the Murray Ridge Bridge, while the corresponding overestimations of the “unlocked” abutment RSA models were 13% and 35%, respectively.

3. Overall RSA results with unlocked abutments compared reasonably to the NRHA results for the bridges and seismic hazard level considered in this study. However, they also showed significant sensitivity to the abutment modeling details. Additional studies would be required to come to a clear conclusion about the reliability and accuracy of RSA for different bridges or different levels of seismic shaking.
4. The proposed DBA procedure, discussed in Chapter 7, appears to provide more reliable and more conservative results as compared to the RSA approach for the example bridges and design earthquakes.

9 Conclusions

This study developed seismic design guidelines for ordinary bridges with columns on rocking foundations with or without controlled plastic hinging at the top of the columns. The seismic design concept results in bridges that sustain very strong seismic excitation with minimal structural damage and small residual displacements and thus in prompt post-earthquake functionality. The proposed seismic design method is based on displacement-based analysis (DBA). The method covers the analysis and design of single rocking bents as well as system-level design of bridges for excitation in the transverse and longitudinal direction.

On the single bent level, the DBA approach estimates the displacement demand using the design linear displacement spectrum and an equivalent linear viscoelastic single-degree-of-freedom (SDOF) model that represents the analyzed structural system.

The equivalent viscous damping of a rocking footing is determined based on parametric nonlinear response history analyses (NRHA) of single stiff columns supported on rocking foundations with different critical contact area ratios (ρ_{ac}) subjected to different types of ground motions (Chapter 4). The rocking foundations are modeled using a calibrated, based on physical tests, beam-on-nonlinear-Winkler-foundation scheme (Chapter 3).

The proposed DBA method covers the analysis of a single elastic flexible column on rocking foundation (Chapter 4), as well as the analysis of a single flexible column with rocking foundation at the base and plastic hinging at the top (Chapter 5). Provisions for the system level analysis of multi-span bridges were also developed (Chapter 6); a complete bridge system approach is used for the longitudinal bridge analysis whereas for the transverse direction the bridge bents are analyzed individually considering bent-to-bent as well as bents-to-abutments interaction through two modification factors. For the latter case, an approximate quantification of the effect of high frictional energy dissipation at the abutments is briefly covered by introducing an additional modification factor (Chapter 7).

To validate the proposed seismic design and analysis methods, two existing bridges of Caltrans are redesigned using rocking foundations for a site of very high seismic hazard located at San Bernardino, 1.5 km from the San Andreas Fault, for which the design earthquake (DE) displacement spectrum has a 1.6 ft/s slope up to a period of 5 seconds. Although Deng et al. [2012] pointed out that, for multi-column bents, column damage may be further reduced by use of pins in place of moment connections, the redesigns in this report were constrained to maintain moment-resistant connections between the tops of the columns and the deck. The first bridge has relatively weak abutments in the transverse (10% of the total lateral-transversal strength) and longitudinal (19% of the total lateral-longitudinal strength) direction (Mono Way Bridge), whereas the second bridge has strong abutments in both directions (24% and 74% of the total lateral transversal and longitudinal strength, respectively) with high energy dissipation (Murray Ridge Bridge). The seismic designs of the two bridges are validated using three-dimensional NRHA of the two bridges (Chapter 7) including modeling of all major components and force-resisting mechanisms. The results of the NRHA are also used to validate the DBA results for the two bridges. Lastly, a response spectrum analysis (RSA) of the redesigned bridges is conducted and compared with the NRHA and DBA (Chapter 8). The main findings of this study can be summarized as follows:

1. Three-dimensional nonlinear response history analyses (NRHA) of the two redesigned bridges using rocking shallow foundations, demonstrated their excellent performance at a site with severe seismic hazard. Mono Way Bridge developed mean peak drift ratios of up to 6% in the transverse direction and up to 3.2% in the longitudinal direction, whereas the corresponding mean peak drift ratios for the Murray Ridge Bridge were 3.6% and 2.4%. The mean peak tensile strain of the longitudinal reinforcement at the top of the columns was 2.2% for the Mono Way Bridge and 1.5% for the Murray Ridge Bridge. The mean residual drift ratios for both bridges were limited to less than 0.5%.
2. The reliability of the proposed displacement-based analysis (DBA) approach was demonstrated. The proposed equivalent viscous damping expression of a rocking footing to be used in DBA results to a prediction that closely matches the median NRHA drift ratio demand. It was also showed that irrespective of the ground motion set used, 68% of

the displacement demands predicted by DBA were within a factor of 2 higher and a factor of 1.3 lower than the drift ratio demand computed from the NRHA.

3. The three-dimensional NRHA of the redesigned bridges, showed that the proposed DBA method for excitation in the transverse bridge direction provides a reasonable, but somewhat conservative (by approximately 20%) estimate of the mean drift ratio demand, when the relative contribution of high energy dissipation mechanisms at the abutments to the overall lateral bridge strength is small (Mono Way Bridge). When the abutment contribution increases (Murray Ridge Bridge), the proposed DBA method significantly overestimates drift demands (by approximately 100%) as it only accounts for the abutments' strength but not for the large energy dissipation expected from abutment sliding mechanisms. When such abutment energy dissipation characteristics are approximately quantified by an additional modification factor, the predicted DBA drift demands improve significantly for the Murray Ridge Bridge (less than 10% error).
4. The coupling between the deck uplift at the abutments and uplift of the bents (due to foundation uplift) under transverse excitation can cause significant variation of axial loads that are not considered in the DBA. The Murray Ridge Bridge, with a relatively wide deck supported on one rocking footing per bent and rotational fixity at the column-deck connection produced more significant coupling than the Mono Way Bridge example. The uplift forces at the abutment could be ameliorated by use of multi-column bents with plastic hinging or a pinned connection at the tops of the columns, but exploration of this alternative was outside the scope of this project.
5. NRHA drift demands in the longitudinal direction of the two re-designed bridges were well predicted by the DBA method (overestimation of 3% for the Mono Way Bridge and 30% for the Murray Ridge Bridge) due to the used bridge-level approach that directly accounts for both the strength and energy dissipation characteristics of all contributing components.
6. Response spectrum analysis (RSA) of the two bridges using 5% damping and two abutment models, a "locked" and an "unlocked" case, did not provide definite conclusions about the reliability and accuracy of the method that assumes validity of the equal displacement rule. Overall, the "unlocked" abutment models compared more reasonably to the NRHA results for the bridges and seismic hazard level considered in

this study. The “unlocked” abutment models underestimated peak displacement demands in the transverse direction by 30% and overestimated displacement demands in the longitudinal direction by 20%.

References

Allmond, J., and Kutter, B. L. (2014). “Design considerations for rocking foundations on unattached piles.” *J. Geotech. Geoenviron. Eng.*, 140(10), 10.1061/(ASCE)GT.1943-5606.0001162, 04014058.

Anastasopoulos, I., Gazetas, G., Loli, M., Apostolou, M., and Gerolymos, N. (2010). “Soil failure can be used for seismic protection of structures.” *Bull. Earthquake Eng.*, 8(2), 309–326.

Anastasopoulos, I., Kourkoulis, R., Gelagoti, F., and Papadopoulos, E. (2012). “Rocking response of SDOF systems on shallow improved sand: an experimental study.” *Soil. Dyn. Earthquake Eng.*, 40, 15–33.

Anastasopoulos, I., Loli, M., Georgarakos, T., and Drosos, V. (2013). “Shaking table testing of rocking—isolated bridge pier on sand.” *J. Earthquake Eng.*, 17(1), 1–32.

Antonellis, G., and Panagiotou, M. (2013). “Seismic design and performance of bridges with columns on rocking foundations.” *PEER Rep. No. 2013/21*, Pacific Earthquake Engineering Research Center, Univ. of California, Berkeley, California.

Antonellis, G., and Panagiotou, M. (2014). “Seismic response of bridges with rocking foundations compared to that of fixed-base bridges at a near-fault site.” *J. Bridge Eng.*, 19(5), 10.1061/(ASCE)BE.1943-5592.0000570, 04014007.

Antonellis, G., Gavras, A. G., Panagiotou, M., Kutter, B. L., Guerrini, G., Sander, A. C., and Fox, P. J. (2015). “Shake table test of large-scale bridge columns supported on rocking shallow foundations.” *J. Geotech. Geoenviron. Eng.*, 141(5), 10.1061/(ASCE)GT.1943-5606.0001284, 04015009.

Applied Technology Council (ATC). (2005). “Improvement of nonlinear static seismic analysis procedures.” *Rep. Prepared for the Dept. of Homeland Security, FEMA, FEMA 440*, Redwood City, California.

Aviram, A., Mackie, K. R., and Stojadinović, B. (2008). “Guidelines for nonlinear analysis of bridge structures in California.” *PEER Rep. No. 2008/03*, Pacific Earthquake Engineering Research Center, Univ. of California, Berkeley, California.

Baker, J., Lin, T., Shahi, S., and Jayaram, N. (2011). “New ground motion selection procedures and selected motions for the PEER transportation research program.” *PEER Report No. 2011/03*, Pacific Earthquake Engineering Research Center, Univ. of California, Berkeley, California.

Blandon, C. A., and Priestley, M. J. N. (2005). “Equivalent viscous damping equations for direct displacement based design.” *J. Earthquake Eng.*, 9(SI 2), 257–278.

Boore, D. M., and Atkinson, G. M. (2008). "Ground-motion prediction equations for the average horizontal component of PGA, PGV, and 5%-damped PSA at spectral periods between 0.01 s and 10.0 s." Earthquake Spectra, 24(1), 99–138.

Boulanger, R. W., (2000). "*The PySimple1, TzSimple1, and QzSimple1 Material Models.*" Documentation for the OpenSees platform, ‹http://opensees.berkeley.edu›.

Boulanger, R. W., Curras, C. J., Kutter, B. L., Wilson, D. W., and Abghari, A., (1999). "Seismic soil-pile structure interaction experiments and analyses." *J. Geotech. Geoenviron. Eng.*, 125, 750–759.

Caltrans. (2010). "*Memo to designers 20-1*." California Department of Transportation, Sacramento, California.

Caltrans. (2013a). "*Seismic design criteria*." California Department of Transportation, Version 1.7, Sacramento, California.

Caltrans. (2013b). "Caltrans ARS Online (v2.3.06)." ‹http://dap3.dot.ca.gov/ARS_Online/›.

Chopra, A. K., and Goel, R. K. (2001). "Direct displacement-based design: use of inelastic vs. elastic design spectra." *Earthquake Spectra*, 17(1), 47–64.

Deng, L., and Kutter, B. L. (2012). "Characterization of rocking shallow foundations using centrifuge model tests." *Earthquake Eng. Struct. Dyn.*, 41(5), 1043–1060.

Deng, L., Kutter, B. L., and Kunnath, S. (2012a). "Centrifuge modeling of bridge systems designed for rocking foundations." *J. Geotech. Geoenviron. Eng.*, 138(3), 335–344.

Deng, L., Kutter, B. L., and Kunnath, S. (2012b). "Probabilistic seismic performance or rocking-foundation and hinging-column bridges." *Earthquake Spectra*, 28(4), 1423–1446.

Deng, L., Kutter, B. L., and Kunnath, S. (2014). "Seismic design of rocking shallow foundations: Displacement-based methodology." *J. Bridge Eng.*, 19(11), 10.1061/(ASCE)BE.1943-5592.0000616, 04014043.

Drosos, V., Georgarakos, T., Loli, M., Anastasopoulos, I., Zarzouras, O., and Gazetas, G. (2012). "Soil-foundation-structure interaction with mobilization of bearing capacity: experimental study on sand." *J. Geotech. Geoenviron. Eng.*, 138(11), 1369–1386.

Dwairi, H. M., and Kowalsky, M. J. (2006). "Implementation of inelastic displacement patterns in direct displacement-based design of continuous bridge structures." *Earthquake Spectra*, 22(3), 631–662.

Dwairi, H. M., Kowalsky, M. J., and Nau, J. M. (2007). "Equivalent damping is support of direct displacement-based design." *J. Earthquake Eng.*, 11(4), 521–530.

European Committee for Standardization (CEN). (1998). "Eurocode 8: Design of structures for earthquake resistance—Part 1: General rules, seismic actions and rules for buildings." *Pre-EN 1998-1*, Brussels, Belgium.

European Committee for Standardization (CEN). (2005). "Eurocode 8: Design of structures for earthquake resistance—Part 2: Bridges." *EN 1998-2*, Brussels, Belgium.

Gajan, S., Hutchinson, T. C., Kutter, B. L., Raychowdhury, P., Ugalde, J. A., and Stewart, J. P. (2008). "Numerical models for analysis and performance-based design of shallow foundations subjected to seismic loading." *PEER Rep. No. 2007/04*, Pacific Earthquake Engineering Research Center, Univ. of California, Berkeley, California.

Gajan, S., and Kutter, B. L. (2008). "Capacity, settlement and energy dissipation of shallow footings subjected to rocking." *J. Geotech. Geoenviron. Eng.*, 134(8), 1129–1141.

Gajan, S., and Kutter, B. L. (2009). "Effects of moment-to-shear ratio on combined cyclic load-displacement behavior of shallow foundations from centrifuge experiments." *J. Geotech. Geoenviron. Eng.*, 135(8), 1044–1055.

Gajan, S., Raychowdhury, P., Hutchinson, T. C., Kutter, B. L., and Stewart, J. P. (2010). “Application and validation of practical tools for nonlinear soil-foundation interaction analysis.” *Earthquake Spectra*, 26(1), 111–129.

Gazetas, G. (1991). *Foundation vibrations.* Foundation engineering handbook, H. Y. Fang, ed., 2nd Ed., Kluwer/Springer, New York City, 553–593.

Gazetas, G., Anastasopoulos, I., and Apostolou, M. (2007). “Shallow and deep foundations under fault rupture or strong seismic shaking.” *4th International Conference on Earthquake Geotechnical Engineering*, Thessaloniki, Greece, 25–28 June.

Grant, D. N., Blandon, C. A., and Priestley, M. J. N. (2005). “Modelling inelastic response in direct displacement-based design.” *Rep. No. ROSE 2005/03*, European School for Advanced Studies in Reduction of Seismic Risk, Pavia, Italy.

Gulkan, P., and Sozen, M. (1974). “Inelastic response of reinforced concrete structures to earthquake motion.” *ACI Journal*, 71, 604–610.

Hakhamaneshi, M., Kutter, B. L., Deng, L., Hutchinson, T. C., and Liu, W. (2012) “New findings from centrifuge modeling of rocking shallow foundations in clayey ground.” *GeoCongress 2012*, 195–204.

Hakhamaneshi, M. (2014). “Rocking foundations for building systems – effect of footing shape, soil environment, embedment and normalized moment-to-shear ratio.” Ph.D. Dissertation, Dept. of Civil and Environmental Engineering, Univ. of California at Davis, Davis, California.

Hakhamaneshi, M., Kutter, B.L. (201X). “Effect of footing shape and embedment on the settlement, re-centering and energy dissipation of shallow footings subjected to rocking.” *J. Geotech. Geoenviron. Eng.*, (in review).

Harden, C. W. and Hutchinson, T. C. (2009). “Beam-on-nonlinear-Winkler-foundation modeling of shallow, rocking-dominated footings.” *Earthquake Spectra*, 25(2), 277–300.

Jacobsen, L. S. [1930] “Steady forced vibrations as influenced by damping.” *Trans. Am. Soc. Mech. Eng.*, 52(1), 169–181.

Jeong, H. I., Sakai, J., and Mahin, S. A. (2008). “Shaking table tests and numerical investigation of self-centering reinforced concrete bridge columns.” *PEER Rep. No. 2008/6*, Pacific Earthquake Engineering Research Center, Berkeley, California.

Khosravi, M., Tamura, S., Boulanger, R. W., Wilson, D. W., Olgun, C. G., Rayamajhi, D., Wang, Y., (2015). “Seismic performance of soil-cement grid supporting a structure over soft clay.” *The Deep Mixing 2015 Conference*, San Francisco, California, 631–640.

Kokkali, P., Abdoun, T., and Anastasopoulos, I. (2015). “Centrifuge modeling of rocking foundations on improved soil.” *J. Geotech. Geoenviron. Eng.*, 10.1061/(ASCE)GT.1943-5606.0001315, 04015041.

Kowalsky, M. J. (1994). “Displacement-based design-a methodology for seismic design applied to RC bridge columns.” Master’s Thesis, Dept. of Structural Engineering, Univ. of California at San Diego, La Jolla, California.

Kowalsky, M. J., Priestley, M. J. N., and McRae, G. A. (1994). “Displacement based design of RC bridge columns.” *Proc., 2nd Int. Workshop Seismic Design of Bridges*, New Zealand Society for Earthquake Engineering, Wellington, New Zealand, 1, 138–163.

Liu, W., Hutchinson, T. C., Gavras, A. G., Kutter, B. L., and Hakhamaneshi, M. (2015). “Seismic behavior of frame-wall-rocking foundation systems. I: Test program and slow cyclic results.” *J. Struct. Eng.*, 10.1061/(ASCE)ST.1943-541X.0001264, 04015059.

Loli, M., Knappett, J. A., Brown, M. J., Anastasopoulos, I., and Gazetas, G. (2014). "Centrifuge modeling of rocking-isolated RC bridge piers." *J. Earthquake Eng. Struct. Dyn.*, 43(15), 2341–2359.

Lu, Y., and Panagiotou, M. (2014). "Characterization and representation of near-fault ground motions using cumulative pulse extraction with wavelet analysis." *Bull. Seismol. Soc. Am.,* 104(1), 410–426.

Mazzoni, S., McKenna, F., Scott, M. H., and Fevens, G. L. (2014). *Open system for earthquake engineering simulation user command-language manual*, Pacific Earthquake Engineering Research Center, Univ. of California, Berkeley, California.

Menun, C., and Der Kiureghian, A. (1998). "A replacement for the 30%, 40%, and SRSS rules for multicomponent seismic analysis." *Earthquake Spectra*, 14(1), 153–163.

Negro, P., Paolucci, R., Pedretti, S., and Faccoili, E. (2000). "Large scale soil-structure interaction experiments on sand under cyclic loading." *12th World Conf. Earthquake Eng.*, International Association for Earthquake Engineering, Tokyo.

Ni, P., Petrini, L., and Paolucci, R. (2013). "Direct displacement-based assessment with nonlinear soil–structure interaction for multi-span reinforced concrete bridges." *Struct. Infrastruct. Eng.*,10(9), 1211–1227.

Paolucci, R., Figini, R., and Petrini, L. (2013). "Introducing dynamic nonlinear soil-foundation-structure interaction effects in displacement-based seismic design." *Earthquake Spectra*, 29(2), 475–496.

Paolucci, R., Shirato, M., and Yilmaz, M. T. (2008). "Seismic behavior of shallow foundations: shaking table experiments vs. numerical modeling." *Earthquake Eng. Struct. Dyn.*, 37(4), 577–595.

Pecker, A. (2006). "Enhanced seismic design of shallow foundations: example of the Rion Antirion Bridge." 4th Athenian Lecture on Geotechnical Engineering, *Bull. Hellenic Geotech. Soc.*, Athens, Greece.

Pecker, A., Paolucci, R., Chatzigogos, C., Correia, A., and Figini, R. (2014). "The role of non-linear dynamic soil-foundation interaction on the seismic response of structures." *Bull. Earthquake Eng.*, 12(3), 1157–1176.

Priestley, M.J.N. (2003). "Myths and fallacies in earthquake engineering, revisited." *The 9th Mallet Milne Lecture*, IUSS Press, Pavia, Italy.

Priestley, M. J. N., and Grant, D. N. (2005). "Viscous damping in seismic design and analysis." *J. Earthquake Eng.*, 9(SI 2), 229–255.

Priestley, M. J. N., Calvi, G. M., and Kowalsky, M. J. (2007). *Displacement-based seismic design of structures,* IUSS Press, Pavia, Italy.

Rosenbluet, E., and Herrera, I. (1964) "On a kind of hysteretic damping." *J. Eng. Mech.*, 90(4), 37–48.

Şadan, Q. B., Petrini, L., and Calvi, G. M. (2013). "Direct displacement-based seismic assessment procedure for multi-span reinforced concrete bridges with single-column piers." *J. Earthquake Eng. Struct. Dyn.*, 42(7), 1031–1051.

Shirato, M., Kouno, T., Asai, R., Nakani, N., Fukui, J., and Paolucci, R. (2008). "Large-scale experiments on nonlinear behavior of shallow foundations subjected to strong earthquakes." *Soils Found.*, 48(5), 673–692.

Tsatsis, A., and Anastasopoulos, I. (2015). "Performance of rocking systems on shallow improved sand: shaking table testing." *Front. Built Environ.*, 10.3389/fbuil.2015.00009.

Ugalde, J. A., Kutter, B. L., Jeremić, B., and Gajan, S. (2007). "Centrifuge modeling of rocking behavior of bridges on shallow foundations." *4th International Conference on Earthquake Geotechnical Engineering*, Thessaloniki, Greece, 25–28 June.

Wang, S., Kutter, B. L., Chacko, J. M., Wilson, D. W., Boulanger, R. W., and Abghari, A. (1998). "Nonlinear seismic soil-pile structure interaction." *Earthquake Spectra*, 14, 377–396.